ACOUSTIC EMISSION ANALYSIS FOR QUALITY ASSESSMENT OF THERMALLY SPRAYED COATINGS

Nadimul Haque Faisal

A dissertation submitted for the degree of Doctor of Philosophy

Heriot-Watt University

School of Engineering and Physical Sciences

November 2009

Abstract

This study describes a new approach to the quality assessment of thermally sprayed carbide and ceramic coatings produced by High Velocity Oxy-Fuel (HVOF) and Air Plasma Spray (APS) processes. The aim of the work was to develop an experimental methodology based on Acoustic Emission (AE) monitoring of a dead-weight Vickers indentation to assess the degree of cracking and hence the toughness of the coating. AE monitoring was also applied to an industrial process as a contribution to the possibility of quality assessment during the deposition process.

AE data were acquired during indentation tests on samples of coating of nominal thickness 250-325 μm at a variety of indentation loads ranging from 49 to 490 N. Measurements were carried out on six different thick-film coatings (as-sprayed HVOF-JP5000/JetKote WC-12%Co, HIPed HVOF-JetKote WC-12%Co, as-sprayed HVOF-JP5000 WC-10%Co-4%Cr, conventional powder APS-Metco/9MB Al_2O_3 and fine powder HVOF-theta gun Al_2O_3) and also on soft and hard metallic samples and metals. The raw AE signals were analysed along with force and displacement history and the total surface crack length around the indent determined. Also, a selection of the indents was sectioned in order to make some observations on the sub-surface damage. The results show characteristic AE time evolutions during indentation for tough metals, hard metals, and carbide and ceramic coatings. Within each category, AE can be used as a suitable surrogate for crack length measurement for assessing coating quality.

Finally, a preliminary observation on AE monitoring during HVOF (JP5000) WC-10%Co-4%Cr thermal spraying was made. It was found that AE is sensitive to individual particle landings during thermal spraying and therefore can, in principle, be used to monitor the spray process.

ACADEMIC REGISTRY
Research Thesis Submission

Name*:*	Nadimul Haque Faisal		
School/PGI:	School of Engineering and Physical Sciences		
Version: *(i.e. First, Resubmission, Final)*	Final	Degree Sought (Award **and** Subject area)	PhD Mechanical Engineering

Declaration

In accordance with the appropriate regulations I hereby submit my thesis and I declare that:

1) the thesis embodies the results of my own work and has been composed by myself
2) where appropriate, I have made acknowledgement of the work of others and have made reference to work carried out in collaboration with other persons
3) the thesis is the correct version of the thesis for submission and is the same version as any electronic versions submitted*.
4) my thesis for the award referred to, deposited in the Heriot-Watt University Library, should be made available for loan or photocopying and be available via the Institutional Repository, subject to such conditions as the Librarian may require
5) I understand that as a student of the University I am required to abide by the Regulations of the University and to conform to its discipline.

* *Please note that it is the responsibility of the candidate to ensure that the correct version of the thesis is submitted.*

Signature of Candidate*:*		Date:	

Submission

Submitted By *(name in capitals):*	NADIMUL HAQUE FAISAL
Signature of Individual Submitting:	
Date Submitted:	

For Completion in Academic Registry

Received in the Academic Registry by *(name in capitals):*			
1.1 Method of Submission *(Handed in to Academic Registry; posted through internal/external mail):*			
1.2 E-thesis Submitted (**mandatory for final theses from January 2009)**			
Signature:		Date:	

Dedication

To my wonderful parents

Farhat Naquib, Naquibul Haque

and lovely wife

Alvia Faisal

Acknowledgements

I have been very fortunate to receive a great deal of support throughout the course of my research and I wish to express my gratitude for the help given by all three of my supervisors, Prof. R. (Bob) L. Reuben, Dr. Rehan Ahmed and Prof. John (Iain) A Steel. I would like to thank to School of EPS, Heriot-Watt University for providing scholarship for my studies.

Importantly, I would also like to express my appreciation to Mrs. A. Blyth, Mrs. M. Thomson, Mrs. J. Jones, Mrs. R. Crawford, Dr. Mohamed, Dr. Virgil, Dr. Hao Yu, Dr. Prabhakara, Dr. Nirav Thakkar, Dr. Neruda, Dr. Mostafa, Dr. Ryan, Shadi, Azamhani, Ghazi, Dr. Carmen, Dr. Angus, Wael, Steven, Stefan, Dr. Khalid and all other friends and researchers of the Mechanical and Chemical department who made my time very memorable and extremely enjoyable.

I owe a sincere depth of gratitude for their invaluable assistance, all the members of the Mechanical Workshop and IT office for helping me with this work, in particular Mr. George Smith, Mr. Alf Buchan, Mr. Mark, Mr. Richard Kinsella, Mr. Aftab Aziz, Mr. Paul Glynn, Mr. Cameron Smith. Special thanks to Ms Marian Millar who helped me throughout the research with XRD and SEM, Dr. Jim Buckman for ESEM, Mr. Kenny Carruthers who helped me in developing the test fixtures for instrumentation of the Vickers hardness machine and Mr. Chris who helped me in developing the test rig using CNC cutting machines used in monitoring AE during thermal spraying.

I would like to thank Deloro Stellite Ltd., UK and Fujimi Incorporated, Japan for supplying the coated specimens for this study and to Metallurgist, Bill Taylor, at Struers Ltd., UK, for his support in the metallurgical preparation of the cross-section of the Vickers indent for sub-surface damage assessment. Further to this, I am very thankful to Mr. Bryan Allcock, Monitor Coatings Limited, for allowing me to perform AE monitoring during HVOF thermal spraying at his company. I would like to express my special thanks to my previous employer and colleagues at Surface Engineering Division of ARCI, India, where I was first introduced with surface coating techniques and its industrial applications. Finally, I would like to thank my family members and other friends for their unlimited moral support and welcome series of social distraction.

Table of Contents

List of publications from this study

1. **N. H. Faisal**, J. A. Steel, R. Ahmed, R. L. Reuben, G. Heaton and B. Allcock, "Application of acoustic emission for monitoring the HVOF thermal spraying process", *Advanced Materials Research*, Vol. 13-14 (2006), pp. 291-297 [*Also Oral and Poster Presentation in the 27th European Conference on Acoustic Emission Testing (EWGAE-2006), 20-22nd Sept. 2006, Cardiff, UK*]
2. **N. H. Faisal**, J. A. Steel, R. Ahmed, R. L. Reuben: "The use of acoustic emission to characterise fracture behaviour during Vickers indentation of HVOF thermally sprayed WC-Co coatings" (Journal: *Journal of Thermal Spray Technology*, Preprint DOI: 10.1007/s11666-009-9334-1, May 2009)
3. R. Ahmed, **N. H. Faisal**, R. L. Reuben, A. Paradowska, M. Fitzpatrick, J. Kitamura, S. Osawa: "Neutron Diffraction Residual Strain measurements in Alumina Coatings Deposited via Air Plasma and High Velocity Oxy-Fuel Techniques", (*International Conference on Neutron Scattering 2009, May 3 - 7, 2009, Knoxville, Tennessee, USA***,** Article submitted**:** *Journal of Physics: Conference Series*, June 2009)
4. **N. H. Faisal**, R. Ahmed, R. L. Reuben, S. Balasubramanian: "Implementing LAMMPS molecular dynamics simulation with focus on thermally sprayed particle impact**",** *EPSRC Symposium Workshop on Molecular Dynamics*, June 1-5, 2009**,** The University of Warwick, UK (poster presented)
5. **N. H. Faisal**, R. L. Reuben, R. Ahmed, J. A. Steel: "Application of acoustic emission to study the Vickers indentation behaviour of thermally sprayed cermet/ceramic coatings" (manuscript in preparation for Journal: *Journal of Thermal Spray Technology*)
6. **N. H. Faisal**, R. L. Reuben, R. Ahmed, J. A. Steel: "An improved measurement technique in instrumented Vickers indentation" (manuscript in preparation for Journal: *Measurement Science and Technology*)
7. **N. H. Faisal**, R. Ahmed, R. L. Reuben, J. A. Steel: "Indentation Testing and Its Acoustic Emission Response: Applications and Emerging Trends" (A critical review in preparation: *International Materials Reviews*)
8. R. Ahmed, **N. H. Faisal**, R. L. Reuben, A. Paradowska, M. Fitzpatrick, J. Kitamura, S. Osawa: "Residual Stresses in Thermally Sprayed Alumina Coatings Deposited Via Air Plasma and High Velocity Oxy-Fuel Techniques", (manuscript in advanced preparation for Journal: *Materials Science and Engineering A*)

Chapter 1

INTRODUCTION

1.1 Research context

The pyramidal diamond Vickers indentation test has been used not only to quantify the hardness of materials [1] but also to study the generation of micro-fracture in brittle materials [2-4]. Various authors have also used crack patterns around indentations at, and beneath, the surface to assess the fracture toughness of ceramics [5-11], study the hardness of plasma-sprayed coatings [12-14], and evaluate the residual stress, adhesive strength and fracture toughness of thermally sprayed HVOF cermet coatings [15-19]. However, no specific work has studied micro-fissuring of thermal sprayed ceramic coating materials during (as opposed to after) the indentation process and the potential that this gives for separation of the various accommodation mechanisms around the indenter and hence an improved understanding of the key microstructural variables which give resistance to wear in extreme conditions.

AE is a non-destructive technique that has been used widely to monitor damage processes in engineering materials [20], as well as for condition monitoring [21-26]. It is well established that crack extension processes give rise to AE which can be recorded using sensors placed on the surface of the structure or sample of interest. There have been some limited studies of the use of AE to study fracture during indentation, for example by Safai *et al*. [27] who found the total AE event count during Brinell indentation tests to be related to the porosity of plasma sprayed alumina coatings. They noted that the high critical loads for this particular coating-substrate couple were not enough to generate de-bonding at the interface during indentation but they suggested that some of the AE sources might be due to mechanically-induced closure of pores. Prasad *et al*. [28] used on-line AE monitoring along with off-line damage assessment by SEM to corroborate the critical loads for plasma-sprayed alumina-titania coating systems subjected to Vickers indentation. They suggested that, when the material is yielding plastically, the AE signal will be of a more continuous type with a lower characteristic frequency content (35-40 kHz) than when the material is cracking, where the instantaneous relaxation produces burst type AE signals with a characteristic frequency in the range 220-280 kHz. Vijayakumar *et al*. [29] applied high-frequency

dynamic impacts (at 20 kHz) with a diamond pyramid indenter to plasma-sprayed alumina-titania coatings with and without subsequent microwave-treatment and found the frequency of the AE signal to be in the range of 200-400 kHz for the as-sprayed coatings and 800-900 kHz for the microwave-treated coatings. Sentruk *et al*. [30] found that the presence of a bond coat layer of NiCrAl in partially stabilized plasma sprayed zirconia (PSZ) ceramic coatings suppresses AE activity during Hertzian indentation, and attributed this to surface compressive stresses inhibiting cracks. Sentruk *et al*. [30] also observed that the critical load (found based on AE energy) during indentation is higher when a bond coat layer is present for both continuously and non-continuously sprayed coatings.

Stoica *et al*. [31] and Stoica [32] give a typical example of the fracture pattern around Vickers indentations in functionally graded HVOF WC-NiCrBSi, preferring qualitative analysis to the empirical models as reviewed by Ponton and Rawlings [33] to obtain fracture toughness. They pointed out that, if micro-fissuring in the sub-surface region takes the place of surface radial cracks at lower loads, this complicates the issue of using empirical models to measure fracture toughness. Factor and Roman [34-35] observed both radial and circular cracks in thermally sprayed coatings, but found that most were of mixed characteristic and were not easy to categorise. The uncertainty in measuring the crack lengths in cracking from indentation [34-36] makes empirical fracture models (e.g. Palmqvist/radial-median) unsuitable, in particular for thermal sprayed coatings, and it is expected that AE monitoring along with load and displacement transducer signals may provide a solution to this problem, given that AE potentially can detect events associated with cracks both on and beneath the surface.

In addition to AE monitoring during Vickers indentation, the relationship between measured AE features and HVOF Thermal Spray (TS) process parameters is also investigated in this work. AE detection during spraying has a potential advantage over current conventional coating quality testing techniques such as indentation, bending and residual stress analysis, which are destructive and cannot be carried out during the process. There are no industrial on-line coating quality monitoring systems and quality control usually involves post-process acceptance sampling/testing of test coupons.

It is widely acknowledged in the thermal spray industry that existing quality control techniques and testing techniques need to be improved. New techniques which help to

understand the effects of coating process parameters on the characteristics of the coating are therefore of value, as are new methods of coating quality assessment with minimal destruction.

1.2 Objective and scope of present research work

The primary aim is to find an AE based method of recognising and characterising the indentation fracture pattern of surface and critical load in thermal sprayed carbide and ceramic coatings with a view to rapid coating quality evaluation. A test that can be applied quickly and efficiently, perhaps as an adjunct to the manufacturing process, and perhaps with better resolution than can be obtained by measurement of surface cracks is of obvious value. The sensitivity of AE offers the potential for minimally invasive indentation tests, provided that the near-surface behaviour can be taken as representative of the coating as a whole. The Vickers indentation technique was chosen because the stages of failure (i.e. surface cracks, sub-surface cracks localised deformation and pore closure and, possibly, sub-surface lateral cracks leading to delamination) are fairly well-studied giving a basis on which to investigate how AE can be used to monitor these processes. This study also aims to determine if the sources of AE generated during HVOF thermal spraying can be characterised in relation to final coating structure and to the spray process parameters such as gun transverse speed and gas pressure for a given powder-particle size and spraying distance.

It is anticipated that this research will ultimately lead to the establishment of AE-based coating quality monitoring to assess residual stresses, porosity, cohesive and adhesive strength and other coating defects quantitatively, by observations of the micro fracture and plastic deformation behaviour as reflected in the AE signal. The applications of this non-destructive test will range from quality control to the optimisation of coating processes and process parameters.

The objectives were therefore:

a) To understand the Vickers indentation behaviour of soft and hard metals and thermal sprayed carbide and ceramic coatings surface as reflected in the AE;

b) To recognise and characterise the Vickers indentation fracture pattern of surface; and critical load in thermal sprayed carbide and ceramic coatings using the raw AE signal;
c) To exploit the various AE features to estimate the fracture toughness of thermal sprayed coatings;
d) To identify various AE sources during thermal spraying process.

1.3 Research methodology

No specific work has studied micro-fissuring of thermal sprayed coating materials during the Vickers indentation process and the potential that AE gives for separation of the various accommodation processes. The methodology was therefore centred on a series of observations of AE during indentation. In a subset of the tests both load and indenter positions were recorded at the same time as the AE for a wide range of materials so that the sources of AE could be characterised. In the main tests, observations were made on the microstructure and cracking patterns both on the surface and across the section of the specimens. The indentation tests were carried out at a range of loads in order that some idea of the development of cracking patterns could be obtained, lower load tests corresponding very roughly to the earlier stages of higher load tests. In this way it was expected that a picture of the accommodation processes could be built up for comparison with the observed time evolution of the AE.

1.4 Thesis outline

Chapter 1: Introduction. This chapter gives a description of how the present work is inspired and addresses its contribution to the development of thermal spray coating indentation testing methodology using AE techniques

Chapter 2: Literature Review. The first section reviews some aspects of indentation testing of materials including potential sources of AE, its application to thermally sprayed ceramic coatings, and the various indentation testing systems. The second section summarizes the state of knowledge on AE techniques applied to indentation testing of bulk materials and coatings including thermally sprayed coatings. The third section briefly describes the thermal spray process with a focus on the High Velocity Oxy-Fuel (HVOF) and Air Plasma Spray (APS) techniques, with a view to identifying

sources of AE during these processes. Finally, the thesis topic is described identifying the contribution to be made.

Chapter 3: Experimental Procedures. This chapter describes the experimental apparatus, materials and methods used for the research including analysis techniques. Two distinct types of experiments were used, the first related to AE monitoring of the Vickers indentation behaviour of metals and thermally sprayed carbide and ceramic coatings, and the second related to AE monitoring of the thermal spraying process itself.

Chapter 4: Results. This chapter presents experimental results from the open loop dead-weight type Vickers indentation testing and its AE response on various metals and thermal sprayed carbide and ceramic coating specimens. It also presents results from AE monitoring during the thermal spraying process.

Chapter 5: Discussion. This chapter provides an overall interpretation of the experimental results covering the important aspects related to the Vickers indentation behaviour of the thermal sprayed carbide and ceramic coatings and monitoring the thermal spraying process.

Chapter 6: Concluding remarks and recommendations for future work are presented.

Contribution to knowledge:

As far as the author is aware, no systematic attempts have been made to relate accommodation processes during indentation to AE on thermally sprayed carbide and ceramic coatings. Furthermore, the identification of fracture stages and zones during indentation of these coatings, the identification of multiple sources in the thermal spraying process, the development of experimental and analytical models for AE during indentation and thermal spraying process, are, to the author's knowledge, significant contributions. The overall outcome of improved assessment of coating quality using on-line AE based measurement during Vickers indentation is therefore the specific area in which a contribution to knowledge is claimed. Additionally, a better understanding of the Vickers indentation behaviour of materials is also presented through a new instrumentation technique.

Chapter 2

LITERATURE REVIEW

This chapter is divided into three main sections. The first section reviews some aspects of indentation testing of materials including potential sources of AE, its application to thermally sprayed coatings, and the force/displacement profiles typical of dead-weight indentation systems. The second section summarizes the state of knowledge on acoustic emission (AE) techniques applied to indentation testing of bulk materials and coatings including thermally sprayed coatings. The third section briefly describes the thermal spray process with focus on the High Velocity Oxy-Fuel (HVOF) and Air Plasma Spray (APS) techniques, with a view to identifying sources of AE during these processes.

2.1 Indentation testing

2.1.1 Mechanics of indentation and potential sources of AE

Indentation essentially consists of pressing a non-compliant indenter into the surface of the material to be tested. The material can accommodate the indenter by elastic or plastic deformation, local cracking, material densification, or a combination of these accommodation mechanisms. Most commonly, the material is assessed by the size of the impression and/or by the cracking pattern left on the surface once the indenter has been removed. There are two main approaches to the mechanics of indentation depending upon the whether the accommodation is by deformation or by fracture.

Elastic, perfectly plastic and hydrostatic pressure models have been developed to describe indentation [1, 37-38]. For an elastic material, the indentation impression disappears after unloading, whereas, for plastic material, permanent deformation occurs around the indentation [1]. Two types of plastic material accommodation can be identified (see **Figure 2.1**) using the slip-line field solution [39], upward extrusion of displaced material very close to the periphery (‘piling-up’), or downward depression of displaced material around the periphery (‘sinking-in’). The ‘piling-up’ effect is expected in materials which work-harden (e.g. soft metals), whereas ‘sinking-in’ is expected in hard materials (e.g. hard metals or brittle thick coatings).

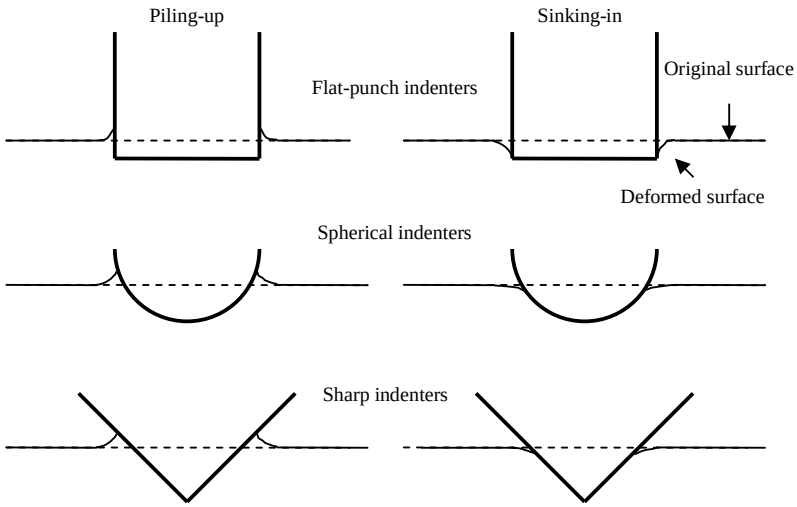

Figure 2.1 2-D deformations in an elastic-perfectly plastic material around the indentation produced by blunt and sharp indenters [adapted from ref. 1]

Slip-line field models calculate deformation under the indenter by allowing plastic deformation along available slip-lines (**Figure 2.2**) once the yield criterion (Tresca or von-Mises) has been met [1, 37-39]. A slip-line is a line of maximum shear stress and the field can be seen as a curvilinear mesh of two orthogonal families of lines radiating from arc centres (A and B in **Figure 2.2**). For example, considering friction-free deformation of an ideal plastic metal (yield stress Y) by an infinitely long, hard and undeformable flat punch, the shear stress at the edges (A and B) of the punch will be relatively high, and the metal in the region of A and B will be in a state of plasticity. In other parts of the metal the overall yielding will be small, but, as the punch load is increased, the size of the plastic region increases allowing the indenter to penetrate. Plastic flow occurs when the maximum shear stress reaches a critical value k, where $2k = 1.15Y$ or where $2k = Y$ for the von-Mises and Tresca criteria, respectively. Using various indenter shapes, the material flow direction under the indenter can be assessed.

In the hydrostatic pressure model [3] as shown schematically in **Figure 2.3**, the ductile material accommodates the indenter due to an outwardly expanding hydrostatic core (plastic region). The hydrostatic core causes the observed symmetry of the stress field under the indenter and it leads to the development of a hemispherical plastic zone around the indenter outside of which the material deforms elastically.

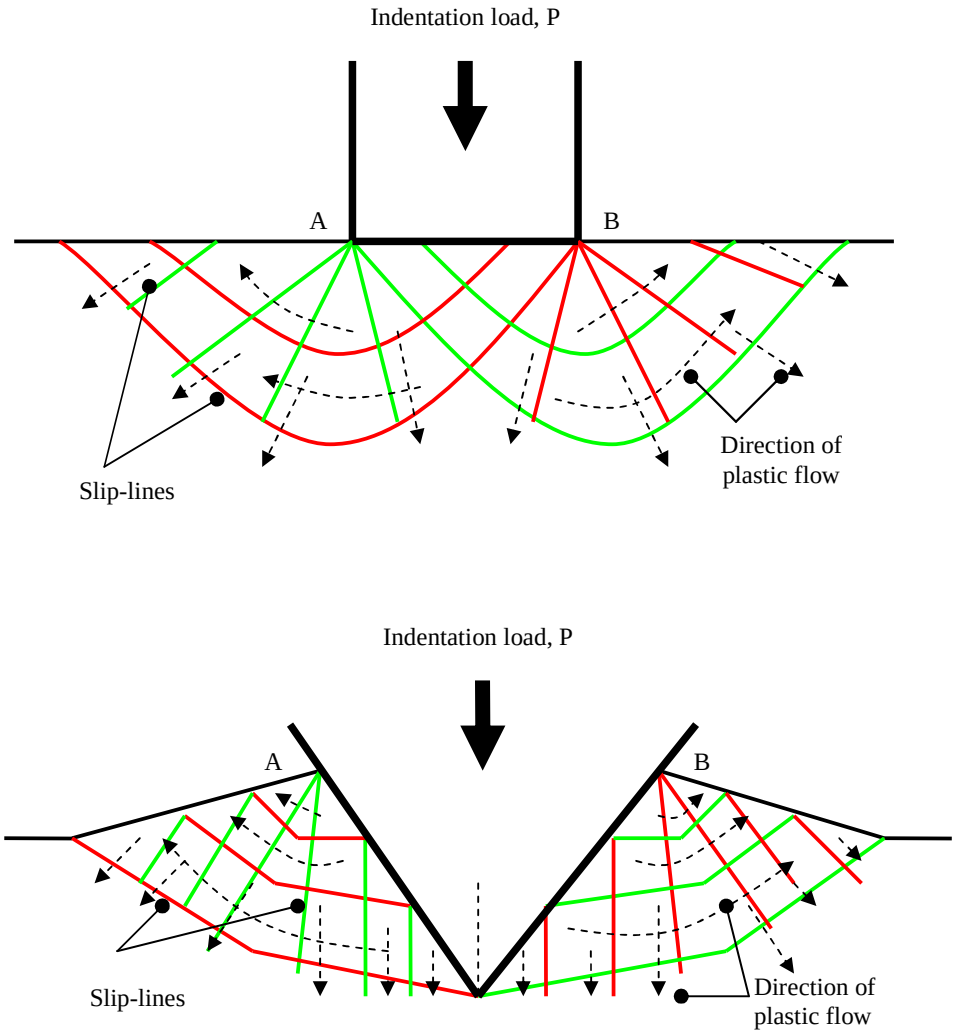

Figure 2.2 Slip-line-field solutions for indentation of rigid-plastic half space solid by a frictionless (a) flat-ended 2-D punch indenter showing no piling-up or sinking-in, (b) wedge shaped 2-D indenter showing piling-up [adapted from ref. 1].

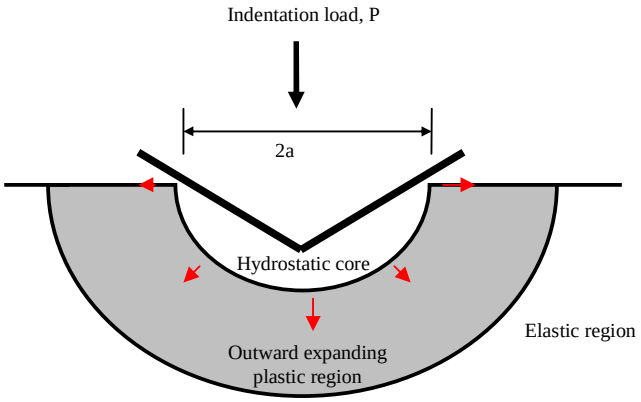

Figure 2.3 Hydrostatic pressure model [adapted from ref. 3].

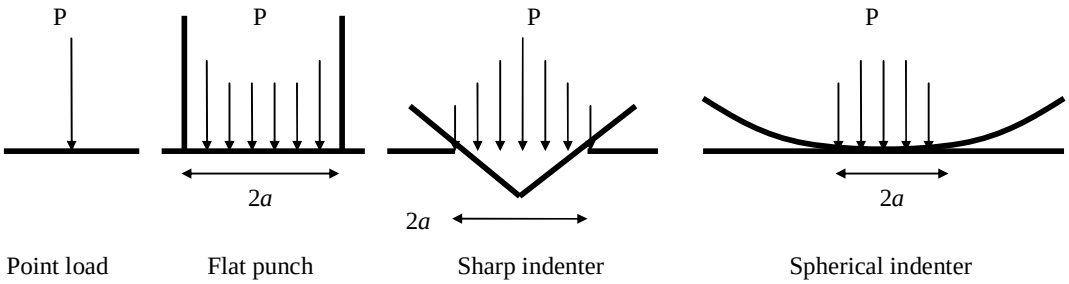

Figure 2.4 Elastic contact pressure distribution for various indentation systems, where P is the applied load and 2*a* is the spatial contact dimension [adapted from ref. 1, 3]

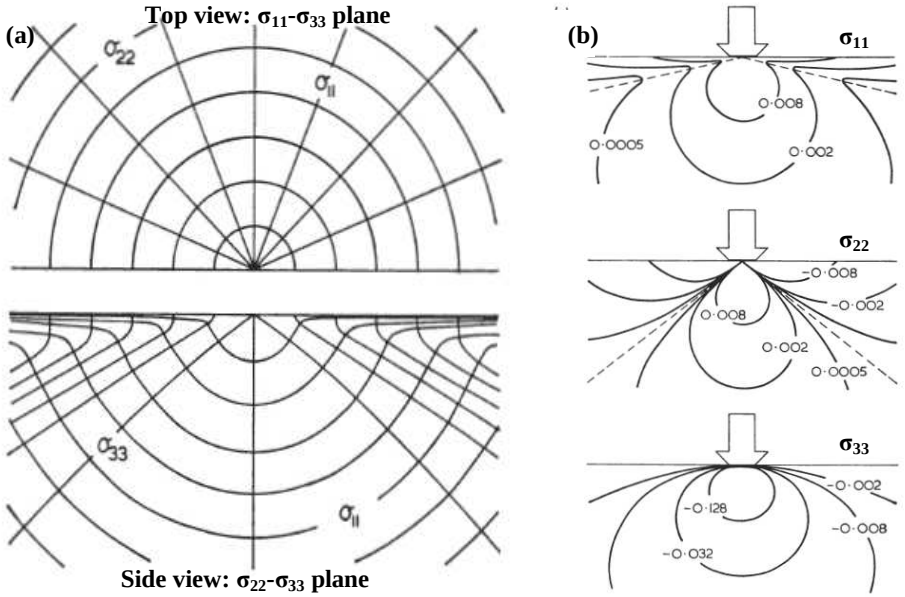

Figure 2.5 Point load Boussinesq stress field for principal normal stresses σ_{11}, σ_{22} and σ_{33} (a) Half surface view (top) and side view (bottom) of stress trajectories, (b) Principal normal stress contours (side view), tangent to trajectories denote direction and points on contours denote magnitude [3-4].

Elastic stress fields are important when considering fracture around the indenter. **Figure 2.4** illustrates how the intensity of the contact stress, which can be described by the mean contact pressure, $p_0 = P/\alpha\pi a^2$, where P the applied load and α a dimensionless indenter geometry constant (α = 1 for axi-symmetric indenters) [3], and a is the spatial contact dimension. Considering an isotropic linear elastic half space subjected to a point load, the solution for the stress field was first given by Boussinesq and **Figure 2.5** [3-4] represents the principal normal stresses ($\sigma_{11} > \sigma_{22} > \sigma_{33}$) in the Boussinesq field. These stresses are the ones responsible for cracking and: σ_{11} is tensile at all points in the field with maxima at the surface and along the contact axis; σ_{22} ('hoop' stress) is tensile subsurface; σ_{33} is compressive everywhere. Since brittle cracks propagate along paths normal to the greatest tensile stresses [4], it is expected that the most fully developed

cracks will lie on either quasi-conical (σ_{22}-σ_{33}) or median (σ_{11}-σ_{33}) trajectory surfaces. Other stress components of the contact field are, shear, (σ_{11}-σ_{33})/2, (σ_{11}-σ_2)/2, (σ_{22}-σ_{33})/2, and hydrostatic compression, -(σ_{11}+ σ_{11} + σ_{33})/3. Whenever tension is suppressed (e.g. immediately under the contact circle, especially sharp contacts), the material may be deformed irreversibly, leaving a residual, 'plastic' impression [4].

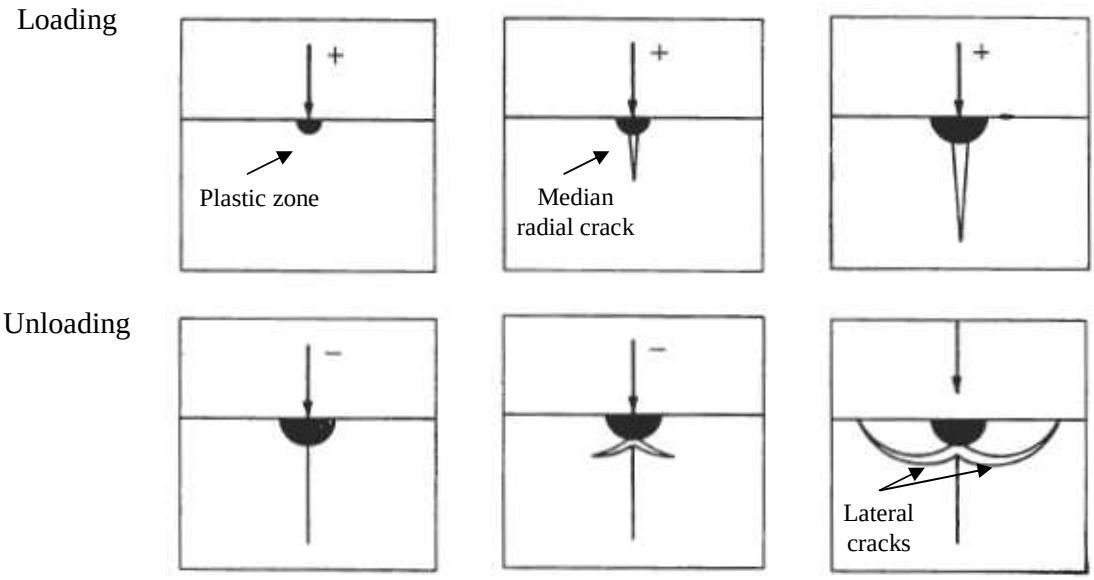

Figure 2.6 Schematic of an ideal vent crack formation under point load indentation. Fracture starts from inelastic deformation dark zone [3].

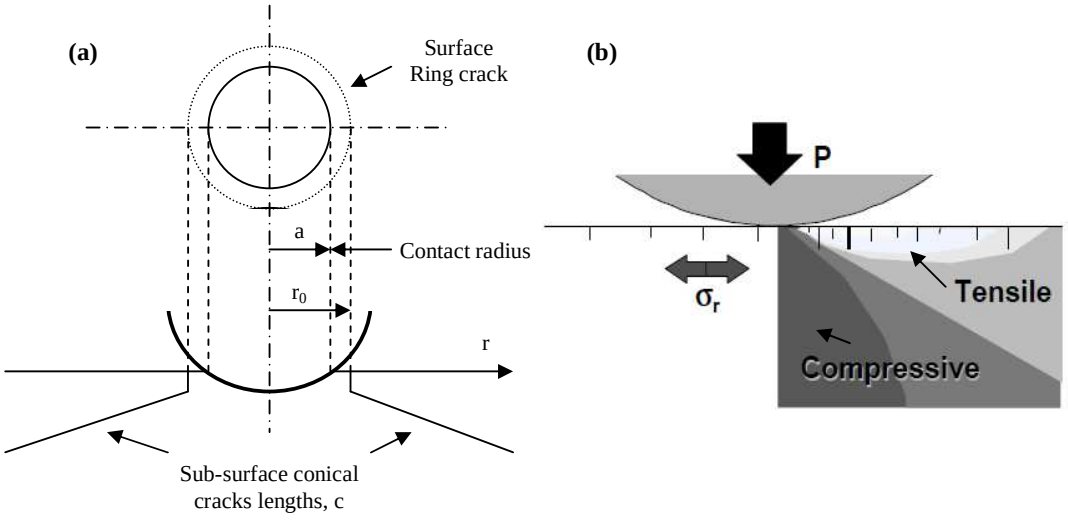

Figure 2.7 Hertzian indentation (a) surface ring and cone fracture and (b) radial tensile and compressive stress distribution [40]

The indentation stress fields shown in **Figures 2.3** and **2.5** can be useful in indicating how cracks will tend to initiate, **Figures 2.6** to **Figures 2.9**. Cracks can initiate from

pre-existing flaws (Griffith [41]) or flaws induced by the indentation itself [3]. Deformation induced flaws tend to nucleate at points of intense stress concentration ahead of locally impeded zones of inelastically deformed material (e.g. piling-up) [3]. Upon attaining some critical configuration, a dominant flaw develops into a well-defined propagating crack, and tends to propagate along trajectories which maintain near orthogonality to a major component of tension [42].

Considering the Hertzian configuration (in **Figure 2.5**), the main change as load increases is a minor flattening of the tensile σ_{11} trajectories immediately below the contact area, with extremely high stress gradients at the edge of the contact [3], meaning that the main crack-forming stress acts in a circumferential direction and is highest in magnitude close to the indenter forming a surface ring crack (**Figure 2.7**). Downward propagation of surface ring cracks follows along the σ_{33} trajectories to form a fully developed Hertzian cone crack. The peak pressure under the Hertzian contact [40, 43] is $p_0 = 3P/2\pi a^2 = (3/2\pi).(P)^{1/3}.(4E^*/3r_0)^{2/3}$, where the contact radius $a = [3r_0P/4E^*]^{1/3}$, P is the indentation load and r_0 is the spherical indenter radius, $1/E^* = (1-\nu_1^2)/E_1 + (1-\nu_2^2)/E_2$; and ν_1, ν_1 and E_1, E_2 are Poisson's ratio and Young's modulus for the indenter and substrate respectively. The resulting radial tensile stress field in the test specimen decays with distance, r (ring crack radius), from the contact centre as $\sigma_{11}(r) = (1-2\nu).P/2\pi r^2$. The radial tensile stress decreases rapidly with depth and shortly becomes compressive as shown in **Figure 2.7**.

Lawn and Wilshaw [3] described crack formation under point loading (e.g. Vickers and Knoop indenters, **Figure 2.6**) including an inelastic deformation zone, opening of a median vent (along the axial stress trajectory, σ_{33}, and orthogonal to the tensile stress $\sigma_{11} = \sigma_{22}$) and its growth during loading. During unloading the median vent closes leading to the development of lateral vents (along σ_{11} trajectories and orthogonally everywhere to the hoop stress σ_{22}).

Since **Figure 2.6** depicts only an ideal sequence of crack events, the median stages (half-penny model: **Figure 2.8**) may be suppressed [4] at lower loads, such that only surface radial (Palmqvist: **Figure 2.9**) segments form. Half-penny cracks develop on symmetrical median planes containing the load axis, whereas Palmqvist cracks are shallow radial surface cracks and extend out from the corners of the indentation.

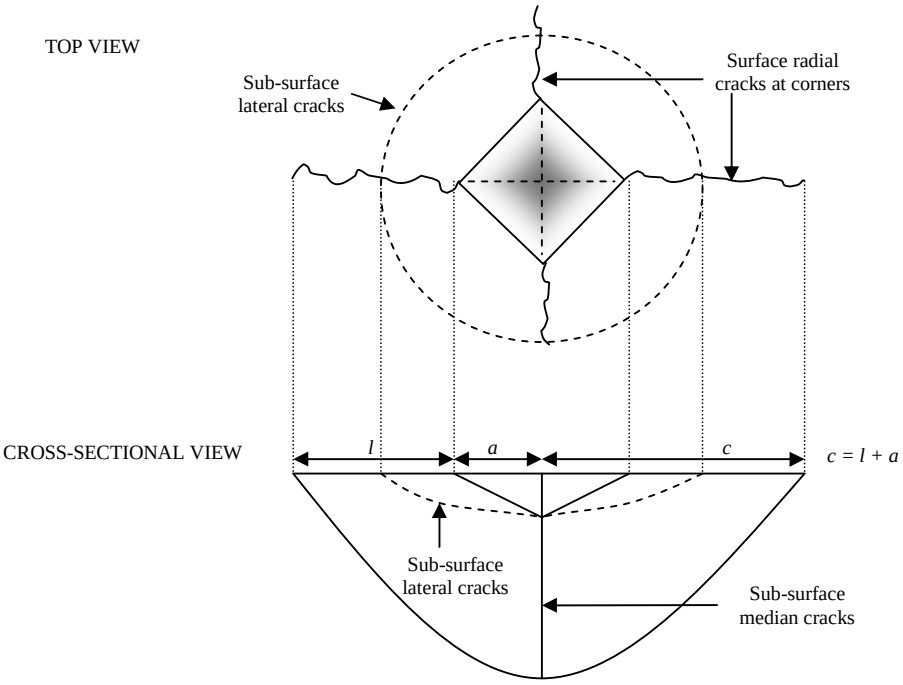

Figure 2.8 Ideal schematic diagram of the Vickers indentation classical fracture model: 'Radial-median' or 'half-penny' model [adapted from ref. 33].

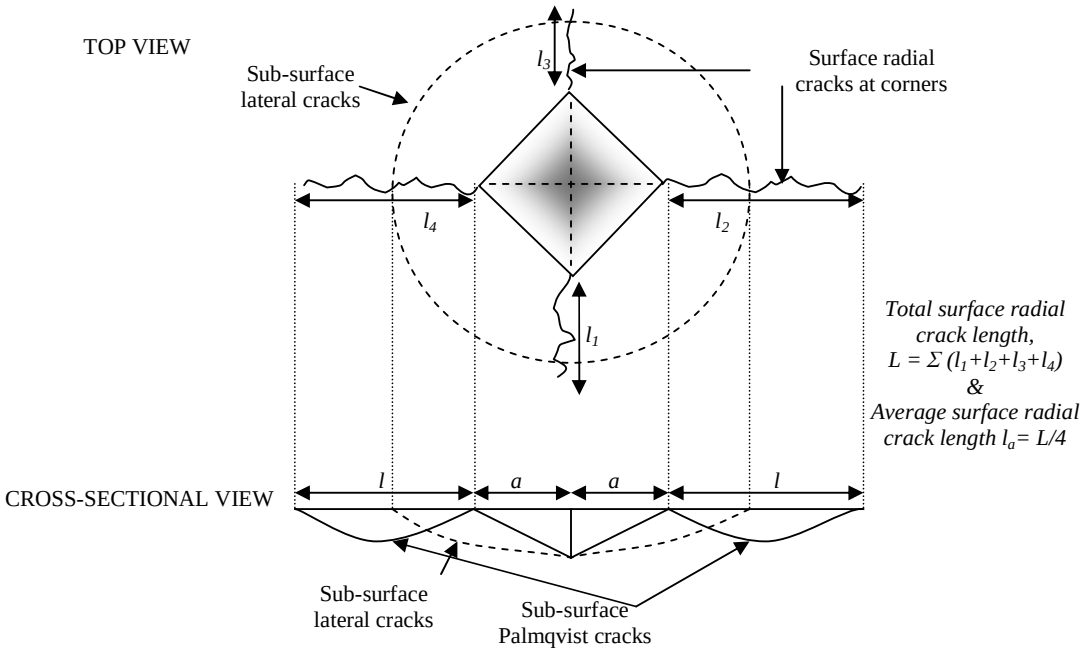

Figure 2.9 Ideal schematic diagram of the Vickers indentation classical fracture model: radial 'Palmqvist' model [adapted from ref. 33].

2.1.2 Vickers indentation fracture of thermally sprayed ceramic coatings

Because of their complex nature, including properties which vary with depth and multi-phase mixture of materials of varying toughness, indentation testing of thermally

sprayed coatings is potentially a very rich area of study, with a number of as yet unanswered questions on the measurement of hardness, fracture toughness and load/depth profile. In this study the main focus has been the cracking patterns developed in HVOF and APS ceramic coatings. It has been suggested that quenching, macro-compressive and peening effects during thermal spraying develop residual stresses in coating materials [44-48]. It is also known (**Figure 2.10a**) that through-thickness residual strain and stress plays a very important role in the extension or suppression of cracking [48-49]. For example (**Figure 2.10b, c**), it has been observed [31] that at the same indentation load, the relatively high residual compressive stresses in HIPed WC-NiCrBSi coatings inhibited the extension of cracks seen in the as-sprayed coating.

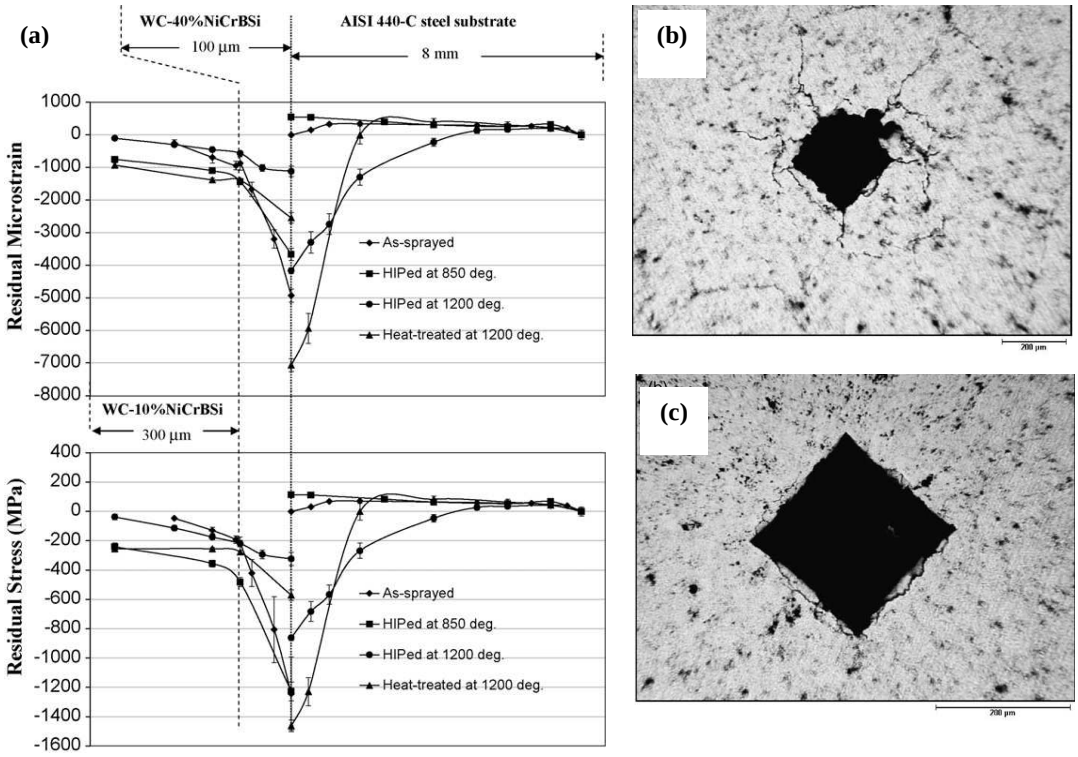

Figure 2.10 (a) Through thickness residual strain and stress distribution obtained via neutron diffraction technique for HVOF WC-NiCrBSi coatings [49]. Static Vickers indentation at 490 N load on corresponding coating surfaces: (b) as-sprayed and (c) HIPed at 850ºC [31]

Stoica *et al*. [31] and Stoica [32] have used the fracture pattern around Vickers indentations in functionally graded HVOF WC-NiCrBSi coating surfaces (**Figure 2.10b, c**), to make a qualitative assessment of fracture toughness because these coatings did not meet the empirical model criteria $c > 2a$ [33] (see **Figure 2.8**). The empirical models tend to be based on an idealised cracking pattern and do not account for micro-fissuring in the sub-surface region especially if this takes the place of surface radial

cracks as it does at lower loads. The uncertainty in measuring the crack lengths in Vickers indentation [34-36] makes empirical models particularly unsuitable for thermal sprayed coatings. Irregular networks of smaller cracks not originating at indentation corners have been observed by other investigators [31, 34-35, 51-53] working on thermally sprayed coatings. For example, Ostojic and McPherson [53] reported 'no dominant cracks' in plasma sprayed coatings even very close to the impression.

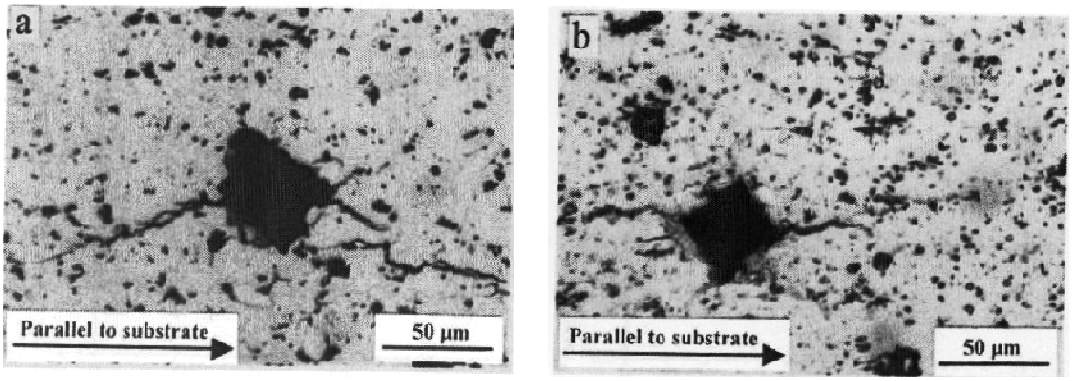

Figure 2.11 Static Vickers indentations at 9.8 N load on cross-section of plasma sprayed Al_2O_3-3%TiO_2 coatings (a) conventional, and (b) nanostructured powder [54]

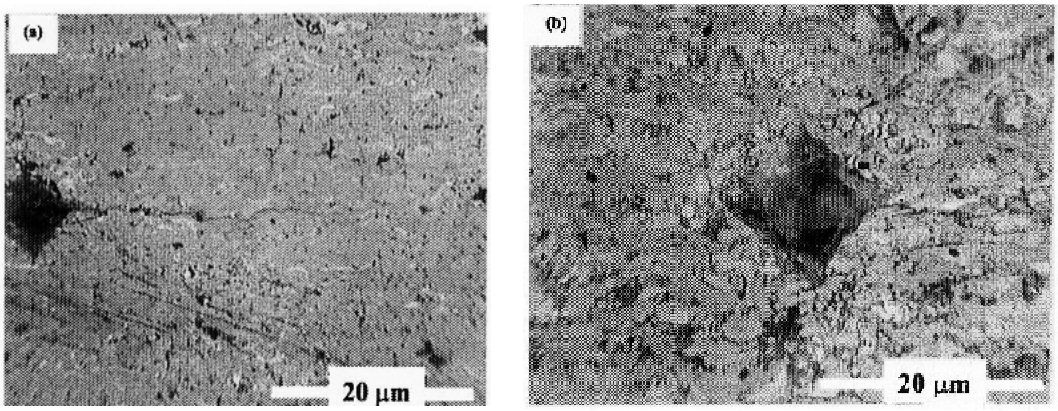

Figure 2.12 Static Vickers indentation at 29 N on cross-section of plasma sprayed Al_2O_3-13%TiO_2 coatings (a) Metco 130, (b) corresponding nanostructured [55]

Typical Vickers indentation fracture patterns for plasma sprayed alumina-titania coatings consist of a network of cracks around the indentation (**Figure 2.11** and **Figure 2.12**). As well as this network, radial cracks emanating from the two opposite indent corners, on a plane parallel to the coating-substrate interface, can also be seen. The indentation fracture in these coatings also tends to be asymmetric, which has been attributed by Ostojic and McPherson [53] to a macroscopic variation in relative density, the presence of pores or other defects around the contact and through thickness residual stresses variation. They [53] suggested that indentation in porous regions of the coatings

results in localised densification about the contact site, resulting in little transmission of indentation stresses to the surrounding materials, and the confinement of cracking to the vicinity of the impression. Interaction with large coating pores or defects near the impression diagonal would then be expected to result in longer cracks, producing a modified Boussinesq stress field. Since the degree of porosity varies between coatings (e.g. HVOF < 1.5 %, APS < 2 % [35]) as well as within a given coating, Ostojic and McPherson [53] also suggested that different loads would be required to produce cracking in different coatings of the same type and even from place to place in a single coating.

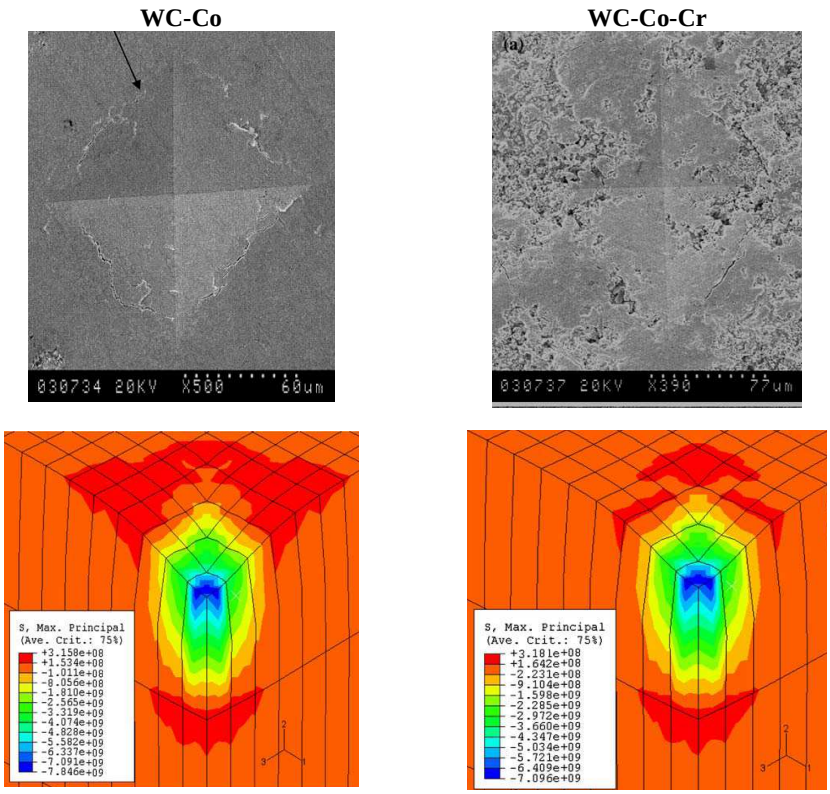

Figure 2.13 Vickers indentation of HVOF ceramic coating surface under 10 N load, SEM images and corresponding FEA maximum principal stress distribution [56].

To model more complex indent shapes, such as those produced by the Vickers indenter requires a numerical approach, such as FEA [56-57]. Despite some theoretical limitations (e.g. considering elastically deformable material, ignoring surface roughness, and taking coating and substrate as solid and homogeneous materials), Baung *et al.* [56] have managed to simulate Vickers indentation on HVOF coatings (e.g. **Figure 2.13**) to determine the stress distributions and critical loads in the coating/substrate systems, relating their findings to the observed cracking profile. As shown in **Figure 2.13**, the highest compressive stress occurs in the area right beneath

the indenter tip and the highest tensile stress occurs in the centre of the indentation edges and decreases along the indentation edge towards the indentation corner. This suggests that edge cracks will initiate first at the coating surface, and will propagate along the indentation edge. Also, the high tensile stress in the area of the indentation corners induces corner cracks to propagate radially outwards along the diagonal of the indentation.

2.1.3 Indentation testing systems and AE measurement

The main features affecting the response of materials under indentation are the load, the shape of the indenter, the size of the indentation and, to a lesser extent, loading rate [3, 58]. Traditional static and quasi-static systems have gradually given way to instrumented systems where load and displacement are measured as a function of time. Hardness indentation testing systems can be classified into open and closed loop systems as shown in the schematic diagram, **Figure 2.14**. In open loop systems, there is no control of load or displacement, whereas, closed loop systems allow control and measurement of the load and/or displacement during the indentation cycle.

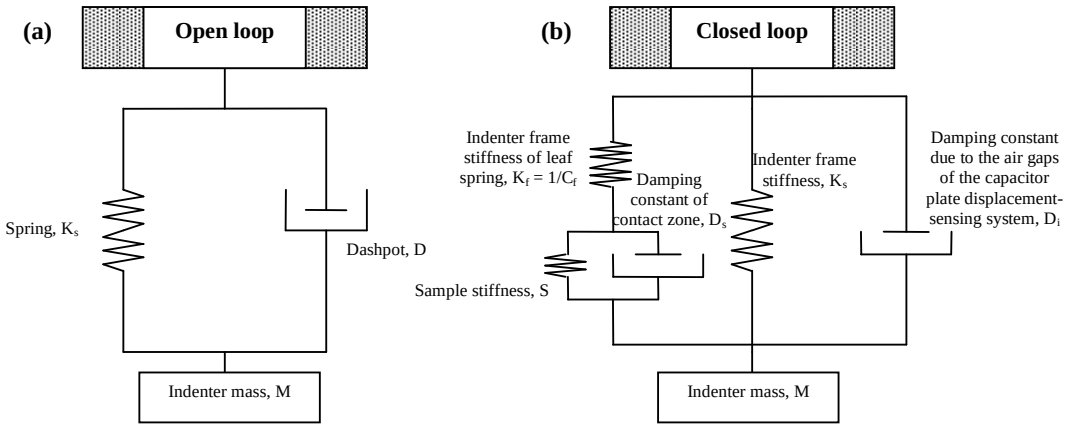

Figure 2.14 Dynamic indentation model: (a) open [59], (b) closed loop [60-63]

Conventional open loop hardness indentation machines operate with a dead-weight counter balanced by a dashpot (or cam). A sequence of levers and arms (**Figure 2.15**) apply the stacked dead-weights to the indenter, and a dashpot (or cam) determines how smoothly the indenter contacts the specimen once the weight is released, primarily to avoid impact [64]. In closed loop indentation systems, there is the potential to control the nominal load or displacement versus time characteristic [65-67], (i.e. impact free with no under-shoot or over-shoot, as shown in **Figure 2.16**). Open loop indentation

systems have been in use for the past 75 years [66], where mechanical control of the descent is limited to avoiding impact and subsequent mechanical control is offered by the material under test depending on its elastic and plastic properties. Calibrated open loop dead-weight indentation systems apply the load approximately uniformly to the nominal level, and are used in cases where the main interest is in producing a quick and easy measure of hardness or toughness.

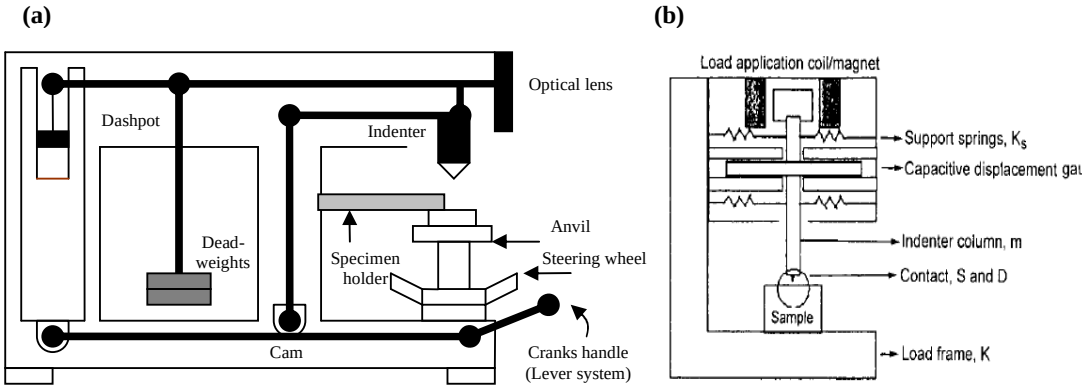

Figure 2.15 Schematic of (a) open loop dead-weight indentation, (b) closed-loop nanoindentation [63]

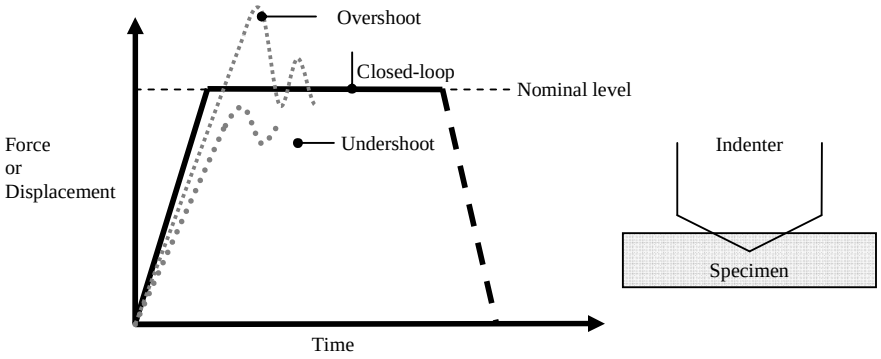

Figure 2.16 Schematic of indentation cycle (force-time and displacement-time)

Closed loop indentation systems [60-63, 65-67] generally have displacement and force control components, for example using a series of capacitors (as opposed to a stack of dead-weights) to apply the force and measuring the displacement through changes in capacitance. The relevant components in closed loop (e.g. instrumented nanoindentation) systems are shown in **Figure 2.14**. One example of the use of such systems is in the dynamic indentation where the imposed driving force is given by $P = P_{os}.exp(i\omega t)$ and the displacement response of the indenter is given by $h(\omega) = h_0.exp(i\omega t+\varphi)$, where P_{os} is the magnitude of the force oscillation, $h(\omega)$ is the magnitude

of the resulting displacement oscillation, ω is the frequency of the oscillation, and φ is the phase angle between force and displacement signals [60].

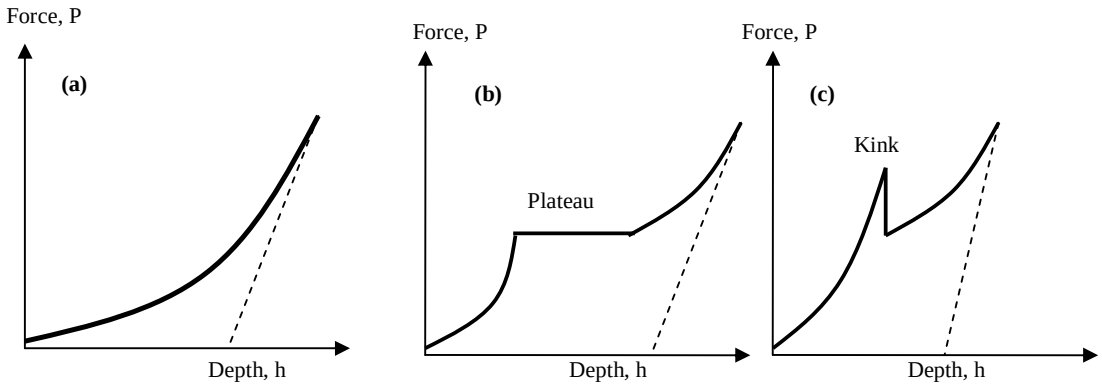

Figure 2.17 Closed loop indentation: Force-displacement curve during loading (a) elasto-plastic material [68], (b) load-controlled [69], (c) displacement-controlled [69]

The loading response of an elasto-plastic material to sharp (e.g. Berkovich, Conical, Vickers) indentation, (**Figure 2.17a**) is governed by Kick's Law, $P = Ch^2$ where C is a constant dependent on elastic and plastic material properties as well as indenter geometry [68]. Under load-control with constant strain rate (e.g. nanoindentation), elastic or plastic deformation give smooth curves (**Figure 2.17a**) but, as the load increases above a certain threshold, a 'displacement burst' or 'pop-in' event occurs [68-70] (**Figure 2.17b**). The initial positive slope corresponds to the response of a purely elastic material and the first displacement burst typically occurs at a load that corresponds to the maximum shear stress under the indenter of the same order as the theoretical shear strength of the indented specimen material [68]. With increased loading above the elastic limit, the material continues to deform in both an elastic and inelastic manner with sequences of bursts. For displacement-control, a 'kink' (load burst) event occurs [69] (**Figure 2.17c**).

Such series of displacement and force bursts and corresponding AE events (e.g. **Figure 2.18** and **2.19**) have been attributed to microstructural changes (e.g. onset of plasticity, crack formation, dislocation or phase transformation), depending on the specific material, loading conditions and tip geometry. For example, in nanoindentation fracture tests 'pop-in' events are observed, where a crack initiates and grows using the stored elastic energy that has been built up in the previous loading period. Jungk *et al.* [70] have suggested that cracks propagate faster than the mechanically constrained indenter tip can respond and the indenter tip loses contact with the material surface. The loss in

contact results in a loss of the driving stress for crack propagation until the indenter tip regains contact at the end of the displacement burst. Subsequent crack extension then requires a replenishing of the elastic strain that was consumed during the crack extension. Consequently, Jungk *et al.* [70] proposed a linear relationship between the indentation load, *P*, and the resulting indentation stress, $\sigma_I = \zeta.P$, where ζ is a conversion factor with units of GPa/mN. Since the residual stress (σ_R) influences the crack extension or suppression, Jungk *et al.* [70] also proposed that the total stress, $\sigma_T = \sigma_I + \sigma_R$.

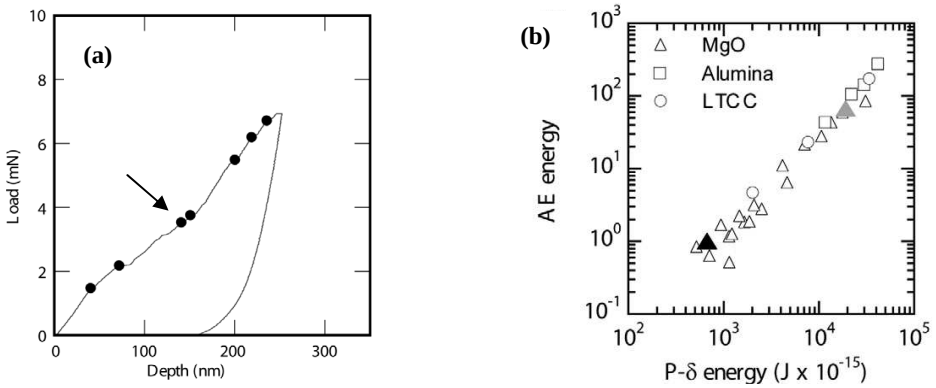

Figure 2.18 AE monitored nanondentations into a 110 nm thick Ta-C film: (a) The dark dots correspond to AE events during loading and are coincident with indenter tip displacement bursts attributed to film cracking, and (b) comparison between the AE energy and the calculated released elastic energy [70].

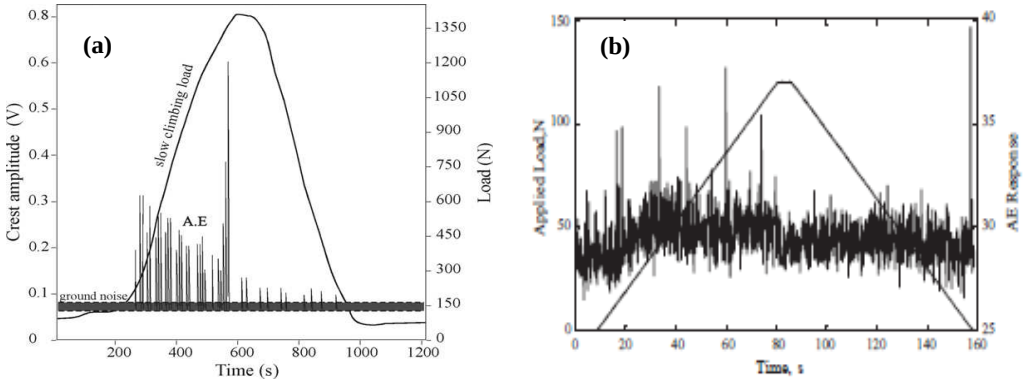

Figure 2.19 AE monitored indentations: (a) Hertzian indentation on polycrystalline alumina [71], and (b) Rockwell indentation on carbon-doped PVD chromium coating [72]. The AE bursts correspond to indenter loading attributed to material cracking.

2.2 AE monitored indentations

Over the past three decades since the first application of AE during compression tests of polycrystalline alumina ceramics by Lankford (1978) [73], there have been numerous

studies undertaken to understand the effect of indentation on various materials using AE sensors. Most observations of AE monitored indentation indicate that the majority of the AE is generated during indenter loading with very little or none during the holding period, while AE may or may not be generated during unloading. AE monitoring has been applied to indentation testing by a very large number of authors using various types of indenters and AE systems (*Appendix A*). Relatively few authors have applied the approach to thermal spray coatings, so the experience in other materials is also reviewed here with the aim of distilling out the key features of AE signals which are relevant for coatings. Since the cracking pattern depends on material type and indentation shape, it makes sense to divide the review by material and indenter type.

2.2.1 AE monitoring of ceramics

Table 2.1 summarises the key information related to the published work on AE monitoring of indentation in bulk ceramic materials.

a. Hertzian (spherical) indenters

Bouras *et al.* [71] and Bouras and Bouzabata [74] observed that the critical load at which Hertzian ring and sub-surface conical cracks appear was accompanied by high amplitude burst-type AE signals. Bouras *et al.* [71] found the critical load corresponding to the final unstable crack extension to be characterised by high amplitude AE events while the crack extension which occurred before reaching the critical load produced low amplitude AE events, while Bouras and Bouzabata [74] observed surface ring cracks with the beginning of a conical form. Usami *et al.* [75] found the load-displacement curves in loading to be approximately linear up to the point where a ring crack occured around the indenter contact area, detected using the AE signal. Further loading after the detection of the first AE signal resulted in another ring crack outside the first ring crack. Although the level of detail varied, the investigations by Bouras *et al.* [71], Bouras and Bouzabata [74] and Usami *et al.* [75] all show the common pattern that classified Hertzian cracks (ring or conical cracks) can be detected by burst-type high amplitude AE signals.

b. Vickers indenters

Xiaoli *et al.* [76], Bergner [77] and Kapoor *et al.* [78] have also attributed the AE during indentation of ceramics to crack extension and have investigated the effect of porosity

and microstructural inhomogenities on the AE. Xiaoli *et al.* [76] found that the fracture toughness (measured by both Vickers indentation and a diametral compression method) of Si_3N_4 was mainly controlled by the local pore distribution rather than the mean porosity distribution and developed an empirical relationship (*Section 2.2.8*) based on AE event count and AE energy distribution to assess the crack extension due to indentation. Bergner [77] observed no AE on loading AlN 3wt.%Y_2O_3 but found multiple events during unloading. Kapoor *et al.* [78], working with sintered UO_2, observed strong burst-type AE signals during loading and attributed these to crack initiation and propagation, while the AE signal observed during dwell time was attributed to the extension of cracks developed during loading.

Table 2.1 AE monitoring of ceramics

Specimen	**Indenter**	**Indentation system**	**Load/Rate**	**Indentation cycle AE**	**AE: Source / *features identified***	**Ref.**
Coarse and fine grained alumina ceramics (2 and 10 µm grain size)	94WC-6Co Hertzian ball, 1 to 14 mm rad.	Instron machine	0-1.35 kN	Loading & unloading	Fissuration of conical crack/ *Amplitude*	[71]
Vitroceramic-alumino silicate and sintered alumina (2 and 10 µm grain size) both as received (*20 x 20 x 5 mm*) and in an implanted state with zirconium ions, Zr^+ (*10 x 10 x 5 mm*)	WC-Co Hertzian ball, 1 and 11 mm radius	Instron machine-model no. 1195	0-1.1 kN 0-1.2 kN	Loading & unloading	Fissuration of conical crack/*Amplitude*	[74]
Alumina ceramics (HD-11 and SSA-999s), (*8 mm thick, 30 mm dia.; 3 x 4 x 40 mm*)	WC-Co, Si_3N_4, Al_2O_3 and hardened steel (SUJ2) spheres of 9.45 mm dia.	Electro-mechanical indentation testing –Shimadzu's AG-10KG machine	0.01 mm min^{-1}	Loading	Crack growth/ *AE signal*	[75]
Pressureless sintered Si_3N_4 (*17 mm dia., 2 mm thick*)	Vickers	Vickers indentation tester	200 N	Loading	Fracture/ *Event count & energy*	[76]
Fine-grained AlN ceramic (*5 mm thick*)	Vickers	Vickers indentation tester	10-50 N	Loading & unloading	Fracture & lateral cracks/ *Amplitude, Frequency, Event count*	[77]
Sintered UO_2 ceramic	Vickers	Vickers hardness tester	1.96, 2.94, 4.9, 9.8 N	Loading, dwelling & unloading	Crack initiation and propagation/ *AE Ring-down count, peak amplitude and energy*	[78]
Ceramic-Sintered Al_2O_3	Vickers	Microhardness tester	10-500 N	Loading & unloading	Deformation & lateral cracks/ *Amplitude, Frequency, Count*	[79]
Alumina (*3 x 4 x 50 mm*)	Vickers	Hardness testing machine	0.3, 0.4, 0.5 and 0.6 kN	Loading & unloading	Crack growth/ *Cumulative AE count*	[80]
Sintered Al_2O_3 and SiC ceramics (*3 x 4 x 20 mm*)	Vickers	Microhardness tester	9.8, 19.6, 49, 98, 196 N	Loading & unloading	Elastic wave/*AE signal, event, freq.*	[81]
Sialon-based ceramic in the Y-Si-Al-O-N system	Vickers	Contact microhardness tester	3-20 N	Loading & unloading	Nucleation of median radial crack/ *Event, amplitude & energy*	[82]

Using dead-weight Vickers indentation where load, AE average amplitude and cumulative event count were recorded as a function of time, Akbari *et al.* [79] reported that AE generated by cracking in sintered Al_2O_3 is of higher magnitude, longer duration and higher frequency than the corresponding signals associated with plastic deformation. They suggested that the lower frequency (around 300 kHz) events were related to median cracks or radial cracks (generated during loading) while frequencies between 550 and 600 kHz were associated with lateral cracks (generated during

unloading). Also working with Al_2O_3, Ray *et al.* [80] found higher cumulative AE counts during loading (material in tensile hoop stress) than unloading (compressive elastic strain is removed) and suggested that this was due to fast crack growth (intergranular fracture) during loading due to the accumulated residual stress energy, although indenter holding time (material in compressive elastic strain) did not produce any AE. Ray *et al.* [80] also noted that the number of AE hits increased with increasing indentation load leading to microscopically observed intergranular fracture and Palmqvist type cracks although they did not directly correlate AE with radial surface crack opening.

Ahn *et al.* [81] observed many AE bursts (attributed to median and micro cracks) during loading and unloading but not during holding in sintered Al_2O_3 and SiC. They found characteristic peaks in the AE spectrum for Al_2O_3 and SiC but no spectral features changed with the type of cracking. Yurkov *et al.* [82] correlated AE records with observations of cracking during indentation of Sialon and attributed AE activity at lower loads with the indentation and growth of median cracks. At higher loads, extensive AE activity was found to be associated with the formation of radial cracks.

2.2.2 AE monitoring of crystals

Table 2.2 summarizes the published work in crystals again showing the main findings and methods. The distinction between 'ceramics' as reviewed in previous section and 'crystals' is somewhat artificial, but this section focuses on aspects of ceramic material which specifically relate to their crystalline nature.

a. Hertzian (spherical) indenters

Guiberteau *et al.* [83] observed discrete AE activity in crystalline Al_2O_3 and related it to the existence of well-defined local instabilities in the deformation-fracture process, including increased AE activity with increasing grain size. From examination of cross-sections of the indentations, the fully developed deformation-microfracture damage zones underneath the indenter were found to be made up of an accumulation of microstructurally discrete events, each consisting of intra-grain shear faulting accompanied by inter-grain microcracking. Most of the AE activity was concentrated towards the end of the loading with minor AE activity during the unloading half cycle.

Table 2.2 AE monitoring of crystals

Specimen	**Indenter**	**Indentation system**	**Load/Rate**	**Indentation cycle AE**	**AE: Source / *features identified***	**Ref.**
Si-single crystal (*0.5 mm thick*)	Vickers	Vickers indentation tester	10-50 N	Loading & unloading	Fracture & lateral cracks/ *Amplitude, Frequency, Event count*	[77]
Monophase polycrystalline aluminas (mean grain size: 3, 9, 15, 21, 35 and 48 µm), (*20 x 2.5 x 2.5 mm*)	WC-Hertzian ball	Indentation using Instron UTM, model 1122	0-2 kN, 1.67 µm s^{-1}	Loading & unloading	Deformation, fracture/*Cumulative & peak AE energy*	[83]
Si and sapphire	Berkovich, Spherical	Ultra-microindentation system (UMIS-2000)	0-500 mN	Loading & unloading	Lateral, radial, edge cracks, twinning/*AE activity*	[84]
Ceria-stabilised tetragonal zirconia polycrystal (Ce-TZP) ceramic	WC-spheres of radius 1.2-12.5 mm	Universal servo-hydraulic testing machine (Instron 8051)	3000 N at 1.0 µm s^{-1}	Loading & Unloading	Phase transformation/ *Cumulative AE amplitude*	[85]
Single crystals-NaCl, Si, Ge and polycrystals-SiC, Al_2O_3	Vickers	Microhardness tester	0.01-60 N	Loading & unloading	Nucleation of lateral, radial cracks/ *Count*	[86]
MgO crystals (1.5-2 mm thick sample cleaved along the {001} planes)	Vickers	Vickers microindentation tester	0.2-5 N	Loading & unloading	Deformation/ *AE signal*	[87]
Single crystal of sapphire (0001) (*1 x 15 x 15 mm*); Polycrystalline Al_2O_3 (10 µm grain size)	Vickers	Microhardness tester	20 N	Loading	Cracking, twinning, dislocation/ *Onset count*	[89]
P type (100) silicon wafers (500 µm thick); Single crystal of tungsten (*10 mm length and 5 mm dia.*)	Nanoindenter	Load controlled nanoindentation	48, 120, 250 mN; 15.5 mN	Loading & unloading	Dislocation, radial & lateral cracks/ *AE signal, events, amplitude*	[90]
Single crystals of W (100), MgO (100)	Nanoindenter: 50, 80, 100, 140, 160 nm tip radius; Nanoindenter (90° included angle) tip radius of 500 nm	TriboScope system, Hysitron, Inc.	0.1-1.6 mN	Loading & unloading	Slip & Twinning/ *AE signal*	[91]
Four different sapphire (Al_2O_3) single crystals: Basal, C(0001); Rhombohedral, R(1012); and two Prismatic, A(1210), M(1010)	Conical nanoindenter (90° included angle) tip radius of 500 nm; Cube corner indenter, tip radius of 100 nm	TriboScope system, Hysitron, Inc.	0.1-1.6 mN	Loading & unloading	Slip & Twinning/ *AE signal*	[92-93]
Beta crystalline SiC (K_{1c} ~ 3.23 MPa.$m^{1/2}$)	Cube-corner nanoindenter	NanoTest Instruments (Micro Materials Ltd.)	25, 125, 225, 250 and 450 mN	Loading and unloading	Radial and wing cracks/ *AE counts, energy, rise time, duration time and amplitude*	[94]
Single crystal of W (100) (5 mm dia and 2 mm thick), Single crystal of Fe-3%Si substrate of *3 mm x 3 mm x 800 µm* to *4 mm x 24 mm x 4 mm* sizes	Nanoindenter	Load controlled nanoindentation	-	Loading & unloading	Sample size, dislocation/ *AE signal, AE energy, frequency, rise time*	[95]

Swain and Wittling [84] investigated the cracking and twinning of silicon and sapphire crystals where, beyond a certain threshold during loading, AE activity rose in steps to the final load. While unloading, no AE activity was observed except at the final stage. For the sapphire crystals, the on-set threshold of AE activity was attributed to large-scale plastic deformation (twinning) with limited evidence of radial or circumferential cracking.

Latella *et al.* [85] investigated Hertzian contact damage leading to phase transformation of polycrystals (9 mol% ceria-stabilised tetragonal zirconia polycrystal: Ce-TZP) of various grain sizes. The micromechanical nature of the damage was predominantly tetragonal-monoclinic (*t-m*) transformation on loading and microcracking on unloading.

For the smallest grain size (1.1 µm) AE activity only occured during the loading cycle whereas, for large sizes (1.6, 2.2 and 3.0 µm), there was an appreciable amount of AE activity also during the unloading cycle, which was ascribed to initiation/extension of microcracks or subsurface microcracks. They suggested that the Hertzian compressive field coupled with the transformation process and associated expansion of the precipitates inevitably raises the compressive stress field further during the loading cycle ultimately restricting microcrack initiation and propagation. On unloading, the compressive stress field gradually reduces, so that microcrack propagation proceeds much more freely. In contrast with the loading cycle, the evolution of the AE amplitude curves for the unloading cycle were generally smooth, and this difference was attributed to the AE activity on loading being largely associated with the *t-m* transformation.

b. Vickers indenters

Lankford and Davidson [86] found that the size of the threshold indentation cracks could be predicted using AE event counts for different crystals (single crystals of: NaCl, Si, Ge and polycrystals of: SiC, Al_2O_3). AE events were also detected in the first half second of indenter unloading, except for fairly high loads, and these were attributed to extension of the radial cracks formed during loading or initiation of lateral cracks during unloading. Based on the AE event count at the threshold indentation load, the least crack resistant material was found to be Ge followed in order of increasing resistance by Si, SiC, Al_2O_3 and NaCl. Bergner [77] found that AE events occurred both during indenter loading and unloading in Si single crystals.

Zhitaru and Rahvalov [87] used AE to observe a type of 'prolonged deformation process' in MgO single crystals, which are characterised by the occurrence of strains after the indenter is removed [88]. Breval *et al.* [89] compared the micro-cracking phenomena in single crystal sapphire (Al_2O_3) and polycrystalline Al_2O_3 on a microhardness tester and the observation of AE counts showed that there was less micro-crack formation in polycrystalline alumina than in single crystal alumina. The main contribution to the AE in single crystal sapphire were observed to be microcracking with high AE amplitude, where as the plastic deformation due to dislocation movements in slip planes, gave low AE amplitude in polycrystalline Al_2O_3.

c. Nanoindenters

Swain and Wittling [84] investigated the cracking and twinning of silicon and sapphire crystals. Whereas median cracks developed in the silicon during loading (identified by SEM examination of indent cross-section) during loading, no AE events were detected. During unloading, there were significant increases in AE events associated with the propagation of lateral cracks. While loading the sapphire crystals, AE activity occurred at higher loads whereas none was observed during unloading. Using microscopical techniques, radial cracks, edge cracks and uplift in the residual impression were observed suggesting considerable twinning of the crystal had occurred under the indentation stress.

Weihs *et al.* [90] applied nanoindentation to P type (100) silicon wafers and annealed single tungsten crystals, parallel to the (100) crystal direction. In both crystals indentation generated sharp AE signals due to radial crack formation at the indentation corners during loading. The displacement profile of the indenter showed a short plateau during loading and during unloading, and low amplitude AE signals were occasionally detected. The upward thrust of the specimen onto the nanoindenter observed during unloading was attributed to lateral crack growth as well as phase transformation in the silicon. During indentation of the annealed tungsten single crystal, it was found that initial elastic deformation was followed by yield and plastic deformation as might be expected. The point of yielding during loading was characterised by a plateau and associated AE was attributed to generation and motion of dislocations in crystals.

Dyjak and Singh [94] investigated the initiation and propagation of local failure processes during nanoindentation of beta crystalline SiC. Due to the crystalline structure of SiC, the AE activity was discrete. After reaching a threshold load, a few discrete AE events of lower amplitude were observed during the loading cycle (i.e. opening of radial cracks) and a higher rate of larger amplitude events was seen during the unloading cycle (i.e. growth of wing cracks). In cases where there were measurable radial cracks, they found that the threshold load for the start of the AE activity could be used as an indicator of fracture toughness of the material. Using the cumulative AE energy parameter, they developed an empirical relationship (*Section 2.2.8*) between the AE energy and the radial crack length (c) during the loading cycle.

Bahr and Gerberich [95] investigated the relationship between AE signals and the dimensions (size or geometry) of specimens of single crystal tungsten and Fe-3%Si. It was found that sample geometry affects the rise time and frequency of the AE signals, and that samples of similar size that generate AE signals from different event types (e.g. dislocations) have similar waveform characteristics. A linear relationship between released elastic energies measured using the nanoindentation technique and the corresponding dislocation AE energies were observed regardless of sample geometry or material under investigation.

Tymiak *et al.* [91-93] investigated the initial stages of indentation-induced plasticity (slip or twinning) for tungsten and MgO on a single crystal plane and four different sapphire (Al_2O_3) single crystal planes [91-93]. Linear relationships between released elastic energies and the corresponding AE energies were observed for all three single crystals [91]. Two types (1 and 2) of yield point AE signals were detected [91-93] and patterns were attributed to slip and highly localized twinning respectively. Type 1 (transient) AE patterns were observed for all the tested crystallographic planes and were attributed to slip, rhombohedral twinning or twin growth. Type 2 AE patterns were observed for the two prismatic crystallographic planes and correlated to linear surface features which were identified as basal twins (twin nucleation and twin growth).

2.2.3 AE monitoring of glasses

Table 2.3 summarizes the published work on AE and indentation of glasses, here defined as ceramic materials with low levels of crystallinity. Since most of the work relates to soda-lime glass, the material of study in the following will only be mentioned if different.

a. Hertzian (spherical) indenters

Kim and Sachse [96] found reproducible AE signals due to Hertzian cone cracking during loading and lateral vent cracking during unloading. Usami *et al.* [97] also observed ring and cone cracks to grow during loading. The AE amplitude decreased with decrease in the cross-head speed and indentation size and was not detectable at the lowest values of each experimental variable. Usami *et al.* [97] proposed an empirical relationship between fracture stress (σ_n) and the ratio of ring crack radius and contact

radius (*r/a*). In correlating this with AE signals they found that the larger values of fracture stress corresponded to when AE is detected.

b. Vickers indenters

Bergner [77] investigated the characteristics of AE signals in amorphous slide glass and found no AE events during loading but multiple events were observed during unloading as well as during holding where it was explained that lateral cracks formed. Ahn *et al.* [81] recorded many burst-type AE signals during loading and unloading but not during holding time. The AE events were found to increase with the increase in the indentation load, and the cracks (median and micro crack) were initiated during indentation and were propagated by release of residual stress during unloading, where the stronger AE signals were detected.

Lee and Kim [98] suggested that median and lateral cracks were the possible sources of AE because, as the indenter penetrates into the specimen, the median crack extends downwards at first then extends radially on unloading. The jumps in the AE event counts during indenter holding time were correlated to the sudden breakthrough of the median vent through the restraining compressive lobes to intersect the free surface. In addition to this, they assumed lateral cracks to be producing minor AE. The level of AE increased with load and the higher indentation loads generated AE almost immediately after the contact between indenter and specimen, the incubation time between contact and AE signal initiation becoming shorter at higher loads. Kim and Sachse [96] found two mutually perpendicular median cracks of half-penny configuration, and the characteristics of the AE source resembled neither that of a dipole nor a vertical force drop but of a mixed type, which can be explained if the driving force for the development of median cracks is governed by hoop tension as described by Lawn and Wilshaw [3]. Tanikella and Scattergood [99] also found that AE measurements can provide enhanced information on crack initiation (median or lateral cracks) at specific points of loading and unloading.

Following their work on the identification of critical loads during the Vickers test using AE, Lee and Kim [98] and Kim and Sachse [96] proposed empirical models (*Section 2.2.8*) for evaluating the mechanical properties of glass or other brittle materials. Lee and Kim [98] proposed that the cumulative AE energy is proportional to the fourth power of the median crack length (*c*), whereas Kim and Sachse [96] proposed using the

amplitude of the first P-wave arrival (associated with the formation of an unloading lateral vent crack) proportional to *n*th power of (P_m-P_t), where P_m and P_t are the maximum and threshold load values, respectively.

The pyramidal shape of the Knoop indenter also induces radial and lateral cracks similar to the Vickers. Tanikella and Scattergood [99] found that AE measurements using a Knoop indenter were not very reproducible but that the AE can be used to monitor the initiation of lateral cracks at specific points of loading and unloading in conjunction with instrumented indentation systems.

Table 2.3 AE monitoring of glasses

Specimen	**Indenter**	**Indentation system**	**Load/Rate**	**Indentation cycle AE**	**AE: Source / *features identified***	**Ref.**
Slide glass (*1mm thick*)	Vickers	Vickers indentation tester	30 N	unloading	Fracture & lateral cracks/ *Amplitude, freq. & pulse length*	[77]
Soda-lime glass (*5 x 10 x 15 mm*)	Vickers	Microhardness tester	9.8, 19.6, 49, 98 and 196 N	Loading & unloading	Elastic wave/*AE signal, event, freq.*	[81]
Soda-lime glass	Cube-corner nanoindenter	NanoTest Instruments (Micro Materials Ltd.)	25, 125, 225, 250 and 450 mN	Loading and unloading	Radial and wing cracks/ *AE counts, energy, rise time, duration time and amplitude*	[94]
Soda-lime glass (*10 x 10 x 1.243 cm*)	Vickers, 90 µm dia. diamond sphere	Indenter fixed on loading frame via a miniature load cell	55.1 N, 50N	Loading & unloading	Cone and lateral vent cracks/ *P-wave amplitude*	[96]
Soda-lime glass (*3 x 4 x 40 mm*)	SiN, Al_2O_3 and hard steel spheres of 9.45 mm dia.	Electro-mechanical indentation testing – Shimazu's AG-10B machine	0.01 mm min^{-1}	Loading	Crack growth/ *AE signal*	[97]
Soda-lime glass (*40 mm dia., 3 mm thick*)	Vickers	Tukon hardness tester	2-80 N	Loading	Median & Lateral cracks/ *Ring down count & AE energy*	[98]
Soda-lime glass (*20 x 20 x 3.125 mm*)	Knoops, Vickers, Rockwell C	Indentation using UTM	5-200 N	Loading & unloading	Median, radial, lateral, Hertzian cracks/ *Amplitude & time duration*	[99]
Soda-lime glass	WC-Conical	Indenter fixed on loading frame via a miniature load cell	26.2 N	Loading & unloading	Penny shaped crack/ *P &S-wave amplitude*	[100-101]

d. Conical indenters

Kim and Sachse [100] studied the generation of penny-shaped cracks of Mode-I type in soda-lime glass plate, and found that their orientation can be accurately determined from the radiation patterns of AE, detected using a circular array of eight sensors. In an extension to this investigation, Kim and Sachse [101] proposed an alternative approach using dipole strength and source-time function analysis of the radiation pattern associated with the amplitude of the first arrival AE signal from a penny-shaped crack. Tanikella and Scattergood [99] found that the AE measurement in soda-lime glass was highly reproducible and can provide information on Hertzian ring crack initiation.

2.2.4 AE monitoring of composites

Table 2.4 summarizes the published work on AE monitored indentation of a variety of composites and polymers.

a. Hertizan (spherical) indenters

Kent *et al.* [102], working on polystyrene injection mouldings, found that the load at first fracture (determined using the AE signal) proved to be a good indicator of the magnitude of the orientation of polystyrene present in the surface layers of the mouldings. Wang and Darvell [103] explored the Hertzian failure of dental restorative composite materials, and found that an AE sensor mounted on the indenter mandrel was useful to detect the first crack while loading. Yang and Han [104-105] monitored the indentation damage of carbon fibre reinforced plastic (CFRP) and fibre-metal laminate (FML), and found that the damage information obtainable from built-in optical fibre vibration sensors was comparable in quality to AE data (amplitude and count rate) which was attributed to reinforcing fibre break.

Kawaguchi *et al.* [106] investigated the indentation fatigue properties of glass-fibre reinforced polyphenyleneether (GFPPE), polyphenylenesulfide (GFPPS) and syndio-tactic polystyrene (GFSPS) thermoplastics, and found that the AE began to occur early in the loading cycle, the AE amplitude reaching its maximum value when the load reached its maximum. The specimen did not show ultimate failure at the maximum load, and the load decreased gradually as the defects such as fibre breakage, micro-voiding, change in the orientation of fibres and plastic deformation of the matrix propagated. Cesari *et al.* [107] investigated damage accumulation (matrix cracking, delamination and fibre breakage) in quasi-isotropic carbon fibre reinforced epoxy resin laminate, and found that sudden arrests in the load-displacement curve due to delamination and fibre failure were accompanied by sudden drop in the ratio of elastic energy to AE energy.

b. Vickers indenters

Ray *et al.* [80] found more AE during unloading than loading cycles in silicon carbide whisker (SiC_w) reinforced alumina composite. Although holding time did not produce any AE signals, Palmqvist type cracks were observed at higher loads. In Al_2O_3 / SiC composites, Ahn *et al.* [81] found less AE during the unloading compared to the loading cycle, possibly because the voids absorbed some energy during the loading cycle. Many

burst-type AE signals due to median and micro cracks were recorded during loading and unloading but not during holding. AE event counts were found to increase with increasing indentation load, but the waveform frequency content (in the bands 50-200, 200-400, 450-550 and 650-700 kHz) was not related to the indentation load.

Table 2.4 AE monitoring of composites

Specimen	**Indenter**	**Indentation system**	**Load/Rate**	**Indentation cycle AE**	**AE: Source/ *features identified***	**Ref.**
25wt. % SiW_w whisker reinforced alumina composites (*3 x 4 x 50 mm*)	Vickers	Hardness tester	0.63, 0.8, 1.0 and 1.2 kN	Loading & unloading	Crack growth/ *Cumu. AE count*	[80]
Al_2O_3-15% vol. SiC composite (*3 x 4 x 20 mm*)	Vickers	Microhardness tester	9.8, 19.6, 49, 98, 196 N	Loading & unloading	Elastic wave/*AE event, frequency*	[81]
Metal-matrix composites (Al/Al_2O_3)	Vickers	Microhardness tester	20 N	Loading	Twinning, dislocation/*count*	[89]
Polystyrene (*2 mm thick*)	Steel balls indenters (2.4 & 1.8 mm radius)	Indentations on Instron tensile testing machine	1.0 mm min^{-1} penetration rate	Loading	Fracture/ *AE signal*	[102]
Amalgam and ceramic reinforced glass ionomer cement, GIC (*0.4-0.8 mm thick*) on 30% glass fiber-reinforced polyamide (*5 mm thick of 10 mm dia.*) substrate	Hard steel ball of 20 mm dia.	-	0.02 mm min^{-1}	Loading	Failure of composites/ *AE signal*	[103]
Carbon fiber epoxy matrix (*70 x 70 x 1.5 mm*)	Hemispherical shape indenter, 12.7 mm dia.	Indentation on Shimadzu's UTM	3 mm min^{-1}	Loading	Fiber damage/ *Count rate & amplitude*	[104]
Al laminate and carbon/epoxy matrix (*100 x 100 mm*)	Hemispherical shape indenter, 12.7 mm dia.	Indentation on Shimadzu's UTM	3 mm min^{-1}	Loading	Damage/*Count rate & amplitude*	[105]
Glass-fiber reinforced polyphenyleneether (GFPPE), polyphenylenesulfide (GFPPS), syndio-tactic polystyrene (GFSPS), (*1.6 x 60 x 60 mm*)	Hertzian shaped indenter	Indentation on Shimadzu's Servopulser	1 mm min^{-1}	Loading	Crack initiation and ultimate failure/ *AE counts*	[106]
Carbon fiber reinforced epoxy resin laminate (*250 x 250 x 1.6 mm*)	Hardened steel ball, 4 and 7 mm radius	Hydraulic Instron 8033/MTS Testar II system	0.05 mm min^{-1}	Loading	Delamination and fiber failure/ *AE energy*	[107]
Mullite matrix embedded with Al_2O_3 and tetragonal zirconia polycrystal (TZP)	Vickers	Instron machine	196-427N	Loading & unloading	Fracture & decohesion/ *Event count & amplitude*	[108]
Tetragonal Zr polycrystal powder ZrO_2 stabilized with 3 mol. % Y_2O_3 with single crystal Al_2O_3 platelets (platelets dia. 3µm) as a reinforcing phase (*28 mm dia., 4.8mm thick*)	Vickers	Vickers indentation tester	49-491N	Loading & unloading	Crack/ *Event, Cumu. event & energy, amplitude*	[109]
Unidirectional SiC (Nicalon fibres)/Mullite composite (*cross-section of 5 mm x 8 mm and 10-12 mm length*)	Vickers	Microhardness tester	Debonding stress 2-12 GPa	Loading	Debonding mechanism/ *Events*	[110]

Baudin *et al.* [108] compared the AE characteristics due to fracture of the mullite matrix with its CMC reinforcing particles of aluminum oxide and tetragonal zirconia polycrystals (TZP). Total numbers of AE events gathered during loading were correlated with the total area of crack surface and found to increase with increasing load in an approximately linear fracture. Shifts in AE signal amplitude distribution were observed for all three components (mullite matrix, and aluminum oxide and TZP particles). The low values of amplitude for TZP (coming from the decohesion of the glassy phase) shows that the total AE energy is divided between a small numbers of events of high amplitude whereas the high values of amplitude for alumina particles and

mullite matrix (coming from the fracture of the matrix and particles) reflects a division into a large number of low-energy events.

Form *et al.* [109] were interested in fracture toughness differences between specimens of zirconia matrix material with alumina platelet reinforcement. AE activity associated with cracking was at the very initial period of indentation, and the higher amplitude bursts were attributed to the influence of the platelets. The small numbers of AE events during the initial elastic indentation period were attributed to friction between the indenter and the specimen.

Breval *et al.* [89] compared the micro-cracking phenomena in a metal-matrix composite of Al/Al_2O_3 with glass (MgO) sintered Al_2O_3. The metal-bonded alumina (Al/Al_2O_3) exhibited less AE counts than glass-bonded alumina (MgO-sintered Al_2O_3) indicating that some of the stress is taken up by the metallic phase. In a SiC (Nicalon fibre) reinforced mullite composite, Rouby and Osmani [110] found that AE event count was a good tool for detecting debonding and the debonding mechanism between fibre and matrix was found to be governed by energy release rate and not by a local failure criterion.

Replacing and rationalising the time-consuming indentation crack length measurement with the AE parameters to determine the mechanical properties of composites and the specific crack sequence in which they form is an important aspect of the work of Baudin *et al.* [108] and Form *et al.* [109]. For example, Baudin *et al.* [108] proposed a power law correlation between AE and fracture toughness (*Section 2.3.8*).

2.2.5 AE monitoring of metals and metal foams

Table 2.5 summarizes the published work on AE monitored indentation of metals and metal foams. Because there are so few studies, these are discussed per material in the following.

Girodin *et al.* [111] studied the static and cyclic Hertzian indentation of hardened martensitic steel (750-800 HV), and identified cracking in spheroidal carbide particles (size ~ 10 µm) observed through surface microscopy at the edge of the plastic zone as

the main source of AE during loading. The AE response of embrittled structural and tool steels during Vickers indentation was studied by Clough and Simmons [112]. They classified the steels in terms of hardness: < 40 HRC, 40-50 HRC, and > 50 HRC and found no AE from the softest group with AE always being observed in the hardest group. The intermediate group only occasionally produced AE. SEM analysis indicated that the AE signals were produced by the nucleation and incremental growth of subsurface penny-shaped cracks in hard steels. Finally, Breval *et al.* [89] observed no AE during Vickers indentation loading of a polycrystalline aluminum alloy and attributed this to fracture-free deformation.

Table 2.5 AE monitoring of metal and metal foams

Specimen	**Indenter**	**Indentation system**	**Load/Rate**	**Indentation cycle AE**	**AE: Source/ *features identified***	**Ref.**
Polycrystalline aluminum alloy (Al 5083 with 3.85% of Mg): Vickers hardness of 1.1-1.6 GPa	Vickers	-	20 N	Loading	Fracture free deformation/No AE detected	[89]
Martensitic steel (X105CrMo17) with M7C3 eutectic carbides	Hertzian	Static or 50 Hz cyclic load	4000-15000 MPa	Loading	Crack initiation/*AE signal*	[111]
Embrittled steel such as pressure vessel steel with embrittled weld and embrittled tool steels (*2.54 cm thick, 7.62cm dia.*)	Vickers	Manual load control on a 10:1 lever arm mechanism	-	Loading	Nucleating & growth of sub-surface cracks/ *Amplitude waveforms*	[112]
Al-based foams, e.g. aluminium-silicon foam (AlSi10) and Alporas foam (AlCa5Ti3) (*40 x 40 x 40 mm*)	Flat-plate circular cylinder punches: 1.5 and 5 mm dia.	MTS hydraulic machine in displacement control-quasistatic compression	$5x10^{-3}$-$1.25x10^{-1}$ mm s^{-1}	Loading	Fracture & plastic yield/ *Count & event & amplitude waveforms*	[113]
Metcomb AlMg1Si0.6CuCr + 15% Al_2O_3 foams (aluminum matrix composite reinforced by Al_2O_3 or SiC particles) with different Si and Mg content, (*30 x 30 x 20 mm*)	Flat-plate circular cylinder punches: 5 mm dia.	MTS hydraulic machine in displacement control-quasistatic compression	0.025 mm s^{-1}	Loading	Fracture & plastic yield/ *Count & event & amplitude waveforms*	[114]

Kàdàr *et al.* [113-114] used flat cylindrical punches to examine the AE response during indentation of metallic foams, e.g. aluminium-silicon foam (AlSi10) and Alporas foam (AlCa5Ti3) and Metcomb (AlMg1Si0.6CuCr + 15% Al_2O_3). The indentation punch stress values were correlated with AE count rates. For Al-based metallic foams [113], the rise time of the AE amplitude was found to be indicative of two different deformation modes; fracture (low rise time) and plastic yield (high rise time). Foam cell wall bending was identified as causing a continuous AE signal whereas cell wall buckling with fracture or yielding was identified as causing a burst-type AE signal. Cell walls were deformed directly beneath the indenter (cell collapse) and densified to form a rigid material. A high AE count rate was found when the stress droped at cell wall failure at which point high AE amplitudes were observed, and attributed to either fracture or the formation of cracks.

2.2.6 AE monitoring of thin solid films

Table 2.6 summarizes the published work on AE monitored indentation of thin solid films, noting also the substrate material.

a. Hertzian (spherical) indenters

Swain and Wittling [84] observed considerable AE activity followed by a major burst during loading of a TiN film on a silicon substrate. With increasing load both the coated substrate and uncoated substrate showed a series of distinct AE burst events with little AE activity during unloading. A TiN film coated on sapphire substrate produced a major AE burst event larger than for the uncoated sapphire which was attributed to spallation of the TiN film from the sapphire substrate by cracking and twinning. Shiwa *et al.* [115] found that AE was able to detect the onset of cracking of a hard TiN film on a softer silicon substrate during loading, and film delamination during unloading. Three stages of indentation were identified during loading: elastic response of coating-substrate system (stage-I), development of circular film cracking and/or shear faulting (stage-II), radial cracks and extended plastic deformation of substrate (stage-III). During unloading, a further three stages were identified: elastic response of coating-substrate system and interfacial delamination (stage-IV), continued radial cracking in films (stage-V) and continued interfacial delamination (stage-VI).

b. Vickers indenters

Tanikella *et al.* [116] observed a reproducible AE signal which did not vary with loading rate which occurred at the fracture threshold in thin amorphous SiC coatings deposited on an Incoloy substrate. Intermittent AE signals of larger amplitude and duration were also detected with increased indentation load but no radial or lateral cracks or de-cohesion were observed. Walter *et al.* [117] investigated indentation-induced cracking patterns of DC magnetron-sputtered boron carbide-DLC coatings with a Ti interlayer leading to adhesive and cohesive failure from the steel substrate. The cracking patterns (e.g. crack openings, corner cracks and crack paths) and their AE activities (counts) for coatings deposited at various flow rate of acetylene gas were found to vary. Ikeda *et al.* [118] observed the initiation and progression of micro-fractures in polycrystalline CVD diamond films deposited on a SiC substrate. They found that the AE event count and energy cannot reveal the fracture type due to indentation, which led them to study the fracture types by analyzing the first arrival (s_o-mode) Lamb waves detected by four sensors. Yonezu *et al.* [119-120] found AE signals

to be very useful in identifying and measuring the Mode-I ripple crack produced by film bending (leading to delamination under the tensile stress in TiN and DLC coatings.

c. Nanoindenters

Jungk *et al.* [70] studied the fracture behavior and toughness of tetrahedral amorphous carbon films deposited on silicon substrates. 'Pop-in' displacement excursion events during loading were attributed to film cracking and were associated with AE energy. They also proposed load-independent empirical models (*Section 2.2.8*) based on the type of cracking (radial or channel) to measure the fracture toughness using AE parameters. The fracture toughness values obtained using the classical approach (3.3-3.7 $MPa.m^{1/2}$) was found to be similar to the values measured using AE parameters (3.0-3.8 $MPa.m^{1/2}$).

Weihs *et al.* [90] investigated Ni films coated onto glass slides and found a displacement plateau equal to the film thickness during loading. This plateau was attributed to debonding of the Ni film, and was associated with sharp AE signals. Swain and Wittling [84] found some AE at very low loads due to asperity deformation and cracking of TiN films on silicon and sapphire crystal substrates. A significant amount of AE activity (counts) was observed during loading, as well as some during unloading. Major bursts of AE activity during unloading were attributed to delamination of the film with no radial cracking. The buckling of the film which led to delamination occurred during the final stages of unloading and was driven by residual compressive stresses within the film. Daugela and Wyrobek [121] also detected AE signals due to nano scale cracking during loading and adhesive failure during unloading of SiN film on polycarbonate substrate.

Table 2.6 AE monitoring of thin solid films

Specimen	Indenter	Indentation system	Load/Rate	Indentation cycle AE	AE: Source/ *features identified*	Ref.
Pulsed laser deposited (PLD) 110nm thick tetrahedral amorphous carbon (ta-C) on (001) silicon substrate	Cube-corner nanoindenter	TriboIndenter	1 to 9 mN at 20 mN s^{-1}	Loading	Radial and channel cracking/ *AE signal, energy*	[70]
Filtered arc PVD TiN film (0.8 µm thick) on Si and sapphire substrate	Spherical, Berkovich	Ultra-microindentation system (UMIS-2000)	0-500 mN	Loading & unloading	Cracks, delamination/ *Counts*	[84]
Nickel films (1 µm thick) evaporated onto glass microscope slides	Nanoindenter	Load controlled nanoindentation	130, 250 mN	Loading & unloading	Delamination/ *AE, events*	[90]
Filtered arc PVD TiN film (2.7 µm thick) on Si single crystal wafer of thickness 1.05 mm	Spherical	Ultra-microindentation system (UMIS-2000)	0-350 mN, 0-650 mN	Loading & unloading	Cracks, delamination, deformation/ *RMS amp. & counts*	[115]
Amorphous SiC coatings of 5µm thickness deposited on an Incoloy (*dia. 12 mm*) by using low temperature plasma-assisted chemical vapor deposition (PACVD) process	Vickers	Indentation on piezo translator (PZT) mounted to cross-head testing machine	0.1-8 N	Loading	Fracture/ *Amplitude*	[116]
DC magnetron-sputtered boron-carbide DLC coating (1, 1.5, 1.9 and 2.5 µm thick) on 52100 steel disk with Ti interlayer (*32 mm dia. and 6.5 mm thick*)	Vickers	Instrumented indentation system	40, 100, 300 and 750 N	Loading	Adhesive and cohesive failure/ *AE counts*	[117]
Polycrystalline diamond films deposited by CVD on sintered SiC substrate (*15 mm wide and 5mm thick*); Micro-crystalline diamond-MCD film thickness of 53 µm for Vickers test; Nano-crystalline diamond-NCD film thickness of 35 µm for Rockwell-C test, NCD film of 33 µm for both test	Rockwell-C, Vickers	Instrumented indentation	10-30 N at 0.02 N s^{-1} ; 10-50 N at 0.49 N s^{-1}	Loading & unloading	Lateral, ring cracks, delamination/ *AE signal*	[118]
PVD-TiN film of thickness 4µm/4µm/3.5µm/1µm on austenitic stainless steel/carbon steel/forging steel/pure iron deposited on substrate such as austenitic stainless steel, carbon steel, forging steel and pure iron respectively (*30 x 30 x 2 mm*)	Vickers	Vickers micro-indentation test using electro magnetic servo-testing machine	20 N at 10 mN s^{-1}	Loading	Mode-I ripple fracture/ *Cumulative count, Lamb wave amplitude*	[119]
DLC thin film by CVD of thickness 3 µm deposited on austenitic stainless steel (*30 x 30 x 2 mm*)	Vickers, Rockwell (0.4 mm tip radius)	Micro-indentation test using electro magnetic servo-testing machine	35 N & 30 N at 100 & 20 mN s^{-1}	Loading	Mode-I ripple fracture/ *Cumulative count, Lamb wave amplitude*	[120]
60 nm SiN thin film on Polycarbonate substrate	Nanoindenter	Instrumented indentation	1000 µN	Loading & Unloading	Nanoscale cracking/ *AE signal*	[121]
Polycrystalline 3C-SiC (a poly-types with cubic structure) CVD thin films of thickness 50-285 nm	Nanoindenter: Cube-corner diamond tips, radius 116 and 685 nm	Nanoindentation in Atomic Force Microscope retrofitted with a Triboscope system, Hysitron Inc.	0-7000 µN	Loading	Fracture, Deformation/ *Amplitude, Energy, Frequency*	[122]
Au alloy film on glass substrate	Conical PbO-TiO2-ZrO2	Microidentation adhesion tester	1.4-20 nm s^{-1} 0-12 mN	Loading	Delamination, cracking/ *Counts, amplitude*	[123]
MPCVD diamond coated (6 µm film thickness) on sintered Si_3N_4 substrate (*15.3 mm dia., 3.1 mm thick*)	Brale diamond cone	Indenter adapted to UTM, Shimadzu's model AG-25TA	50 µm/min	Loading	Lateral & radial cracks, debonding, *AE signal, amplitude*	[124]
Polycrystalline diamond films (30 µm thick with 10 µm grain size) deposited on sintered Si_3N_4 ceramic substrate; Micro-crystalline diamond-MCD film using MPCVD; Nano-crystalline diamond-NCD film using HFCVD	Brale diamond cone	Indenter adapted to UTM, Shimadzu's model AG-25TA	50 µm min^{-1} at discrete load range of 0-1000 N	Loading	Fracture and cleavage/ *AE amplitude peaks*	[125]
MPCVD diamond films of thickness 5µm (heat-treated/untreated of as-deposited sample) deposited on dc sputtered Ti-interlayer of 0.6 µm thick on Cu substrate (*10 x 10 x 1 mm*)	200µm radius Rockwell-C	Indentation using CSEM-Revetest scratch tester	0-100 N, 0-200 N at 30 N min^{-1}	Loading	Delamination/ *Amplitude*	[126]
MPCVD diamond films of 1.5 µm thickness on pure substrate such as Ti, Cr, Si and Ti coated on Cu substrate (*5 x 5 x 1 mm*); Sputtered Ti-interlayer of 0.6 µm thickness on Cu substrate before CVD process	200 µm radius Rockwell-C	Indentation using CSEM-Revetest scratch tester	0-180N at 30 N min^{-1}	Loading	Delamination/ *Amplitude*	[127]
Nitrogen-doped stainless-steel PVD coatings (10 µm thick) deposited by reactive magnetron sputtering	Rockwell-C	Indentation using LSRH-Revetest scratch tester	0-40 N	Loading & unloading	Tensile ring cracks/ *Amplitude & FFT*	[128]

Ma *et al.* [122] suggested that crack nucleation and growth along grain boundaries in polycrystalline silicon carbide thin films with columnar microstructure was the most likely accommodation mechanism during indentation. AE signals were always produced just before commencement of a 'pop-in' but not at any other point of the loading curve, which they look to be indicative of a combination of deformation and fracture processes in films and not associated with frictional slip at the indenter tip/film contact interface. The load at the instant of 'pop-in' excursion (i.e. critical load) and the associated AE energy increased with film thickness. Bahr and Gerberich [95] investigated the relationship between the measured elastic energy using the nanoindentation technique with the AE energy during indentation of brittle thin films of Ti_2N on sapphire substrates. A linear relationship between released elastic energies and the corresponding delamination AE energies was observed regardless of sample geometry.

d. Conical indenters

Tsukamoto *et al.* [123] observed sudden fluctuations in load during loading of thin Au films on a glass substrate along with synchronous AE, which they related to the film delamination from the substrate. Indenting at 30° and 45° to the horizontal produced a typical 'kink' in the load-displacement hysteresis during loading with synchronous high amplitude AE which was attributed to film delamination, cracking and slip of the indenter. Tsukamoto *et al.* [123] also studied the adhesive strength of diamond coatings on Si wafer substrates and showed that the substrate was the main source of most of the AE peaks (mainly due to deformation and cracking).

Belmonte *et al.* [124] compared the adhesive behaviour of diamond film coated onto Si_3N_4 ceramic substrates polished to two different roughnesses. The 'ground' material (R_a: 0.178 μm) exhibited the most intense AE peak due to spalling of the film and this occured at a higher load, while the 'polished' material (R_a: 0.013 μm) exhibited delamination of the film at lower load. Amraval *et al.* [125] investigated the fracture, cleavage and adhesive behaviour of polycrystalline diamond films coated onto sintered Si_3N_4 ceramic. Although no correlation between the star shaped radial cracking around indentations and AE was attempted, the observed high amplitude peaks were attributed to fracture, cleavage and adhesion of the diamond films while in contact with the indenter.

Fan *et al.* [126-127] and Ikeda *et al.* [118] have investigated the adhesion of diamond films deposited on different substrates by analysis of the critical loads. Fan *et al.* [126] identified and compared the critical loads during loading, which caused delamination of as-deposited and post-treated diamond films deposited on Cu substrates with Ti interlayers. For the post-treated films, the higher annealing temperature and/or longer annealing time were thought to lower the critical load and be exhibiting worse adhesion, due to changes in the structure of the diamond film/interlayer/substrate interface. For diamond coatings on Ti and Cr substrates, Fan *et al.* [127] found that the indentations caused substrate cracking prior to the failure of the film/substrate interface. The diamond coated Ti specimen exhibited regular AE peaks of low intensity, while a very intense AE peak was detected for the diamond coated Cr substrate. The small AE peaks for diamond coated Ti specimens were attributed to film cracking and localized detachment. They concluded that film cracking followed by film delamination was associated with high intensity AE, and a number of failure modes could be detected using AE, such as substrate cracking, film cracking and localized detachment, and film delamination and its propagation. In nano-crystalline diamond (NCD) film coated onto sintered SiC substrates, Ikeda *et al.* [118] detected and separated the outer ring-shaped cracks due to tensile stresses and inner ring-shaped crack due to compressive stresses using AE signals. They found that delamination of NCD films was caused by Mode-II fracture or buckling of the film due to compressive residual stress in the film. Higher numbers of ring shaped cracks were attributed to the weak inter-granular cohesive strength of the diamond film, whereas the few radial cracks in NCD film were found to be due to the difference of the compressive residual stresses.

Stebut *et al.* [128] developed an on-line AE tool using instrumented indentation (depth-time) to identify brittle, cohesive and adhesive failure mechanisms of nitrogen-doped stainless-steel thin films. The sharp and high amplitude AE signals corresponded to brittle and tangential ring cracking during holding, whereas continuous low amplitude AE signals corresponded to background noise identified right through the indentation cycles. They found that ring cracks developed through the coating thickness but no delaminations from the substrate were observed.

2.2.7 AE monitoring of thermal spray coatings

Table 2.7 summarizes the published work on AE monitored indentation of thermal spray coatings surfaces, which is the material of most relevance to this work.

a. Hertizan (spherical) indenters

Safai *et al.* [27] used Brinell indentation to characterise the porosity of plasma and flame sprayed alumina coatings. The amount of cracking due to porosity in the plasma sprayed coatings was approximately one-half that of the flame sprayed coatings, evaluated using the average AE event counts. It was therefore concluded that a reduction in AE event count was representative of reduced porosity. These authors also used high indentation loads to study the debonding mechanisms of sprayed coatings from the substrate, but did not report any finding about AE.

The influence of a bond coat on the cracking features of plasma spray coatings were investigated by Sentruk *et al.* [30] using Hertzian indentation. They found that a bond coat layer of NiCrAl under plasma sprayed partially stabilized zirconia (PSZ) ceramic coatings suppresses AE activity and associated this with surface compressive stresses inhibiting cracks. They also observed that the critical load (determined on the basis of AE energy) was higher when a bond coat layer was present for both continuously and non-continuously sprayed coatings. The cracking phenomena occurring during indentation and the associated AE activity were also influenced by the thermal spray process parameters.

Table 2.7 AE monitoring of thermal spray coatings

Specimen	**Indenter**	**Indented surface**	**Indentation system**	**Load/ Rate**	**Indentation cycle AE**	**AE: Source/ *features identified***	**Ref.**
Al_2O_3 (oxyacetylene: 15% porosity), Al_2O_3 (plasma: 8-9% porosity), Al_2O_3-13%TiO_2 (plasma-fused: 4% porosity), Al_2O_3-40%TiO_2 (plasma-fused: 6% porosity), Al_2O_3-40%TiO_2 (plasma-composite: 4% porosity) on mild-steel substrate; 130 µm thick coating	Brinell, 10 mm dia.	Coating surface	Brinell's indentation	5 kN	Loading & unloading	Densification of pores/*Total counts*	[27]
Top coat (500 µm) of Plasma-sprayed Al_2O_3-40% TiO_2, Al_2O_3-13% TiO_2, Al_2O_3-3% TiO_2 with Ni-Al bond coat (60-80 µm thick) on low carbon steel substrate (*75 x 10 x 5 mm*)	Vickers	Coating surface	Depth sensing indentation: Instron 4301	20-300 N	Loading	Fracture & Deformation/ *RMS amplitude and frequency*	[28]
Top coat (900 µm) of Plasma-sprayed Al_2O_3-13% $TiO_2$with Ni-Al bond coat (100 µm) on low carbon steel substrate (*5 mm thick*) as-sprayed and micro-wave treated	Vickers	Coating surface	High-frequency dynamic impact (at 20 kHz impact duration of 5 minutes)	5-15 N	Loading	Fracture & Deformation/ *RMS amplitude and frequency*	[29]
Top coat (900-1100 µm) of Plasma-sprayed Yttria stabilized zirconia (YSZ) ceramic coatings with and without NiCrAl bond coat (150-200 µm thick) on mild steel substrate (*60 x 7 x 2.54 mm*)	Hertzian WC ball, 3.175 mm dia.	Coating surface	Servo-hydraulic machine: Instron 8502	10 µm s^{-1} load up to 3 kN	Loading	Pore coalesce, layered cracking/ *Energy and Event*	[30]

The results from Safai *et al.* [27] and Sentruk *et al.* [30] indicate that soon after the Hertzian indenter touches the plasma sprayed surface, AE events occur which could be associated with crack nucleation beneath the indenter and some of the AE sources could be related to sub-surface effects such as mechanically induced closure of pores and/or densification due to the compressive stresses acting below the indenter. This has been described further by Factor and Roman [34-35] working on micro-indentation testing of thermally sprayed coatings with a metal matrix. When indenting these coatings, the material beneath the indenter experiences compaction (due to Hertzian compressive stresses) facilitated by failure of weakest links. The compaction may involve plastic deformation of the metal matrix leading to development of additional residual stresses, failure of the matrix-reinforcement interface, or local cracking of the hard phase particles. In thermal spray coatings, the main contributor to the indenter accommodation is porosity closure in the stress field of the indentation.

b. Vickers indenters

Prasad *et al.* [28] carried out on-line AE monitoring along with off-line damage assessment by scanning electron microscopy (SEM) to corroborate the critical loads for three grades of plasma-sprayed alumina-titania coatings (Al_2O_3-40% TiO_2, Al_2O_3-13% TiO_2, Al_2O_3-3% TiO_2) on a carbon steel substrate with a Ni-Al bond coat. They found that the RMS AE increased at a critical load just before the onset of rupture of coatings, after which the RMS decreased. It was found that, as the percentage composition of alumina increased; the critical load decreased. Further, they classified the AE response into two categories according to AE frequency; deformation mode (35-40 kHz) and fracture mode (220-280 kHz). According to Prasad *et al.* [28], plastic deformation produces continuous AE with low frequency, whereas cracking produces burst-type AE signals.

In an extension to the work of Prasad *et al.* [28], Vijayakumar *et al.* [29] used high frequency dynamic impact of a pyramidal diamond indenter to compare the critical load for rupture for plasma as-sprayed and microwave-treated (post-processed) alumina-titania coatings. It was found that, during the 'deformation mode' the frequency of the AE was in the range 200-400 kHz for as-sprayed coatings and 800-900 kHz for microwave treated coatings. They observed that post-treatment (microwave treatment in this case) of coatings increases the micro-hardness and reduces porosity so that microstructure exhibits higher resistance to dynamic impacts for a longer time. Also,

post-treatment will reduce the residual stresses which might otherwise drive further coating damage during dynamic impact.

2.2.8 Prospects of AE monitored indentation testing

It is clear from the foregoing review that cracks formed during indentation of bulk materials and coatings generate AE. It is also clear that the uncertainty in quantifying and measuring the total crack lengths in indentation makes a simple fracture-mechanics based assessment of coating toughness difficult for all but the simplest cracking patterns. It is therefore expected that correlation between AE and fracture patterns will lead to an improved method for coatings quality evaluation. **Table 2.8** summarizes those empirical relationships which have been published using AE, fracture toughness and cracking pattern. The review has indicated very limited work on thermally sprayed coatings certainly much less than on thin solid films. Such work as has been done, along with structural bulk materials, such as ceramics and composites suggests that cracking patterns will be rather complex for coatings where there is a ductile (metallic) and brittle component, so challenges were expected in observing cracking patterns. Furthermore, the difficulty in measuring the cracking makes the case of AE for coating quality estimation all the more advantageous.

Table 2.8 Empirical formulations for AE and cracking

Material group	Materials	Indenter/Indentation	Mechanical properties evaluation using AE	Ref.
GLASS	Soda-lime glass	Vickers/Tukon hardness tester	Accumulated AE energy, $\varepsilon \sim (K_c^{\,2}/E)c^4$; 'c' is median crack length, K_c is stress intensity factor, and E is Young's modulus.	[98]
GLASS	Soda-lime glass	Vickers/ Indenter fixed on loading frame via a miniature load cell	P-wave amplitude; AE amplitude '*A*' of first P-wave arrival of the unloading crack signal, $A = a\,(P_m\text{-}P_t)^n$; where a, n is a constant of curve fit, P_m is max. load prior unloading, P_t is threshold load for unloading cracks.	[96]
CERAMIC	Si_3N_4	Vickers/ Vickers indentation tester	AE Energy/Event ratio, $\varepsilon = AK_{1c}^{\,-2.1}$, A is a constant, K_{1c} is indentation fracture toughness	[76]
COMPOSITE	Mullite matrix embedded with aluminum oxide and tetragonal zirconia polycrystal (TZP)	Vickers/ Instron machine	Power law: Cumulative distribution of AE events, $F(A) = (A/A_0)^{-b}$; A is lowest detectable AE amplitude, index '*b*' gives a measure of fracture toughness	[108]
CERAMIC	Al_2O_3	Vickers/ Microhardness tester	The AE energy rate $\dot{U} = n\sigma^2 c/E$, where σ is applied stress, c is crack length, η is a constant, and E is Young's modulus	[79]
CRYSTAL	MgO	Vickers/ Microindentation tester	Stress deformation relaxation, $K = (N\text{-}N_1)/N$; N_1 is AE signal due to indenter penetration and N is AE signal during al indentation process (N)	[87]
GLASS	Soda-lime glass	Cube-corner nanoindenter	AE energy = 0.007 $c^{4.1}$; c is radial crack length	[94]
CRYSTAL	beta-SiC	Cube-corner nanoindenter	AE energy = 0.202 $c^{2.1}$; c is radial crack length	[94]
THIN FILM COATINGS	Pulsed laser deposited (PLD) 110nm thick tetrahedral amorphous carbon (ta-C) on (001) silicon substrate	Cube-corner nanoindenter/ TriboIndenter	Radial crack, $c = \left[(2/\alpha\pi K_1).\sum AE_{crackextension}\right]^{1/2}$; α is a sensor constant, K_1 is fracture toughness, and, Channel crack $c = (1/\alpha t_f K_1).\sum AE_{crackextension}$, t_f is film thickness	[70]

There are no fixed standards (except on the thickness) for the size of the indentation test specimens, although much of the reported work is on relatively small specimens, as

little as 0.5 mm [e.g. 77] to 1 mm thick [e.g. 77, 89-90, 115, 126-127, 129-130]. Extending findings to real structural components requires consideration of the fact that AE experimental data is influenced by specimen geometry [131-132]. There are some guidelines for specimen thickness for indentation induced cracking and deformation. For indentation induced cracking, the thickness should be at least five times the distance radial cracking extends from the centre of the indentation, or ten times the depth of penetration, whichever is greater [133]. For indentation induced deformation, the thickness should be at least 1.5 times the length of the diagonal [134-135]. These limitations need to be considered when designing specimens for AE monitored indentation, although other considerations might influence specimen geometry.

2.3 Thermal spray coatings

Since the work involves thermally sprayed coatings and the monitoring of the thermal spray process, it is appropriate to review this process briefly.

2.3.1 Thermal spray principle and sources of AE

"Thermal spraying" is a generic term used for processes whereby a sprayed layer is built up by partially melting a powder in a high temperature zone (a flame or plasma) and propelling the resulting spray towards the substrate in the form of splats [136-137]. Various thermal spraying process exist (e.g., High Velocity Oxy-Fuel: HVOF, Air Plasma Spray: APS, Detonation Spray: DS and Cold Spray Gas Dynamic: CGDS) and all are used to produce thick-film coatings to combat surface degradation of engineering components by wear, corrosion and fatigue crack initiation. The kinetic energy of small particles has been found to dissipate within the substrate material in the form of elastic energy [138], and AE can, in principle, be used to characterize this because it is generated by rapid release of strain energy within a material. Part of the energy radiates from the source in the form of elastic waves which propagate over the material surface and can be detected using AE sensors. This can be relatively simply shown for single elastic impacts, but the situation is more complicated in spraying where the particles undergo significant plastic deformation, and there are many, perhaps overlapping events and a number of secondary processes (such as the collapse of particle agglomerations and phase changes) going on [139].

The sequence of events leading to the formation of the coating by a thermal spray process is shown in schematically in **Figure 2.20**. Virtually any material that melts without decomposing can be sprayed, and sprayed coatings are built up layer by layer. Although the desired thickness of the deposit may vary depending upon the application, protective coatings are typically 100-500 μm thick.

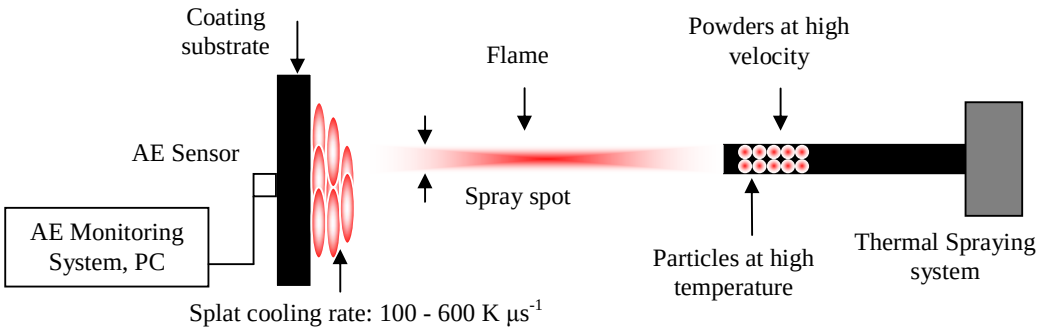

Figure 2.20 Formation of coating by a thermal spray process

This work uses two processes, HVOF and APS. The benefits of HVOF over APS are lower porosity, higher bond and cohesive strength, lower oxide content where required, better retention/control over particle chemistry and phases, and the ability to produce thicker coatings. Typical values of thermal spray process variables for HVOF Spray and APS are shown in **Table 2.9.**

Table 2.9 Thermal spray process variables [137]

Variants	**HVOF Spray**	**Air Plasma Spray**
Heat Source	Oxy-fuel combustion	Plasma flame
Flame Temperature (˚C)	3000-3500	10000-15000
Gas Velocity (m/s)	1500-2000	400-500
Particle Temperature (˚C)	1500-2000	2700-3500
Powder Particle Velocity (m/s)	600-800	100-200

2.3.2 High Velocity Oxy-Fuel (HVOF) spraying and HIPing

The HVOF processes [136-137, 140] rely on continuous internal combustion of a fuel gas with oxygen to produce a high temperature, high velocity exhaust gas stream into which powder particles are delivered. Propylene, propane and hydrogen are the most commonly used fuel gases. Flame temperatures are around 3000˚C, the flame velocity is hypersonic (in the range 1500-2000 m s^{-1}) and it is reported [32] that uniform heat input

and acceleration are available over almost a 12" distance. The powder material to be used for coating is injected into a carrier gas (nitrogen, argon or helium) and delivered to the process system using a pressurised powder feeder. The powder is partially melted and propelled by the combustion gases to impact the substrate at very high speeds producing highly adherent and dense coatings. The quality of thermal spray coatings is governed significantly by the coating powder characteristics as well as other factors like the spray process, operating variables and substrate surface preparation. The spray parameters most commonly varied are oxygen and fuel flow rate, powder carrier gas flow rate, powder feed rate, spray distance, and gun scan speed. There are a number of commercial HVOF spraying systems (JetKote, DiamondJet, JP-5000, THETA), and coated samples from JetKote, JP5000 and THETA-gun HVOF spraying systems are used in this study.

In thermal spray coating technology, the term Hot Isostatic Pressing (HIPing) refers to a post spray treatment of the coatings. HIPing has the advantage of uniform densification in all directions and can thus offer homogenous microstructures. It involves the application of a hydrostatic gas pressure up to 300 MPa and heating to a temperature of up to 2300 K [32]. HIPing greatly reduces porosity and the hardness and wear resistance of the coating are improved [31-32, 48-49].

2.3.3 Air Plasma Spraying (APS)

A Plasma is a partially ionized state of gas, produced either by passing a plasma generating gas through a high intensity arc struck between two electrodes (arc plasma) or by high radio-frequency excitation of the plasma gas (RF plasma). In APS, the plasma serves as a heat source to melt the injected powder, which is then propelled as spray onto the substrate where it deposits and forms the coating. Typical arc gases include argon, helium hydrogen and nitrogen, which can be used independently or in combination. Usually a mixture of monoatomic gases (e.g. He, Ar) is used to provide a good combination of high velocity and high temperature in the plasma flame. Typical plasma temperatures are in the range of 10000 to 15000 °C, whereas typical velocities in the range of 400-500 m s^{-1} at the nozzle exit have been reported [137]. The spray parameters generally varied are electrical current, voltage, working gas flow rate, spray distance, powder carrier gas flow rate, powder feed rate, and gun scan speed.

2.3.4 AE monitored thermal spraying process

On-line AE monitoring during spraying of thermally sprayed coatings has an advantage over current conventional coating quality testing techniques which are all off-line (e.g. mechanical testing procedures such as indentation, bending and residual stress analysis). There has been some research undertaken on AE monitoring of the thermal spray process such as arc spraying [141] and atmospheric plasma spraying [142-144]. In their introductory work, Bohm *et al.* [141] found the energy of the AE signal calculated using an auto-correlation function to be proportional to the kinetic energy of the impacting particles. Crostack *et al.* [142] and Lugscheider *et al.* [143] developed a model which relates the particle velocity and diameter of powder particles with the amplitude of AE signals. Most recently Nishinoiri *et al.* [144] used a laser-based AE technique to study microfracturing, delamination and cooling process during spraying. If AE features can be successfully correlated with spray process parameters and coating properties then it may be possible to use AE as a process control parameter to improve cohesive and adhesive strength, hardness, porosity and tribo-mechanical properties of thermal spray coatings using this technique.

2.4 Identification of thesis topic

AE monitored indentation testing has provided insights into the fundamental mechanisms involved in fracture of brittle materials. It considerably enhances the information on a material's AE response, particularly when using instrumented indentation systems. Currently, there appears to exist no comparable experimental evidence concerning force, displacement and AE characteristics during Vickers indentations of thermal spray coatings. Some relationships have been observed between parameters of indentation deformation, fracture and the AE signal but none of these have been applied to thermal spray coatings. Finally, there is much to be learned about the behaviour of multi-phase brittle materials under indentation, and monitoring of the AE could considerably enhance this understanding.

Chapter 3

EXPERIMENTAL METHODS

This chapter describes the experimental apparatus, materials and methods used for the research. Two distinct types of experiments are described, the first related to AE monitoring of the Vickers indentation behaviour of metals and thermally sprayed ceramic coatings, and the second related to AE monitoring of the thermal spraying process itself. First, the materials are described, along with the various characterisation tools used. Next, the AE monitoring apparatus and signal processing technique is described, followed by the basic Vickers indentation apparatus and its instrumentation for obtaining time-correlated measurement of force and depth during indenter loading. The analysis techniques for crack length measurement including the classical approach and the AE-based indentation fracture toughness measurement model are also described. Finally, the apparatus and procedure for AE monitoring of the thermal spraying process is presented, followed by a summary of all experiments.

3.1 Material selection, specimen details and characterisation tool

Three metals and six thermally sprayed coatings were selected for indentation testing (**Table 3.1**), although the full range was only tested for the preliminary experiments. The materials were chosen to give a range of accommodation mechanism from purely plastic deformation through a combination of plastic deformation and hard particle fracture to fracture with little or no plastic deformation. For the main tests, two types of thermally sprayed thick coatings were chosen, one single phase (Al_2O_3) and the other multi-phase (metal carbides), each coating having a variation in the deposition conditions and/or post-deposition treatment. Most of the coated specimens used in this study were prepared by thermal spraying onto one side of a substrate consisting of an AISI 440C martensitic stainless steel disc of diameter 31 mm and thickness 8 mm. Prior to spraying, the substrate was grit-blasted and cleaned according to international standards [145], and the spraying process parameters were those which had been industrially optimized for the relevant coating material. There are a number of factors which dictate the residual stress profile in thermal spray coatings [48-49], but the final pass is always different in its residual stress profile due to the absence of the shot-

penning effect, which is caused by the high velocity of impacting particles on the underlying deposit.

Table 3.1 Vickers indentation test specimens

Materials (*Industrially optimized coatings [Appendix B])	**Specimen details**	**Coating thickness (µm)**	**Surface roughness (Ra, µm)**	**Microhardness values ($HV_{1.96\ N}$)**
Metals				
Copper metal	99.99% pure	-	0.021±0.01	93±5 HV
Aluminium metal	99.99% pure	-	0.034±0.03	108±2 HV
Hardened steel	Martensitic (high carbon)	-	0.023±0.05	771 ± 19
Carbide coatings				
*WC-12%Co	As-sprayed (HVOF, JP5000)	300-325	0.043±0.01	1002±159
*WC-12%Co	As-sprayed (HVOF, Jet-kote)	300-325	0.045±0.03	1050±70
*WC-12%Co	HIPed (1123K/150 MPa/1 hr) (HVOF, Jet-kote)	300-325	0.047±0.03	1018±177
WC-10%Co-4%Cr	As-sprayed (HVOF, JP5000)	50-60	0.134±0.07	1097±110 990±18
Ceramic coatings				
*Conventional Al_2O_3 (> 98% pure)	APS (Metco 9MB)	250-260	0.27±0.02	683±38 (Gold Sputtered)
*Fine powder Al_2O_3 (> 98% pure)	HVOF (Theta-gun)	250-260	0.096±0.02	632±29 (Gold Sputtered)

X-ray diffraction (XRD) analysis was used to identify the crystalline phases present in the coatings. A Bruker AXS, Model D8 ADVANCE X-Ray diffractometer was used operating at 40 kV and 40 mA. Cu-$K\alpha$ radiation was used (wavelength, λ = 0.1542 nm) and the goniometer was run from 5.000° to 84.997° with a step size of 0.009° (2θ) at 15.4 seconds per step. Data were collected at room temperature.

In preparation for the indentation tests, specimens surface were ground and polished using, consecutively, 15, 6 and 1 µm diamond paste in order to reduce surface residual stresses which can affect crack lengths during indentation [2], and also to remove any obvious asperity effects. It is possible that such polishing can still induce stresses [146] and cause pull-outs of hard particles in a metallic matrix, and that scratches could act as initiation sites, perhaps giving rise to more surface cracking during indentations than if the surface were unprepared. However, any effect was expected to be broadly similar for all specimens and to give more consistent results than an unprepared surface would. The microhardness of the polished specimens was measured in order to assess the microstructural uniformity and for comparison with the macroscale values. The Vickers microhardness was obtained using a calibrated Mitutoyo, MVK-H1 machine for five

indentations applied to the surface of specimens at 1.96 N (or 200 g) load. Before each set of microhardness measurements the calibration system was checked using a test block of hardness 304HV.

The microstructure of the specimens, the surfaces for indentation, the cross-sections and pyramidal surfaces of the indentations, the powders and the tip of the diamond Vickers indenter were all examined using an optical microscope (Nikon, with N50 monochrome camera), at various magnifications and, where necessary, using a Scanning Electron Microscope (Hitachi: S-2700) or Environmental Scanning Electron Microscope (Philips: XL30). Before the indentation tests, the coated specimens were examined using the microscope in order to identify the level of contrast of different coated specimens. It was found that the microstructure of the HVOF (WC-12%Co: as-sprayed and HIPed, WC-10%Co-4%Cr: as-sprayed) coated specimens could be seen clearly, whereas contrast in the APS Al_2O_3 (conventional powder) and HVOF Al_2O_3 (fine powder) was poor. These specimens were gold sputtered (~10-20 nm thin layer) to increase the surface contrast level to allow focussing of the specimen surface using the optical lens of the indentation testing machine. To provide additional metallographic information, a small section of each coated specimen (APS and HVOF Al_2O_3 coatings) was crushed to remove some coating from the substrate as flakes, and flakes refrigerated in liquid nitrogen, placed in a vice and broken by bending (cryogenic fracture). The broken flakes were warmed to room temperature and rinsed with acetone and dried, before microscopic examination of the fracture, porosity and splat morphology.

3.2 Acoustic Emission testing and measurement

3.2.1 AE apparatus

The AE acquisition system and set-up are shown in **Figure 3.2a**. The system was assembled in-house and comprised; AE sensors with preamplifiers, a signal conditioning unit, a connector block, a data acquisition card, and a computer with LabVIEW software for controlling the acquisition and storage of data in the PC.

The AE sensors were of type Physical Acoustics (PAC, see *Appendix-C*), Micro-80D, based on lead zirconate titanate (PZT). These are broadband differential AE sensors

producing a frequency response between 0.1 and 1 MHz with a 340 kHz resonant frequency, and an operating temperature range from − 65 to +177ºC.

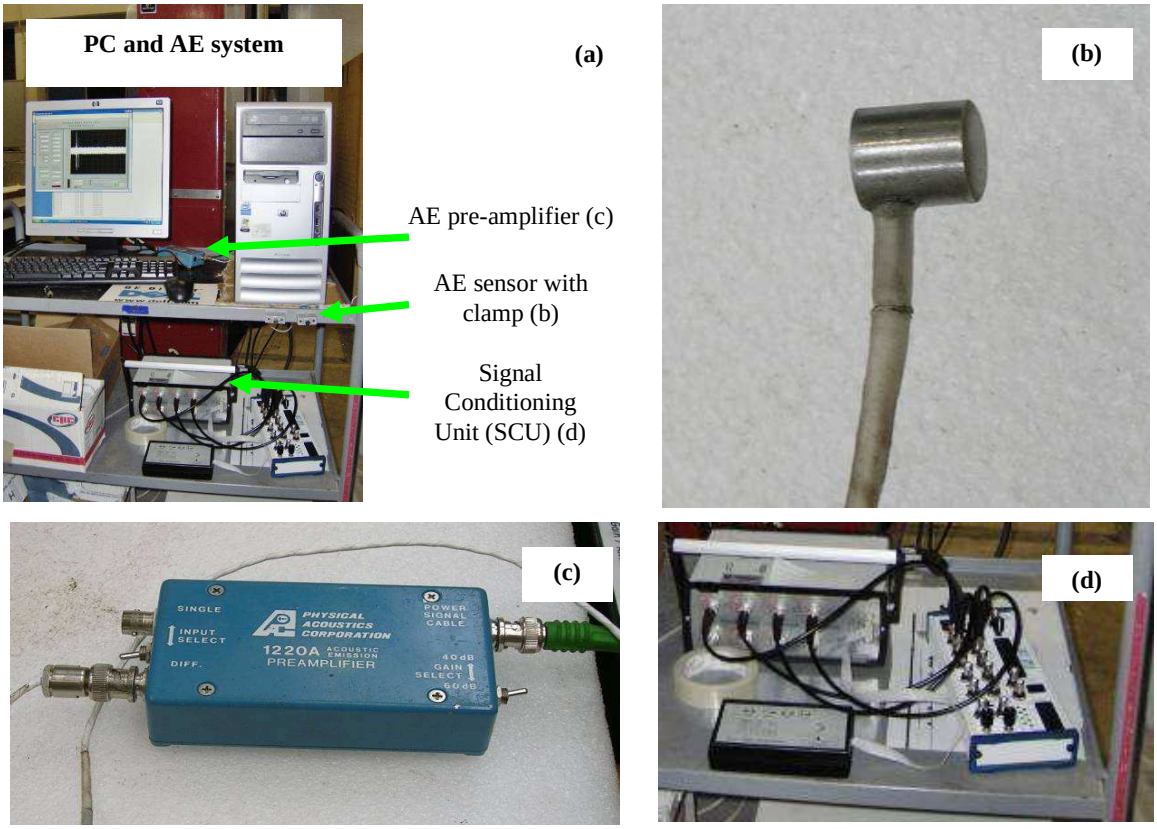

Figure 3.2 Acoustic Emission testing apparatus (a) PC and AE system, (b) Broadband PZT AE sensor (PAC, Micro-80D), (c) Pre-amplifier (PAC series 1220A) and (d) Signal Conditioning Unit, connector block and gain programmer

The AE sensor converts elastic waves propagating through the material under examination into a time varying voltage signal, which is known to be reproducible although the possibility of reflection of AE waves at the edge of the specimens exists. The sensors (**Figure 3.2b**) are 10 mm in diameter and 12 mm high and were held onto the flat test specimen surface using 100 μm thick aluminium tape and custom made magnetic clamps. In order to obtain good transmission of the AE signal, the surface was kept smooth and clean and silicone high vacuum grease was used as couplant to fill any gaps caused by surface roughness and to eliminate air which might otherwise impair wave transmission. Before every test, the sensitivity of the sensor was checked by breaking a lead pencil close to it to ensure signal detection.

Preamplifiers of type PAC series 1220A (**Figure 3.2c**) were used to amplify the AE signal to a level that can be carried by a BNC cable and converted by an Analogue to

Digital Converter (ADC). The amplifier had a switchable 40/60 dB gain and an internal band pass filter between 0.1-1 MHz. The preamplifier was powered by a + 28 V (0.2 A) power supply and used a single BNC connection for both power and signal. The programmable 4-channel signal conditioning unit (SCU) and gain programmer (high-high: +6, high-low: 0, low-high: -6 and low-low: -12 dB) were of in-house construction and were used to power the AE sensors and pre-amplifiers, as shown in **Figure 3.2d**. **Table 3.2** shows the amplification level used for different studies.

A National Instruments BNC-2120 connector block (**Figure 3.2d**) was used was to carry signals from the sensor to the data acquisition system. This was a shielded connector block with signal-labelled BNC connectors and included an LED so that it can test the functionality of the hardware. Signals from the PZT AE sensor, linear variable differential transducer (LVDT) and load cell were acquired through this connector block.

Table 3.2 Amplification levels of AE signals

AE monitoring during	Material type	Materials	Amplification (dB)	
			@ Pre-amplifier	@ SCU
Vickers indentation	Metals	Hardened martensitic steel (high C)	60	+6
		Aluminium	60	+6
		Copper	60	+6
	Carbide/ Ceramic coatings	HVOF (JP5000) as-sprayed WC-12%Co	60	0/+6
		HVOF (JetKote) as-sprayed WC-12%Co	60	+6
		HVOF (JetKote) HIPed WC-12%Co	60	+6
		HVOF (JP5000) as-sprayed WC-10%Co-4%Cr	40	+6
		APS (Metco 9MB) conventional Al_2O_3	60	-12
		HVOF (theta-gun) fine powder Al_2O_3	60	+6
Thermal spraying	Carbide coatings	HVOF (JP5000) WC-10%Co-4%Cr	40	0

The acquisition of raw AE signals requires high performance data sampling and compatible computer systems, so a National Instruments (NI), PCI-6115 board data acquisition card (DAQ) which has 12 bit resolution was used, assembled into an in-house built desktop PC as shown in **Figure 3.2a**. The board can be used to acquire simultaneously the raw signal at up to 10 M samples/s for up to four channels (i.e. 2.5 M samples/channel) and uses a full length PCI slot. The DAQ voltage input range was set at ± 42 V on the total on-board memory of 64 MB per channel. The board supports only a 4-pseudodifferential input configuration and has maximum voltage protection of 42 V (channel-to-earth and channel-to-channel). LabVIEW software from National Instruments was used to control and to obtain the raw signals from the PCI-6115 board

and in-house developed LabVIEW code [23] was used to control sampling frequency, number of acquired samples per channel, number of records, input range, pre-trigger data, trigger channel and trigger level. The data in this study were acquired at 2.5 M samples/s for two seconds, unless otherwise stated.

3.2.2 AE signal processing techniques

Generally, AE waveforms (amplitude-time) are very complex and difficult to use directly to determine the condition of a system under test. A number of conventional features [20] have been developed specifically (see **Figure 3.3**) to describe non-continuous AE, characterized by time-series burst signals, where the amplitude usually rises rapidly to a maximum value and decays nearly exponentially to the background noise level.

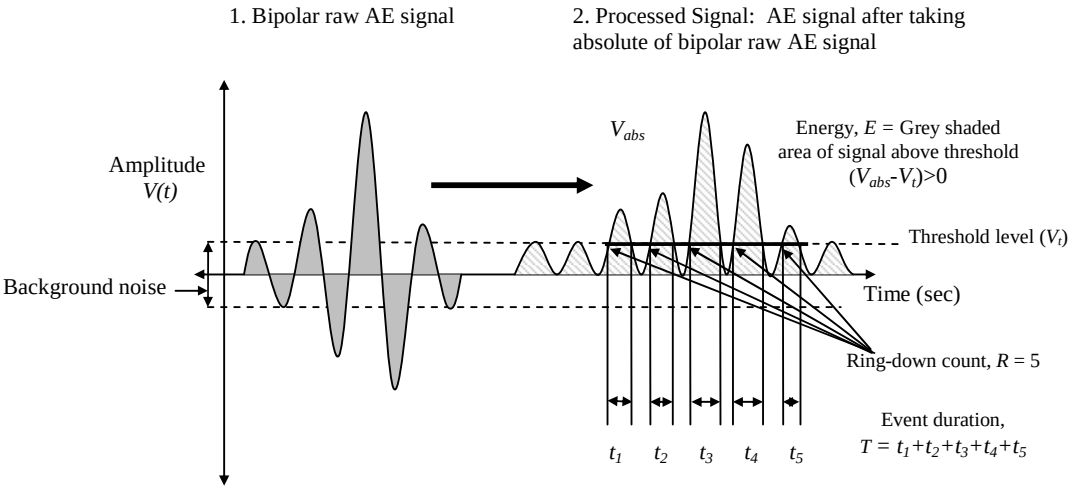

Figure 3.3 Schematic diagram showing calculation of the AE features: ring-down count *R*, energy *E* and event duration *T*

In practice, even at 2.5 MHz sampling rate, the AE associated with individual cracking events may well overlap and the specimen is small enough that a given event will probably be recorded, because of reflections from the specimen boundaries. Thus the AE must be regarded as representing the cumulation of a number of events within a given time window and so only an averaged energy can be obtained in the time window.

For the purposes of making an assessment of the correlation between AE and cracking, one can suppose that the energy associated with the significant AE is approximately proportional to the area of new crack surface formed. Continuous background noise amplitude was found throughout the study at all indentation loads, so an automatic

analysis threshold level of 15% above the continuous background noise level was chosen to define significant AE activity. An AE ring-down count (*R*) was obtained from the number of times that the signal amplitude crossed the preset threshold in the positive direction. The AE energy was calculated as the area under the absolute of the signal above threshold:

$$E = \int_{t=0}^{t} \left(V_{abs} - V_t\right) dt \qquad \text{if } \left(V_{abs} - V_t\right) > 0 \tag{3.1}$$

where V_{abs} is the absolute voltage, V_t is threshold voltage and t is the time (above threshold) from the beginning of the event, as illustrated schematically in **Figure 3.3**. The event duration (*T*) is the total time that the signal spends above threshold was calculated as follows:

$$T = \sum_{i=1}^{R} t_i \tag{3.2}$$

where t_i is the individual time duration for each of the excursion above threshold, *R* (**Figure 3.3**). In such analysis, overlapping events are not distinguished from each other, although this will only have an effect on ring-down count and event duration, and not on energy. The frequency spectrum of the raw AE signal was also calculated (using Welch's power spectral density method [23-25]) to establish any frequency characteristics of the AE generated. Prior to any signal processing all data were corrected for gain in the data acquisition system using Equation 3.3 [25].

$$A = 20 \log\left(U_0 / U_i\right) \tag{3.3}$$

where *A* is signal gain expressed in dB and U_0/U_i is the ratio of output to input signal amplitudes.

3.2.3 AE transmission in small test specimens

Since the test specimens are relatively small and the indentation process is continuous, it is necessary to determine the characteristics of AE wave propagation in the coated AISI 440C stainless steel discs of diameter 31 mm and thickness 8 mm. Such a calibration allows an assessment of the approximate temporal resolution with which AE events can be determined, as well as understanding any time or frequency domain characteristics introduced by the specimen.

The characteristics were determined by placing an AE sensor near the circumference of the specimen on the coated surface, much as it is placed during the experiments, and

recording AE from a simulated source. A pencil with an in-house machined guide was used to generate simulated AE sources by breaking a 0.5 mm diameter and 2-3 mm length 2H pencil lead [147] (the so-called Hsu-Nielsen source) at three different locations as shown in **Figure 3.4**, and data were sampled at 2.5 MS/s for two seconds for each test, and a total of 5 tests were done at each location.

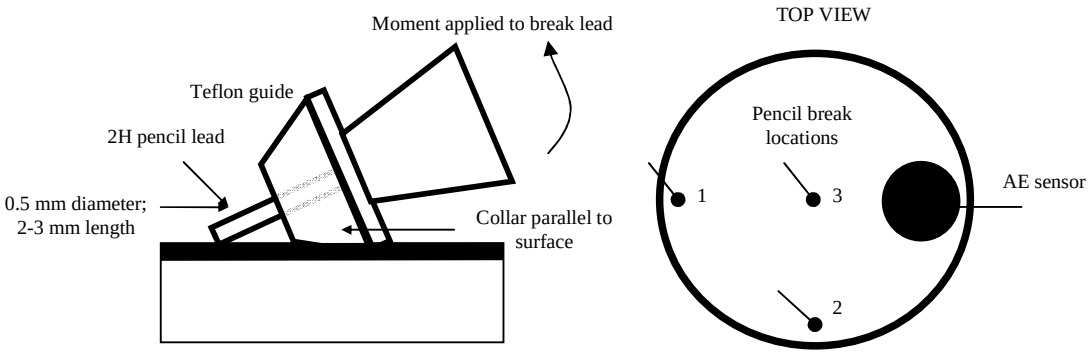

Figure 3.4 AE characteristics in small test specimen using a point impulse source

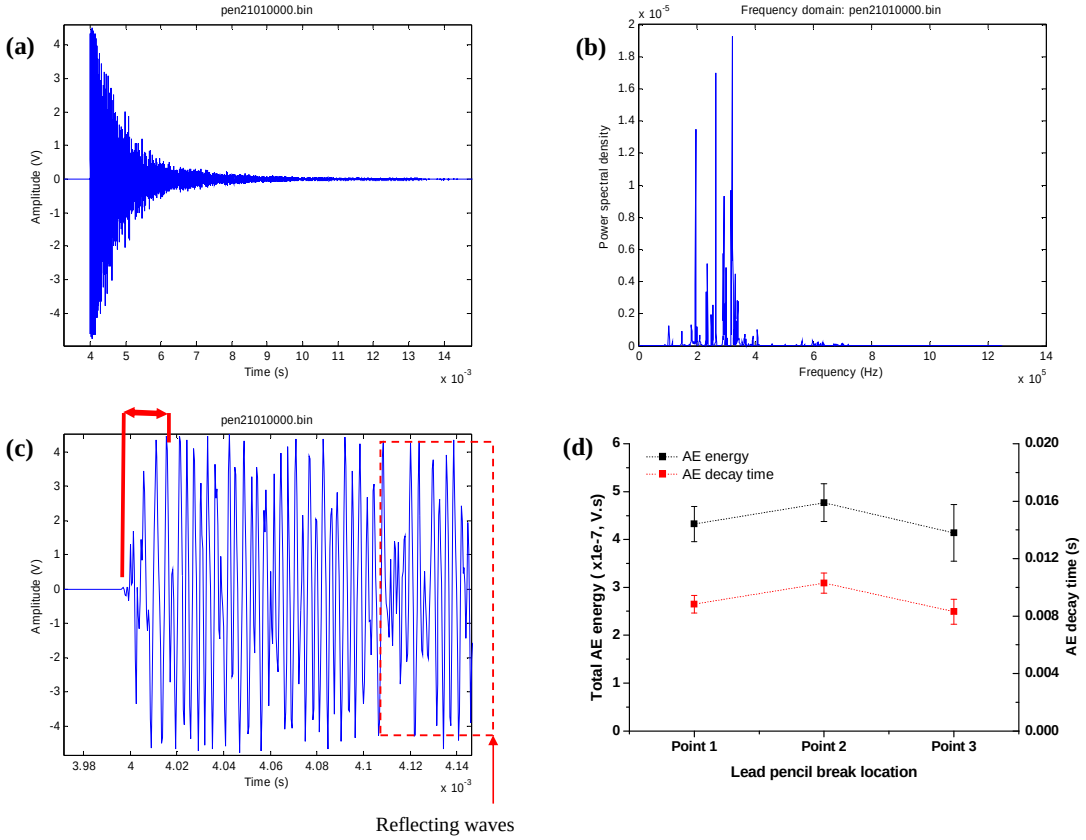

Figure 3.5 AE signal for pencil lead break at location 2 [amplification 60/0 dB]: (a) raw AE signal, (b) power spectrum of first 12 milli-seconds, (c) magnified raw AE signal showing the rise-time of 20 μs, and (d) AE energy and decay time at all three locations

Figure 3.5a shows the key features of the recorded AE signals for a typical pencil lead break at location 2 (which did not vary much for the other tests). The power spectrum (**Figure 3.5b**) shows responses between 200 and 400 kHz, with the largest peak at 340 kHz (resonant frequency) which reflects the characteristics of the sensor (as shown in the calibration certificate, *Appendix C*). The AE signal rise time varied between 20 and 30 µs (**Figure 3.5c**) whereas the decay time varied between 8 and 10 ms (**Figure 3.5d**) and the variation in total AE energy and AE decay time was small. Given that the pencil break represents a step unload, its frequency content and decay characteristics can be used to establish a datum for the spectrum and time resolution.

3.3 Vickers indentation tester and instrumentation

A conventional Vickers macrohardness testing machine was used with loads ranging from 49 to 490 N, applied to a diamond Vickers indenter. It was found that debris from the coated specimens adheres to the area around the tip (**Figure 3.6a**) and so the indenter was cleaned after each indentation by pressing it into a weak proprietory adhesive (**Figure 3.6b**).

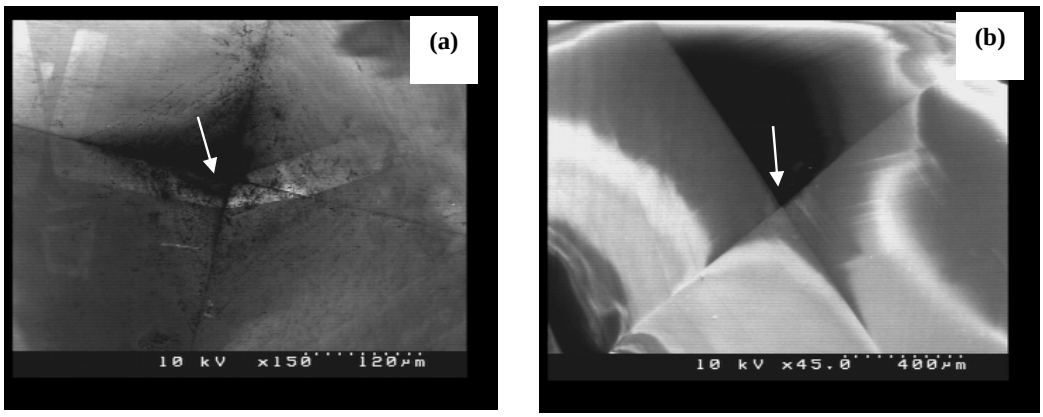

Figure 3.6 SEM image (top view of tip) of new diamond Vickers indenter: (a) debris concentrated and spread around tip after indenting as-sprayed HVOF (JP5000) WC-12%Co coatings at 490 N load, and (b) indenter after cleaning with mild adhesive. Arrow shows the indenter tip

The Vickers indentation testing machine is shown in **Figure 3.7** (W&T Avery Ltd.), and its instrumentation is shown in **Figure 3.8**. The machine was designed to work open loop according to international standards [134-135] using a constant dead-weight, the load being selected by adding weights to a stack. A sequence of levers and cams picks up the stacked weight(s), and a dashpot smoothes the descent of the indenter once the weight is released manually. As with all indentation tests, the specimen surface is

focussed using a microscope objective lens prior to loading, which ensures a fixed small initial gap between the indenter and specimen surface. A 15 second dwell time was used before unloading as specified by international standards [134-135].

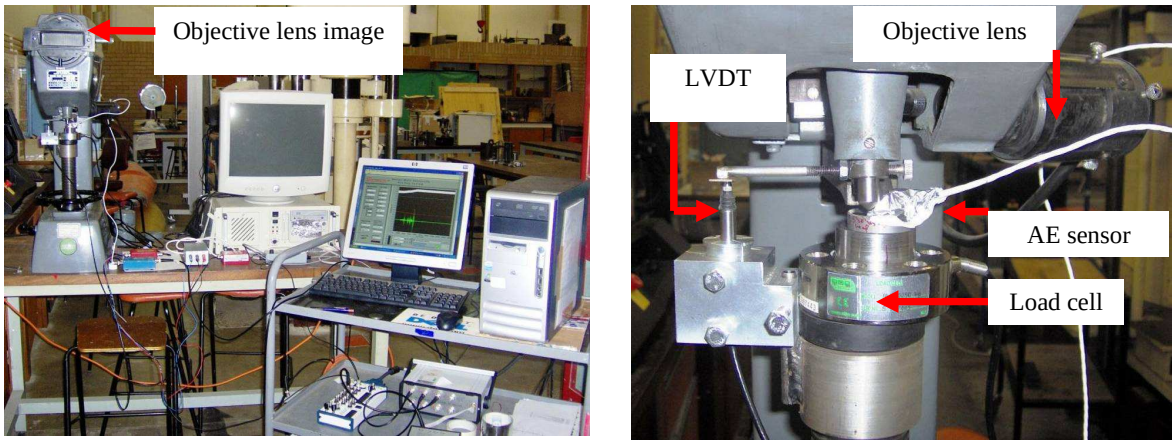

Figure 3.7 Instrumented Vickers indentation experimental set-ups

A load cell based on a strain gauge transducer with a capacity of 2.45 kN in tension or compression (Model RLU, RDP Electronics Ltd, UK) was used to measure the reaction force in the specimen as the indenter descends. A low noise, high precision strain gauge amplifier (Model: S7DC, RDP Electronics Ltd, UK) was used to convert the load cell output to voltage. The load cell was laid on the bottom anvil of the indentation machine, and the specimen was laid on the top surface of the load cell, leaving a clearance of 0.2 mm to bring in the indenter. The load cell was calibrated by loading and unloading a range of dead-weights and the resulting curve is shown in **Figure 3.9**.

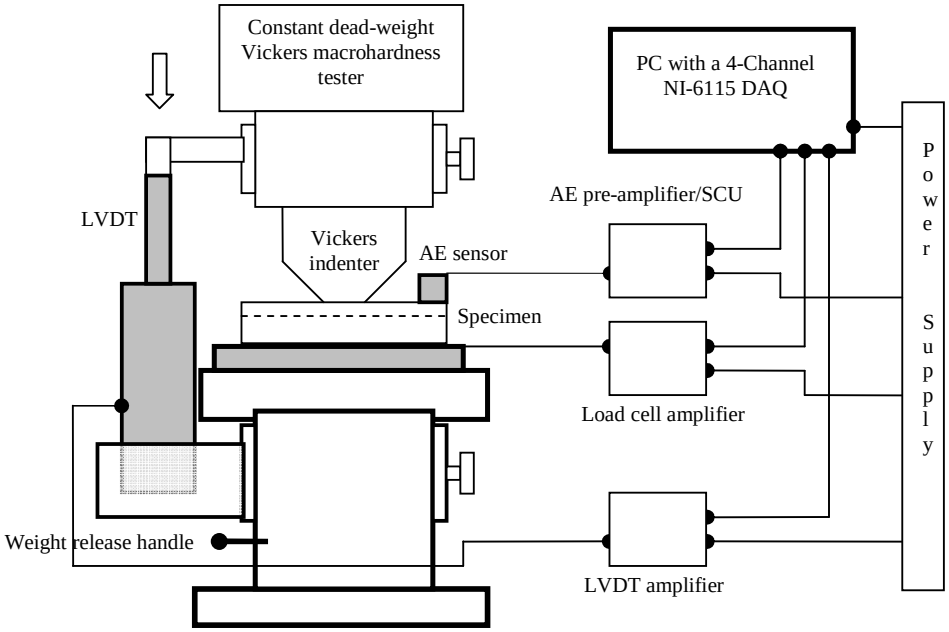

Figure 3.8 Schematic of the above experimental set-up for load, depth and AE monitoring during Vickers indentation

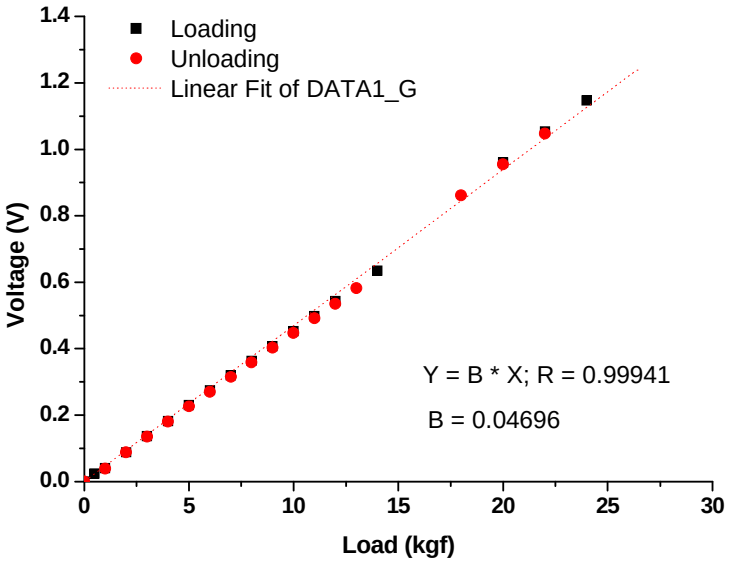

Figure 3.9 Load cell calibration

A calibrated spring return inductive displacement transducer (LVDT, Model: GT 1000-1.25, RDP Electronics Ltd, UK was used to measure the indenter head vertical displacement. The LVDT had a range of ±1.0 mm, linearity of 0.25% and uncertainty of calibration of 1.25 μm). It was mounted in a holder to present the armature to a cantilever bar attached to the indenter head as shown schematically in **Figure 3.10**. Power was supplied to the LVDT from a ±15 V DC/500 mA (Model: TML 15215C,

Traco Power, UK) unit and a calibrated in-line DC amplifier (Model: S7AC, RDP Electronics Ltd, UK) was used to provide the signal proportional to indenter displacement.

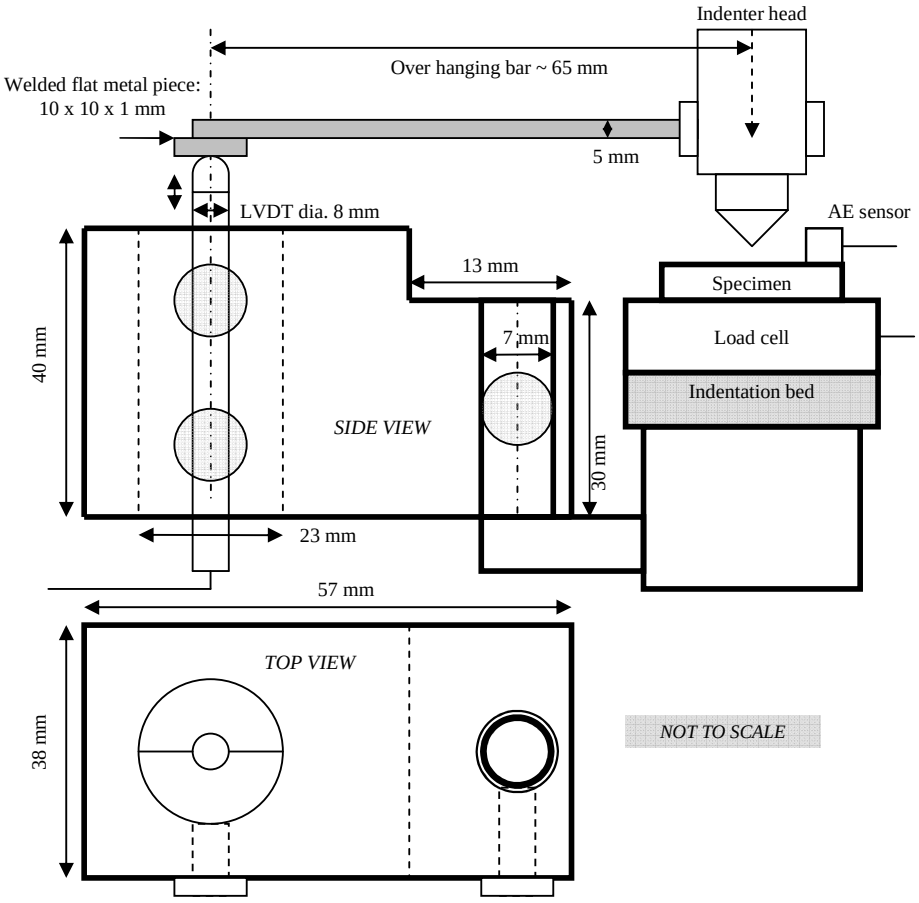

Figure 3.10 Design and set-up of LVDT holder

3.4 Vickers indentation measurements

All the indentation tests were carried out open loop with an AE sensor mounted on the specimen surface. In a sub-set of the tests, the indentation was instrumented to include a measurement of the force and the displacement. In open loop indentation tests no feedback is used between force and depth (or displacement) during loading cycle. The approach taken here was to measure the AE signal and use the force and depth against time during the indentation to understand the processes that might occur in a production environment using a simple open-loop test. The apparatus was assembled as shown in **Figure 3.7**. Data acquisition software as described in *Section 3.2.1* was used to record the stream of data from up to three input channels (force-*F*: channel 1, displacement-*h*: channel 2 and acoustic emission-*V*: channel 3) as a function of time (*t*). For fullly

instrumented tests, the LVDT (channel 2) was used as a trigger channel and, otherwise, data acquisition was triggered through the AE channel with 40 ms pre-trigger.

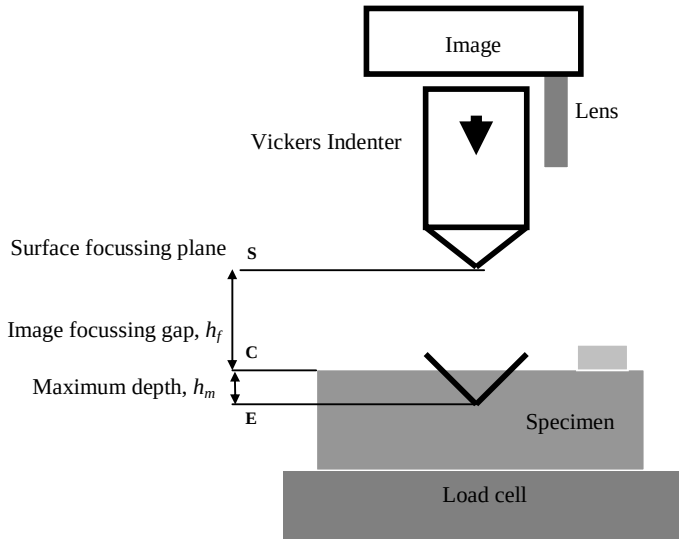

Figure 3.11 Principle used to measure the indentation displacement and force

For AE based instrumented testing, the specimens were placed directly on to the inbuilt plinth and the AE sensor placed on the coated surface. Five indentations were carried out at each of the ten loads and the AE signals recorded during loading of the indenter. No AE signal was detected during indenter unloading for any of the specimens at any of the indentation loads. The duration of the application of the test force was 15 seconds but AE was only observed during the first two seconds for all loads tested.

The principle used for measuring the indentation displacement and force during loading is illustrated in **Figure 3.11**. The inbuilt microscope was used to focus the surface and the image focussing gap (h_f) and maximum depth (h_m) was measured using the LVDT transducer. Release of the load following the image focussing process triggered the LVDT transducer as the indenter passed the surface focussing plane (*S*). The load cell time history starts when the indenter touches the specimen (at *C*) and ends when the indenter stops (at *E*), although some oscillation was detected in the load cell at this position. Consequently, the indentation depth (h_m) could be determined from the load and displacement time histories.

In the fully instrumented tests, data from the three sensors (load cell, LVDT and AE) data were acquired synchronously at 2.5 MS/s for 2 seconds. The data from the load cell

and the LVDT did not need to be sampled at such a high sampling rate, which was dictated by the need to record raw AE data. Therefore, the load-displacement data were low-pass filtered digitally at 1 kHz for the load cell and 0.1 kHz for the LVDT.

As mentioned earlier, the indentation force was observed to oscillate at the end of the descent, with the oscillations damping over a time of around 1 second. Dead-weight indentation can be modelled using a 2nd order differential equation where solution is a damped oscillation (*Appendix F*). A measure of the contact stiffness could be made from the overall slope of the loading force-displacement (*P*-*h*) curve.

The mechanical loading energy (E_m) of indentation was assessed from the area under the force-displacement loading curve (Equation 3.4):

$$E_m = \int_{h=0}^{h=h_m} F dh \tag{3.4}$$

where F is the loading force and h is the displacement from the beginning of the loading (i.e. after the indenter contacts the surface), as illustrated schematically in **Figure 3.11**.

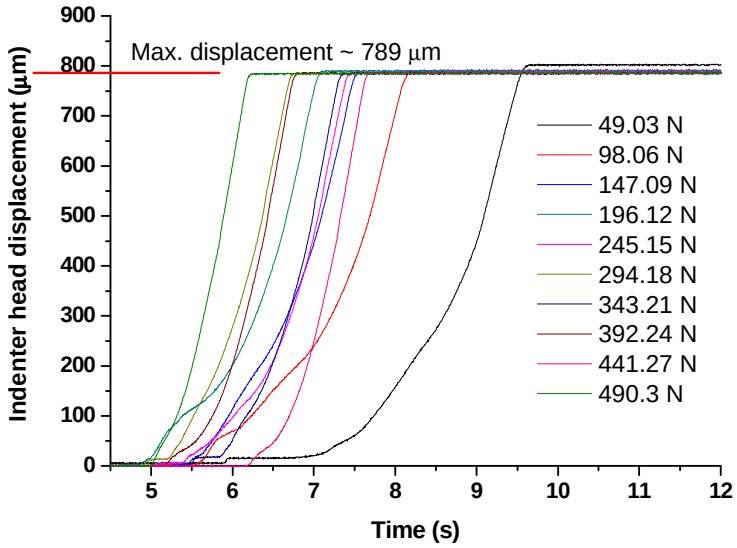

Figure 3.12 Displacement of indenter with no specimen in place

The indenter displacement curve has two phases during the loading cycle, one between release and contact and one between contact and final settling. **Figure 3.12** shows displacement-time curves with no specimen beneath the indenter and the average velocities ranged from 225 to 630 μm s^{-1} depending on the load. With the specimens beneath the indenter the average approach velocity at the specimen surface was

measured at 85 to 385 µm s^{-1}, depending on the load. **Table 3.3** shows the international standards for the approach velocity of indenters. The main consequence of this analysis is that the approach speed of the indenter will vary significantly with load and this may affect the response, particularly for more brittle materials.

Table 3.3 Requirements and standards on Vickers hardness tests

Standards	Indenter approach velocity, Load	Time of application of the full test load	Ref.
JIS R 1610	Gradual contact	---	[58]
DIN 51-225	F < 49.03 N	0.3-8 sec	[58]
--	300 µm sec^{-1}	---	[64]
BS EN ISO 6507-3: 1998	50-200 µm sec^{-1}: (F < 1.96 N) 50-200 µm sec^{-1}: (1.96 < F < 49.03 N) 50-1000 µm sec^{-1}: (F >= 49 to 981 N)	<=10 sec 6-8 sec 13-15 sec	[134]
BS EN ISO 6507-1: 1998	200 µm sec^{-1}	2-8 sec	[134]
ASTM: E-384-89	15-70 µm sec^{-1}	10-15 sec	[148]
BS 5411-6: 1981 ISO 4516: 1980	15-70 µm sec^{-1}	10-15 sec	[149]

Experimentally, there are two ways to measure indentation depth, one using instrumentation techniques (e.g. LVDT), which measures the actual maximum depth (or experimental depth, h_m, **Figure 3.13**) at peak load. The second way is to measure the impression diagonals (geometrically measured depth, h_r, **Figure 3.13**) using an optical microscope after complete indenter removal relying on the known geometry of the indenter to infer the depth.

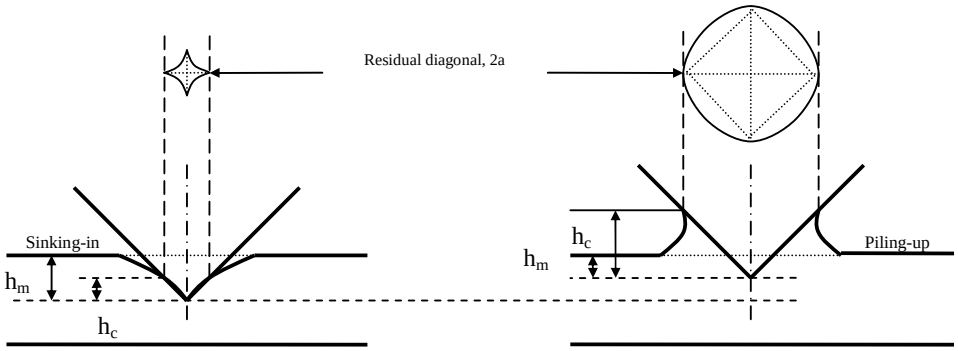

Figure 3.13 Vickers indentation depths where h_m is maximum indentation depth and h_c is contact depth

As shown in **Figure 3.13**, the contact depth (h_c) is lower than the actual maximum depth (h_m) in 'sinking-in' and vice-versa in a 'piling-up' mechanism. The residual geometrical depth was measured from the geometry of the impression using Equation 3.5 [38]:

$$h_r = \frac{2a}{7} \tag{3.5}$$

where, $2a = \frac{2a_1 + 2a_2}{2}$ is the average diagonal size. The geometrical measurement technique of indentation depth is also subject to additional error due to elastic recovery in some materials leading to reduced impression size of indent. The percentage difference between actual maximum depth (h_m) and geometrically measured depth (h_r) was calculated using Equation 3.6:

$$\%\Delta = \left(\frac{h_m - h_r}{h_r} \right) \times 100 \tag{3.6}$$

At least five indentations were made for each load and the macrohardness (HV) was determined by measuring the two diagonals of the impression after indenter removal (indentation hardness), excluding any diagonal cracks, and using Equation 3.7 [134]:

$$HV = 0.1891 \left[\frac{P}{(2a)^2} \right] \tag{3.7}$$

where P is the applied load in Newtons. Indentations were spaced greater than 2.5 times the diagonal apart [135], to avoid any interaction between the surface and sub-surface fractures of neighbouring indentations. Before each set of indentation testing the calibration system of the indentation machine was tested using a standard test block (35 mm × 20 mm × 10 mm) which had a hardness of 762/792HV.

3.5 Surface crack length measurement and sub-surface damage assessment

The conventional method of measuring the crack length around indentations is to take the average of the radial crack lengths at corners using a direct straight-line method. The method simply determines the average diagonal size (including radial cracks, 2c) and subtracts half the average impression diagonal size $a = (2a_1 + 2a_2)/4$, so that l_a, the average of the radial crack lengths at the four indent corners, is given by: $l_a = c - a$. Because the cracks were branched in all cases a profiling method was used in this study as shown in **Figure 3.14** on the basis that it is the overall extent of cracking during indentation that is indicative of the volumetric damage and reflects the brittleness of the surface region. This is a particularly important distinction in less homogeneous materials where the corners of the impression may coincide with relatively tough or relatively brittle parts of the microstructure.

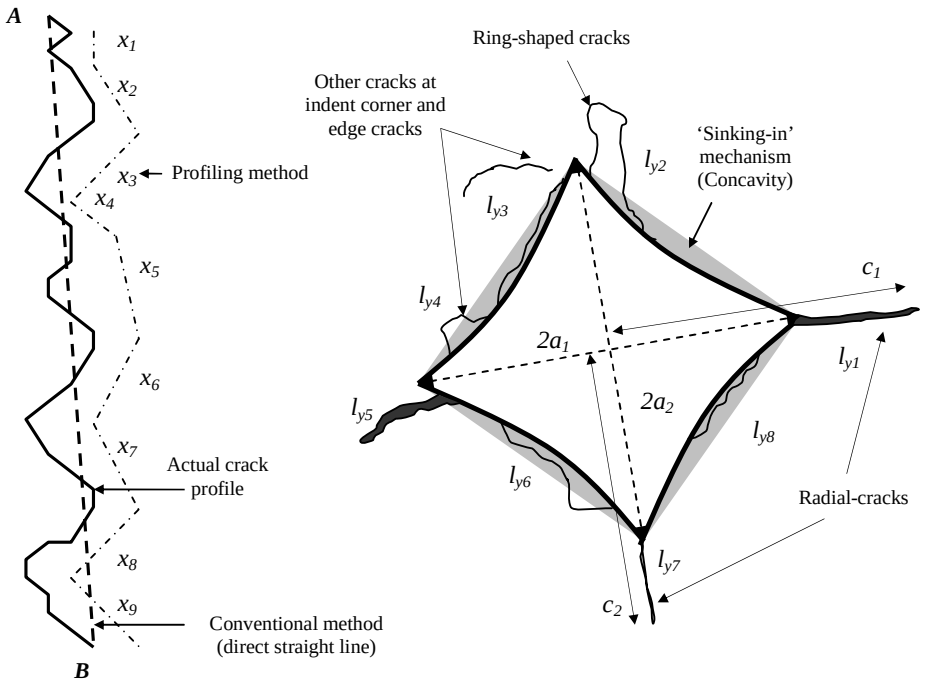

Figure 3.14 Scheme for measuring the total surface crack length

Accordingly, the surface crack length was measured, including radial cracks at corners, edge cracks, ring-shaped cracks and other small cracks around the indentation as shown in the schematic diagram in **Figure 3.14**. As illustrated in **Figure 3.14** (left), crack lengths in the surface plane between points A and B were assessed using a profiling method by adding together the serrated crack path unit lengths, $l_{yn} = x_1 + x_2 + ... + x_{n-1} + x_n$. The minimum unit length was determined by the resolution of the micrograph (here 2 - 3 μm). The total surface crack length was then obtained from the sum of the two diagonal sizes plus all the *n* resolvable crack lengths:

$$L_{total} = \sum_n l_{yn} \tag{3.8}$$

Also, for comparison with conventional approaches, l_a, the average of radial crack lengths at the four indent corners was determined and the dimension, *c*, calculated from [7]:

$$c = l_a + a \tag{3.9}$$

There are, of course, other sub-surface cracks which are not measurable using the optical microscope without sectioning and are therefore not included in the above technique. However, since the primary purpose of measuring surface crack length is to correlate it with indentation load and AE features this is not an insurmountable

difficulty. Surface crack length measurements were made on an optical microscope (Nikon, with N50 monochrome camera) at various magnification levels (5×, 10×, 20×, 40×) appropriate to the size of indentation. The crack length measurements were made just after each set of indentations, as some cracks can close up with time (called time-aging).

Whereas it was not a primary measurement, some indentations (e.g. as-sprayed HVOF WC-12%Co) were cross-sectioned using a low speed diamond saw to provide an assessment of the sub-surface damage in order to enhance understanding of the way in which the material accommodates the indentation. Specifically, cross-sectioning should help identify if classical indentation crack regimes as described in *Section 2.1*, such as 'surface-radial or Palmqvist cracks' and 'sub-surface radial-median or Half-Penny cracks' were present and to what extent surface observations can serve as a measure of the total amount of cracking [11, 17].

An example position for the cross sectioning is shown schematically in **Figure 3.15**. The samples, which included many indentations on one side of the coated surface, were mounted using cold embedding resin, sectioned and polished, and, whereas it was not possible to section a specific cross section of any single indentation, it was possible to view a number of indentations in each section. Thus, inspection of the sections permitted a semi-quantitative assessment of the effects of loading on the three-dimensional crack distribution and an observation of other ways in which the microstructure accommodates the indentation, such as densification by reduction in the amount of porosity.

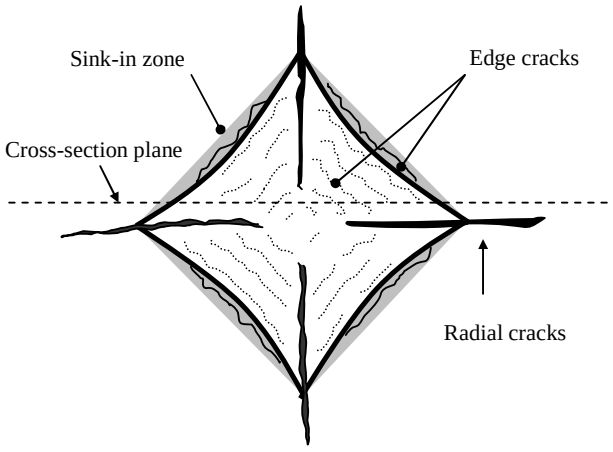

Figure 3.15 Schematic diagram of Vickers indentation cross-sectioning

The sample was vacuum impregnated in a Struers Epovac system using a transparent, low viscosity Struers Epofix resin and then cut very near to an indentation at a given load using a low speed diamond saw, cutting in the direction from the coating towards the substrate, to avoid delamination. Polishing was done carefully to reach the indentation cross-section using increasingly fine grit [with 220 (or, 68μm), 600 (or, 26 μm) and 1200 (or, 15μm) size, Struers MD-Piano system] and a diamond grinding disc. Once the required indentation was reached, the section was finally polished with diamond paste (6, 1 and 0.5 μm) to enable a sharp cross-sectional view of the indentation sub-surface zone. The vacuum impregnation technique [150-151] enables the low viscosity resin to reach most of the surface-linked cracks and pores, and, upon solidification, the resin acts as reinforcement before, during and after sample preparation and reduces the possibility of further damage during cutting and polishing of the area of interest. The diamond bond used in MD-Piano ensures an even material removal from both hard and soft phases and avoids smearing of soft phases or chipping of brittle phases during grinding. Following grinding and during polishing, the cross-sections were regularly monitored under an optical microscope. Finally, the cross-sections were examined using a Scanning Electron Microscope (SEM).

3.6 Vickers indentation fracture toughness measurement

As explained in *Section 2.1.1*, there are two main classical models ('Half-penny' and 'Palmqvist') which underlie the determination of Vickers indentation fracture. In this study, an analysis has been carried out based on these classical models and an alternative approach has been identified.

3.6.1 Classical approach

According to the various published analyses of the indentation of brittle materials, the main types of cracking observed are either surface-radial cracks (Palmqvist cracks), or radial-median cracks (Half-penny cracks). Nihara *et al.* [7] have distinguished between the two in terms of the classical dimensions a, l_a and c described in *Section 2.1.1*: Palmqvist cracks, $l_a/a \leq 2.5$ or $c/a \leq 3.5$ and half-penny cracks, $c/a \geq 2.5$ [11]. In this study, the average value of l_a/a and c/a were well within the Palmqvist régime, and this was also supported by the absence of sub-surface radial-median cracks. Shetty *et al.* [10] have devised an empirical model for Palmqvist cracks, which allows the fracture

toughness (in units MPa.m$^{1/2}$) of the coating to be determined from the load and crack dimensions:

$$K_{1c} = 0.0319\left[\frac{P}{a\sqrt{l_a}}\right] \tag{3.10}$$

where P is the indentation load (in Newtons), a is the average indent half-diagonal size and l_a is the average of the radial corner crack lengths, both in metres. The above formula for the determination of fracture toughness assumes that the surface is initially stress free.

3.6.2 Alternative approach

In their review on the formulation of standardised indentation fracture toughness equations Ponton and Rawlings [33] have developed a series of generic fracture toughness equations (based on Palmqvist and Half-penny crack models), to describe the relationship between the surface radial crack length, l, indent half diagonal, a, and indentation load, P. They recommended 'generic equations' (GEs) which summarise much of the practice observed, but all essentially use a crack length measurement and, implicitly utilise the relationship $K_I = \psi\sigma_A\sqrt{c}$ [4]. Here, the GE has been modified to replace the average radial-corner crack length l_a, with either the total surface crack length L, the AE ring-down count R, the total AE energy E or the total AE event duration T to give a modified generic equation for AE-based fracture toughness estimation (K_{1c}) for Palmqvist type cracks:

$$K_{1c} = k_L\left[\frac{P}{a\sqrt{L}}\right] \tag{3.11a}$$

$$K_{1c} = k_{AE}\left[\frac{P}{a.\sqrt{X}}\right] \tag{3.11b}$$

where X is one of variables, R, E or T and k_L and k_{AE} are empirical constants which can be determined for any given indenter/specimen/AE system combination. The dimension of k_{AE} depends on the dimension of X; a is in metres, L is in metres, R is a number, E is in Volt.seconds and T is in seconds. As mentioned in the introduction, it is expected that the AE arises from crack extension process and therefore it might be expected that the AE record and total crack length will be correlated.

3.7 AE monitoring during HVOF thermal spraying

This experiment involved an HVOF (TAFA JP-5000, Monitor Coatings Ltd., UK) thermal spraying system using spherical and porous WC-10%Co-4%Cr powders (AMPERIT® 558.074) of size 45/15 μm (see **Figure 3.16**), an AE sensor, data acquisition system (discussed in *Section 3.2*) and an experimental rig for in-process AE monitoring shown in **Figure 3.17** and **Figure 3.18**.

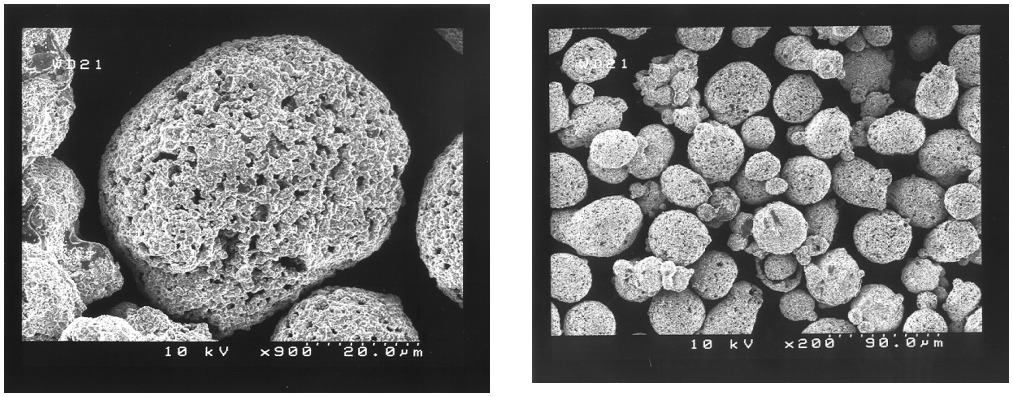

Figure 3.16 SEM images of WC-10%Co-4%Cr powders

Table 3.4 HVOF spraying parameters

Spraying system	Oxygen flow ($l\ min^{-1}$)	Kerosene flow ($l\ min^{-1}$)	Spraying distance (mm)	Spraying rate ($g\ min^{-1}$)
JP5000/HVOF	920	0.27 and 0.20	380	80

Table 3.5 Experimental matrix (AE monitoring of HVOF thermal spraying process)

Fuel Pr.	High Pressure (P1): 0.27 litre min^{-1} (fuel)				Low Pressure (P2): 0.20 litre min^{-1} (fuel)			
Slit width	A (3 mm)	B (2 mm)	C (1 mm)	D (0.5 mm)	A (3 mm)	B (2 mm)	C (1 mm)	D (0.5 mm)
HVOF gun speed (mm/sec)	250 500 750	250 500 750	250 500 750	250 500 750	250 500 750	250 500 750	250 500 750	250 500 750

The test was devised to observe whether or not a clear signal could be recorded while the substrate material is being coated, and whether this signal is distinguishable from that associated with the continuous background noise. A fixed set of parameters with no air jet cooling for the HVOF spraying system was chosen (**Table 3.4)**, and the process parameters were varied as summarised in **Table 3.5**: four spray gun lateral speeds (250, 500, 750 mm sec^{-1}) and two kerosene fuel flow rates, 0.27 and 0.20 litre min^{-1} corresponding to two levels of fuel pressure, P1 and P2. The spray was directed through a series of slit arrangements (*Appendix D*) labelled as follows; A: 3 mm × 10 mm, B: 2

mm × 10 mm, C: 1 mm × 10 mm, D: 0.5 mm × 10 mm, and discussed in more detail below.

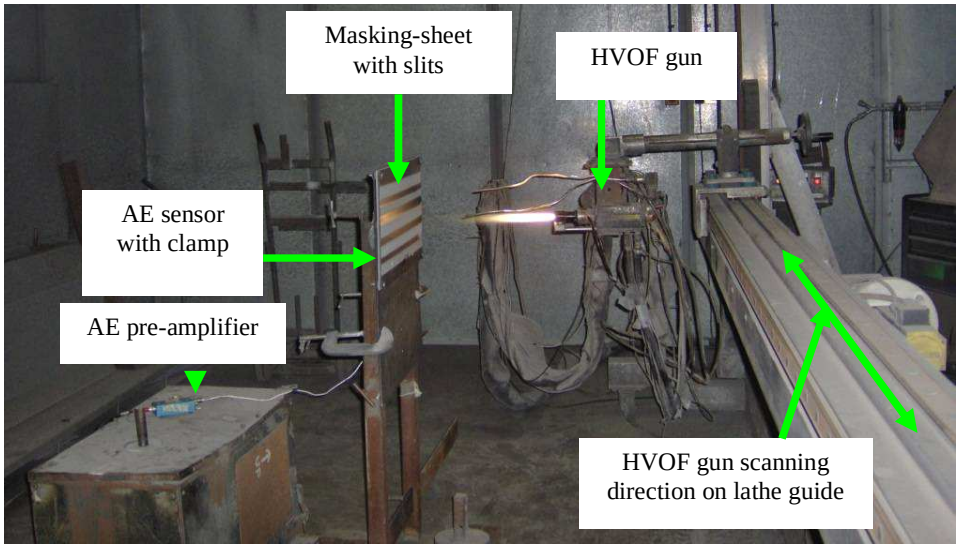

Figure 3.17 Experimental set-up: AE monitoring during JP5000 HVOF WC-10%Co-4%Cr thermal spraying in coating chamber (Monitor Coatings Ltd, UK)

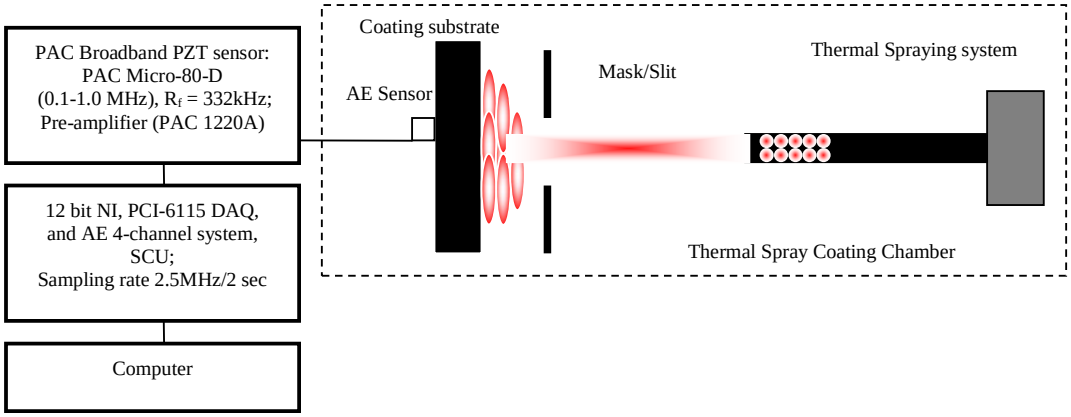

Figure 3.18 Schematic diagram of AE monitoring during thermal spraying process

The masking sheet, coating substrate and holder were made of mild steel sheet of size 300 mm × 500 mm × 3 mm thick and the mask had an array of varying width slits of height 10 mm cut into it using a Ferranti MF600 CO_2 laser CNC machine tool. Each row of the array consisted of a set of one particular width of slit, equally spaced with a 27 mm edge-to-edge gap across the width of the mask (*Appendix D*). The substrate and holder were both securely clamped to a stand as shown in **Figure 3.19a**, and an AE sensor was located in the middle of the grit-blasted substrate on the reverse side to that being sprayed as shown in **Figure 3.19b**, and held in place using a magnetic holder with

silicone grease. It was verified that no measurable AE was transmitted from the mask to the substrate using a simulated source (pencil lead break test [151]).

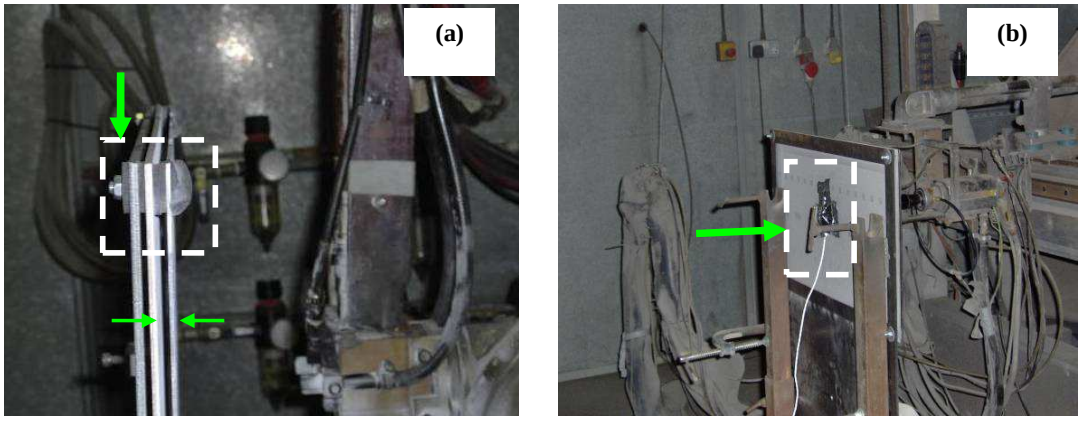

Figure 3.19 (a) Fixture of masking-sheet, stand, coating substrate with rubber bush and nut-bolt (2.5 mm gap between sheets) and (b) Location of AE sensor behind coating sheet

Apart from the above-mentioned experimental matrix (spraying through slits), an experiment was carried out using continuous multilayer HVOF thermal spraying to compare with the AE signal through slits, and give a more industrially realistic assessment. To this end, a brief test was carried out by spraying with 200 mm sec^{-1} gun scanning speeds on a flat mild-steel substrate for 5 layers. From the multilayer experiments, two rectangular specimens of sizes 72 mm × 58 mm (100 mm sec^{-1} gun speed) and 72 mm × 27 mm (200 mm sec^{-1} gun speed) each of thickness 3 mm were cut for indentation testing. In preparation for the indentation test, both specimens were ground and fine polished to a mirror finish. After fine polishing, the coating thickness was between 50 and 60 μm.

3.8 Summary of experiments

Overall three types of measurement were performed. Fully instrumented indentations, AE monitored indentations and thermal spray process monitoring. Fully instrumented indentation was carried out on copper, aluminium, hardened steel, as-sprayed HVOF (JP5000) WC-12%Co coatings. AE monitored indentation was carried out on five coating types: as-sprayed HVOF (JetKote) WC-12%Co, HIPed HVOF (JetKote) WC-12%Co, as-sprayed HVOF (JP5000) WC-10%Co-4%Cr, APS (Metco, 9MB) Al_2O_3 (conventional powder) and HVOF (theta-gun) Al_2O_3 (fine powder). AE monitored HVOF (TAFA JP5000) thermal spray process monitoring was carried out using WC-

10%Co-4%Cr powders. The experimental matrix for the indentation tests is shown in **Table 3.6**.

Table 3.6 Vickers indentation experimental matrix

No.	Materials/ Indentation surface	Experimental variables, P (indentation loads, N)	Number of repeats per load	Measured quantities (force, displacement, AE, surface crack length)
1	Hardened steel	49, 98, 147, 196, 245, 294, 343, 392, 441 and 490	5	Force, displacement and AE
2	Aluminium	292 and 490	5	Force, displacement and AE
3	Copper metal	292 and 490	5	Force, displacement and AE
4	as-sprayed HVOF/JP5000 WC-12%Co coating / coating surface	49, 98, 147, 196, 245, 294, 343, 392, 441 and 490	5	Force, displacement and AE, surface crack length
5	as-sprayed HVOF/JetKote WC-12%Co coating / coating surface	49, 98, 147, 196, 245, 294, 343, 392, 441 and 490	5	AE, surface crack length
6	HIPed HVOF/JetKote WC-12%Co coating / coating surface	49, 98, 147, 196, 245, 294, 343, 392, 441 and 490	5	AE, surface crack length
7	as-sprayed HVOF/JP5000 WC-10%Co-4%Cr coating / coating surface	49, 196 and 343	1	AE
8	Conventional Al_2O_3 coating (APS/Metco, 9MB) / coating surface	98, 147, 196, 245, 294, 343, 392, 441 and 490	5	AE, surface crack length
9	Fine powder Al_2O_3 coating (HVOF/theta gun) / coating surface	98, 147, 196, 245, 294, 343, 392, 441 and 490	5	AE, surface crack length

Chapter 4

EXPERIMENTAL RESULTS AND ANALYSIS

This chapter presents the experimental results, mostly on the AE response from open loop dead-weight Vickers indentation testing of thermal sprayed ceramic coatings. First, general observations are made from the fully instrumented indentation tests on coated and uncoated specimens using load and displacement transducers alongside an AE sensor. General observations include the microstructure, indentation deformation and fracture, surface crack lengths, indentation sub-surface damage assessment and raw AE signal analysis (frequency and time domain) and its derived features. These observations inform the handling of the AE data from the main set of experiments. Finally observations from AE monitoring during thermal spraying of one of the sample sets are also presented.

The chapter is arranged into four main sections, dealing, respectively with:

- Fully instrumented indentation of as-sprayed HVOF (JP5000) WC-12%Co coatings, hardened steel, copper and aluminium
- AE monitored indentation of HVOF (JetKote) WC-12%Co in the as-sprayed and HIPed conditions and HVOF (JP5000) WC-10%Co-4%Cr coatings in the as-sprayed condition
- AE monitored indentation of APS (Metco, 9MB) and HVOF (theta gun) sprayed Al_2O_3 coatings
- AE monitoring of the thermal spray process for HVOF (JP5000) WC-10%Co-4%Cr

Finally, the results are summarised in preparation for the discussion.

4.1 Fully instrumented indentation testing

The purpose of this set of experiments was to establish the relationship between load, displacement and AE during indentation of metals and metal-ceramic combinations. Accordingly, four materials were chosen for examination; commercially pure aluminium and pure copper (99.99%), a high hardness steel (762-792 HV) and an as-sprayed HVOF (JP5000) WC-12%Co coating of the type studied in detail in *Section 4.2*. The Cu and Al were both considerably softer and more uniform than the other two

specimens, and were of similar macrohardness. Also, the only accommodation mechanism expected in the pure metals was plastic deformation, whereas, for the other two specimens, other accommodation mechanisms are possible, including fracture at the micro-scale and macro-scale. The microstructure of the as-sprayed HVOF (JP5000) WC-12%Co coatings is described in detail in *Section 4.2*, but for the present purpose, these can be considered as two-phase materials containing hard WC and W_2C particles of approximate size 1-6 µm. **Figure 4.1** contains various micrographs of a polished and etched surface of the hardened steel showing roughly spheroidal carbide particles of approximate diameter 1-2 µm and volume fraction around 0.15 dispersed in a martensite matrix, which itself probably probably contains some smaller temper carbides.

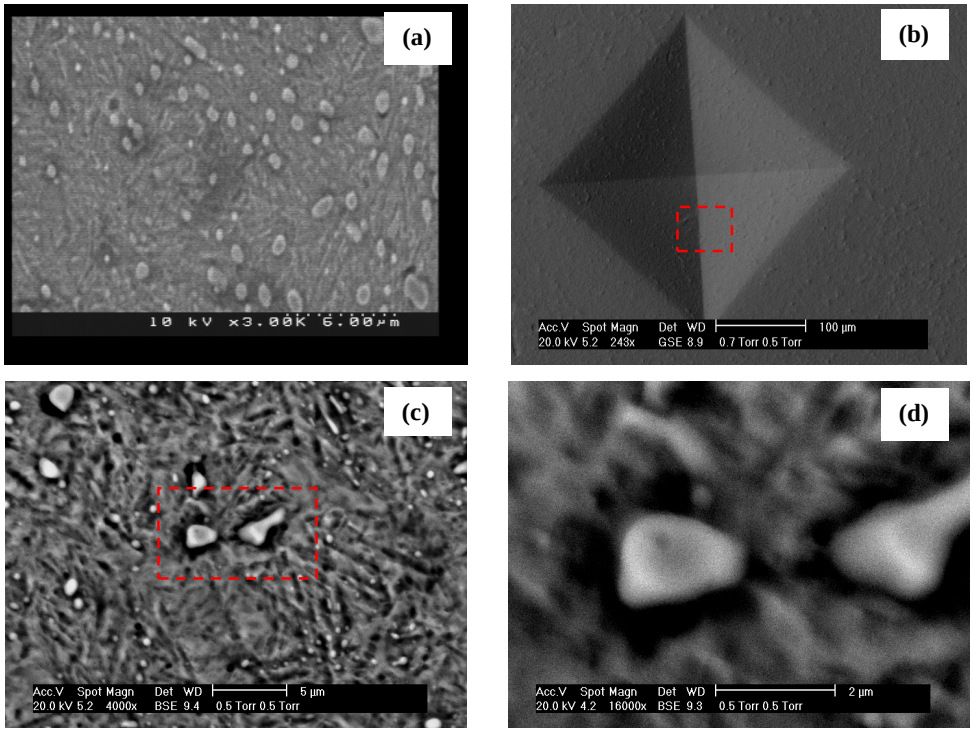

Figure 4.1 Surface of hardened steel showing martensitic laths and coarse carbides: (a) unindented area, (b) Vickers indentation at 490 N load, (c) and (d) corresponding back scattered ESEM images of boxed area in indentation showing the dark separation zone (microvoids) between carbide particles and martensitic matrix due to indentation

4.1.1 Loading force-displacement profile

Figure 4.2 and **Figure 4.3** show sample force-displacement profiles for the as-sprayed HVOF WC-12%Co coatings and hardened steel over the range of indentation loads tested. These profiles are essentially bi-curvilinear with two characteristic slopes separated by an arrest ('knee') which occurs at a depth after contact of around of 25 µm for the harder materials and 45 µm for the softer materials, and a force of around 100 N

(**Figure 4.4**). The two slopes (around 3.5 N/µm and 8 N/µm, shown in **Figure 4.5**) correspond to the effective indentation stiffness, slope 1 being reasonably constant irrespective of load, and slope 2 being rather more variable for different indentations.

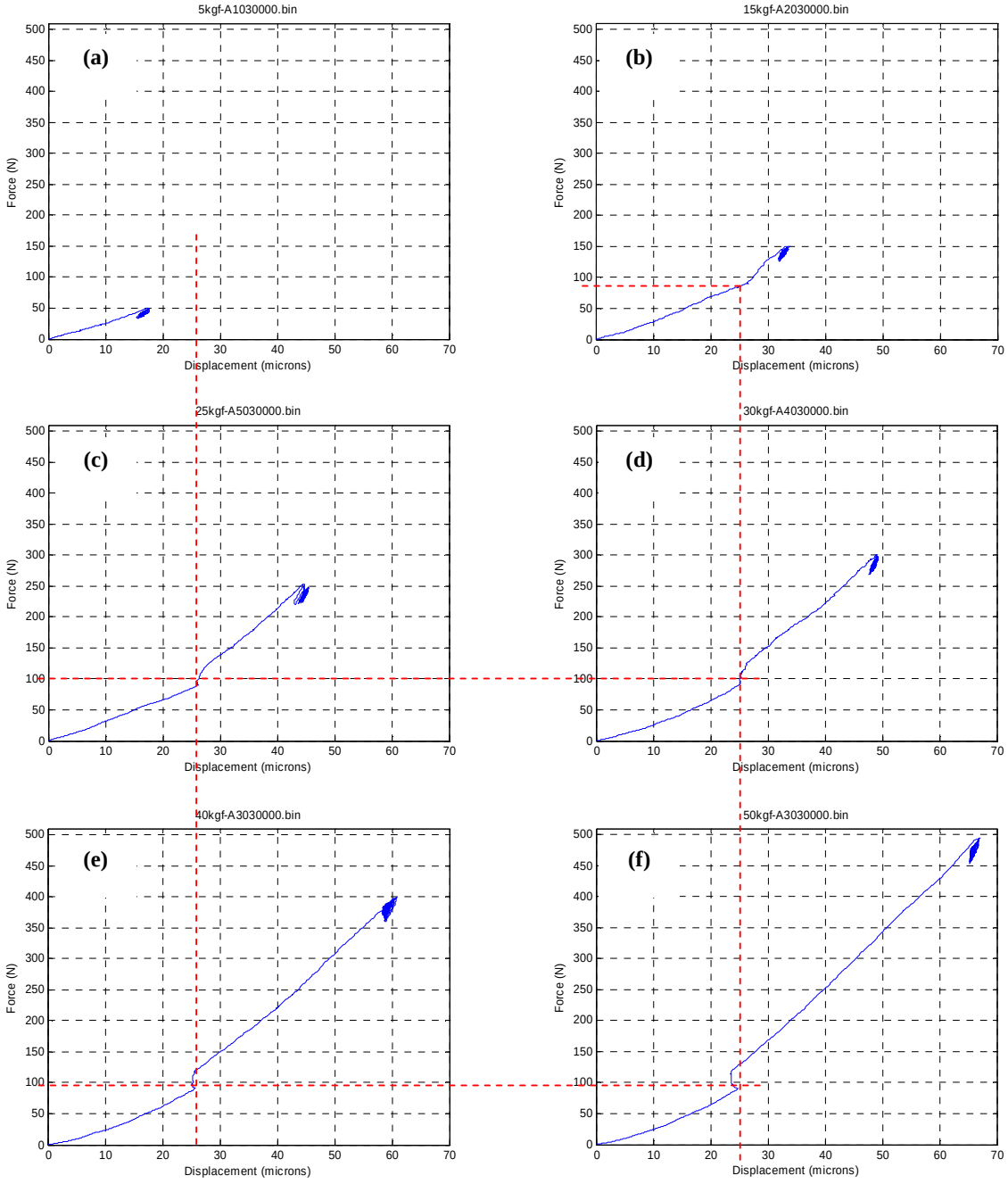

Figure 4.2 Vickers indentation force-displacement curves for as-sprayed HVOF (JP5000) WC-12%Co coatings at (a) 49 N (b) 147 N (c) 245 N (d) 294 N (e) 392 N and (f) 490 N Indentation load

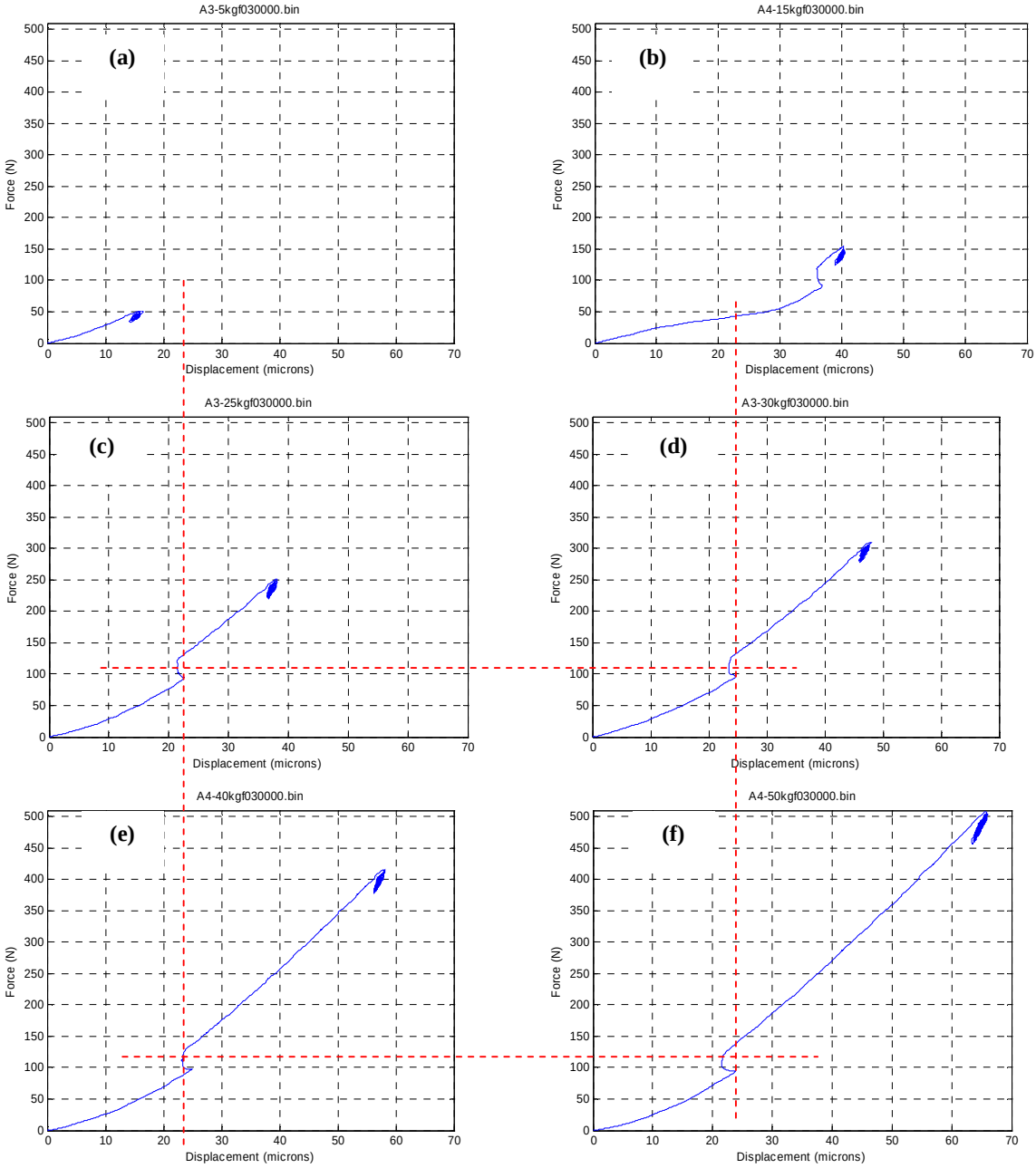

Figure 4.3 Vickers indentation force-displacement curves for hardened steel at (a) 49 N (b) 147 N (c) 245 N (d) 294 N (e) 392 N and (f) 490 N indentation load.

Sample force-displacement curves for the hardened steel are shown in **Figure 4.3**. Apart from the somewhat anomalous result for the 147 N indentation load, these are rather similar to the curves for as-sprayed HVOF (JP5000) WC-12%Co coatings except that the arrest is of a generally different shape and occurs at a slightly higher force of around 94 N, although similar displacement of around 25 µm. The slopes of the two lines (4 N/µm and 8 N/µm) are broadly similar to those for the as-sprayed HVOF (JP5000) WC-12%Co coatings, **Figure 4.5**.

Generally, the nature of the arrest is fairly consistent, corresponding to a step increase in force at the 25 µm displacement, of magnitude about 30 N (**Figure 4.6**) remaining relatively constant at all loads, and being somewhat smaller and more consistent for the softer materials. The damped oscillatory motion of the indenter at the end of each load-displacement curve is discussed in more detail later in this section. It might be noted that the 49 N curve does not show an arrest as the force and displacement never reach the critical values of 90 N and 25 µm, respectively.

Figure 4.7 shows the force-displacement curves for the two soft metals which were only tested at 294 and 490 N indentation loads. The most striking difference between these curves and the ones for the harder materials is the lower slopes of the two lines (Al: 2.0 N/µm and 4.5 N/µm and Cu: 1.9 N/µm and 4.0 N/µm) and the fact that the arrest occurs at a larger depth (Al: 45 µm and Cu: 47 µm).

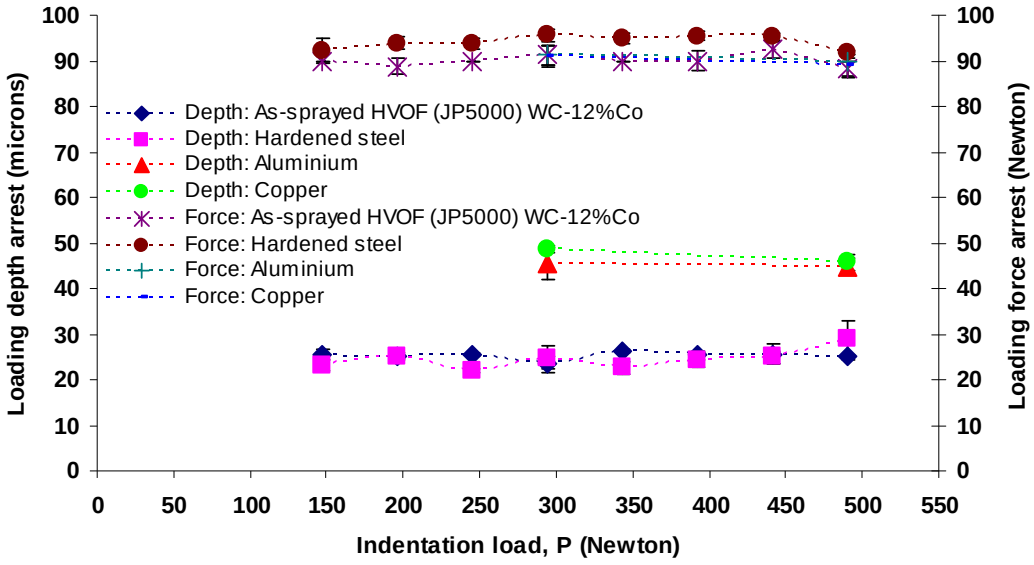

Figure 4.4 Loading depth and force arrest at arrest point

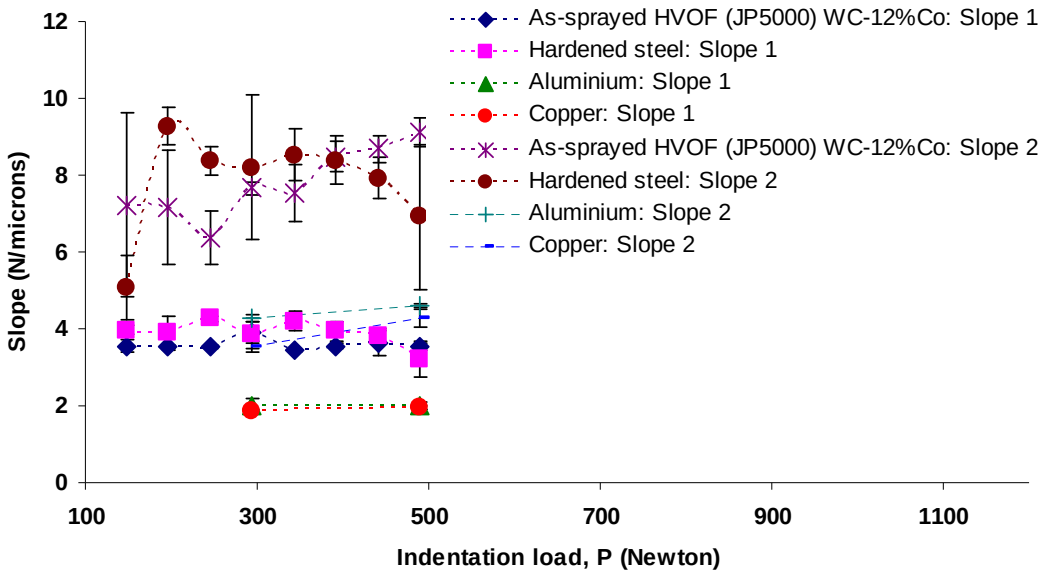

Figure 4.5 Comparison of force-displacement slopes

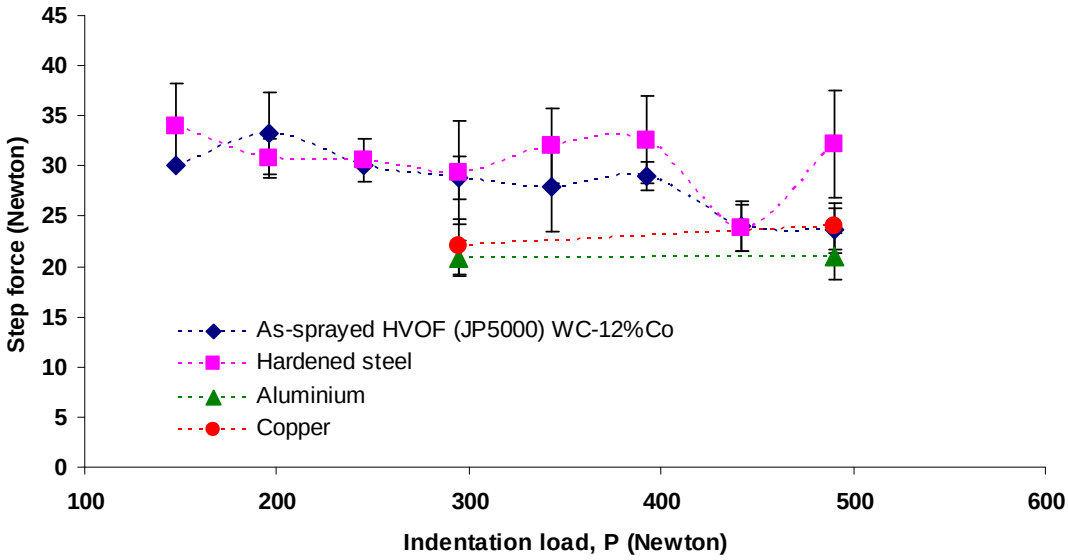

Figure 4.6 Comparison of force step at arrest in force-displacement curves

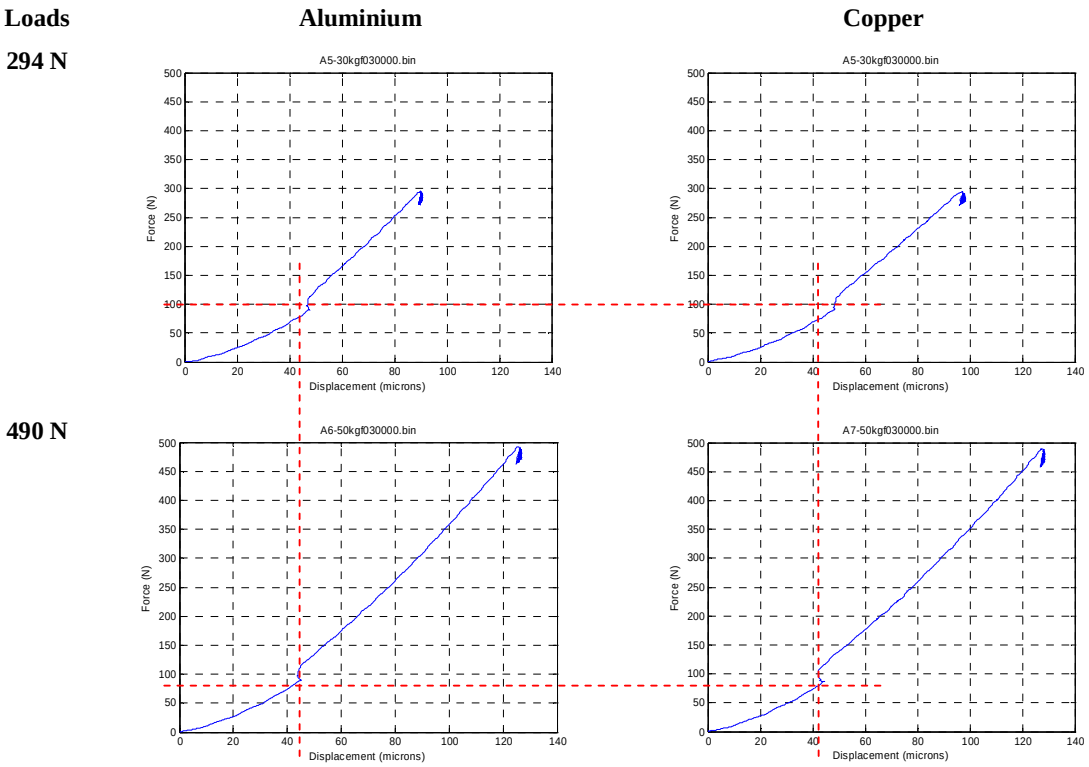

Figure 4.7 Vickers indentation force-displacement curves for soft metals (Al and Cu) at 294 N and 490 N indentation load

Figure 4.8 shows magnified views of the loading arrest for all materials at 294 and 490 N loads. Taken with the observations above, these suggest that, at a force of around 90 N (almost independent of the material type), there is an instability which results in a sharp increase in force, sometimes accompanied by a reduction in displacement. Because the reduction in displacement, if it occurs, is rather small (1-2 µm) and, because the force is a fixed one, it is possible that the arrest is something to do with the load placement mechanism in the machine. Irrespective of this, the material response before and after the arrest is clearly different.

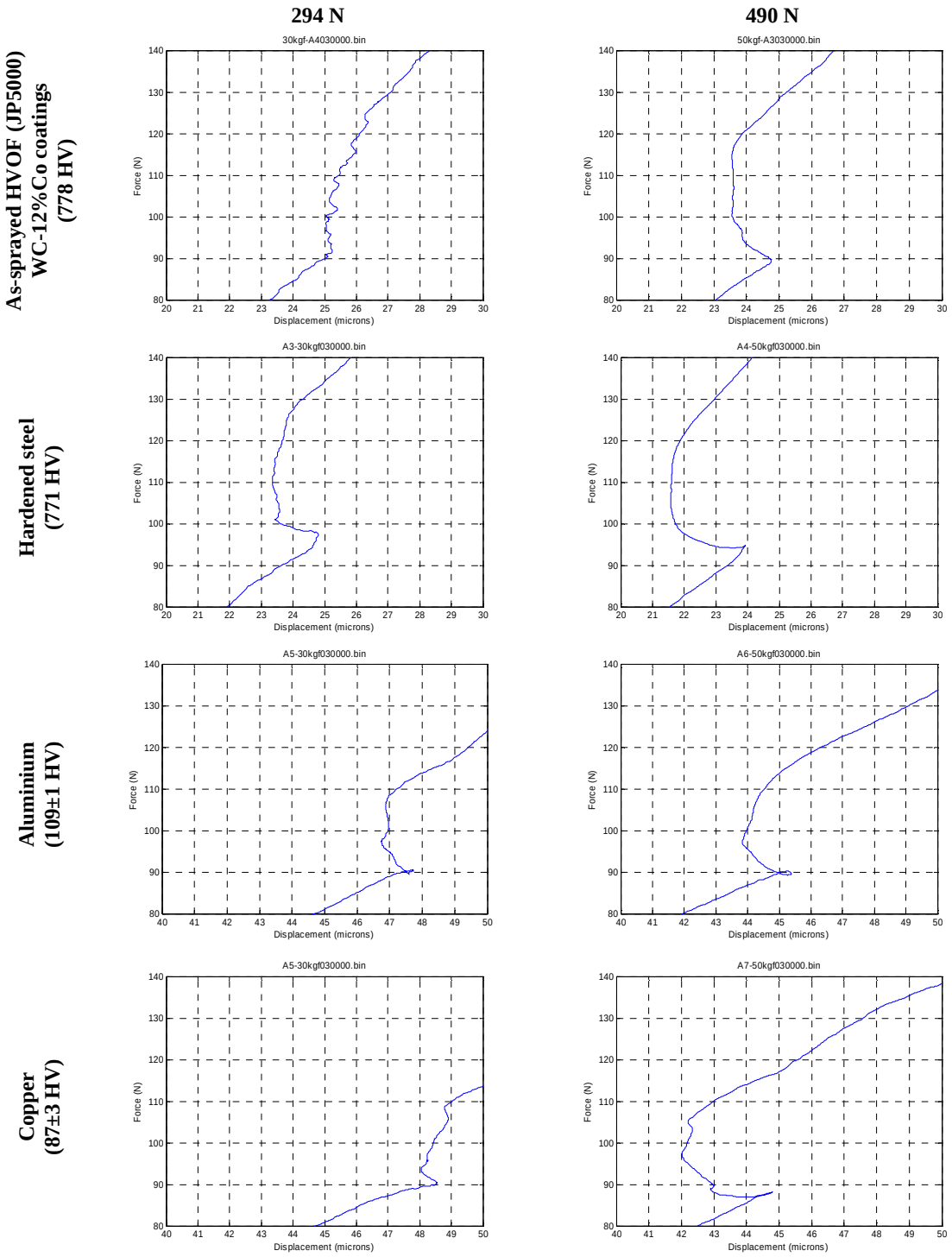

Figure 4.8 Comparison of force-displacement profiles at the arrest at 294 N and 490 N

Figure 4.9 summarises a schematic model, based on the observations above, which allows the identification of three distinct stages of indentation and the energy associated with each. In Stage I, load and displacement are curvilinear and the curve terminates at P_I, h_c. Stage III commences at P_{III}, h_c and continues until the indenter settling point P_m,

h_m. The approximate overall work associated with Stage I is therefore $W_I = \frac{P_I h_c}{2}$ and that associated with Stage III is $W_{III} = P_{III} h_c + \frac{(P_m - P_{III})(h_m - h_c)}{2}$. The total energy involved in forming the impression is therefore $W_I + W_{III}$, although it does not necessarily follow that all of this energy is manifest as acoustic emission, or that the proportion of the mechanical energy converted to AE will be constant within or between indentations. Specifically, it is expected that accommodation mechanisms which involve plastic deformation will generate little AE, whereas those which involve fracture or micro cracking will generate significant AE.

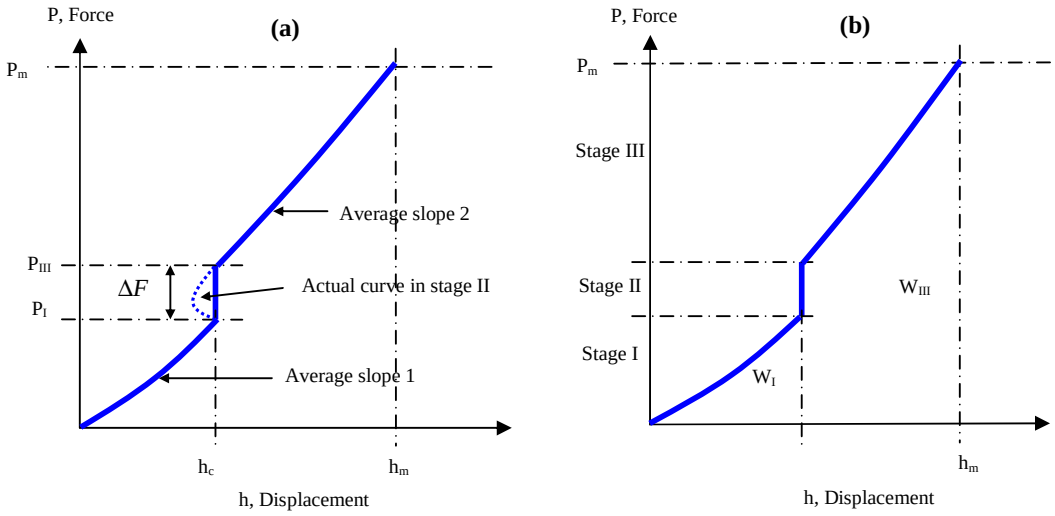

Figure 4.9 Schematic models for an open loop dead-weight Vickers indentation: (a) force-displacement (*P*-*h*) curve during loading, where P_m is the terminal force and h_m is the maximum depth, and (b) measurement scheme for total mechanical energy

Since the arrest is distinct, the values of P_{III} and P_I are determined, for all force-displacement curves by fitting two straight lines on the two distinct bilinear curves on either side of the arrest and determining the step force (ΔF) between these two curves at the arrest. The intersection point of one end of the straight lines on either side of arrest (**Figure 4.10**) with the force-displacement curve determines the co-ordinates of force and displacement.

Figure 4.11 shows a typical force-time and displacement-time curve, in which it can be seen that the final stages of indentation are associated with damped oscillation of the force and the displacement. The small amplitude of the displacement oscillations make these difficult to analyse, but Fourier analysis of the oscillating part of the force curve

yielded the main harmonic frequency for each curve, shown in **Figure 4.12**, plotted against $P^{-1/2}$. The slope of this curve yields an indentation stiffness for each material indicative of its terminal settling position (*Appendix F*).

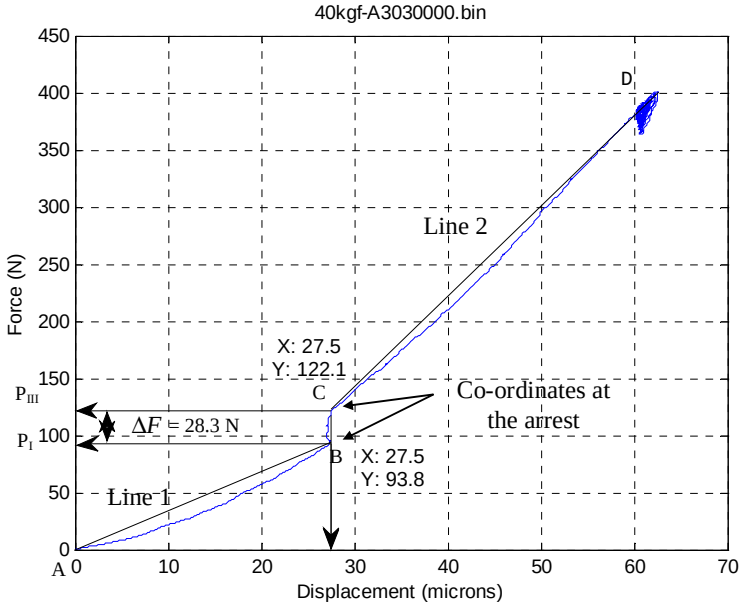

Figure 4.10 Measurement schemes of different features from typical *P-h* curve [example curve shown for as-sprayed HVOF (JP5000) WC-12%Co coatings at 392 N load]

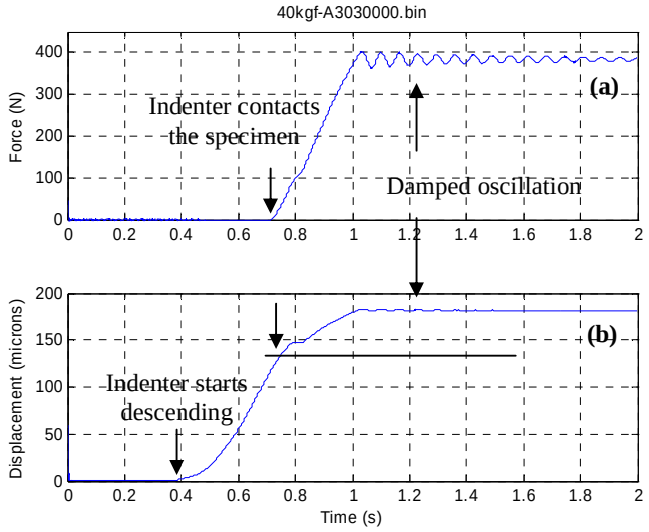

Figure 4.11 Vickers indentation loading curve showing the damped oscillation (a) force-time and (b) displacement-time [as-sprayed HVOF (JP5000) WC-12%Co coatings at 392 N load]

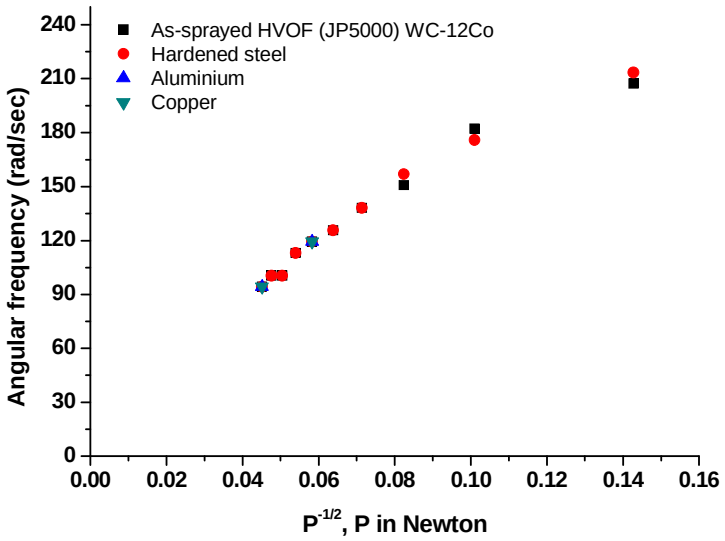

Figure 4.12 Angular frequency of damped oscillation (during indenter settling)

4.1.2 Indentation depths

Figure 4.13 shows experimental and geometrical indentation depths (as described in *Section 3.4*) for each material and each load, each point showing the average and the range over the five indentations.

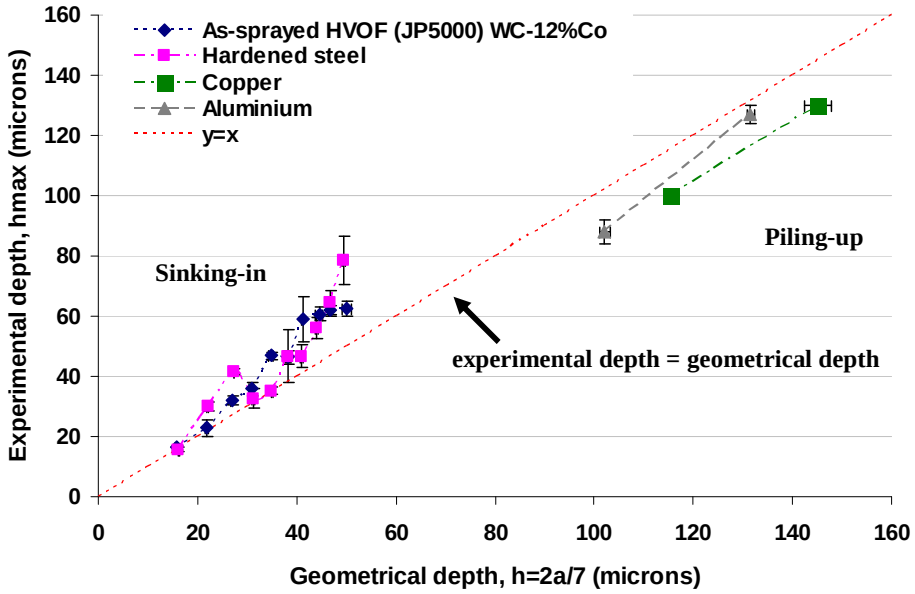

Figure 4.13 Comparison of experimental and geometrical indentation depths

The geometrical depth was determined from the impression size using Equation 3.5 and is compared with the experimental maximum depth measured from the force-

displacement curve (**Figure 3.13**). Two types of material accommodation can be identified (**Figure 3.13**), according to whether values fall above or below the line $y = x$, which indicates neither 'piling-up' nor sinking-in'. As expected, the soft metals (Al, Cu) show piling-up, whereas, the two hard materials (WC-12%Co coatings and hardened steel) show sinking-in as can be seen in the micrograph in **Figure 4.14**. **Figure 4.15** shows the percentage difference between experimental depth and geometrical depth for WC-12%Co and hardened steel, which increases with load. As can be seen, there is a general increase in the difference with load although some results (e.g. 147 N for hardened steel) fall outside the trend.

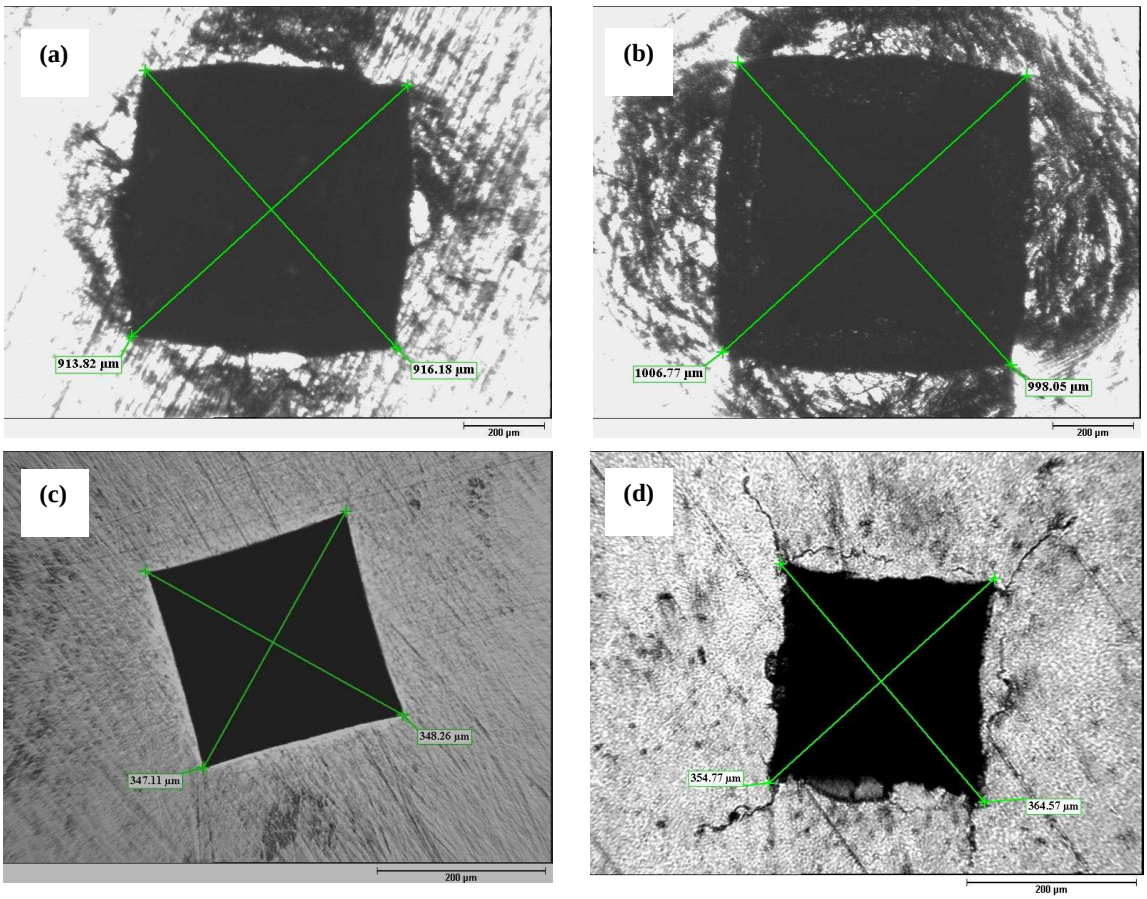

Figure 4.14 Vickers indentations at 490 N load showing piling-up in (a) aluminium and (b) copper; sinking-in (c) hardened steel and (d) as-sprayed HVOF (JP5000) WC-12%Co coatings

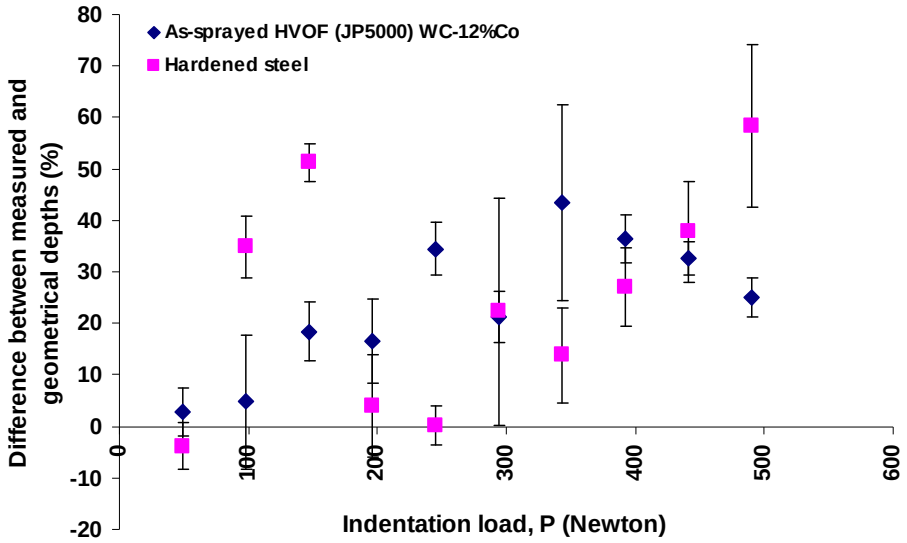

Figure 4.15 Percentage difference between Vickers indentation depths

4.1.3 Relationship between work of indentation and AE energy

Figure 4.16 shows that, for a given load, the mechanical work (using Equation 3.4) associated with the indentation loading process (Stage I and Stage III, **Figure 4.9**) is similar for the as-sprayed HVOF (JP5000) WC-12%Co coatings and hardened steel specimens for both Stages I and III and that Stage III generally increase with load. For the two soft metals, the work is similar and Stage I generally has lower energy and Stage III higher energy than the harder materials at a given load.

Figure 4.17 shows the total AE energy plotted against the total mechanical indentation work for each load. As can be seen, the AE energy is significantly greater for the hard materials and these show a general increase in AE energy with indentation work, although there is considerable scatter within this. Other features of the AE, e.g. total duration, show similar evolution with work of indentation.

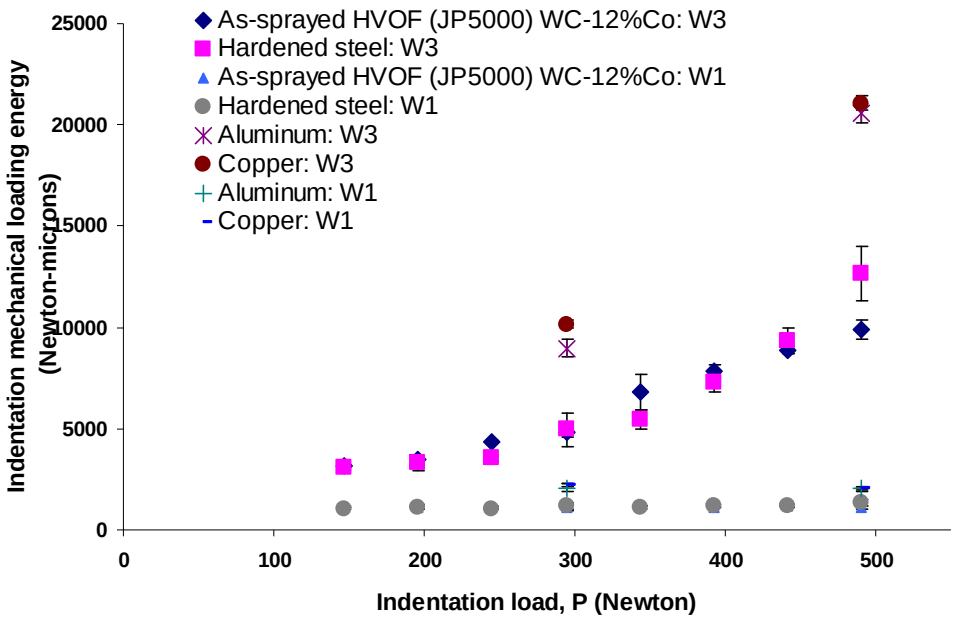

Figure 4.16 Indentation mechanical energy (*P-h* area, Stage I and Stage III) during loading

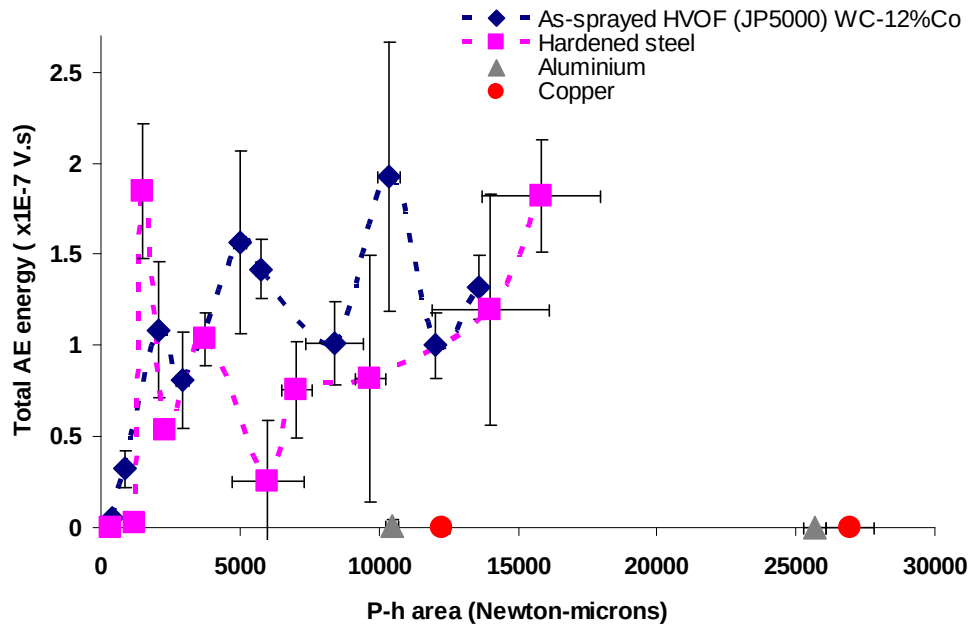

Figure 4.17 Indentation mechanical energy (*P-h* area) plotted against total AE energy

4.1.4 Loading force, depth and AE relationship

Because the total indentation work and total AE energy are not closely related and the sequence of AE during loading was examined more closely. To do this, representative examples have been chosen to show typical time evolution features which are then calculated for all data. Since very little or no AE was detected for the two soft metals, only examples of the two other hard materials are discussed here. The analysis takes into account optical micrographs of the Vickers indentations (**Figure 4.18**) and the relevant time evolutions of load, displacement and raw AE.

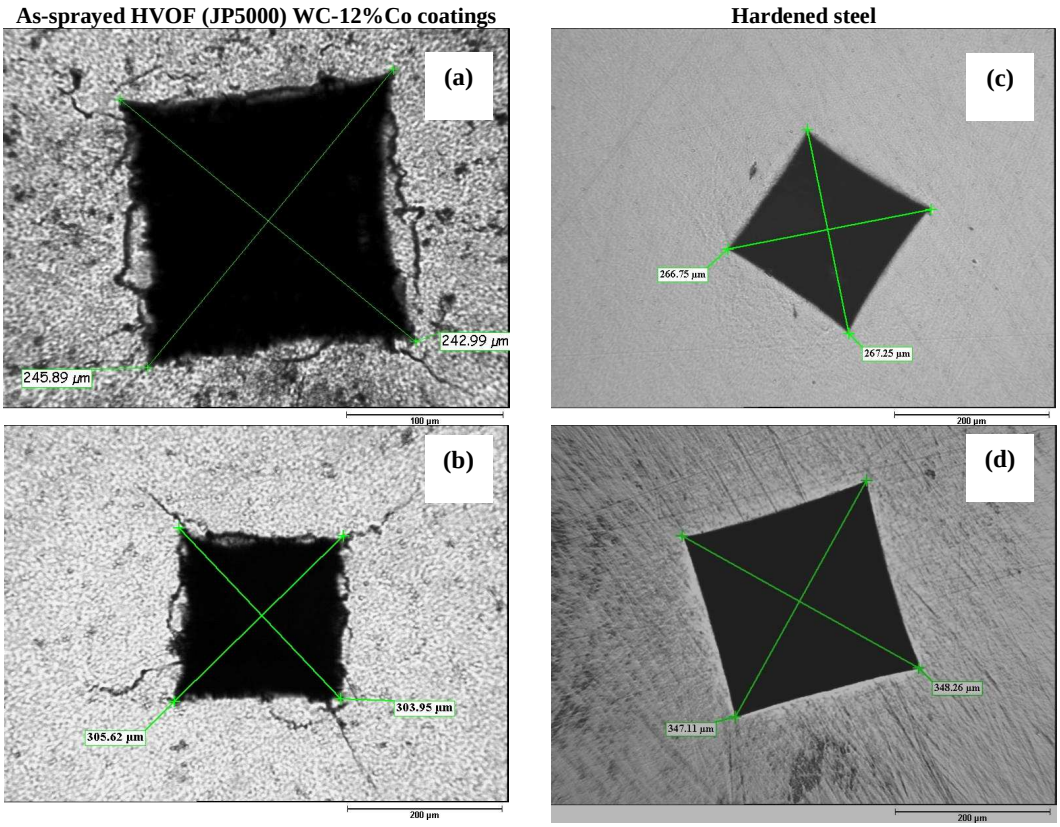

Figure 4.18 surface views of Vickers indentations on as-sprayed HVOF-JP5000 WC-12%Co coatings (a) 245 N, (b) 392 N, and hardened steel (c) 294 N and (d) 490 N

In all the following figures in this section, the point where the indenter touches the specimen is shown with a red down-arrow (↓) and at the point where the indenter reaches its lowest point is shown with a red up-arrow (↑). The displacement-time history records when the indenter load was released, and this is shown with a green down-arrow (↓), and the arrest which indicates Stage II is shown with a blue up-arrow (↑). **Figures 4.19** and **4.20** show detailed representations of the force, displacement, AE amplitude time evolution along with a magnified view of the 'knee' for 245 N and 392 N loads on the as-sprayed HVOF (JP5000) WC-12%Co specimen. The micrograph

(**Figure 4.18**) shows sinking-in with macro-scale cracking and edge cracking, with generally larger corner cracks in the 392 N indentation. It should be noted that the indentations shown in **Figure 4.18** do not necessarily correspond to those shown in **Figures 4.19** and **4.20**. **Figures 4.21** and **4.22** show the corresponding AE, force and displacement data for 294 N and 490 N loads for the hardened steel. The micrographs also show a sinking-in mechanism although, in contrast with the as-sprayed HVOF (JP5000) WC-12%Co, there is no macro-scale cracking.

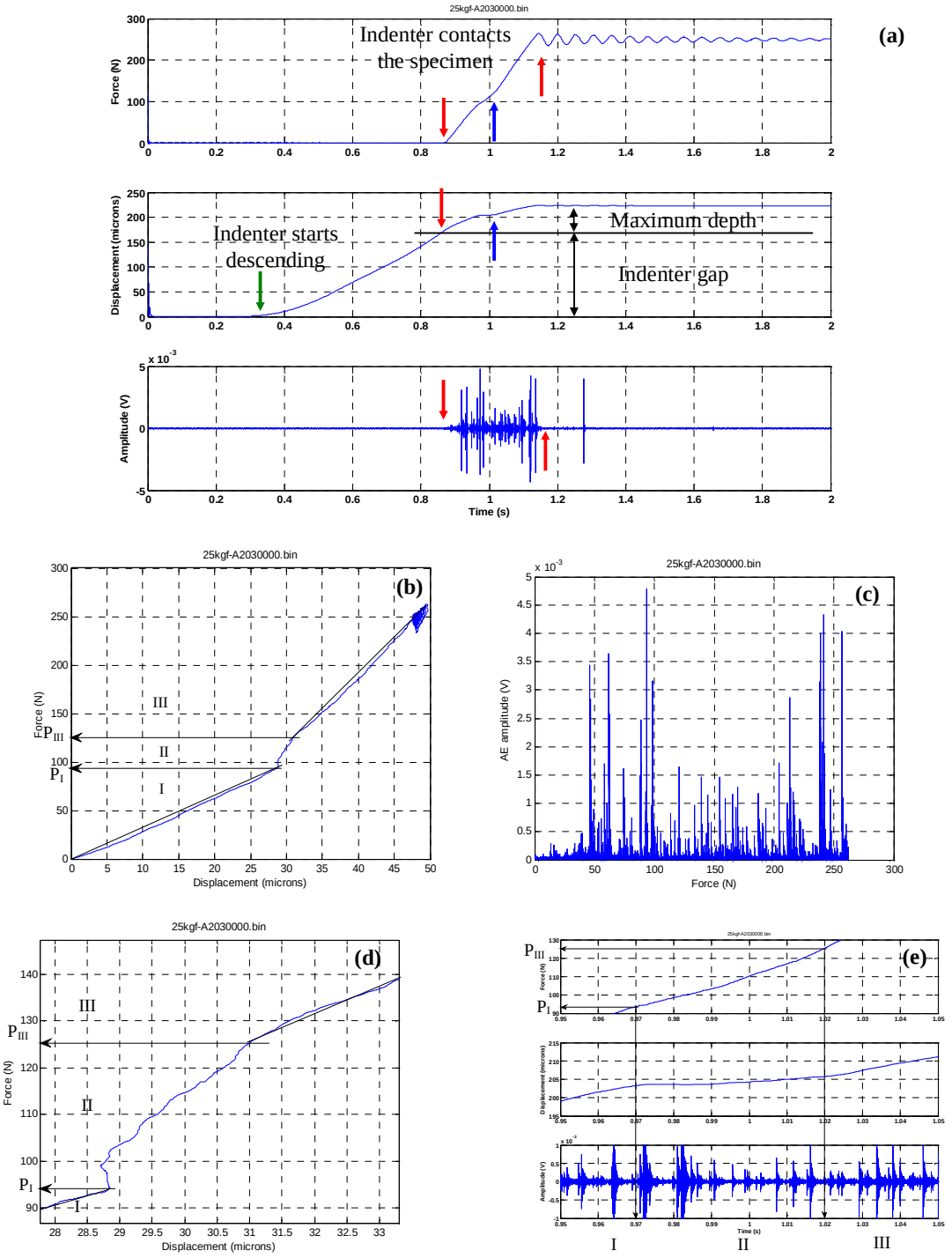

Figure 4.19 Vickers indentation of as-sprayed HVOF (JP5000) WC-12%Co coatings at 245 N load: (a) force-time, displacement-time and AE voltage-time signal, (b) *P-h* curve, (c) AE voltage-force, (d) magnified view of *P-h* curve showing three stages, (e) magnified view in time series

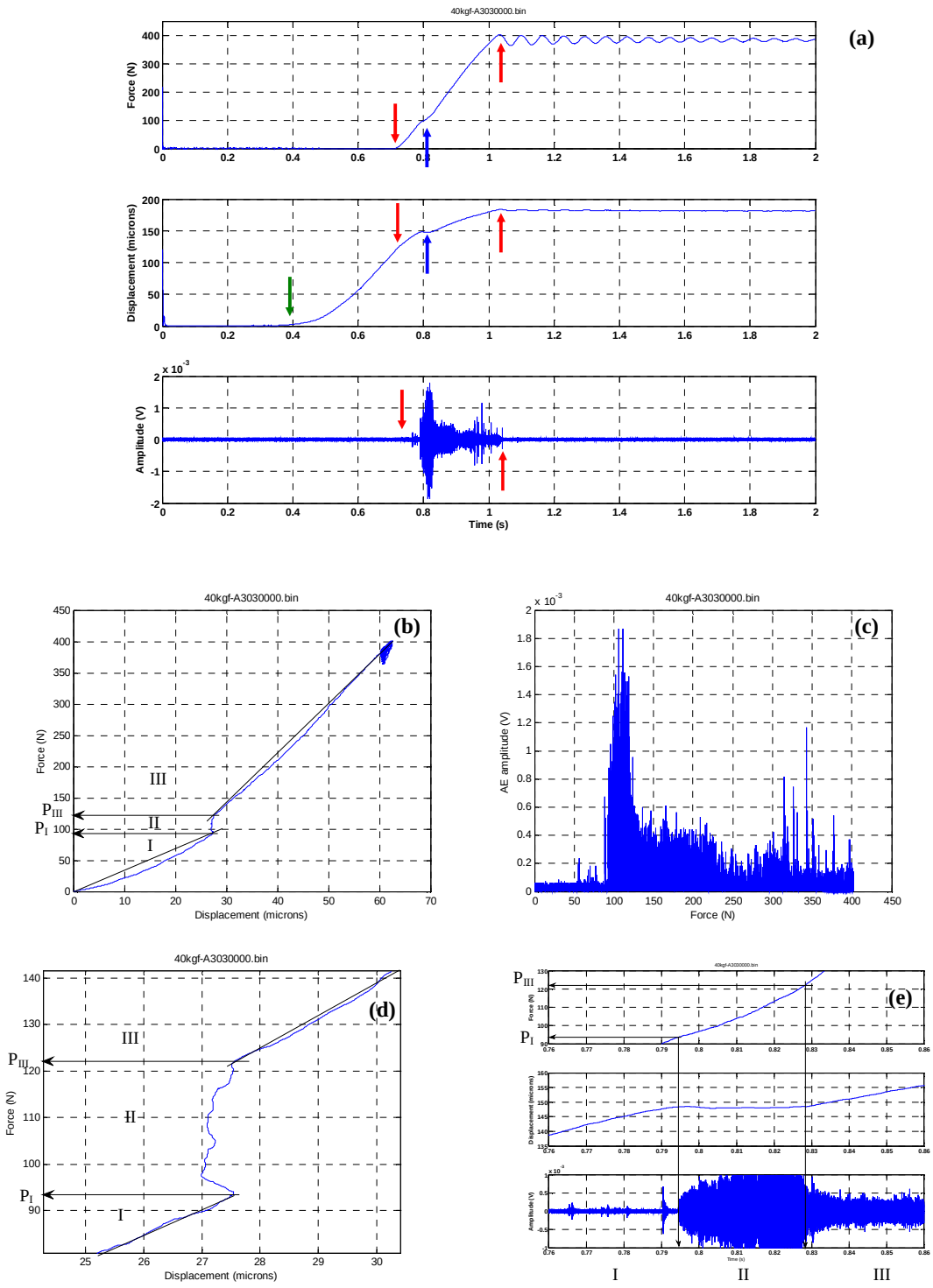

Figure 4.20 Vickers indentation of as-sprayed HVOF (JP5000) WC-12%Co coatings at 392 N load: (a) force-time, displacement-time and AE voltage-time signal, (b) *P-h* curve, (c) AE voltage-force, (d) magnified view of *P-h* curve showing three stages (e) magnified view in time series

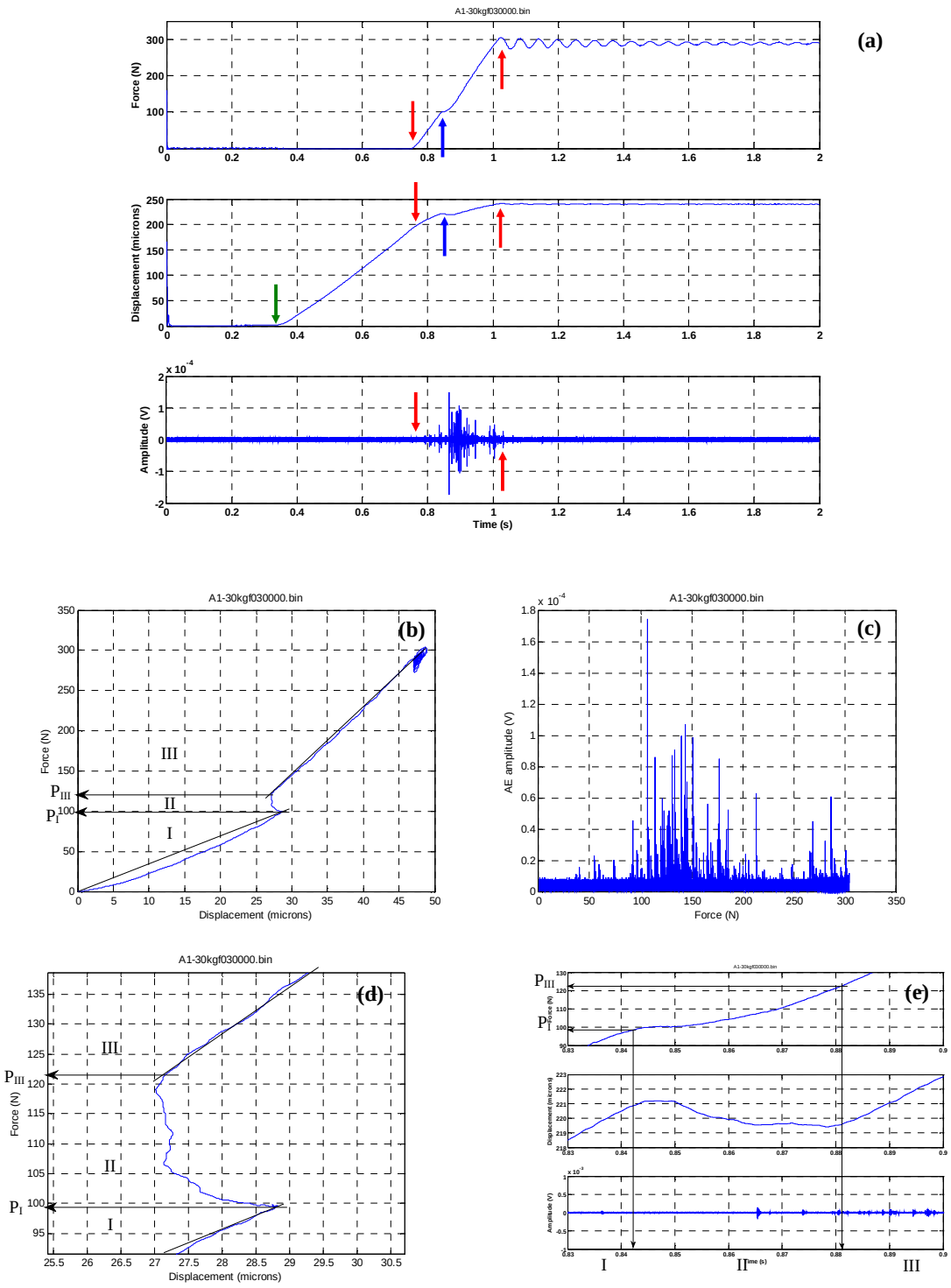

Figure 4.21 Vickers indentation of hardened steel at 294 N load: (a) force-time, displacement-time and AE voltage-time signal, (b) *P-h* curve, (c) AE voltage-force, (d) magnified view of *P-h* curve showing three stages, (e) magnified view in time series

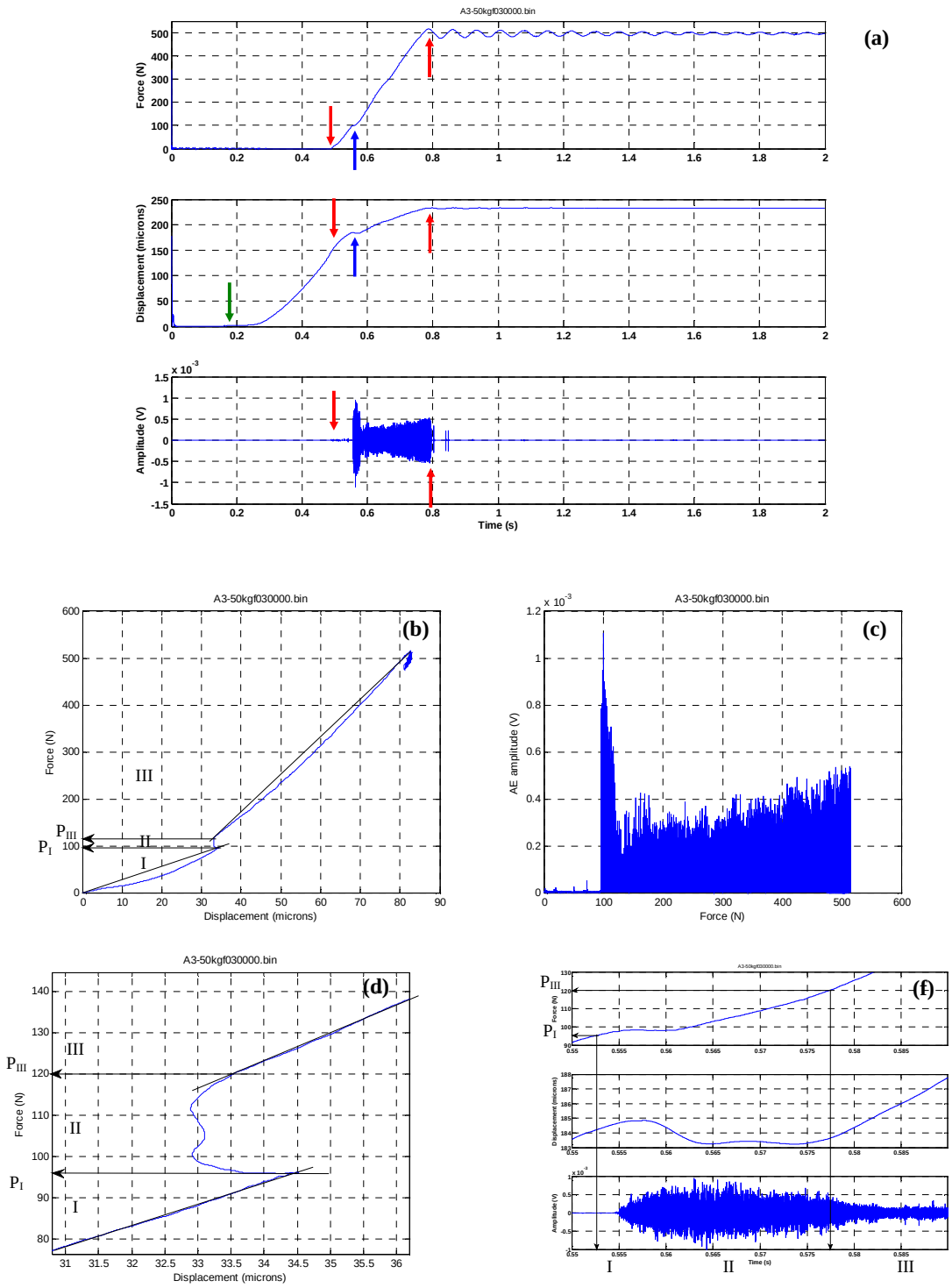

Figure 4.22 Vickers indentation of hardened steel at 490 N load: (a) force-time, displacement-time and AE voltage-time signal, (b) *P-h* curve, (c) AE voltage-force, (d) magnified view of *P-h* curve showing three stages, (e) magnified view in time series

A comparison of **Figure 4.19(a)**, **4.20(a)**, **4.21(a)** and **4.22(a)** shows the distribution of AE to be quite variable both in time and magnitude although, in most cases, there is relatively little AE in Stage I and almost none after indenter settling. The magnified

views (**Figure 4.19(d)**, **4.20(d)**, **4.21(d)** and **4.22(d)** show Stage II, as defined by the load step, mapped onto the magnified AE time series, and it can be seen that, in some cases at least, there is concentration of AE around Stage II, itself characterised by a flattening of the displacement-time graph.

It is also evident from **Figures 4.19** to **4.22** that AE is rather sparse on first contact of the indenter with the specimen. In order to quantify the effect, the time gap was measured (**Figure 4.23**) for each AE record by identifying the point of contact, C1, as determined by the first appearance of a load signal above a threshold of 0.1% above the specimen holding force and the first appearance of AE above a threshold level of 15% above the continuous background noise level at C2. **Figure 4.24** shows this time gap measured for all indentations at all loads, and shows that, despite considerable scatter, AE appears generally earlier in the as-sprayed HVOF (JP5000) WC-12%Co coating than in the hardened steel, at low loads, whereas the time gap is similar at high loads.

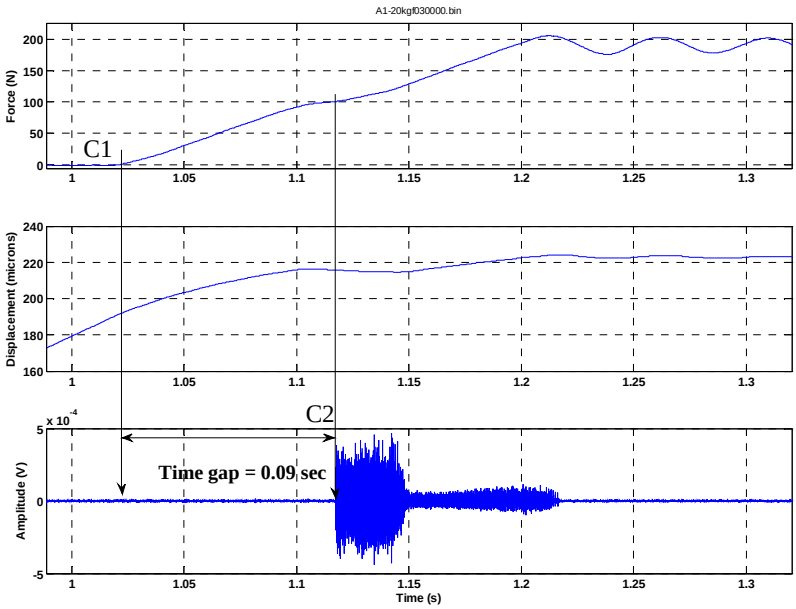

Figure 4.23 Measurement scheme of the time gap: Vickers indentation of hardened steel at 196 N load showing the indenter touching the specimen at point C1 and the occurrence of first AE above threshold at point C2.

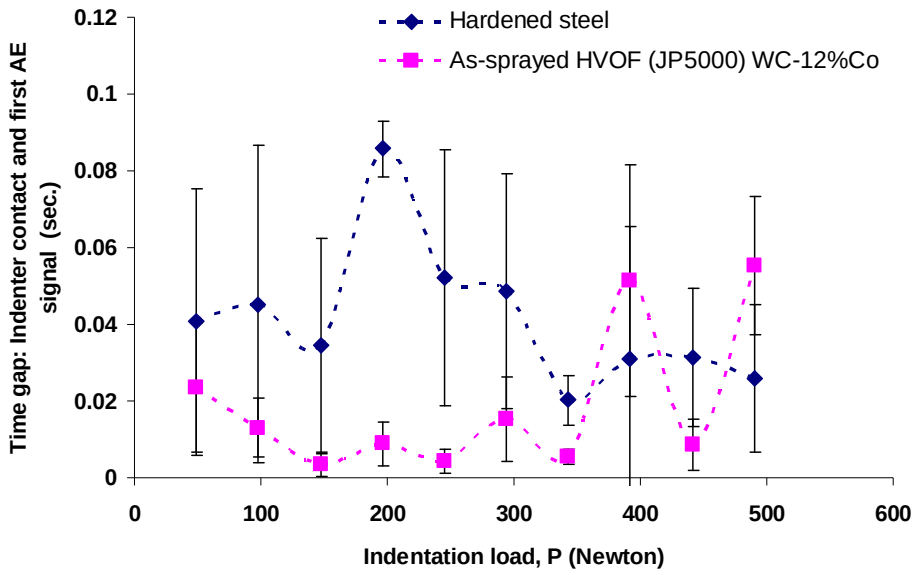

Figure 4.24 Time gap against indentation load

The stages identified for the force-displacement curve (**Figure 4.10**) were used to divide up the AE record into three separate sections (e.g. **Figure 4.25**), using the stage sectioning algorithm described in **Figure 4.26** and the AE features calculated within each of the Stages (I, II and III).

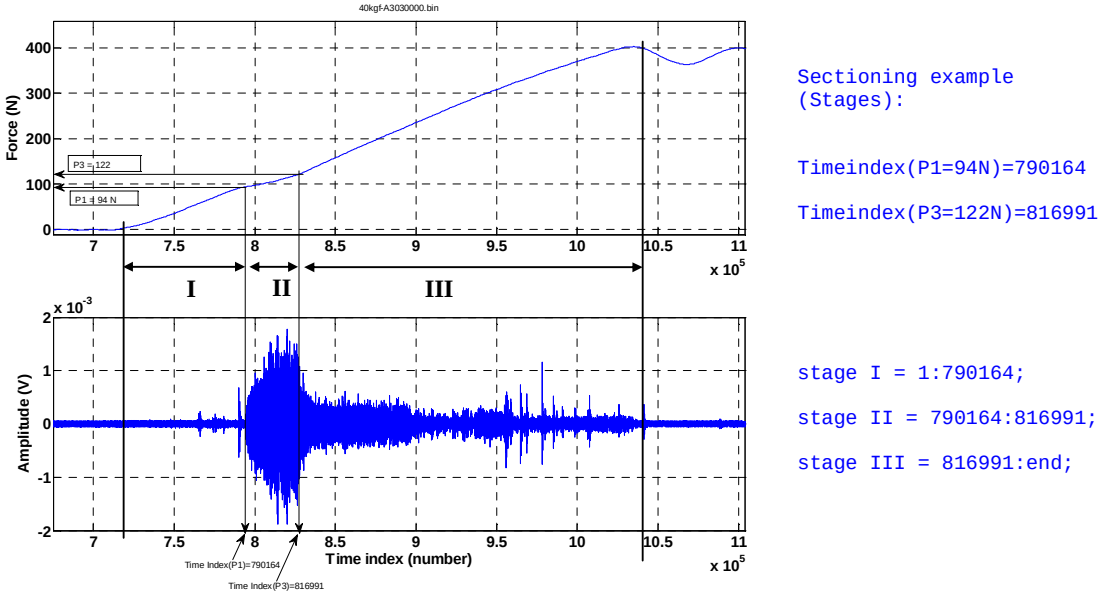

Figure 4.25 Example of separation of Stages (I, II and III) from the force-time signal [as-sprayed HVOF (JP5000) WC-12%Co coating at 392 N load]

In the main series of experiments, there is no record of force and displacement and so a means needs to be found to analyse the AE without the use of a force-displacement

record. In many cases, three clear zones can be identified in the AE record and, where they can, these zones appear to be associated with the stages identified above (e.g. **Figures 4.20** and **4.22**). The zone boundaries were identified (**Figure 4.26**) automatically by first smoothing the absolute raw AE signal using an average of 2000 data points and then applying an automated threshold of 60% below the peak AE amplitude of the total 2 second record, chosen so that its upward crossing (upcross time index, *tu*) identified the Zone A – Zone B boundary and its downward crossing (downcross time index, *td*) the Zone B – Zone C boundary. If there is more than one upcross and downcross, then no distinct zones are identifiable.

Figure 4.27 and **4.28** show the operation of the algorithm for examples where zones can and cannot be identified. Where three separate zones could be identified, AE features were calculated within each of the AE zones (A, B and C). **Figure 4.29** shows the numbers of indentations which exhibited clear AE zones, and it is clear that hardened steel showed zones for many more of the indentations (33 of 50) compared to as-sprayed HVOF (JP5000) WC-12%Co coatings (9 of 50).

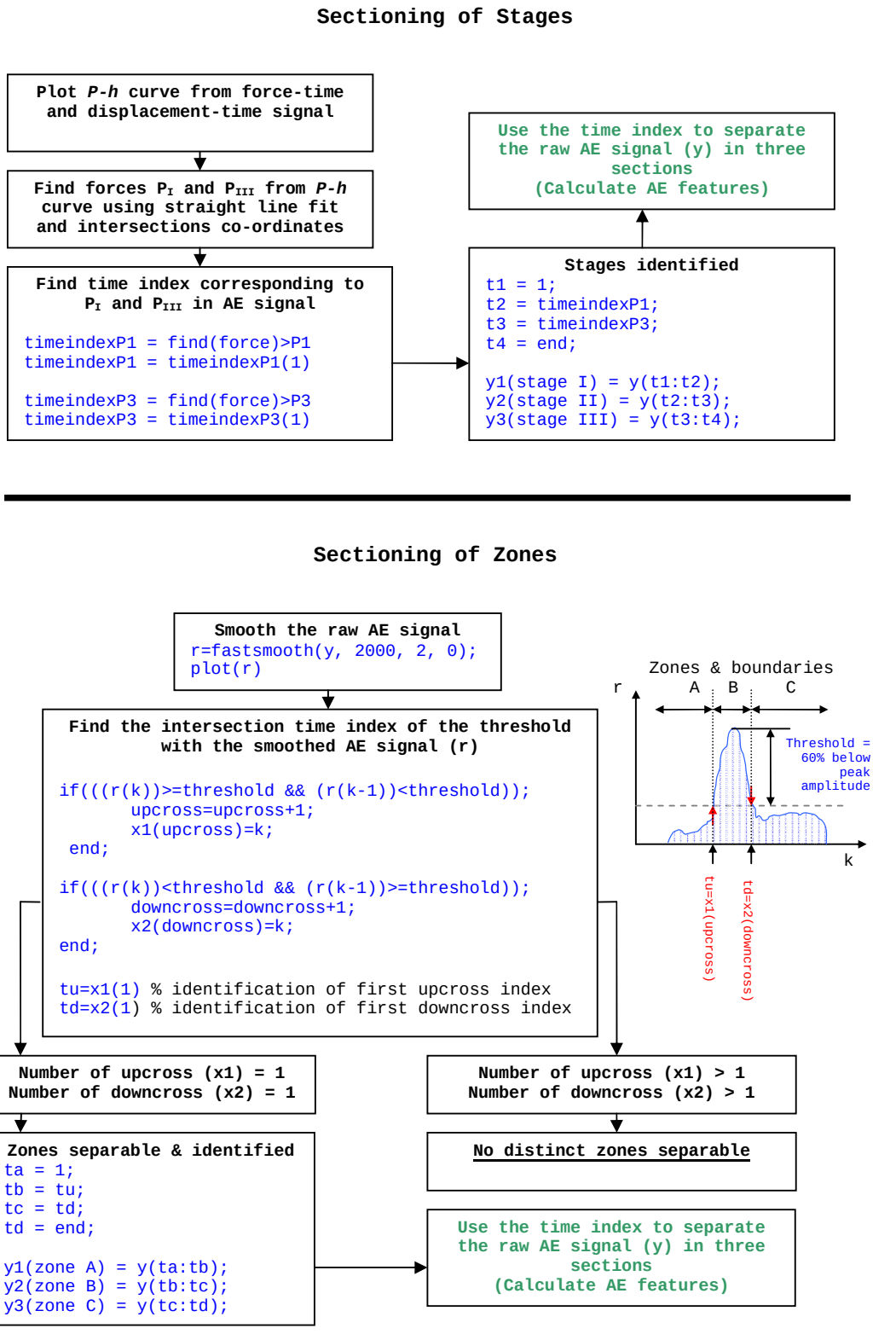

Figure 4.26 Main algorithm and scheme used to section the AE record by stages and zones

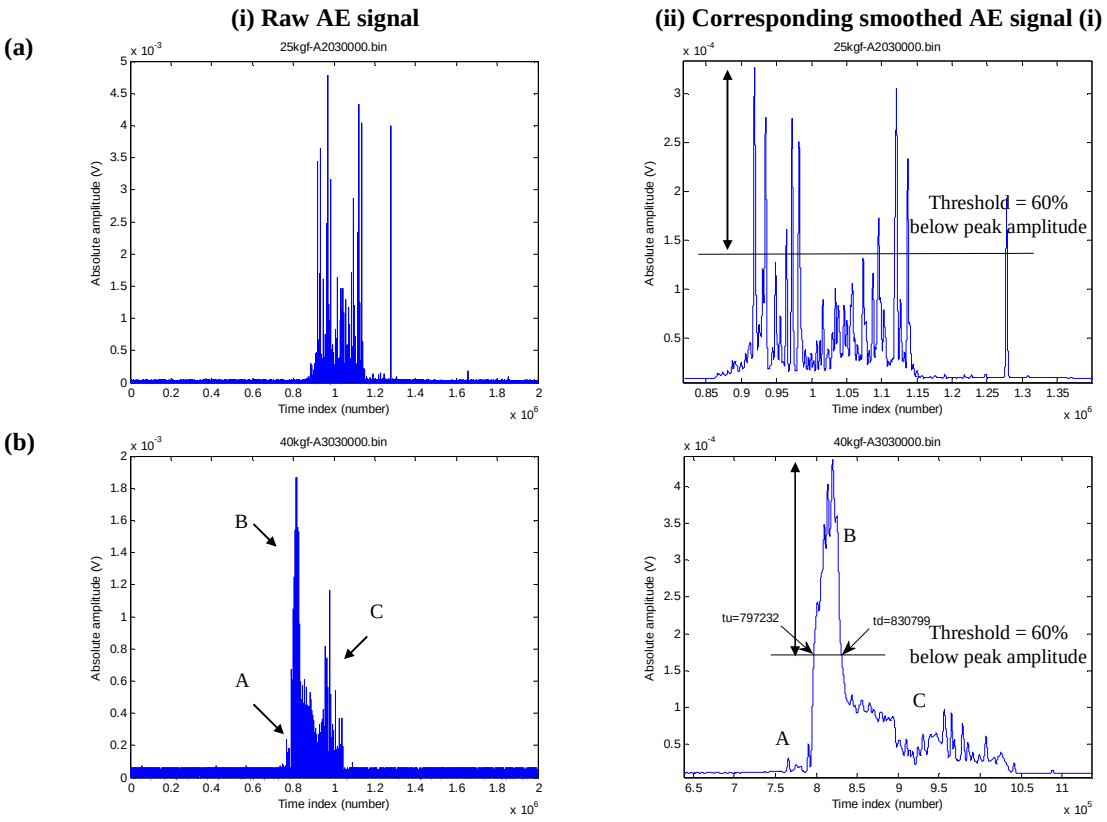

Figure 4.27 Absolute AE signal time series from Figures 4.19 and 4.20 (both as-sprayed HVOF-JP5000 WC-12%Co coatings): (a) 245 N (no distinct zones, criteria of distinct zones broken due to more than one crossings of the threshold), (b) 392 N (showing all three zones: A, B and C)

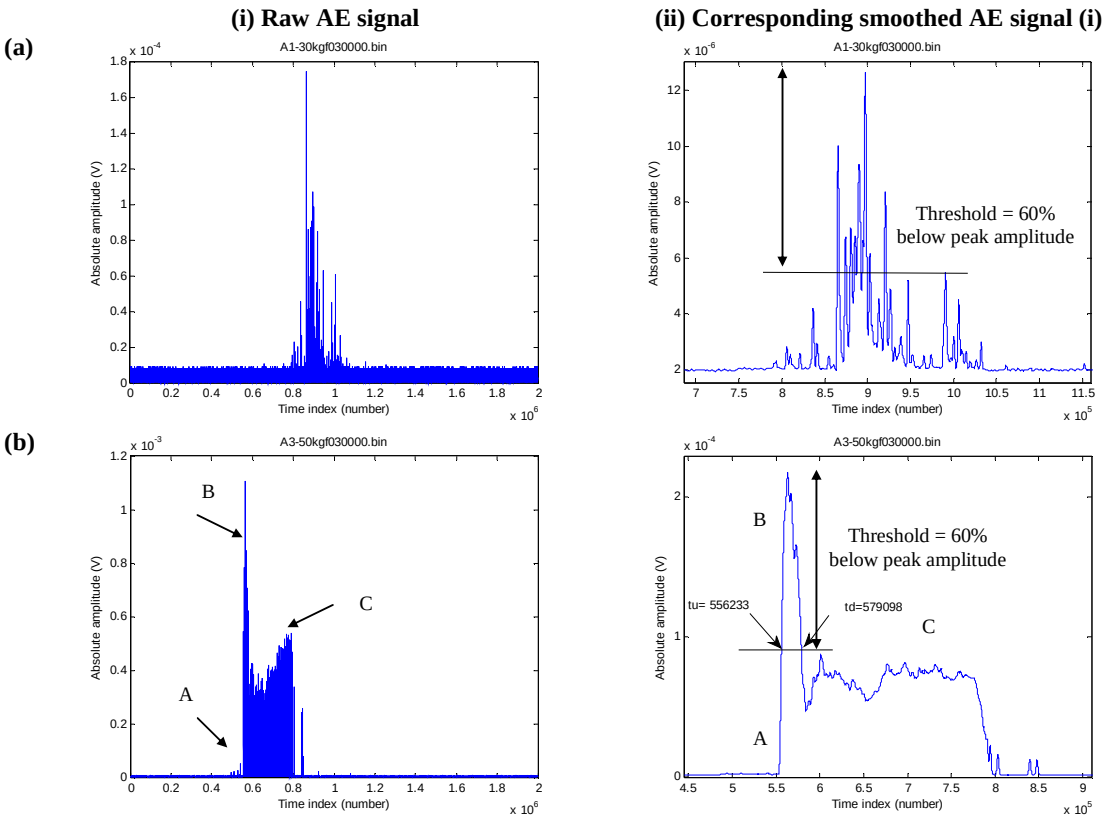

Figure 4.28 Absolute AE signal time series from Figures 4.21 and 4.22 (both hardened steel): (a) 294 N (no distinct zones, criteria of distinct zones broken due to more than one crossings of the threshold), (b) 490 N (showing all three zones: A, B and C)

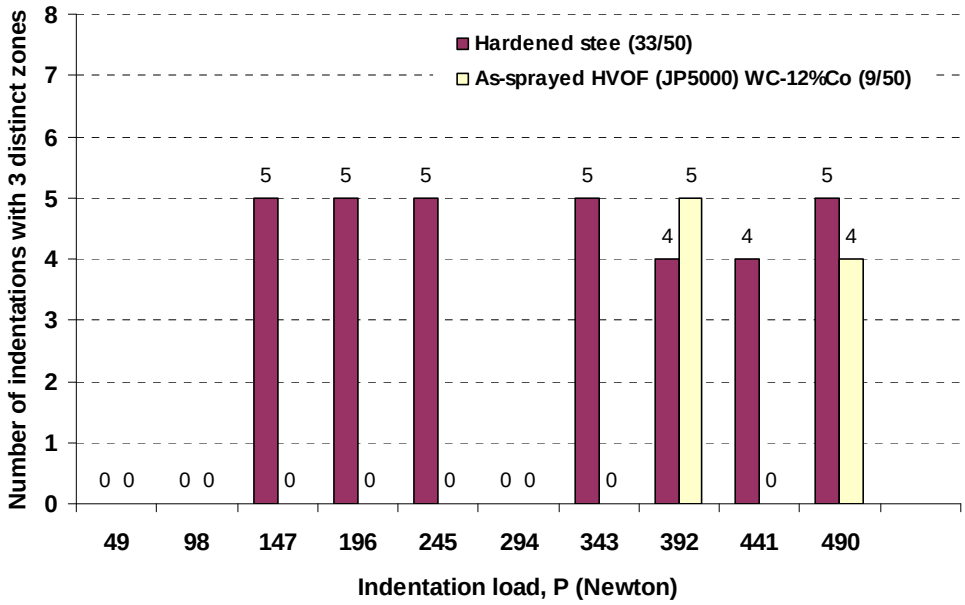

Figure 4.29 Number of indentations with distinct AE zones A, B and C

Figures 4.30 and **4.31** show the AE energy and duration, respectively, analysed per stage and per zone. It is clear that, in the cases where clear zones can be identified, the zone and stage analyses coincide reasonably well.

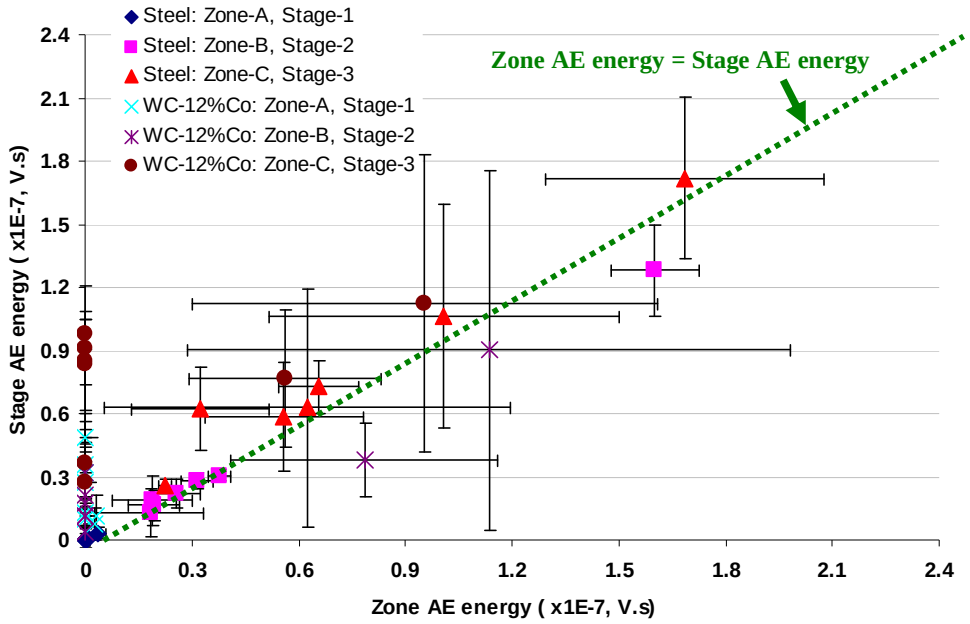

Figure 4.30 Zone AE energy plotted against stage AE energy

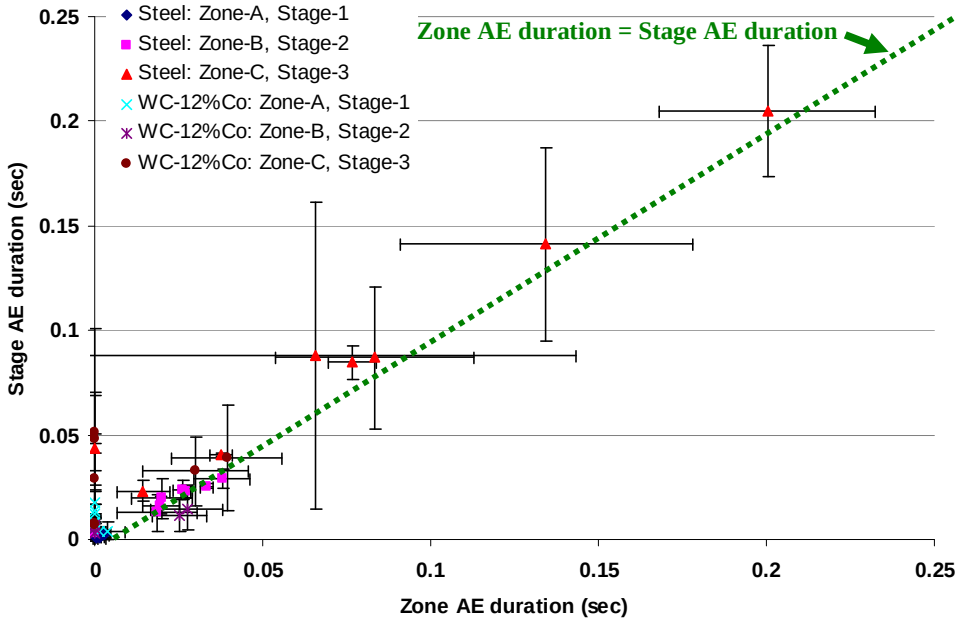

Figure 4.31 Zone AE duration plotted against stage AE duration

Figure 4.32 (i) show the AE energy and duration partitioned per zone for those cases where sectioning was possible. **Figure 4.32 (ii)** shows the AE energy and duration

sectioned per stage for each case. Comparing with **Figure 4.17**, it would appear that Zone C for steel gives a more consistent evolution with mechanical energy. Little can be observed for as-sprayed HVOF (JP5000) WC-12%Co coatings since those signals which could be partitioned were confined to two loads.

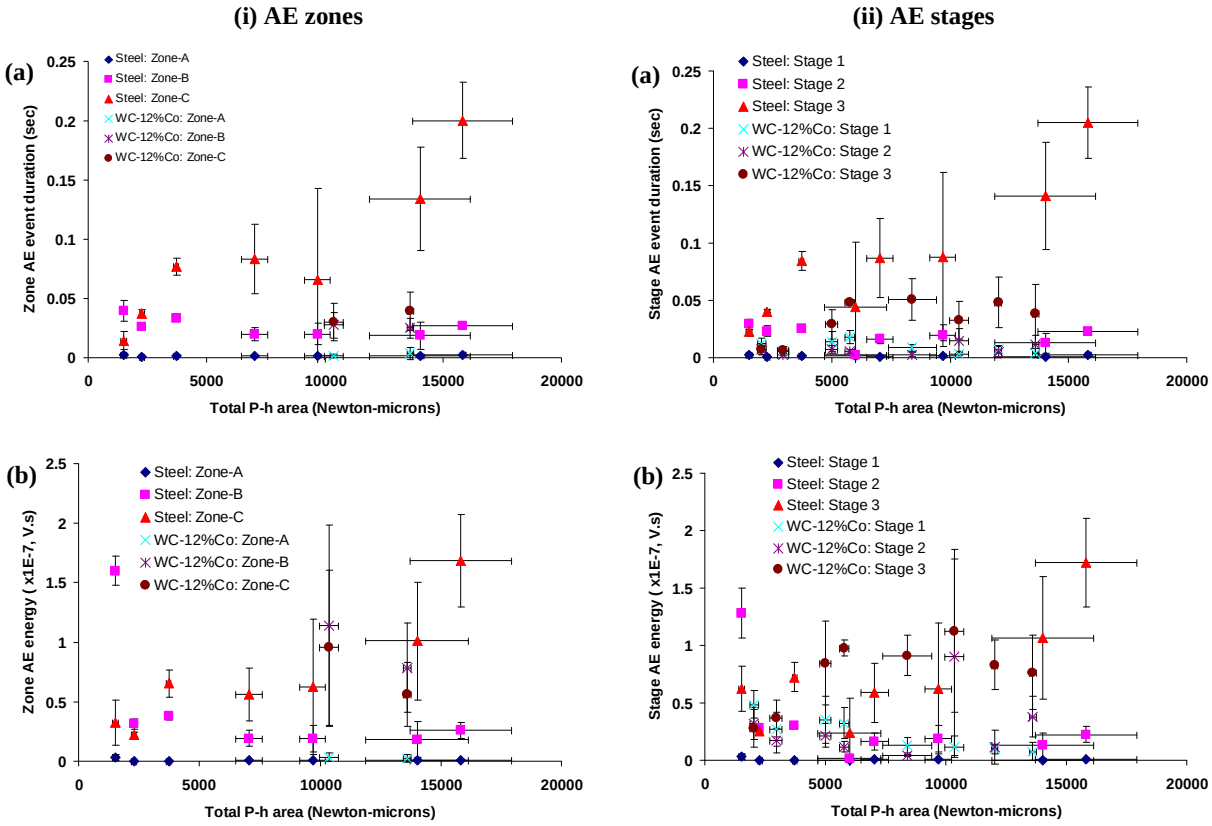

Figure 4.32 Zone and stage AE features: (i) zones and (ii) stages *vs* total *P-h* area

4.2 AE monitored Vickers indentation testing of WC-Co coatings

The coatings investigated were; as-sprayed HVOF (JetKote) WC-12%Co, HIPed HVOF (JetKote) WC-12%Co and as-sprayed HVOF (JP5000) WC-10%Co-4%Cr. This section presents the results for the microstructure, the surface and subsurface fracture patterns, and analysis of the raw AE signals. The analysis of the AE signals follows the findings of *Section 4.1* in that AE features are calculated per zone in cases where zones can be identified and the total AE features are calculated for all indentations.

4.2.1 Microstructural characterisation

For WC-12%Co, the raw powder particles exhibited the typical angular shape of sintered and crushed powders with a size distribution between 15 and 50 μm and mean

particle size of about 30 μm [32]. For WC-10%Co-4%Cr, the raw powder particles were typically of spherical shape with a size distribution between 15 and 45 μm. As shown in the SEM images taken at random locations (**Figure 4.33**), the polished surfaces are quite smooth, with a homogeneous microstructure and little surface connected porosity, and no evidence of non molten or semi molten particles. The carbide particles are relatively angular. Notwithstanding the poor contrast, the HIPed WC-12%Co does not appear much different to the as-sprayed, although other coatings with similar materials [32] have noted lower porosity, and a greater level of homogeneity in the HIPed microstructure. The WC-10%Co-4%Cr material is not generally distinguishable from the WC-12%Co.

XRD analysis of the both as-sprayed HVOF (JP5000, JetKote) WC-12%Co coatings (*Appendix E:* Figure E.2 and E.4) showed then predominantly to contain the primary tungsten carbide (*WC*) phase with some of the harder secondary phase tungsten carbide (W_2C) and a very small amount of metallic tungsten (*W*). The HIPed HVOF WC-12%Co coatings (*Appendix E:* Figure E.5), exhibited significant changes from the pattern of the as-sprayed coating. Although the main phase was again primary tungsten carbide (*WC*), some *eta*-carbides (Co_6W_6C) formed by the interaction of the Co matrix and WC. None of the recorded peaks could be related to the secondary tungsten carbide (W_2C) phase or metallic tungsten (*W*). The as-sprayed HVOF WC-10%Co-4%Cr coatings (*Appendix E*: Figure C.6) predominantly contained WC with small amounts of W_2C, chromium (*Cr*) and cobalt (*Co*), and therefore had more in common with the as-sprayed WC-12%Co than the HIPed material.

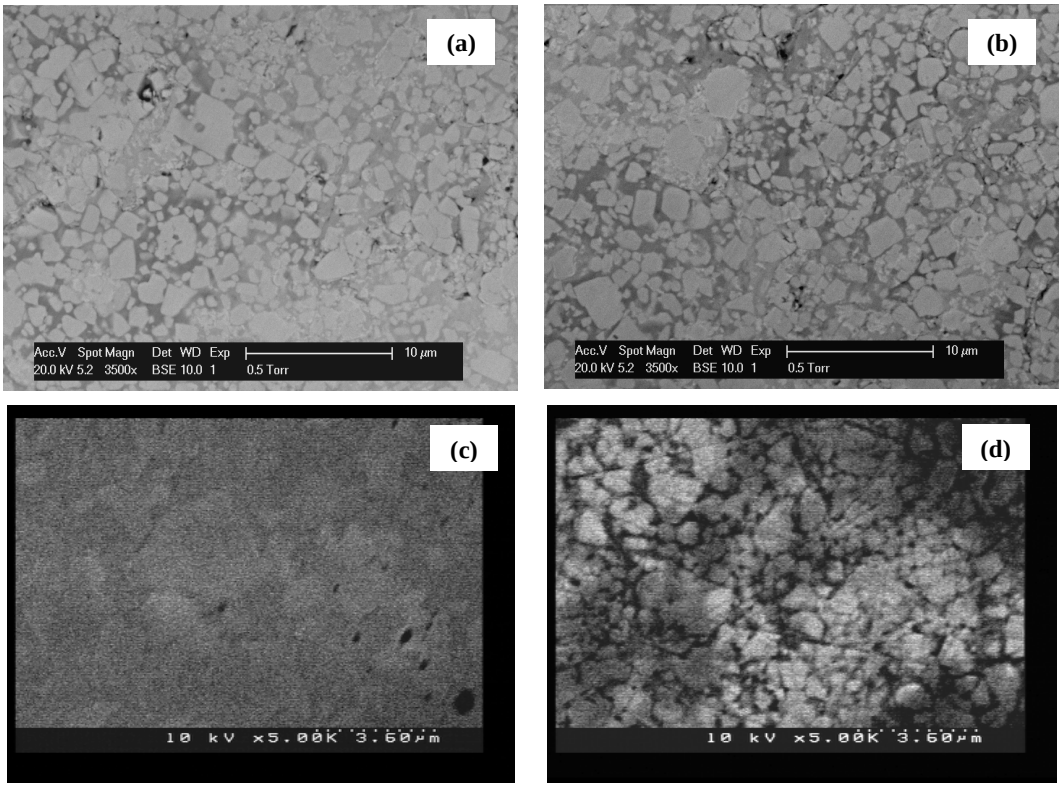

Figure 4.33 The surface morphology of WC-Co coatings: (a) as-sprayed HVOF (JP5000) WC-12%Co (coating material in *Section 4.1*), (b) as-sprayed HVOF (JetKote) WC-12%Co, (c) HIPed HVOF (JetKote) WC-12%Co, and (d) as-sprayed HVOF (JP5000) WC-10%Co-4%Cr

4.2.2 Vickers indentation derived properties

Figure 4.34 shows the cracking patterns around typical indentations for a representative selection of loads and coating type. The surface fracture pattern includes radial cracks at the four corners, edge cracks (or edge chipping), ring cracks and other small cracks around the indentation, as illustrated in the schematic diagram **Figure 3.15**. All cracks visible were measured according to the scheme described in *Section 3.5*.

For as-sprayed HVOF (JetKote) WC-12%Co coatings (**Figures 4.34a, b**), radial cracking from all or any of the four corners of the indentation was seen for loads of 98 N upwards, whereas, at 49 N (**Figure 4.34a**), only minor cracks around the perimeter (edge cracks) and on the surface of the indentation were found. In contrast, the HIPed HVOF (JetKote) WC-12% Co coating showed only measurable edge cracks and other small cracks around the indentation with no visible radial cracking for any of the indentations at any of the loads (**Figures 4.34c, d**). Similarly, the as-sprayed HVOF (JP5000) WC-10%Co-4%Cr coatings showed only measurable edge cracks with no radial cracks being observed at any of the loads (**Figures 4.34e, f**).

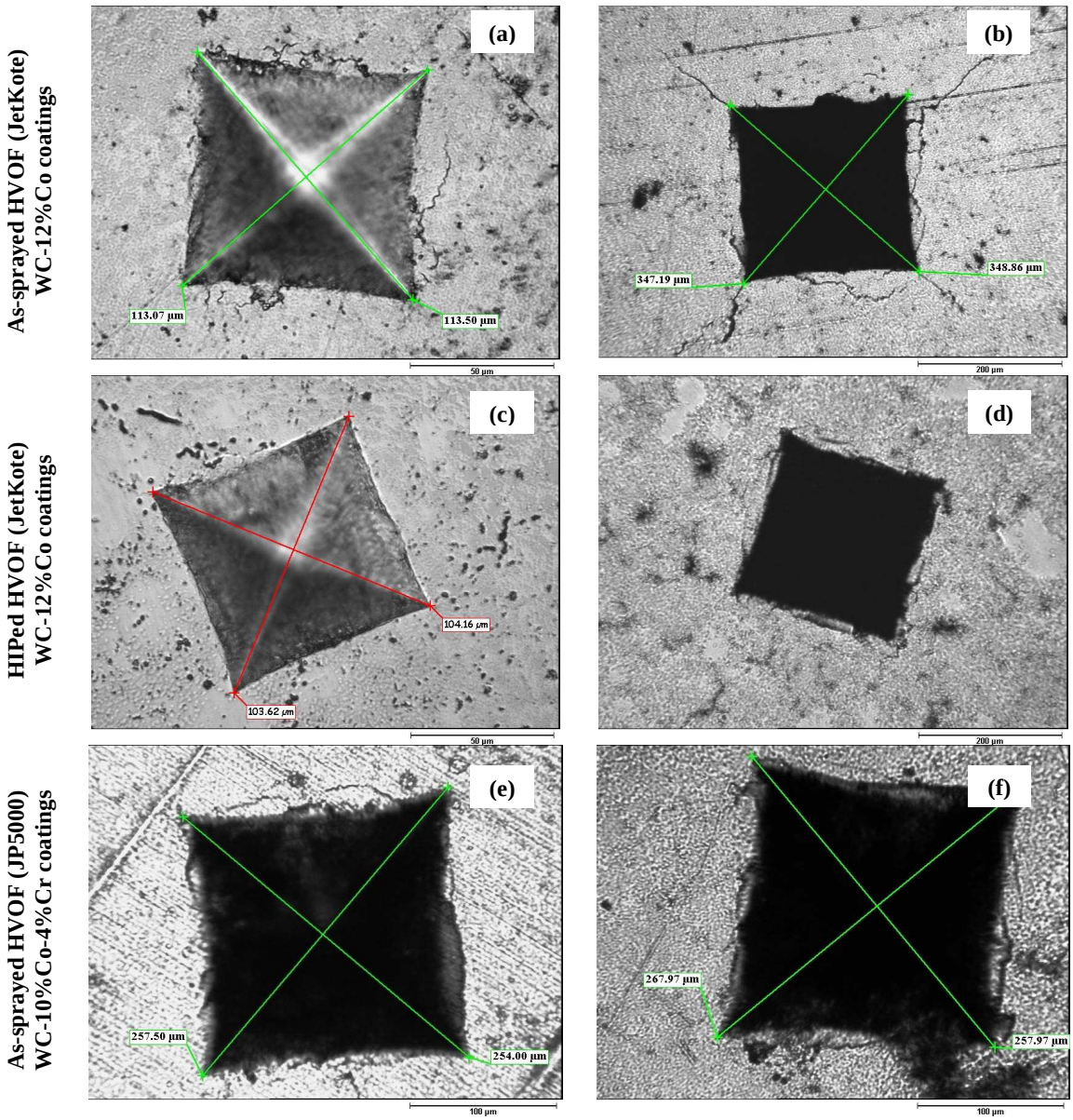

Figure 4.34 Typical Vickers indentation cracking patterns for HVOF WC-Co coatings (a) as-sprayed WC-12%Co 49 N, (b) as-sprayed WC-12%Co, 490 N, (c) HIPed WC-12%Co, 49 N, (d) HIPed WC-12%Co, 490 N, and (e) at high pressure, P1 at gun speed 100 mm s^{-1} and (f) low pressure, P2 at gun speed 200 mm s^{-1}, as-sprayed WC-%10Co-4%Cr both at 343 N

Since the contact of the Vickers indenter is spread over four planar surfaces and, since the indenter takes a finite amount of time to come to rest during indentation, the possibility of AE emanating from cracks propagating below the surface needs also to be considered as well as how the surface cracks might be expected to grow with time during the indentation. The fracture pattern in all WC-Co coatings studied here also tends to be asymmetric, which is attributed to a macroscopic variation in relative density (i.e. the presence of pores or other defects around the contact) [53] and the

relative coarseness of the microstructure. In particular, the propagation of cracks does not emanate equally from all four corners (e.g. **Figure 4.34a**) as is generally observed in homogeneous glass and ceramic materials.

Figure 4.35 shows cross-sectional views around indentation for the as-sprayed HVOF (JetKote) WC-12%Co coating, one at each of the loads 245 N and 441 N, where areas with sub-surface densification and lateral cracks can be seen. The cross-sectional image at 147 N load also showed lateral cracks with little densification.

The regions beneath the indenter (densified region) and away from indentation zone can be compared using the rectangular areas identified in the micrographs, the porosities immediately under the indenter being 0.15% for the 245 N and 0.80% for 441 N loads. The corresponding average porosities in the areas just away from the indentation were 4.5% and 3.5% for the 245 and 441 N loads, respectively. The densified zone (which can be imagined to be approximately spherical in three dimensions) corresponds with the compressive stress lobe as discussed by Lawn and Swain [2] and, whereas the degree of densification does not account for all of the visible surface depression produced by the indenter in these cross-sections, it could contribute to the accommodation and densification could generate AE. The extent and orientation of the lateral cracks appears to vary with load, judging from the limited evidence that can be seen in **Figure 4.35**. For the 245 N load, the lateral crack has multiple branches both in the lateral and vertical directions and the overall length is almost the size of the indent half diagonal. For the 441 N load, the lateral delamination crack can be seen to emerge onto the surface at a distance over twice the indent diagonal, running at a depth almost equal to the indentation depth.

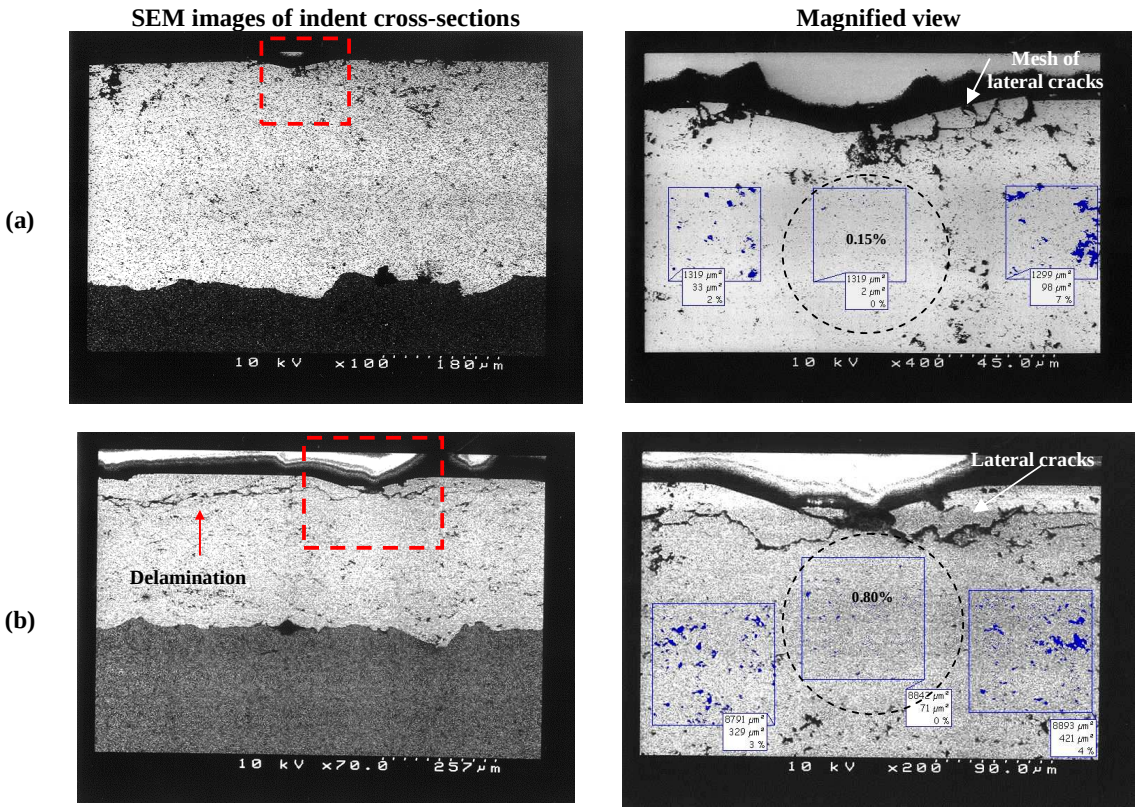

Figure 4.35 SEM images of Vickers indentation cross-sections of as-sprayed HVOF (JetKote) WC-12%Co coatings showing the 'sinking-in' and mesh of lateral cracks around the indenter and sub-surface damage, (a) 245 N and (b) 441 N.

Once the indenter has landed, the surface of the coating bends plastically ("sink-in" zone) around the periphery of the indenter, the displacement of material being taken up by plastic flow around hard particles accompanied by a certain amount of cracking of the particles under the tensile stresses (**Figure 4.35a**). The other mechanism clearly visible in **Figure 4.35** is sub-surface lateral cracking, not dissimilar in its morphology to the edge cracks seen on the upper surface. The partially developed sub-surface lateral cracks for both loads appear to originate at the base of a surface layers extend in a plane parallel to the surface [53] and may eventually emerge some distance from the indentation.

Other events which may appear in the AE record include fracture of hard phase particles [35] beneath the pyramidal surface of the indenter, and a typical case at 441 N load is shown in **Figure 4.36**. It may be that crushing and cracking of hard phase particles [35] is the initiating event for the development of sub-surface lateral cracks of the type seen in **Figure 4.35**.

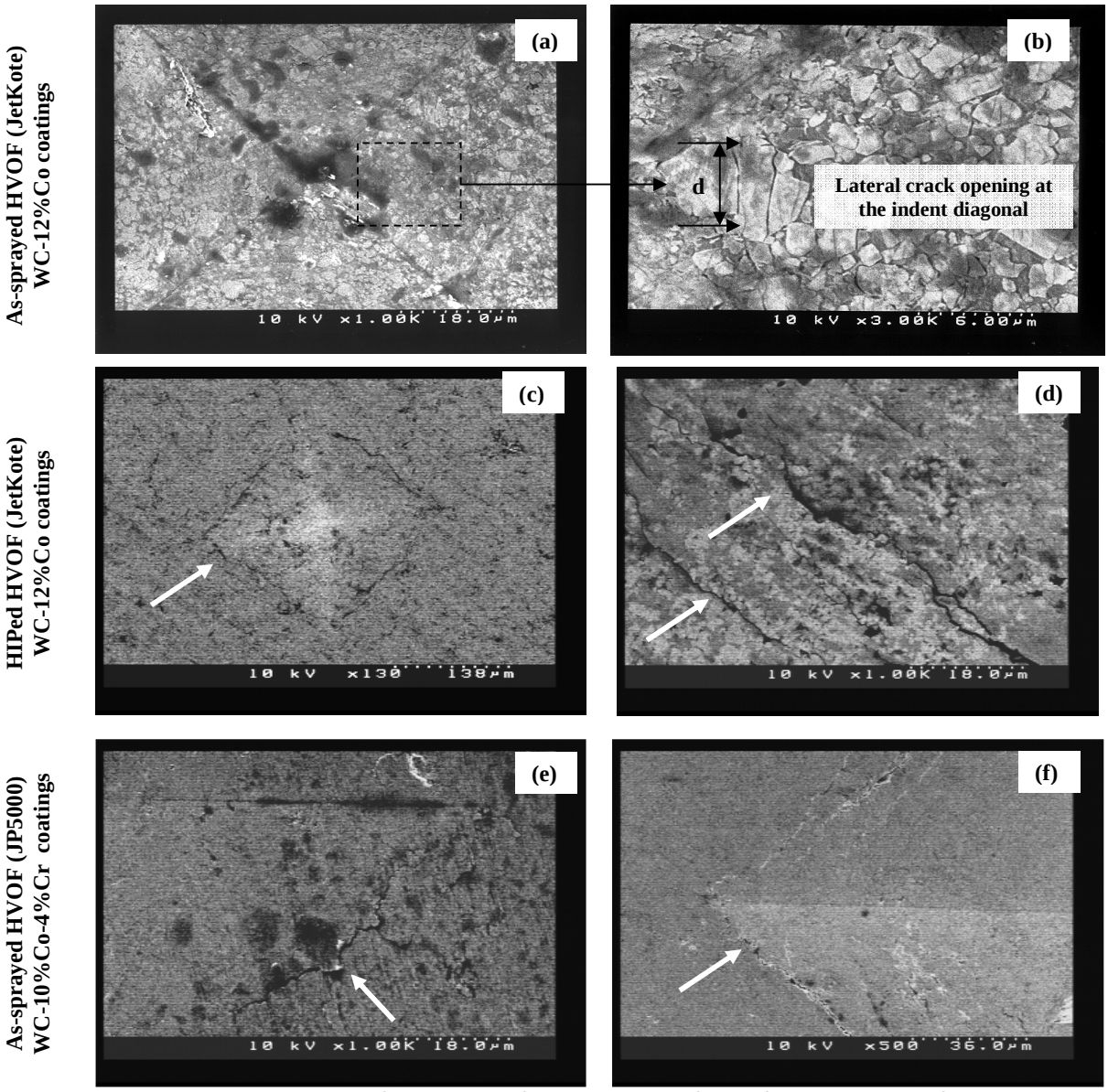

Figure 4.36 SEM images of top view of pyramidal surface of indentations of WC-Co coatings: (a) at 441 N load showing indent diagonal at tip, and (b) at higher magnification showing a WC particle (d ~ 6μm) crushed under the load; (c) at 441 N showing full view of indent corner and edge shown with arrow, and (d) showing edge crushed under the load; (e) at 196 N (100 mm s^{-1} gun speed, high pressure, P1), and (f) 343 N (at 200 mm s^{-1} gun speed, low pressure, P2)

The effect of microstructural variation can be seen in the micro- and macro-hardness values (**Table 4.1**). The average macrohardness (five indentations at each load) was highest for the WC-10%Co-4%Cr coatings, and least for the as-sprayed WC-12%Co. The microhardness values (again five indentations) show, as expected, a wider variation, especially taking account of the fact that the load is constant. It is a little surprising that the values do not rank in the same way as the macro-hardness tests, but this may not be significant.

Table 4.1 Vickers indentation hardness of HVOF WC-Co coatings

Materials	Microhardness ($HV_{1.96\ N}$)	Macrohardness
As-sprayed HVOF (JetKote) WC-12%Co	1050±70	759 ± 28 $HV_{49\text{-}490\ N}$
HIPed HVOF (JetKote) WC-12%Co	1018±177	839± 48 $HV_{49\text{-}490\ N}$
As-sprayed HVOF (JP5000) WC-10%Co-4%Cr (high pressure, P1)	1097±110	977± 19 $HV_{49\text{-}343\ N}$
As-sprayed HVOF (JP5000) WC-10%Co-4%Cr (low pressure, P2)	990±18	915± 79 $HV_{49\text{-}343\ N}$

4.2.3 AE signals

This section presents AE signals of as-sprayed HVOF (JetKote) WC-12%Co, HIPed HVOF (JetKote) WC-12%Co and as-sprayed HVOF (JP5000) WC-10%Co-4%Cr coatings, and the analysis follows the findings of *Section 4.1* in that AE features are calculated per zone in cases where zones can be identified. **Figure 4.37** shows the number of indentations which exhibited clear AE zones (criteria described in **Figure 4.26**), and the most striking aspect is that HIPed HVOF (JetKote) WC-12%Co and as-sprayed HVOF (JP5000) WC-10%Co-4%Cr coatings showed no distinct zones at any of the loads. The as-sprayed HVOF (JetKote) WC-12%Co showed distinct zones for most of the loads (43 of the 50 indentation in stark contrast to the behaviour of nominally similar material in the fully instrumented tests (**Figure 4.29**).

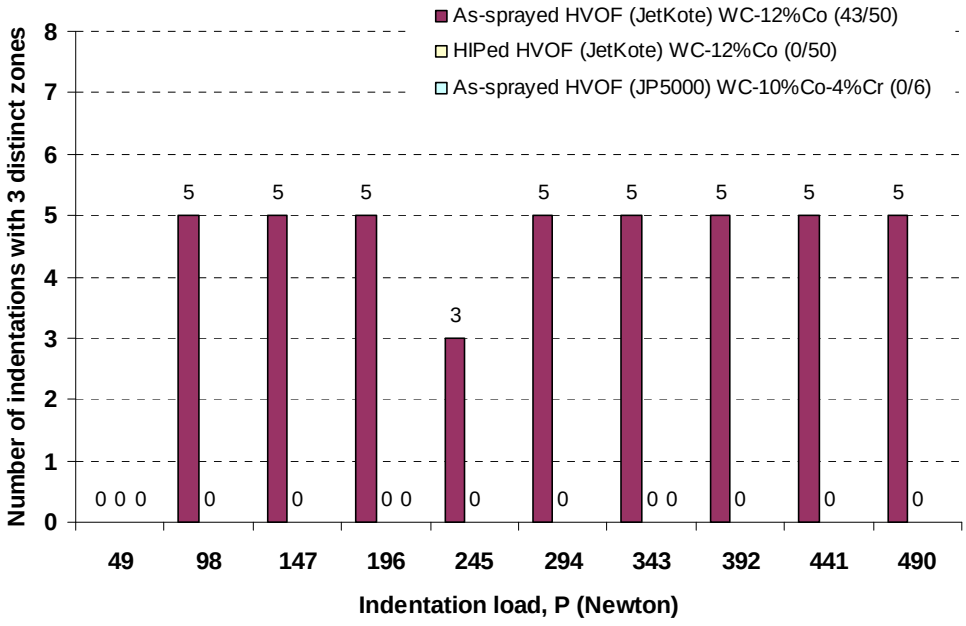

Figure 4.37 WC-Co coatings: Number of indentations with distinct AE zones A, B, C

Figure 4.38 shows typical time- and frequency-domain plots for as-sprayed HVOF (JetKote) WC-12%Co coatings, showing the clear zones evident at most of the loads. The spectra show most of the power to be in the two bands at 100 kHz to 250 kHz and 300 kHz to 400 kHz with a minor component discernible between 550 kHz to 650 kHz. Other than this, little can be seen immediately to distinguish the spectra apart from a series of high frequency spikes at 49 N load which is attributed to noise and corresponds to a long period in the 2-second record where no events are perceptible above the noise.

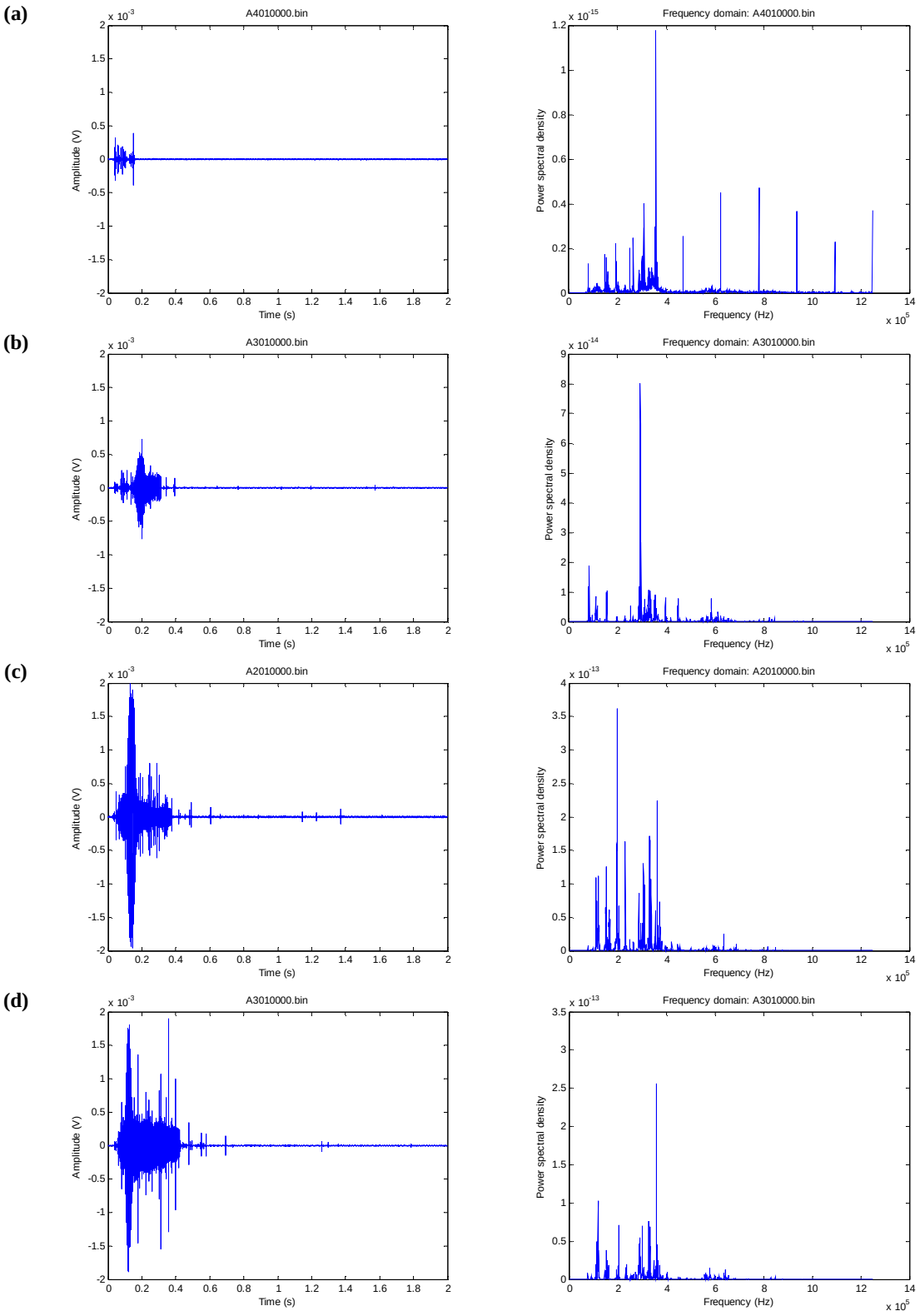

Figure 4.38 Typical AE signal structures (amplitude and frequency) during indentation at loads: (a) 49 N (b) 196 N (c) 343 N and (d) 490 N [as-sprayed HVOF (JetKote) WC-12%Co coatings]

Figure 4.39 shows a more detailed representation of the AE time series for one case where the signal did not (**Figure 4.39a**) and one case where the signal did (**Figure**

4.39b) meet the zoning criteria in as-sprayed HVOF (JetKote) WC-12%Co coatings. Clearly, the dispersion of the signal in **Figure 4.39a** is not as widespread as it is in other signals (i.e. **Figure 4.19**) which do not meet the criteria.

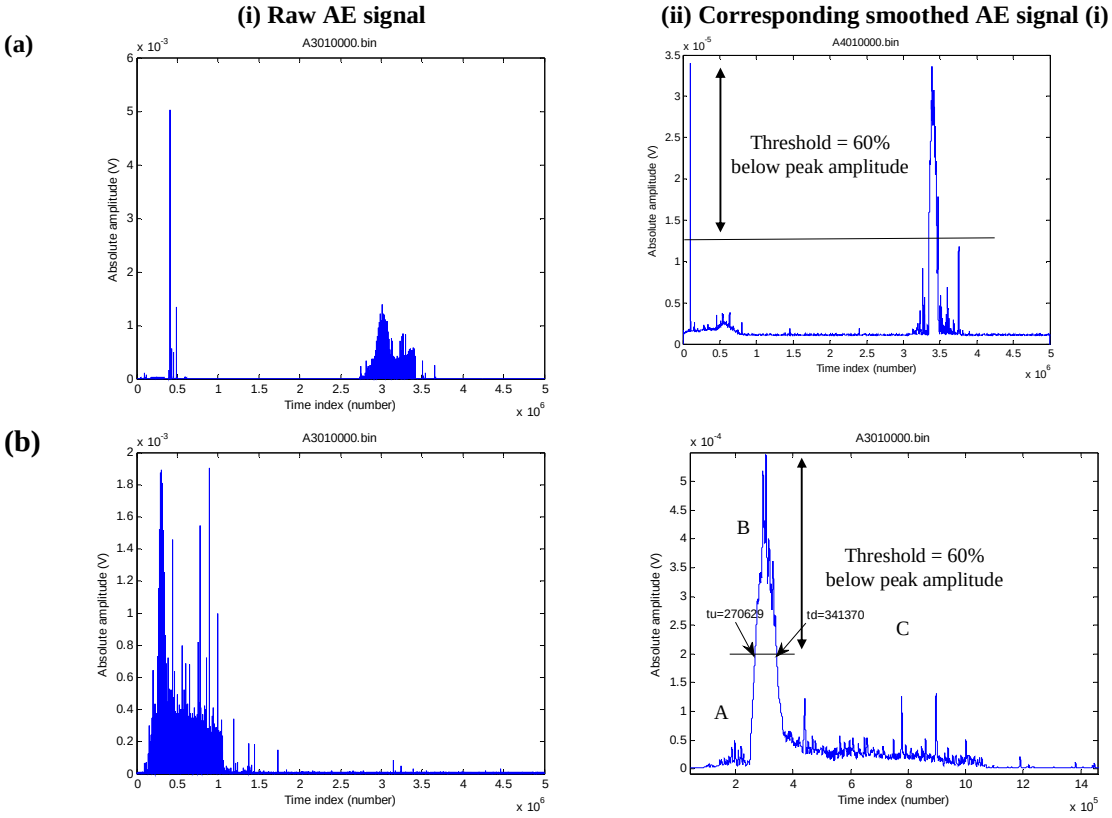

Figure 4.39 Absolute AE signal in time series (as-sprayed HVOF-JetKote WC-12%Co coatings): (a) 245 N (criteria of distinct zones broken due to more than one crossings of the threshold), (b) 490 N (showing all three zones-A, B and C from Figure 4.38d)

Figure 4.40 shows examples of frequency spectra for each of the three zones, while **Figure 4.41** shows the ratio of power in the low frequency band (0-250 kHz) to the power in the high frequency band (250-750 kHz) for each of the zones for each of the loads. This ratio does not show any particular pattern between loads or zones.

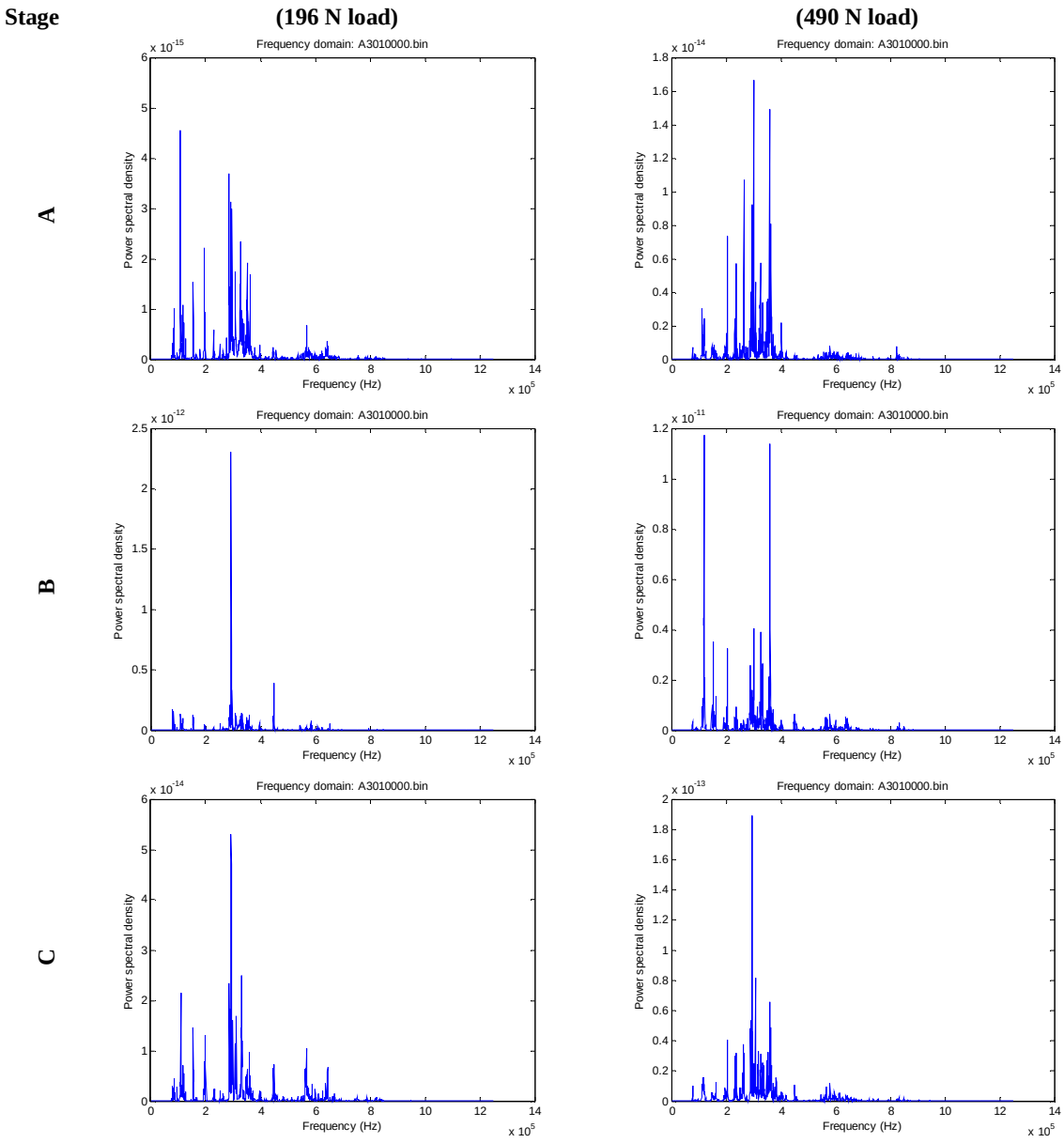

Figure 4.40 AE spectra for the distinct zones (A, B and C) of indentation identified in Figure 4.38 for indentations at 196 and 490 N [as-sprayed HVOF (JetKote) WC-12%Co coatings]

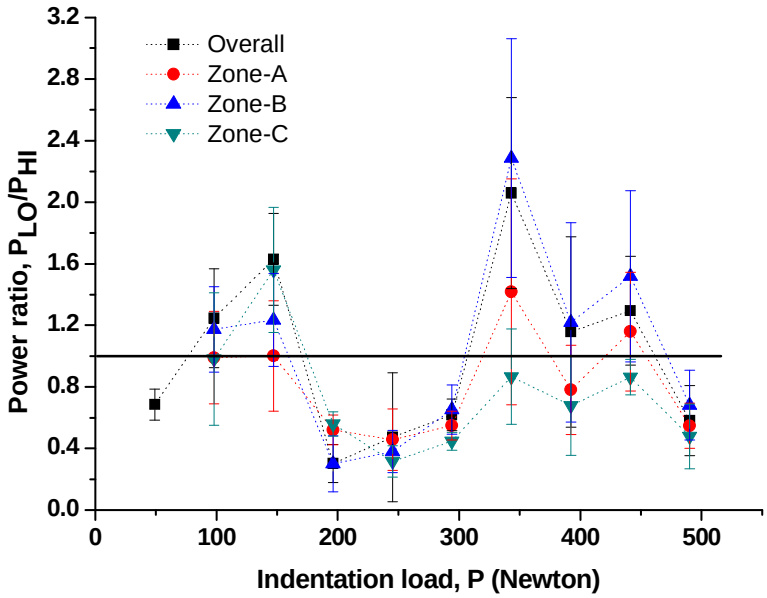

Figure 4.41 Power ratio in as-sprayed HVOF (JetKote) WC-12%Co coatings

For HIPed HVOF (JetKote) WC-12%Co, as-sprayed HVOF (JP5000) WC-10%Co-4%Cr coatings (**Figure 4.42** to **4.44)**, AE activity is not evenly spaced in time, and similar behaviour was seen for all loads, with no distinct zones of AE being separable at any of the loads.

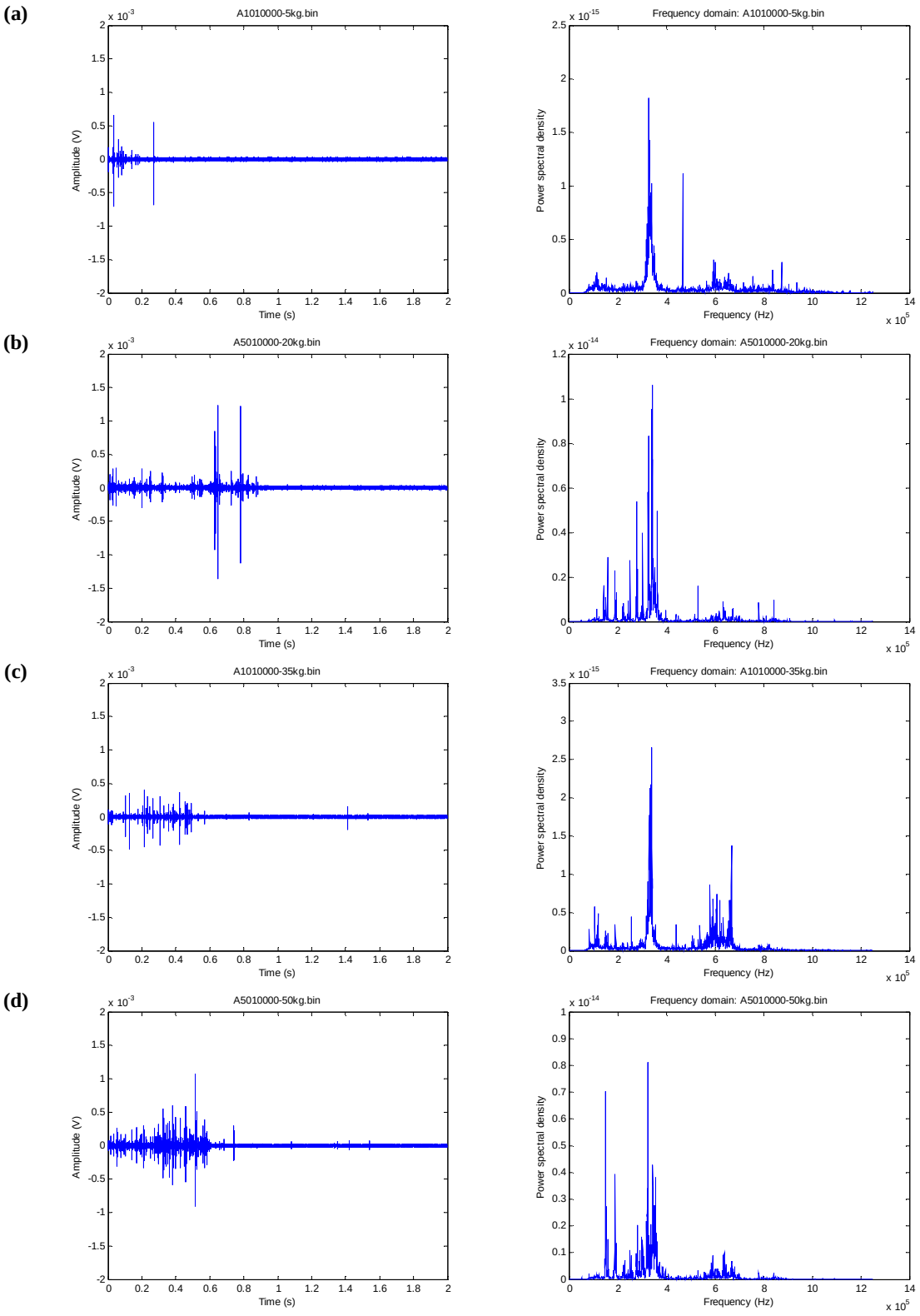

Figure 4.42 Typical AE signal structures (amplitude and frequency) during indentation at loads: (a) 49 N (b) 196 N (c) 343 N and (d) 490 N [HIPed HVOF (JetKote) WC-12%Co coatings].

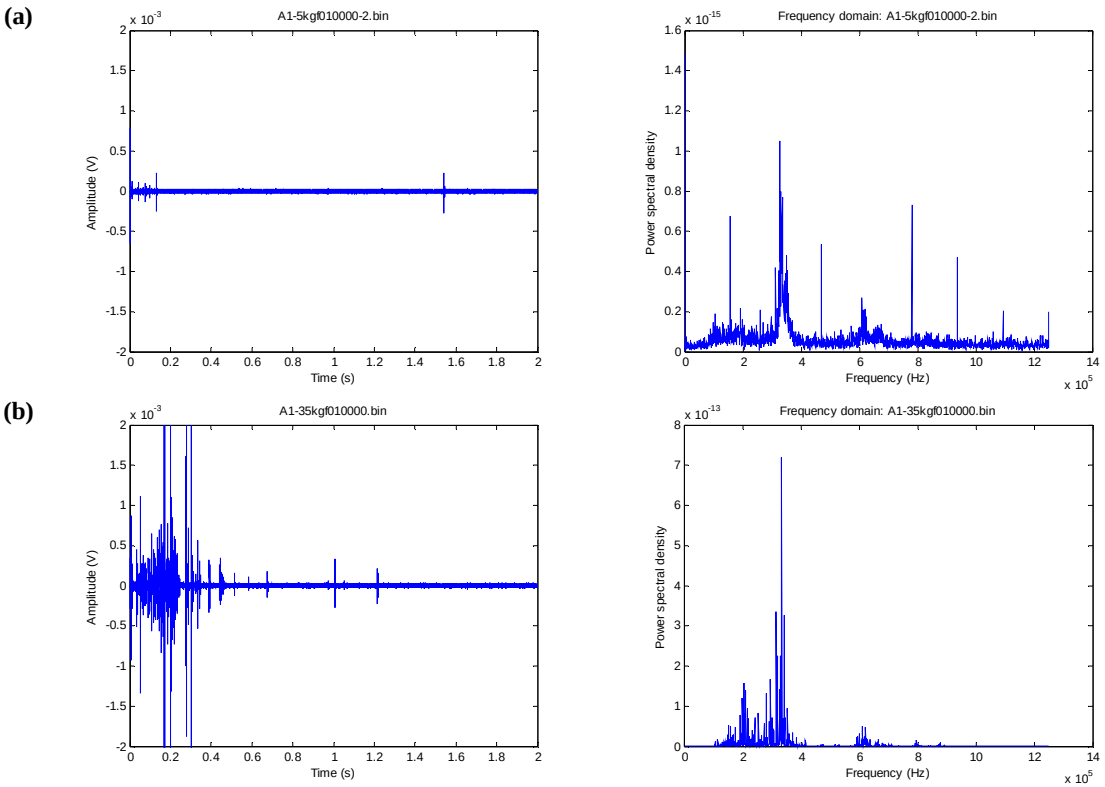

Figure 4.43 Typical AE signal structures (amplitude and frequency) during indentation of as-sprayed HVOF (JP5000) WC-10%Co-4%Cr coatings at loads: (a) 49 N and (b) 343 N [100 mm s^{-1} gun speed at high pressure, P1]

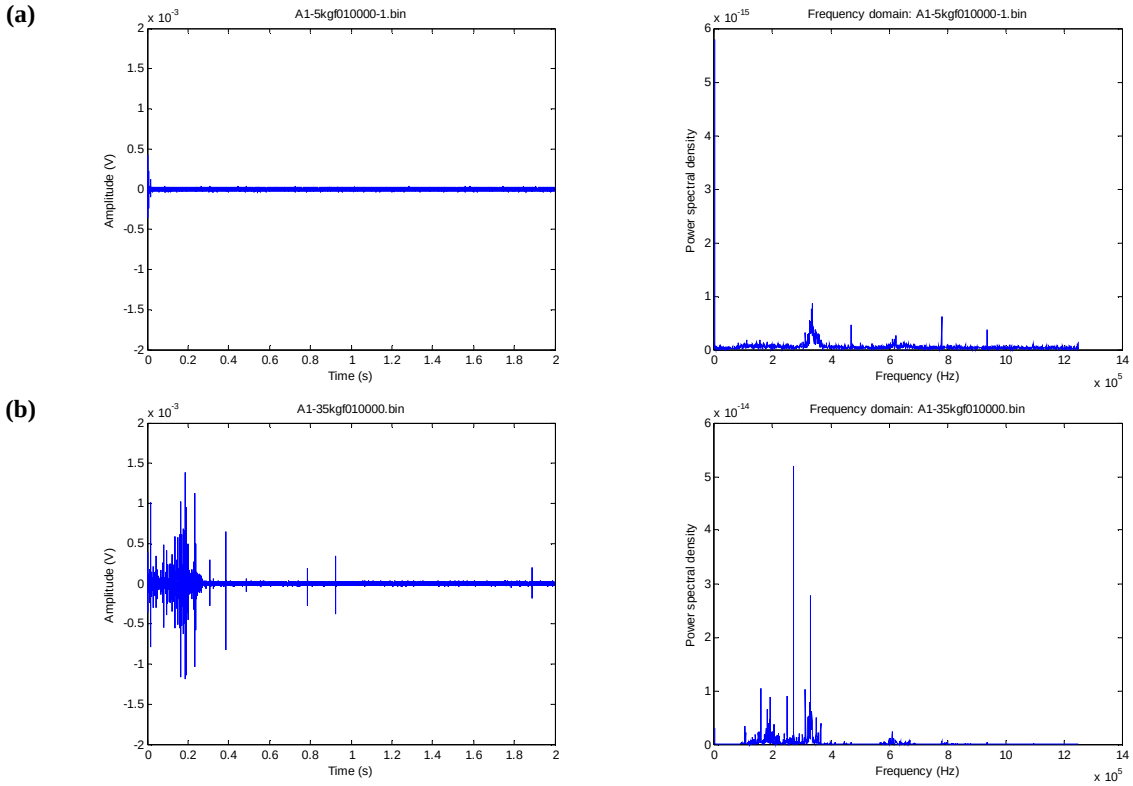

Figure 4.44 Typical AE signal structures (amplitude and frequency) during indentation of as-sprayed HVOF (JP5000) WC-10%Co-4%Cr coatings at loads: (a) 49 N and (b) 343 N [200 mm s^{-1} gun speed at low pressure, P2]

Figure 4.45 shows a more detailed representation of the AE signal time series for HIPed HVOF (JetKote) WC-12%Co and as-sprayed HVOF (JP5000) WC-10%Co-4%Cr coatings, both examples breaking the zoning criteria due to multiple crossings of the threshold. These signals are a contrast even to the example of as-sprayed coatings which does not meet the zoning criteria (**Figure 4.39a**).

Figure 4.46 shows the ratio of frequency power for HIPed HVOF (JetKote) WC-12%Co and as-sprayed HVOF (JP5000) WC-10%Co-4%Cr and it can be that the HIPed coating (and, possibly, the WC-10%Co-4%Cr) has a significantly higher high frequency component than other coatings (**Figure 4.41**). The ratio of low to high AE frequency does not show any pattern with indentation load.

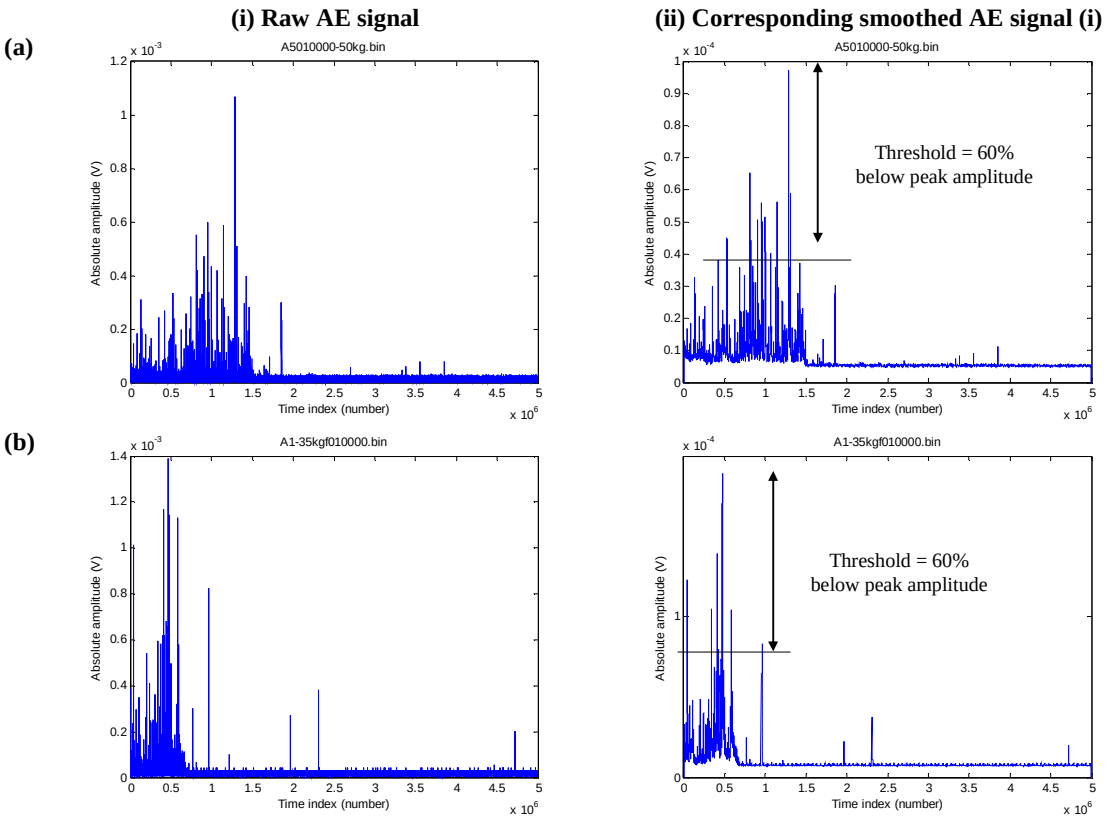

Figure 4.45 Absolute AE signal in time series from Figures 4.42 and 4.44: (a) 490 N (HIPed HVOF-JetKote WC-12%Co coatings) (b) 343 N (as-sprayed WC-10%Co-4%Cr, 200 mm s^{-1} gun speed at low pressure, P2), criteria of distinct zones broken due to more than one crossings of the threshold

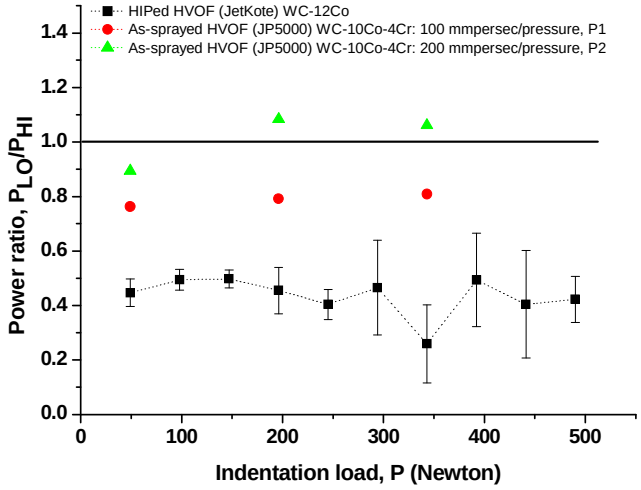

Figure 4.46 Power ratio [HIPed HVOF (JetKote) WC-12%Co, as-sprayed HVOF (JP5000) WC-10%Co-4%Cr]

4.2.4 AE features and total surface crack length

Figure 4.47 shows total surface crack length (*L*), total AE ring-down count (*R*), total AE energy (*E*) and total AE event duration (*T*) plotted against indentation load for as-sprayed HVOF (JetKote) WC-12%Co coatings. As can be seen, each of these features increases in roughly the same way with load.

Figure 4.48 shows the same AE features calculated for each of the three zones for each of the individual indentations. As can be seen from **Figures 4.48a, b, c**, it is zone C which shows the clearest increase in AE features with load. Focussing on AE energy, it can be seen, in particular, that the zone C energy increases quite steeply with load, and that it becomes the largest part of the AE indentation energy at loads above about 245 N. **Figure 4.48d** shows the total AE energy, and those for zones A, B and C plotted against total surface radial crack length, and again, it is clear that zone C energy gives the sharpest indication of radial crack length.

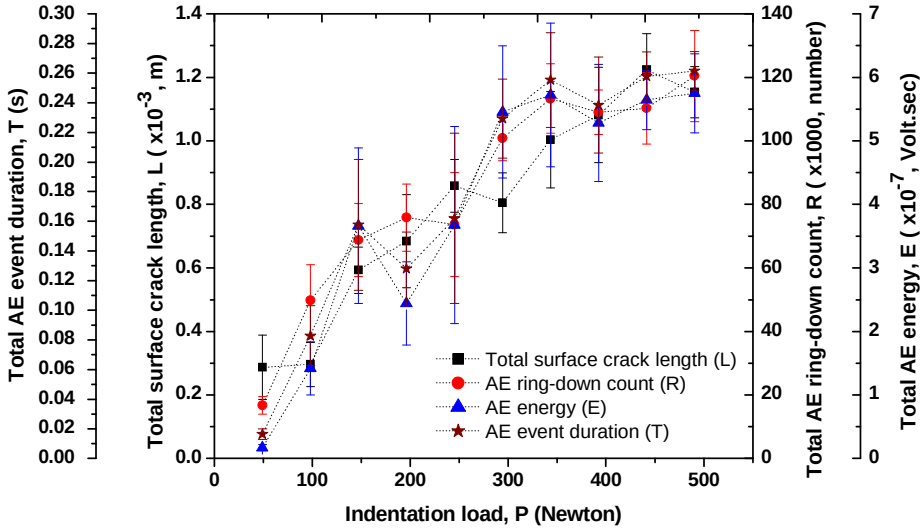

Figure 4.47 Effect of indentation load (P) on total surface crack length (L) and AE features [as-sprayed HVOF (JetKote) WC-12%Co coatings]

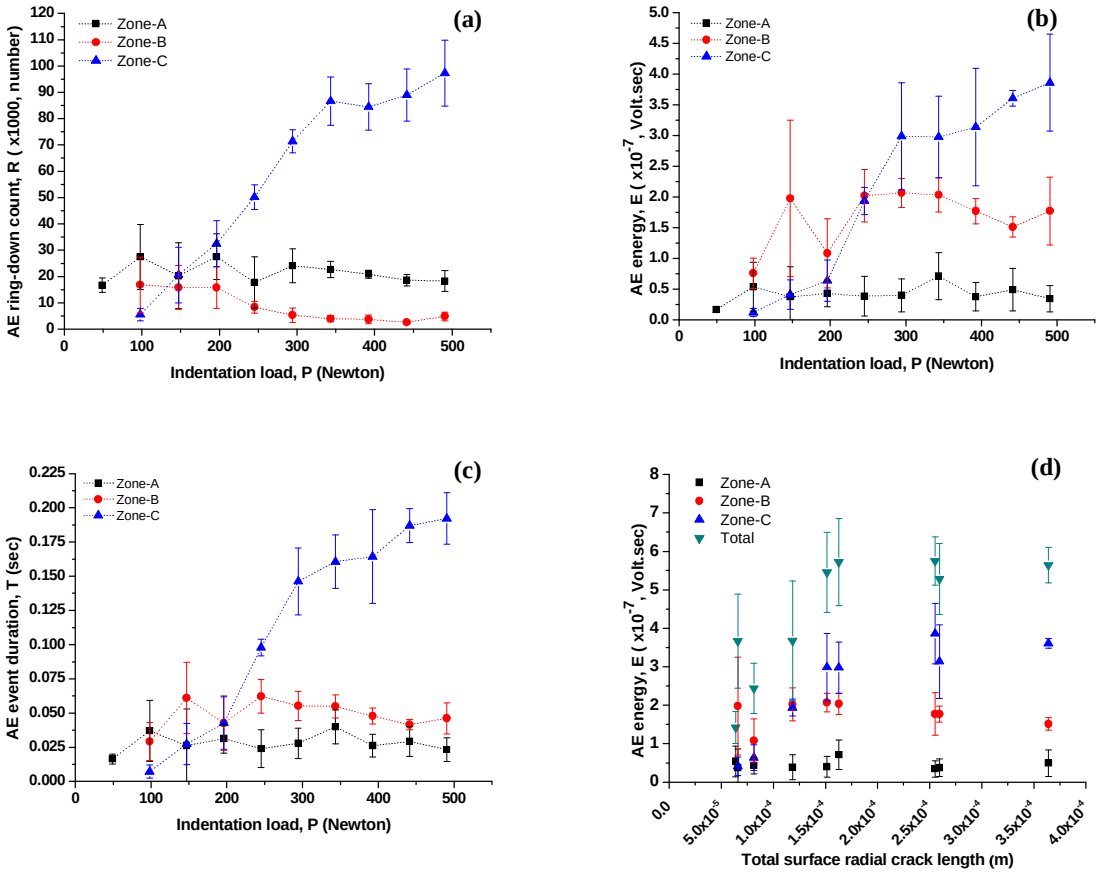

Figure 4.48 Zone AE features: (a) ring-down, *R*, (b) energy, *E* and (c) event duration, *T* *vs* indentation load for the zones shown in Figure 4.31**,** (d) AE energy of zone-A, B and C against total surface radial crack lengths [as-sprayed HVOF (JetKote) WC-12%Co coatings]

Figure 4.49 shows total surface crack length (*L*), total AE ring-down (*R*), total AE energy (*E*) and total AE event duration (*T*) against indentation load for HIPed HVOF WC-12%Co coatings and, as can be seen, all of the AE features broadly remain constant with load but increase between 343 N and 392 N, remaining roughly constant thereafter but with significant scatter.

Figure 4.50 shows total AE energy plotted against total surface crack length for HIPed HVOF (JetKote) WC-12%Co coatings, which shows a general positive correlation, although there is considerable scatter in each parameter for a given indentation load.

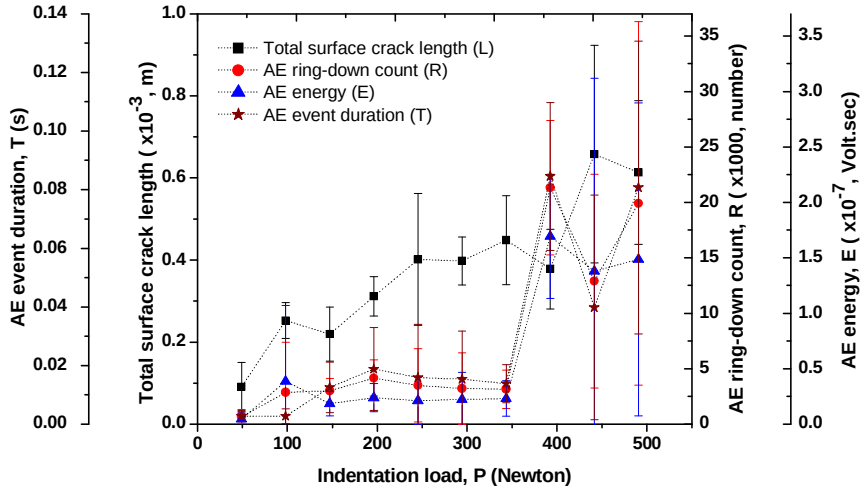

Figure 4.49 Effect of indentation load (P) on total surface crack length (L) and AE features [HIPed HVOF (JetKote) WC-12%Co coating]

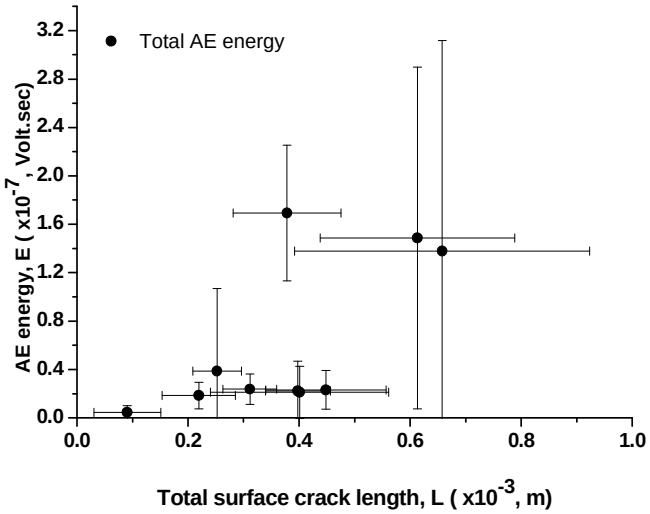

Figure 4.50 Total AE energy plotted against total surface crack lengths; (49 to 490 N) [HIPed HVOF (JetKote) WC-12%Co coating]

Figure 4.51 shows total AE energy (*E*) against indentation load for as-sprayed HVOF (JP5000) WC-10%Co-4%Cr coatings (only one indentation at each load and surface crack length was not measured). From the limited information, it seems that these coatings do not show any behaviour which can be distinguished from either the as-sprayed or HIPed WC-12%Co coatings.

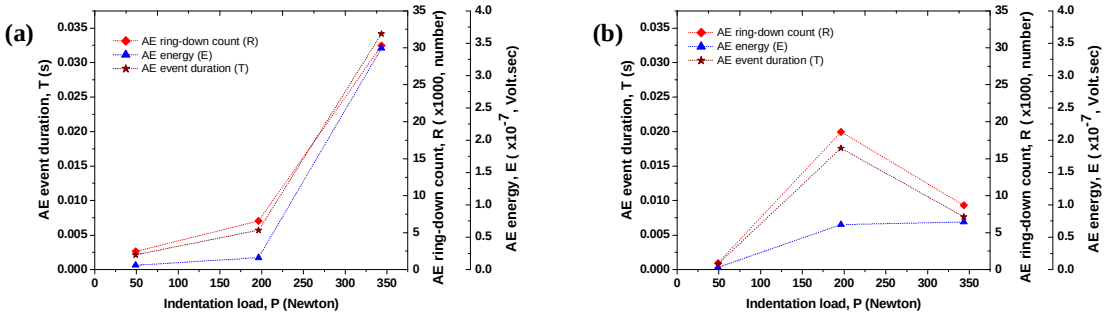

Figure 4.51 Effect of indentation load (P) on total AE features [as-sprayed HVOF (JP5000) WC-10%Co-4%Cr coatings]: (a) high pressure, P1 (with 100 mm sec^{-1} gun speed), (b) low pressure, P2 (with 200 mm sec^{-1} gun speed)

4.3 AE monitored Vickers indentation testing of Al_2O_3 coatings

This section presents the results for the microstructure, fracture pattern, and analysis of the raw AE signals and frequency spectrum of the APS (Metco, 9MB) Al_2O_3 and HVOF (theta gun) Al_2O_3 coatings. The analysis of the AE signals again follows the findings of *Section 4.1* in that AE features are calculated per zone in cases where zones can be identified and the total AE features are calculated for all indentations.

4.3.1 Microstructural characterisation

The processed powders used had size ranges of 10-45 µm for the APS Al_2O_3, and 1-5 µm for the HVOF Al_2O_3 coatings. Both of the powders had an angular and irregular morphology **Figures 4.52a, b**. The SEM images of the sprayed surface (**Figures 4.52c, d**) show that the molten alumina droplets have spread significantly and it is not possible to distinguish any non molten or semi molten particles. The coating cross-sections (**Figures 4.52e, f**) show a higher porosity for the APS Al_2O_3 (conventional) than HVOF Al_2O_3 (fine powder). The liquid nitrogen freeze fracture images (**Figures 4.52g, h**) show the splats, porosity, and some through thickness linear cracks in the coating. The splat size appears to be similar in the two coatings despite the very different powder sizes, and the splats appear more lamellar but less cohesive in the APS material.

XRD analysis (*Appendix E*: Figures E.7 and E.9) shows the two alumina powders to consist essentially of corundum (α-Al_2O_3). The pattern of the APS Al_2O_3 (conventional

powder) coating (*Appendix E:* Figure E.8) shows it predominantly to contain γ-Al_2O_3 (due to rapid solidification) with some corundum, presumably due to partial melting of the powder. The pattern of the HVOF Al_2O_3 (fine powder) coating (*AppendixE*: Figure E.10) shows it predominantly to contain corundum with very little γ-Al_2O_3.

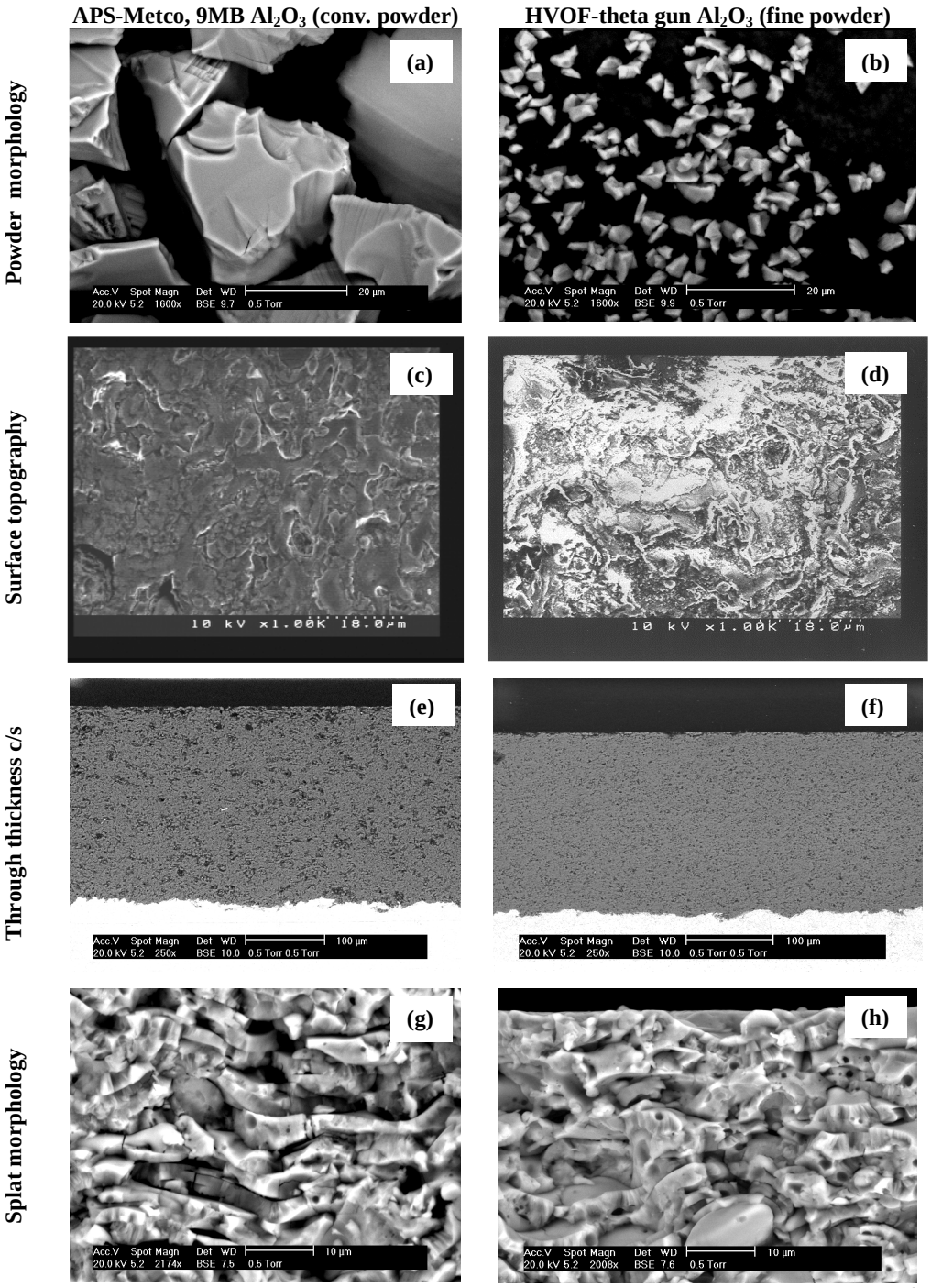

Figure 4.52 Al_2O_3 powder and coatings: (a) and (b) powders, (c) and (d) typical surface topographies exhibiting definite splat morphologies with densely packing splats, (e) and (f) through thickness coating cross-sections (g) and (h) liquid nitrogen freeze fracture image of coating splat morphologies, revealing splats, presence of porosity, and through thickness linear cracks

4.3.2 Vickers indentation derived properties

SEM observation of the indentations of the Al_2O_3 coatings revealed two strikingly different responses, **Figure 4.53**. The indentations of the APS Al_2O_3 (conventional) coatings showed a high degree of crushing fracture and spallation and the pyramidal impressions were barely discernible in contrast to all the other coated specimens examined. Because of the nature of the cracks (meshed and spalled asymmetrically around indentations), it was not possible to measure crack lengths either using the direct straight line or profiling method for the APS Al_2O_3 coatings. In contrast, the HVOF coated indented samples showed visible radial cracking from all four corners at all loads, and the surface fracture pattern included edge cracks around the indentation. Surface crack lengths were measured as described for the other coatings.

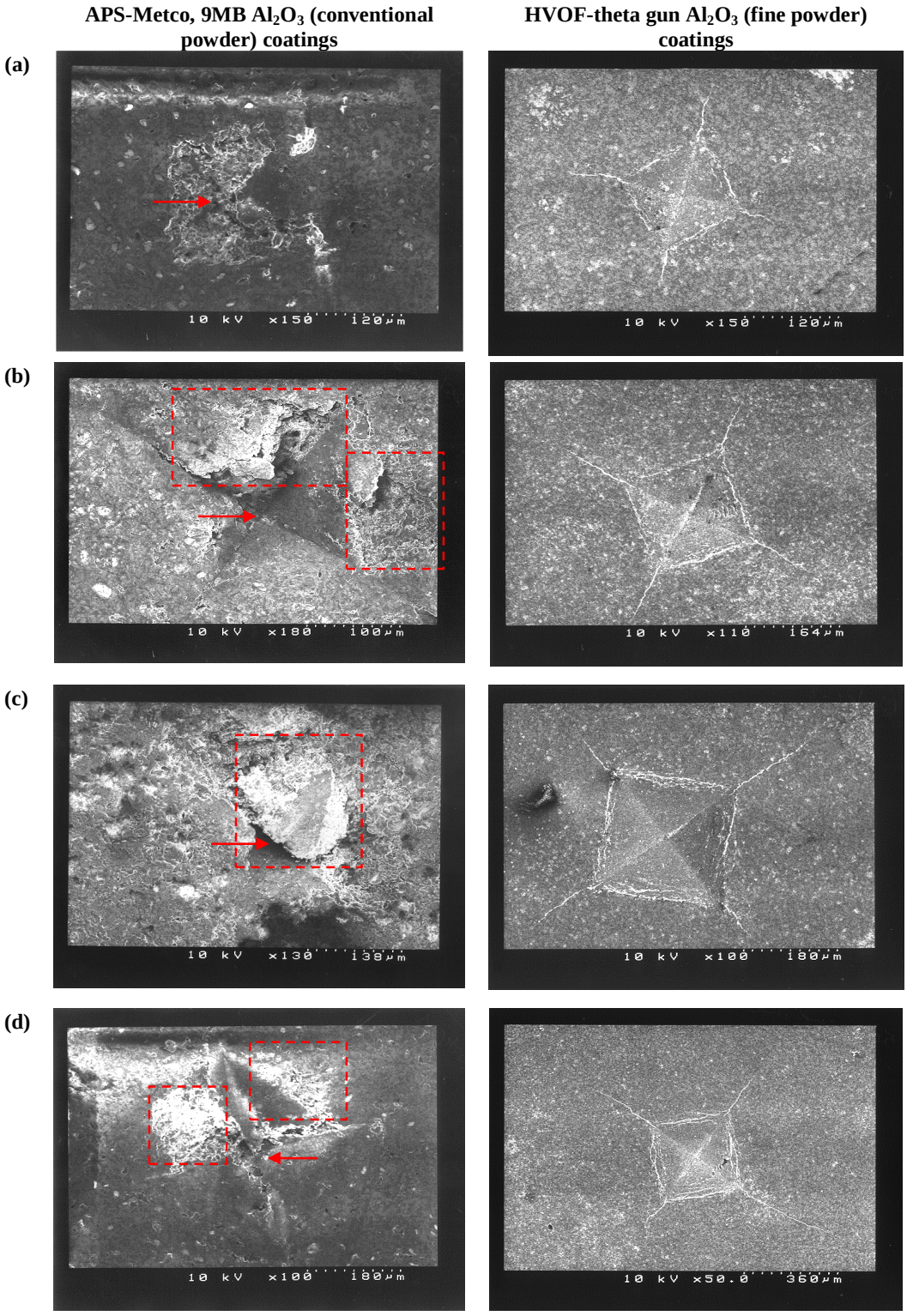

Figure 4.53 SEM images showing typical Vickers indentation cracking patterns of Al_2O_3 coatings at loads (a) 98 N (b) 245 N (c) 392 N and (d) 490 N [Arrows indicate centre of indentation for APS coatings and red dotted rectangles indicate area of spallation]

Although the quality of the image was poor under the optical microscope, indentation diagonals could be measured sufficiently to determine the macrohardness values. The resulting average values of the five indentations at each load along with the microhardness (five indentations) as shown in **Table 4.2**. As can be seen, the hardness values are essentially the same for both coatings and, as before, the macrohardness is somewhat lower than the microhardness and this is consistent with a decrease in hardness with increasing load.

Table 4.2 Vickers indentation hardness of Al_2O_3 coatings

Materials	**Microhardness ($HV_{1.96\ N}$)** (Gold Sputtered)	**Macrohardness** (Gold Sputtered)
APS-Metco, 9MB conventional Al_2O_3 coatings	683±38	588 ± 42 $HV_{98\text{-}490\ N}$
HVOF-theta gun fine powder Al_2O_3 coatings	632±29	584 ± 64 $HV_{98\text{-}490\ N}$

4.3.3 AE signals

Figure 4.54 shows the number of indentations which exhibited clear AE zones (criteria described in **Figure 4.26**), with 32 of the 45 APS and 39 of the 45 HVOF indentations showing zoning.

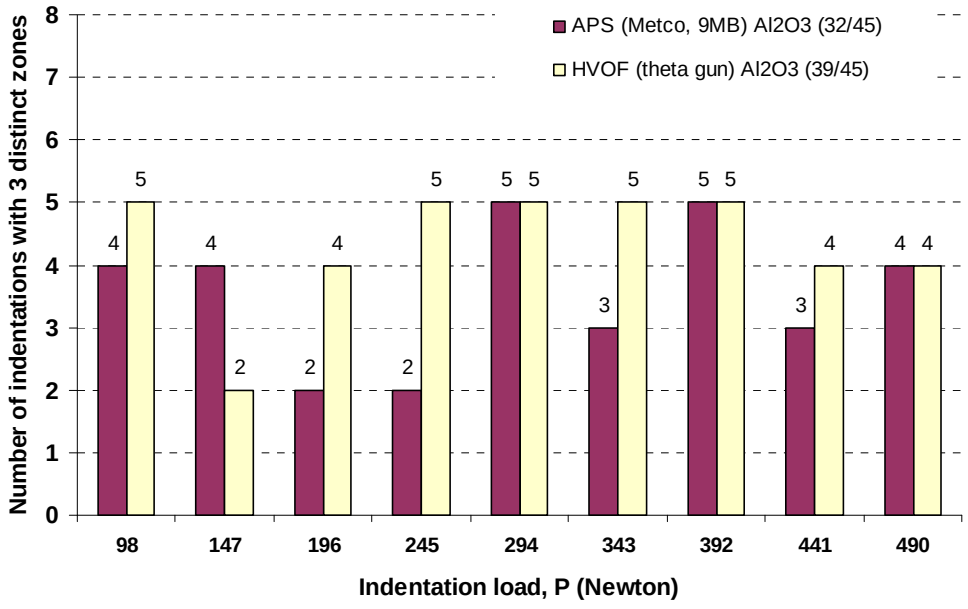

Figure 4.54 Al_2O_3 coatings: Number of indentations with distinct AE zones A, B and C

Figures 4.55 and **4.56** and **Figures 4.57** and **4.58** show time series and spectra for example indentations on the APS and HVOF Al_2O_3 coatings, respectively. These data

were treated in the same way as those for the other coatings and the summary plots of AE features are shown later in the section.

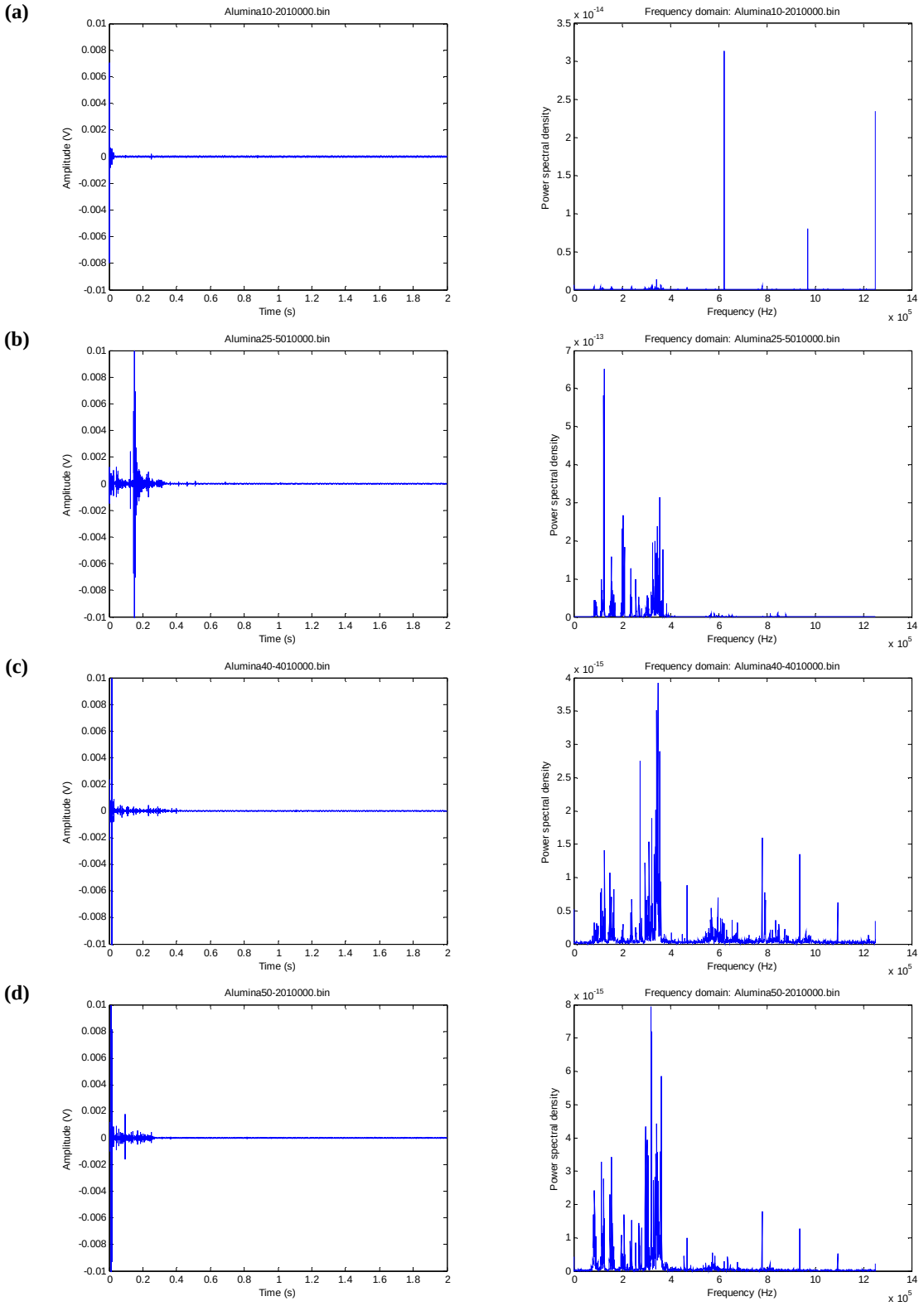

Figure 4.55 Example AE signal structures (amplitude and frequency) during indentation of APS-Metco, 9MB Al_2O_3 (conventional) coatings at loads: (a) 98 N (b) 245 N (c) 392 N and (d) 490 N

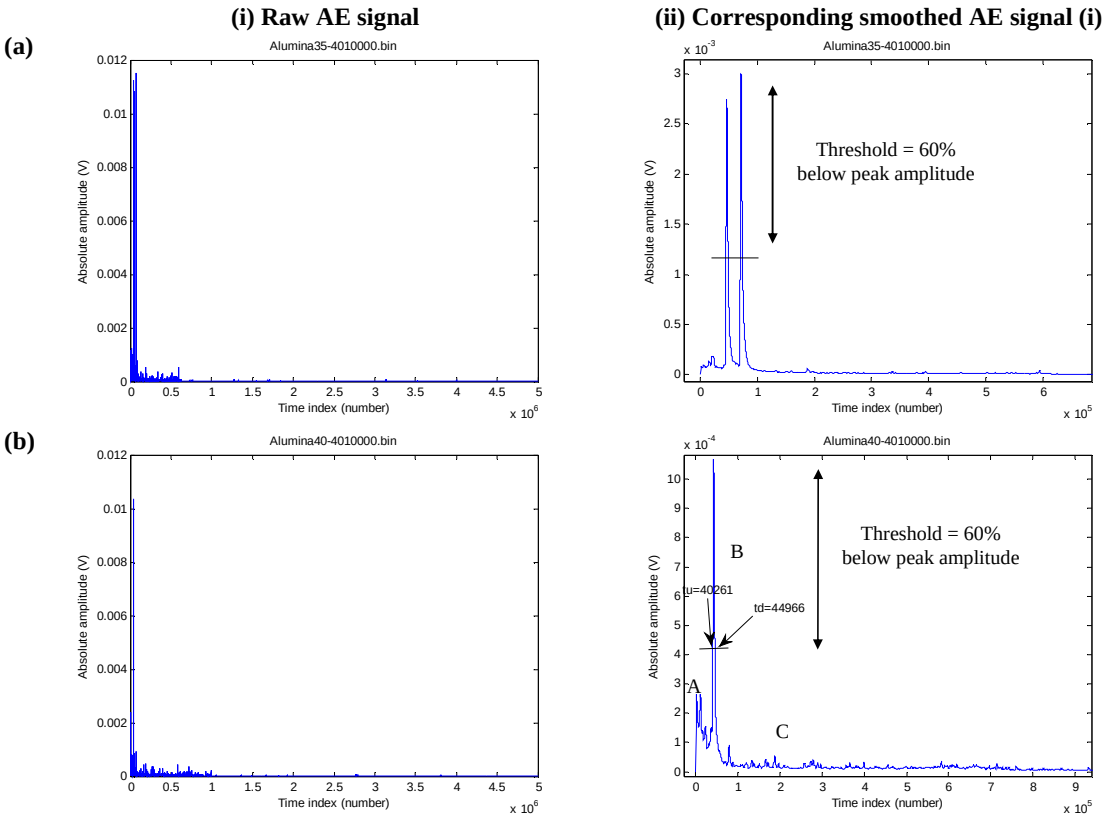

Figure 4.56 Absolute AE signal time series (APS-Metco, 9MB Al_2O_3 conventional coatings): (a) 392 N (criteria of distinct zones broken due to more than one crossings of the threshold), (b) 392 N (showing all three zones-A, B and C from Figure 4.55c)

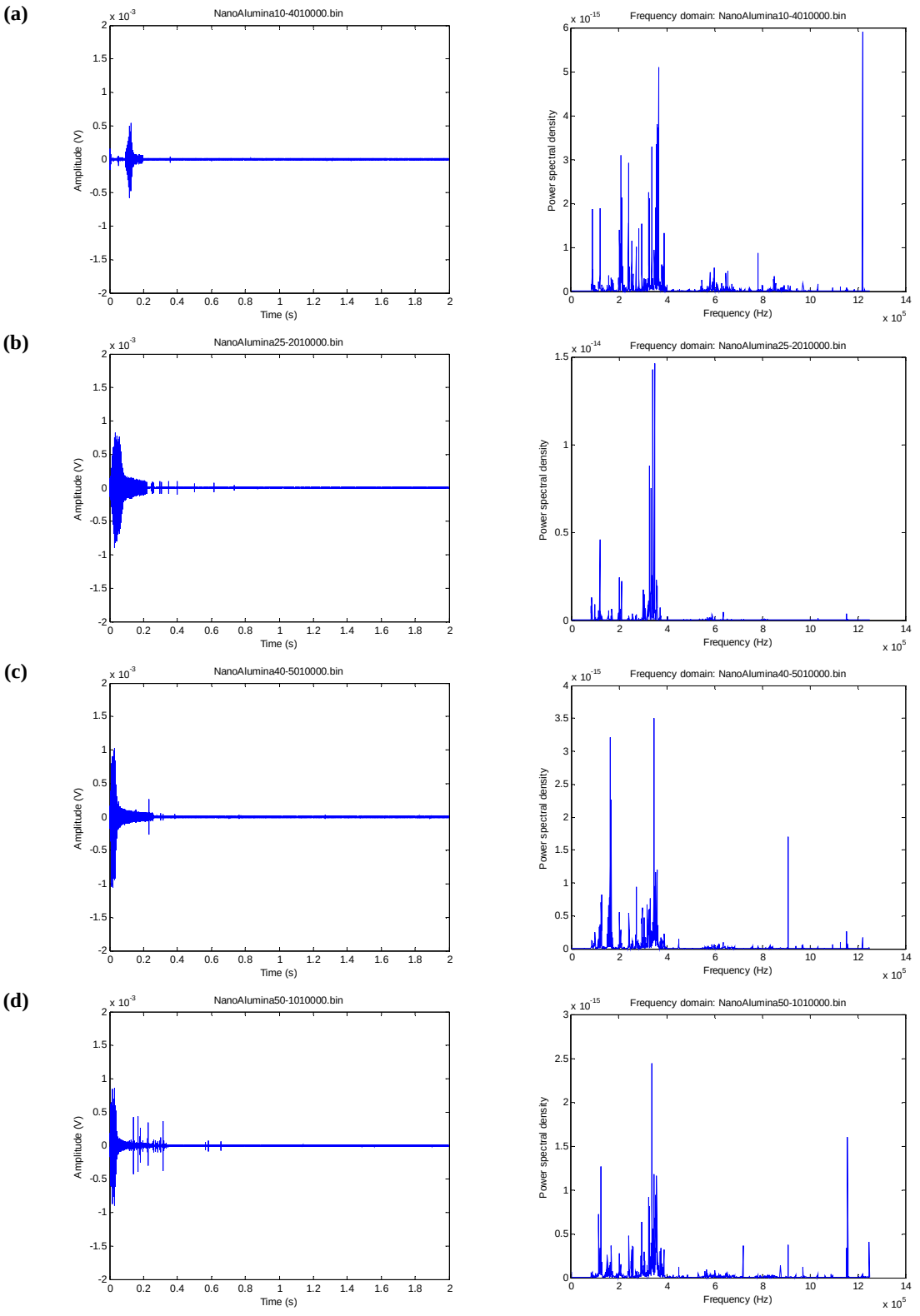

Figure 4.57 Example AE signal structures (amplitude and frequency) during indentation of HVOF-theta gun Al_2O_3 (fine powder) coatings coatings at loads: (a) 98 N (b) 245 N (c) 392 N and (d) 490 N

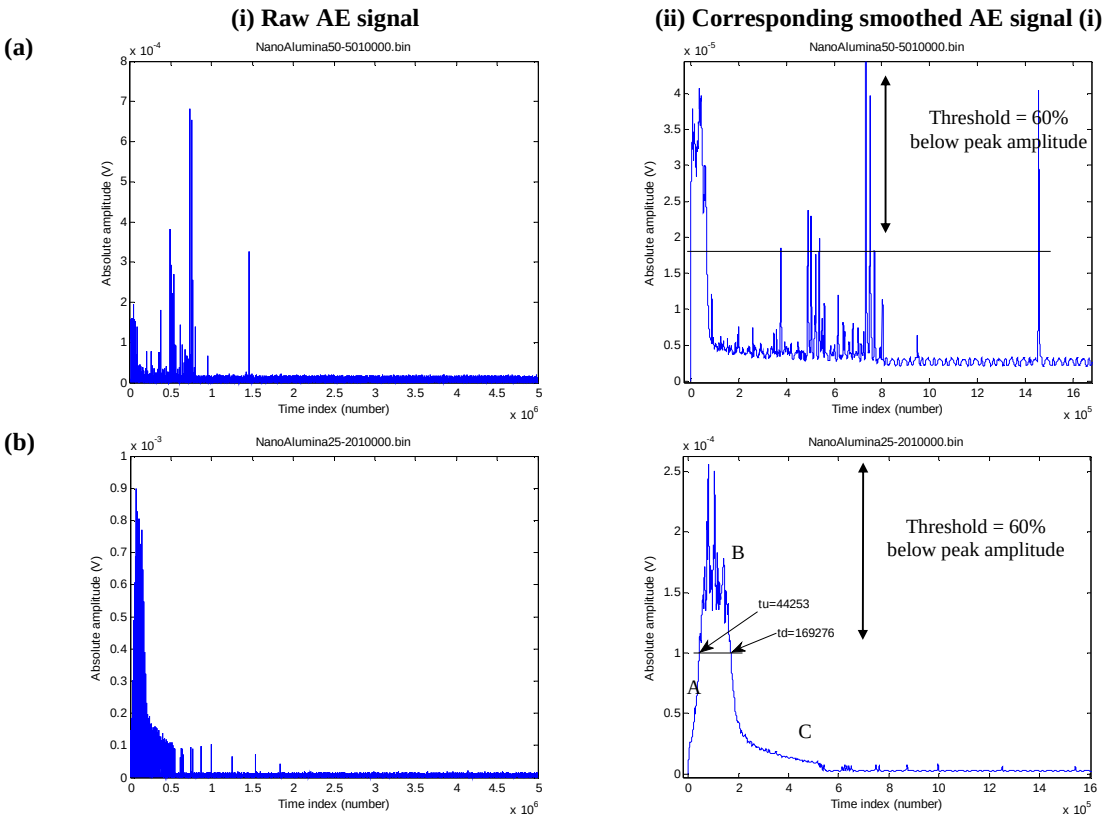

Figure 4.58 Absolute AE signal time series (HVOF-theta gun Al_2O_3 fine powder coatings): (a) 490 N (criteria of distinct zones broken due to more than one crossings of the threshold), (b) 245 N (showing all three zones-A, B and C from Figure 4.57b)

Figures 4.59 and **4.60** show the ratio of power in the low frequency band (0-250 kHz) to the power in the high frequency band (250-750 kHz) for APS and HVOF Al_2O_3, respectively. Again, the ratio for the whole AE series remains around unity and does not show any particular pattern with load, except for a possible trend towards increasing ratio with load in the APS coating.

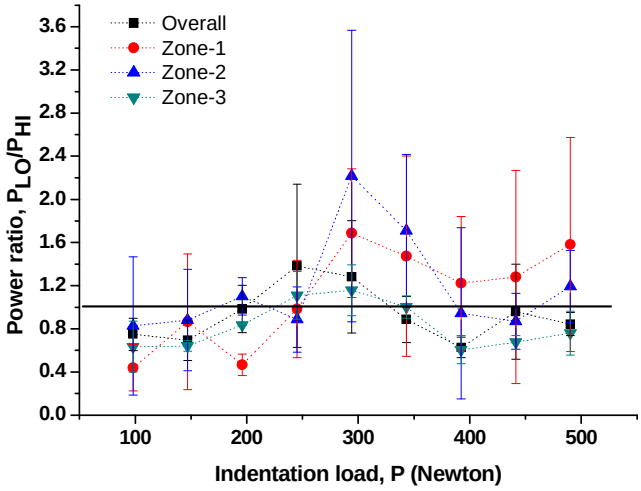

Figure 4.59 Power ratio in APS-Metco, 9MB Al_2O_3 (conventional) coatings

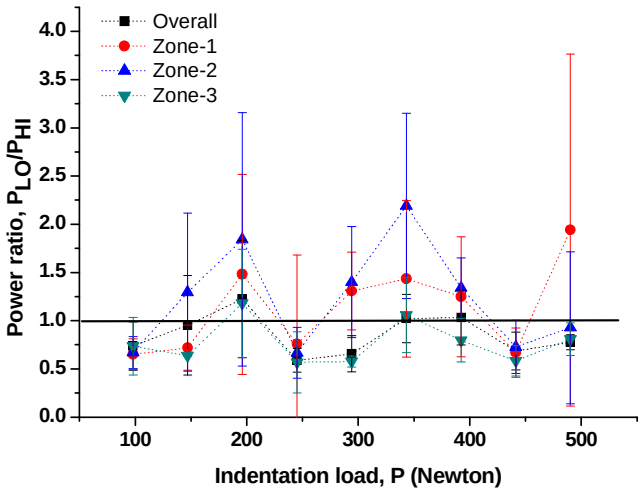

Figure 4.60 Power ratio in HVOF-theta gun Al_2O_3 (fine powder) coatings

Figure 4.61 shows total AE ring-down count (*N*), total AE energy (*E*) and total AE event duration (*T*) against indentation load for APS Al_2O_3 (conventional) coatings and, as can be seen, each of these features shows a rather complex variation with load. The pattern for AE energy for those signals which could be zoned (**Figure 4.62**) was not much clearer.

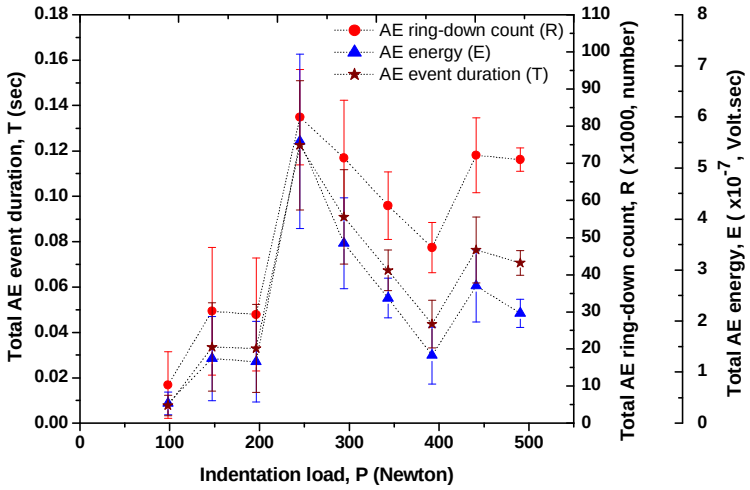

Figure 4.61 Effect of indentation load AE features [APS-Metco, 9MB Al_2O_3 (conventional) coatings]

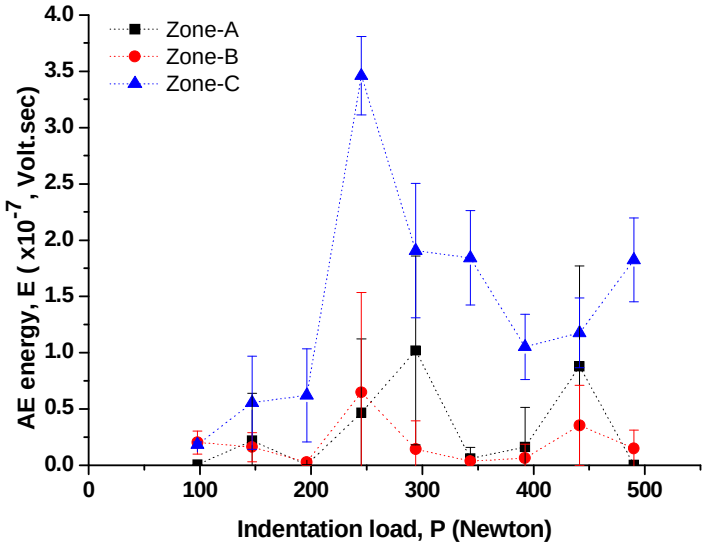

Figure 4.62 Zone AE features: (a) ring-down, *R*, (b) energy, *E* and (c) event duration, *T* *vs* indentation load [APS-Metco, 9MB Al_2O_3 (conventional) coatings]

4.3.4 AE features and total surface crack lengths

Figure 4.63 shows total surface crack length (*L*), total AE ring-down count (*R*), total AE energy (*E*) and total AE event duration (*T*) against indentation load for the HVOF-theta gun Al_2O_3 (fine powder) coatings and, as can be seen, none of the AE features show a particular pattern with load, although the total surface crack length increases in an approximately linear fashion.

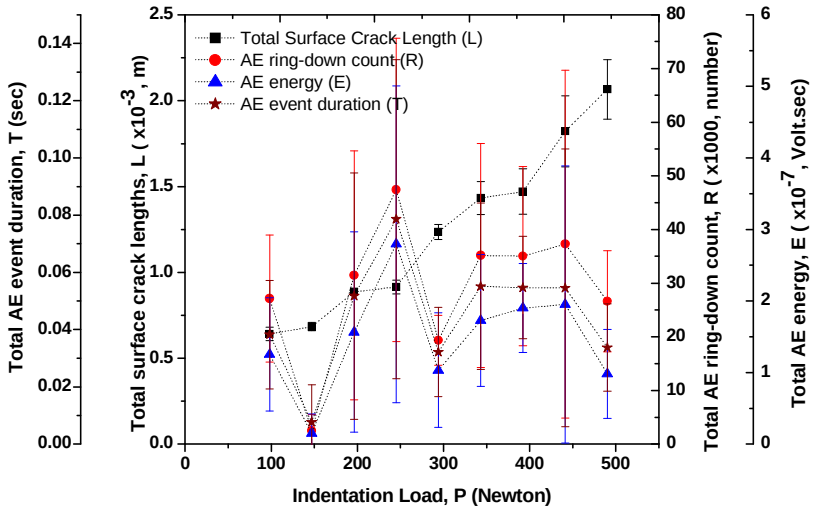

Figure 4.63 Effect of indentation load on total surface crack length (L) and AE features [HVOF-theta gun sprayed Al_2O_3 (fine powder) coatings]

Figure 4.64 shows the AE energy separated between the three zones. Again, the AE energy does not show a particular pattern with load, but, in common with other materials, the zone C energy becomes the largest part of the AE indentation energy at higher loads.

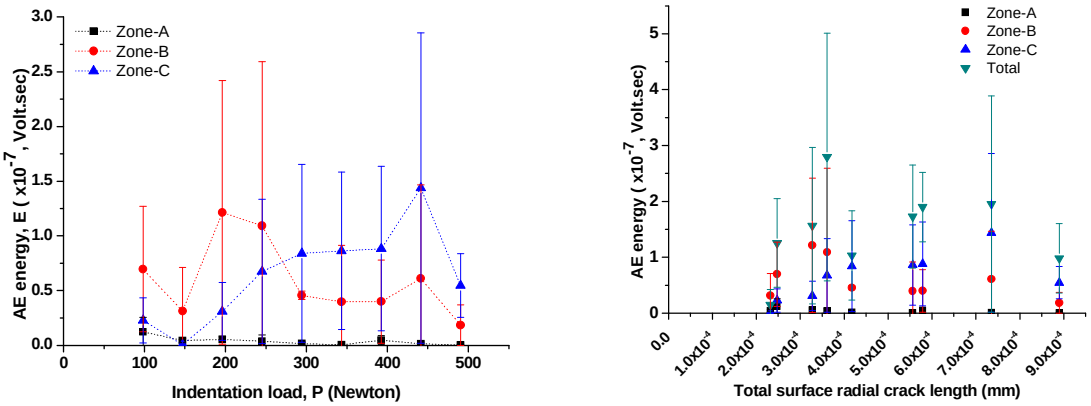

Figure 4.64 Zone AE energy: (a) zone energy, *E vs* indentation load, and (b) zone energy, *E vs* total surface radial crack length [HVOF-theta gun Al_2O_3 (fine powder) coatings]

4.4 AE monitoring of HVOF thermal spraying process

This section deals with the AE signals recorded during HVOF (TAFA JP5000) spraying of WC-10%Co-4%Cr powder. As with the monitoring of indentations, the AE signals were acquired at full bandwidth so that spectral analysis could be carried out on the raw signal and also so that time domain characteristics could be examined up to the waveform resolution.

4.4.1 AE noise during spraying process

To differentiate between the signals generated due to flame noise and powder particle impact, three reference conditions were used, those being (a) spraying with flame and powder particles not directed at the sample (b) spraying with flame only onto the sample (no powder), and (c) spraying with flame only not directed at the sample. **Figure 4.65** shows time and frequency domain plots of a 2-second record taken under each conditions (a), (b) and (c). The raw AE spectra all show similar characteristics with distinct spikes below the analogue filter frequency of 100 kHz. To investigate the low frequency characteristics of the signals, it was averaged over 10000 points using a root-mean square (rms) algorithm (i.e demodulation). The results (**Figure 4.66**) show a characteristic frequency of 100 Hz. The rms values of entire 2 second records for conditions (a), (b) and (c) were 5.579×10^{-4} V.s, 5.387×10^{-4} V.s and 5.642×10^{-4} V.s. The similarity of the characteristics of the three conditions suggests that the background noise is largely airborne.

Accordingly, the remaining analysis is carried out on data which has been high-pass filtered at 200 kHz. The effect of this filtering can be seen in **Figure 4.67**, which show averaged (rms averaging time of 0.004 s) signal spraying through a slit alongside inter-pass background before and after filtering. The 100 Hz periodicity is clearly visible in the filtered signal and filtering breaks down the periodicity and reduces the rms noise by a factor of about 3 whilst only reducing the signal by a factor of about 0.8 (i.e. about a factor of 2.5 improvement in signal-to-noise ratio, SNR).

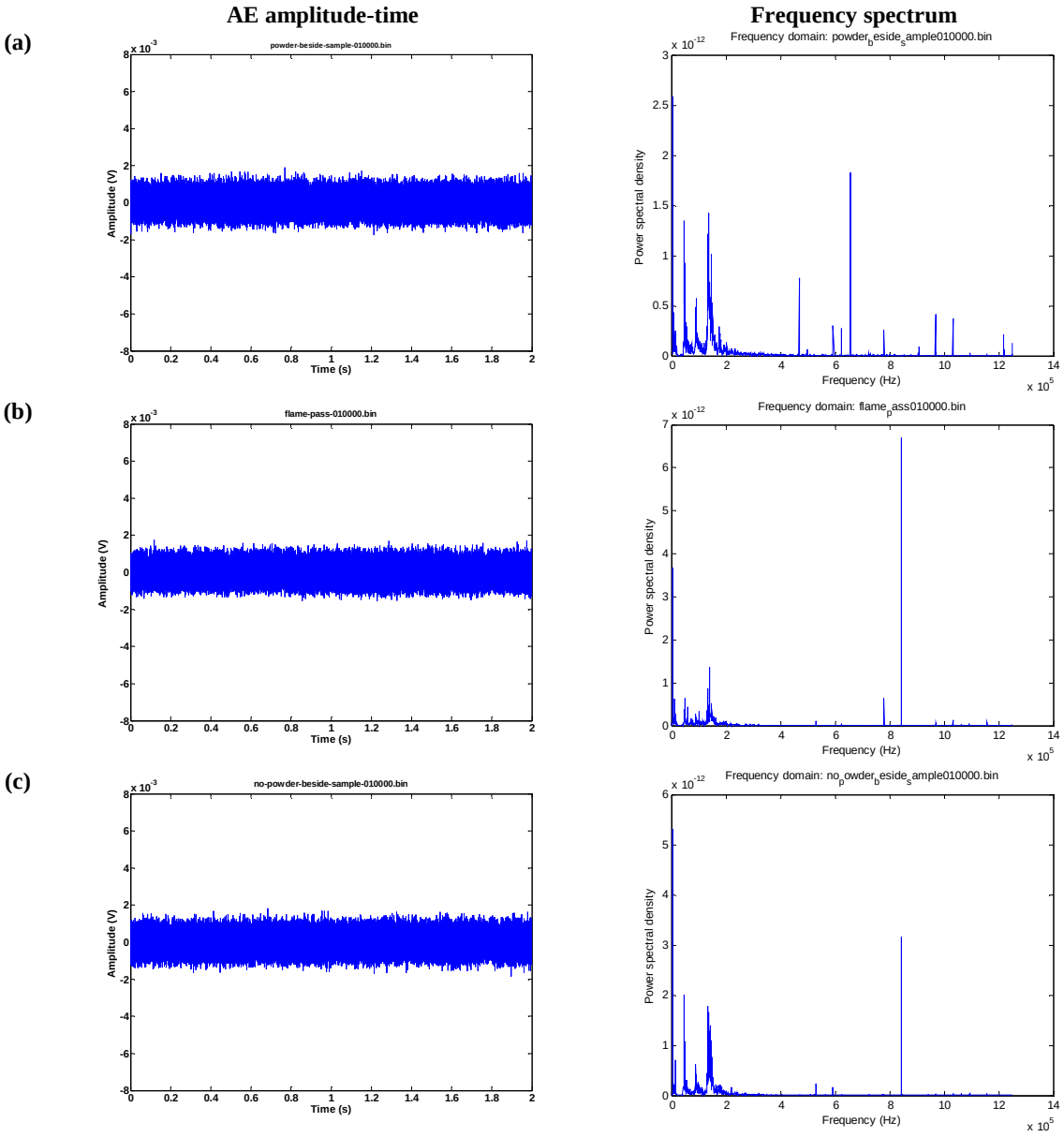

Figure 4.65 AE signal structure (amplitude and frequency) for 2 seconds noise record during HVOF WC-10%Co-4%Cr spraying: (a) spraying with flame and powder particles not directed at the sample (b) spraying with flame only onto the sample (no powder), and (c) spraying with flame only not directed at the sample.

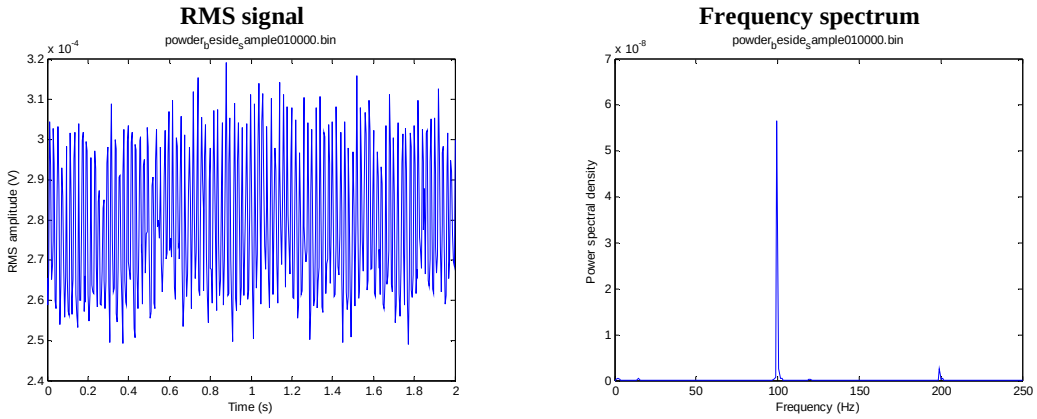

Figure 4.66 RMS signal structure (amplitude and frequency) for 2 second noise record during HVOF WC-10%Co-4%Cr spraying with flame and powder particles not directed at the sample (from Figure 4.65a)

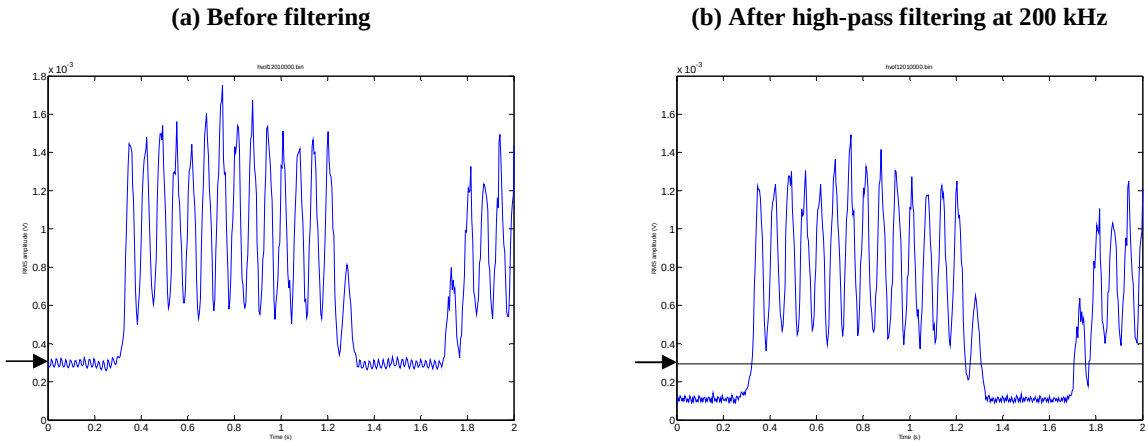

Figure 4.67 AE signal recorded during HVOF WC-10%Co-4%Cr full spraying (both flame and powder) onto substrate through slit-A (3 mm × 10 mm) at 500 mm sec^{-1}: (a) RMS signal before filtering, and (b) RMS signal after high-pass filtering at 200 kHz.

4.4.2 AE from thermal spraying through slits

Figure 4.68a shows two examples of high-pass filtered signals for spraying directly onto the substrate through a set of slits. Pulses of amplitude around 0.6-0.7 mV (high pressure, P1) and 0.3-0.4 mV (low pressure, P2), are clearly visible above an inter-pass background of amplitude around 0.2 mV.

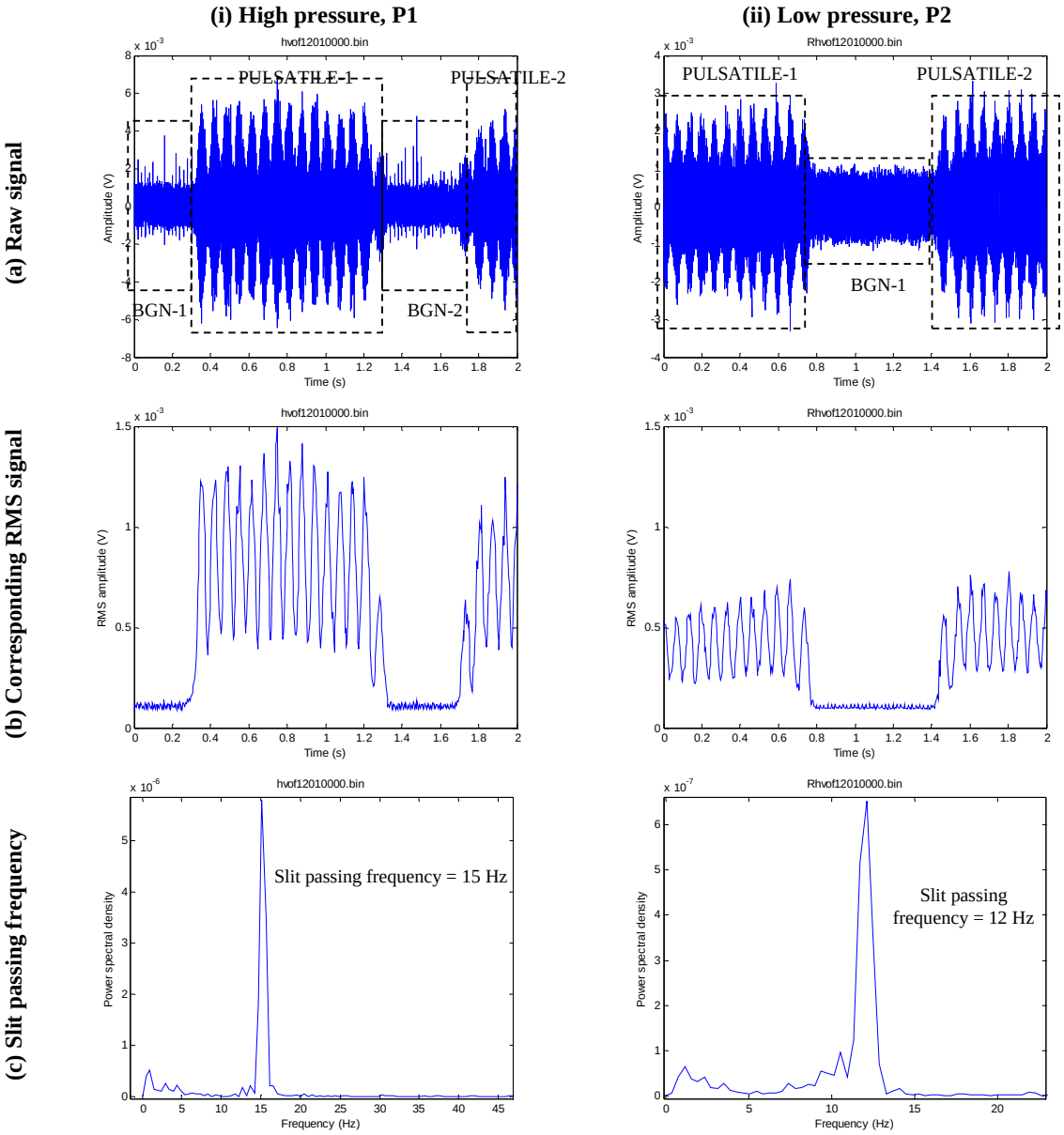

Figure 4.68 AE signal recorded during HVOF WC-10%Co-4%Cr full spraying (both flame and powder) onto substrate through slit-A (3 mm × 10 mm) at 500 mm sec^{-1}, (Background section-BGN, PULSATILE sections)

As expected, different temporal structures for the AE were detected when spraying through slits of different size, the example of slit-A (3 mm wide) is being shown in **Figure 4.68a**. Every pulse in the AE signal corresponds to the position of a slit, there being 14 pulses per traverse of the specimen. Because the record length is 2 seconds (i.e. 2 layers at 500 mm sec^{-1} gun speed), the second group of pulses is associated with the return of the gun on its subsequent traverse, the gap between the two groups being associated with the slit offset distance of 150 mm. Each pulse also shows a gradual increase in amplitude followed by a fall associated with the passage of the circular spray spot across the slit. **Figure 4.68a** (column ii) also shows that the AE amplitude

decreases by almost half when spraying across the same 14 slits if the pressure is reduced by 25%. **Figure 4.68b** shows the corresponding rms signals (10000-point average) and **Figure 4.68c** shows the slit-passing frequency determined from the pulsatile sections.

4.4.3 Correlation between process parameters and signal-to-noise ratio

Varying the gun transverse speed should alter the sprayed particle flux per unit area (given slit width) landing on to the substrate, and increasing the slit width should increase the total flux landing on the substrate in one pass. In order to examine the strength of the high-pass filtered signals and its variation with process parameters, the signal-to-noise ratio (SNR) was calculated using equation: $SNR = \frac{RMS_{pulsatile}}{RMS_{pulsatile+noise} - RMS_{pulsatile}}$, where $RMS_{pulsatile}$ and $RMS_{pulsatile+noise}$ correspond to RMS of slit-passing sequences and overall signal, respectively. The SNR shown in **Figure 4.69** plotted against slit width for each of the process parameters. As expected, the SNR increases with increase in the width of the slit, spraying pressure and decreases with increasing gun transverse speed.

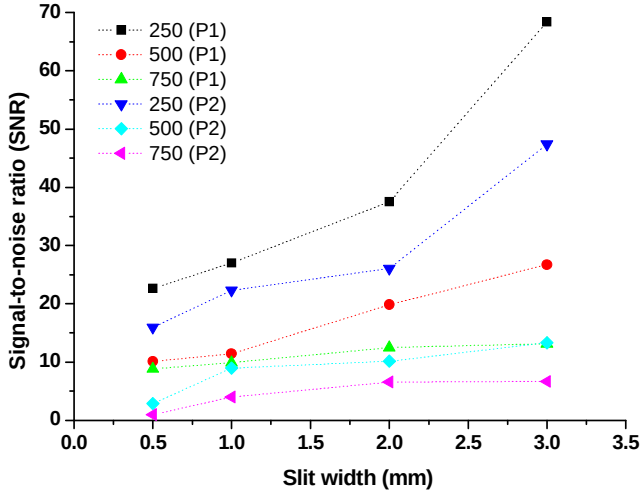

Figure 4.69 Signal-to-noise ratio against slit width for varying speed and pressure

4.5 Summary of the experimental test results

4.5.1 Fully instrumented indentation of materials

Force-displacement profiles are essentially bilinear with two characteristic slopes separated by a distinct arrest for all loads above 98 N. Comparison of experimental and geometrical indentation depths is useful in identifying the material accommodation mechanism (i.e. 'piling-up' or 'sinking in'). The force-displacement curve indicates three distinct loading stages (I, II and III) and the stage III mechanical energy increases with loads. Plastic deformation in copper and aluminium produced little or no AE, whereas hardened steel and thermally sprayed ceramic coatings produced significant amounts of AE, which generally increased with total indentation mechanical energy. About 66% of the hardened steel indentations but only about 18% of the as-sprayed HVOF (JP5000) WC-12%Co indentations exhibited an AE record that could be separated into distinct zones. Where zoning was possible the AE corresponding to a zone correlated well with the AE associated with a loading stage.

4.5.2 AE signal during Vickers indentation of thermally sprayed coatings

Those indentations exhibiting clear zones (A, B and C), the AE features in zone C becomes the largest part of the AE at higher loads for coating materials such as as-sprayed HVOF (JetKote) WC-12%Co, APS (Metco, 9MB) Al_2O_3 (conventional powder), HVOF (theta gun) Al_2O_3 (fine powder). For HIPed HVOF (JetKote) WC-12%Co, as-sprayed HVOF (JP5000) WC-10%Co-4%Cr coatings, individual AE peaks are not evenly spaced and are all of irregular amplitude, and similar characteristics was seen for all loads, and no distinct zones were separable at any of the loads. The ratio of power in the low frequency band (0-250 kHz) to the power in the high frequency band (250-750 kHz) for the whole AE series and for each of the zones largely remains constant with loads. HIPed HVOF (JetKote) WC-12%Co as well as as-sprayed HVOF (JP5000) WC-10%Co-4%Cr has significantly higher high frequency component than other carbide coatings. .

4.5.3 Vickers indentation fracture pattern of thermally sprayed coatings

The surface fracture pattern of as-sprayed HVOF (JP5000) WC-12%Co, as-sprayed HVOF (JetKote) WC-12%Co and HVOF (theta gun) Al_2O_3 (fine powder) includes radial cracks at the four corners, edge cracks, ring cracks and other small cracks around

the indentation. In contrast, the HIPed HVOF (JetKote) WC-12% Co and as-sprayed HVOF (JP5000) WC-10%Co-4%Cr coatings showed only edge cracks and other small cracks around the indentation with no visible radial cracking at any of the loads. The surface fracture pattern APS (Metco, 9MB) Al_2O_3 (conventional powder) coatings showed a high degree of crushing fracture and spallation and its pyramidal impression was badly discernible in contrast to all the other coated specimens examined. Those coating materials with visible surface cracks measured show approximately linear increase with loads. Cross-sectional views around indentation for the as-sprayed HVOF (JetKote) WC-12%Co coating produced, there appears to be areas with sub-surface densification, lateral mesh of cracks and lateral delamination cracks.

4.5.4 AE monitoring during HVOF thermally spraying

The raw AE spectra of background noise during HVOF (JP5000) WC-10%Co-4%Cr thermal spraying show similar characteristics with distinct spikes below the analogue filter frequency of 100 kHz, and the characteristic frequency for air borne noise record at 100 Hz. The SNR increases with increase in the width of the slit, spraying pressure and decreases with increasing gun transverse speed.

Chapter 5

DISCUSSION

This chapter provides an analysis and interpretation of the experimental results covering AE based monitoring of the indentation behaviour of coatings and of the thermal spraying process. The foregoing chapter has established the key features of the AE record and the observed post-test cracking patterns and this chapter is mainly concerned with assessing the extent to which AE can be used as a more convenient measure of mechanical behaviour and fracture toughness of coatings than conventional means. It starts with discussing the interaction of the Vickers indenter with the materials studied and the information that this generates about mechanical properties. Next, the place of AE in monitoring the indentation process is discussed. Finally, the role of AE monitoring the quality of coatings during the spraying process is assessed.

5.1 Vickers indentation behaviour and fracture toughness

This section is confined to assessing the extent to which the indentation residual impression can be used as a conventional and alternative means of fracture toughness measurement of coatings both of which techniques which rely heavily upon metallographic assessment. It is clear from the surface metallographic evidence and also the comparison between measured and geometrical depth (*Section 4.1*) that piling-up is the dominant accommodation mechanism at all indentation loads for copper and aluminium whereas sinking-in is the dominant process for thermal sprayed ceramic coatings. The hardened steel sample occupies a position between the two extremes. In the most brittle materials, accommodation is by crumbling of the surface to the extent that cracking cannot be entirely be quantified by metallographic means.

These findings are summarised in **Figure 5.1**. Clearly, in the materials studied, the cracking behaviour is generally much more complex than is assumed for either the classical models of Palmqvist (Nihara [8]) or median (Lawn and Fuller [9]) cracking. **Figure 5.2** summarises the behaviour of the materials studied under indentation, along with the metallographic observations and literature values of the fracture toughness and also the measured hardness. Clearly, there is no simple relationship between hardness and cracking pattern, although the amount of cracking is probably related to toughness

and its distribution depends both on toughness and homogeneity. In the hard, multi-phase materials, inhomogeneity means that the areas of highest fracture toughness do not always correspond to the areas where cracking occurs and the size and distribution of the phases, their respective K_{1c} values, and the existence of brittle surfaces (e.g. splat boundaries) will all influence the cracking pattern.

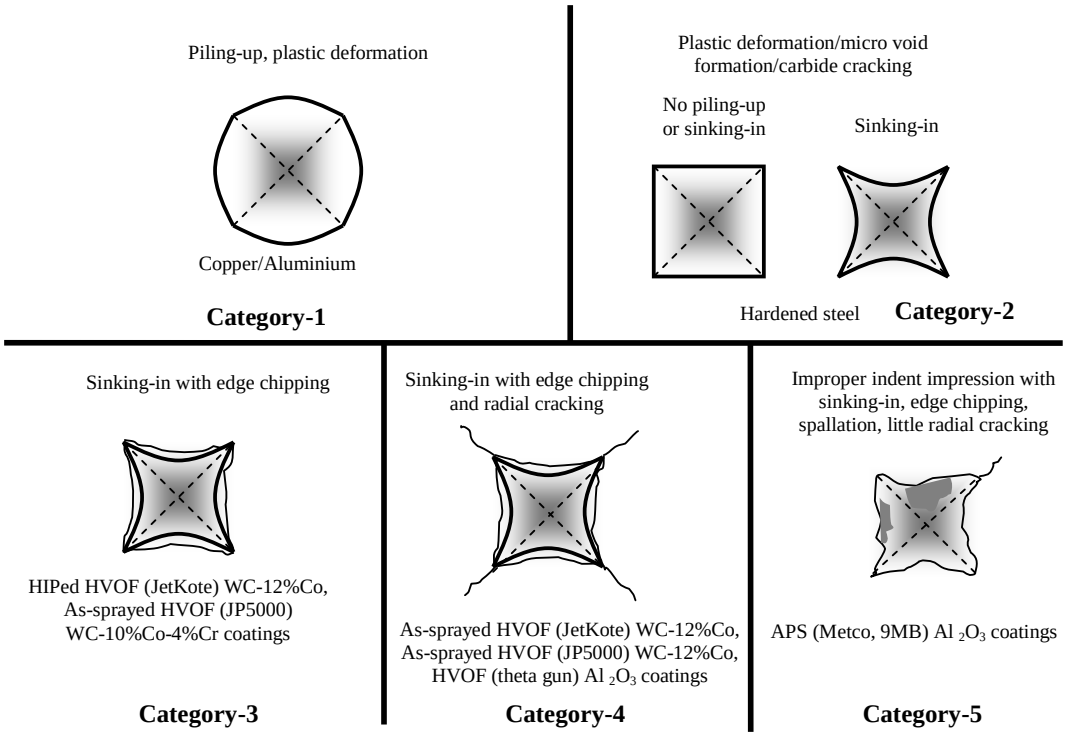

Figure 5.1 Category of Vickers indentation residual impressions

In the high-carbon steel, the carbides are much harder than the tempered martensitic matrix so that any plastic deformation gets concentrated in the matrix and is impeded by the carbides [152], leading to an accommodation mechanism including plastic deformation and carbide cracking [111]. The details of this mechanism are not visible at the magnifications used in this work, although some evidence of cracking at the carbide-matrix interface is visible for some of the larger particles (e.g. **Figure 4.1**). Since no macro cracks (other than those referred above) were visible on the surface around the indentation edges or corners, it is supposed that the very fine distribution of the brittle phase leads to generate micro-cracking in the areas of highest tensile stress. Since the stress is tensile over the entire indentation edge (*Section 2.1*), and the maximum principal stress at the indentation corner is tensile, it is expected that micro-cracking will be present in these areas.

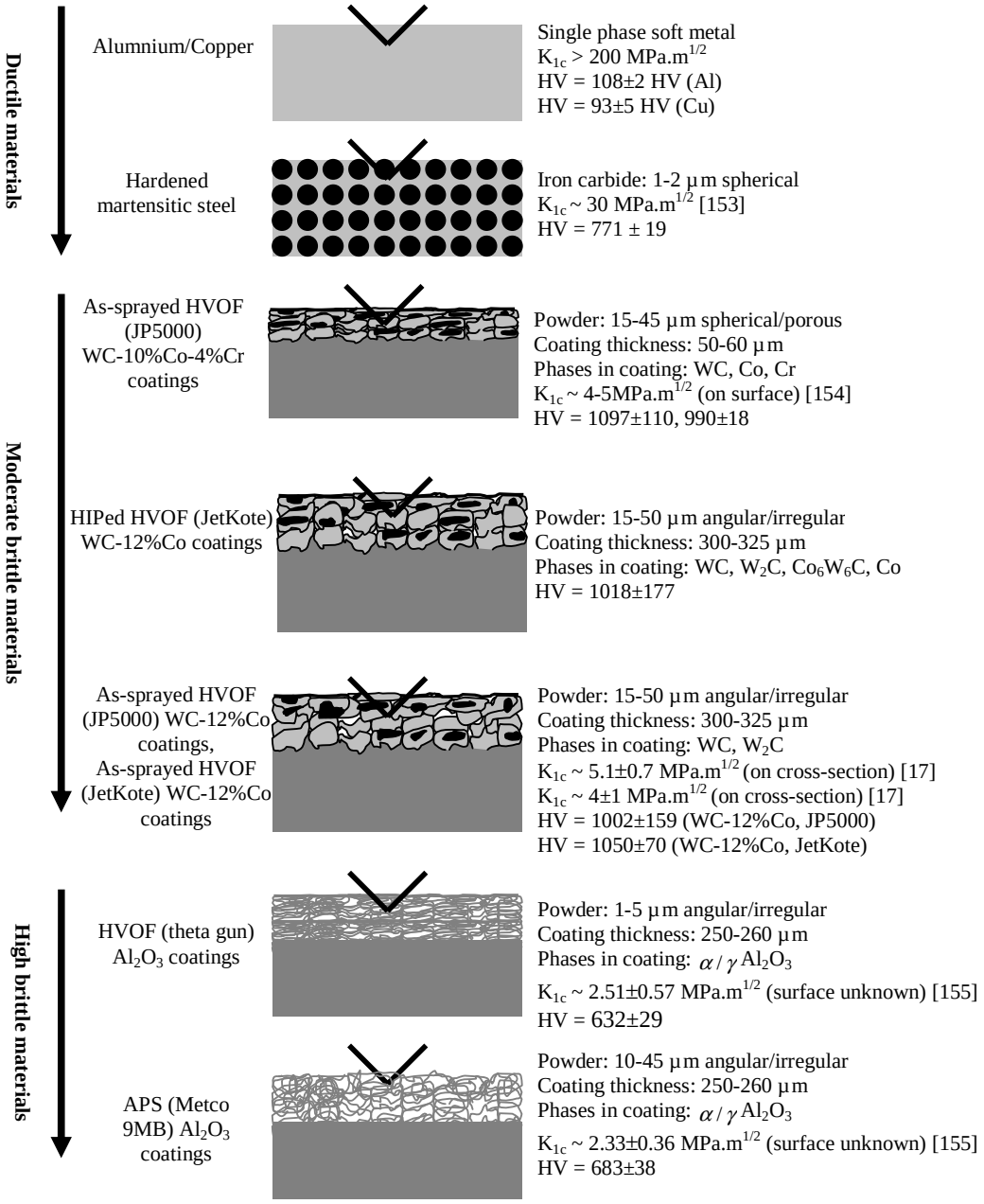

Figure 5.2 Summary of metallographic observations and relevant mechanical properties

Based on the surface and cross-sectional microscopic observations of the indentations on the various coatings (*Chapter 4*), the probable evolution of cracking during an indentation can be summarised in **Figure 5.3**. It is reasonable to expect that the finer surface cracking patterns at higher loads are representative of the early stages of cracking at heavier loads. Taking this information into account allows the identification of tensile cracking of edges and corners to as the major mechanism in the WC-Co and

WC-Co-Cr coatings with varying degrees of inter-splat cracking at its most significant in the APS Al_2O_3.

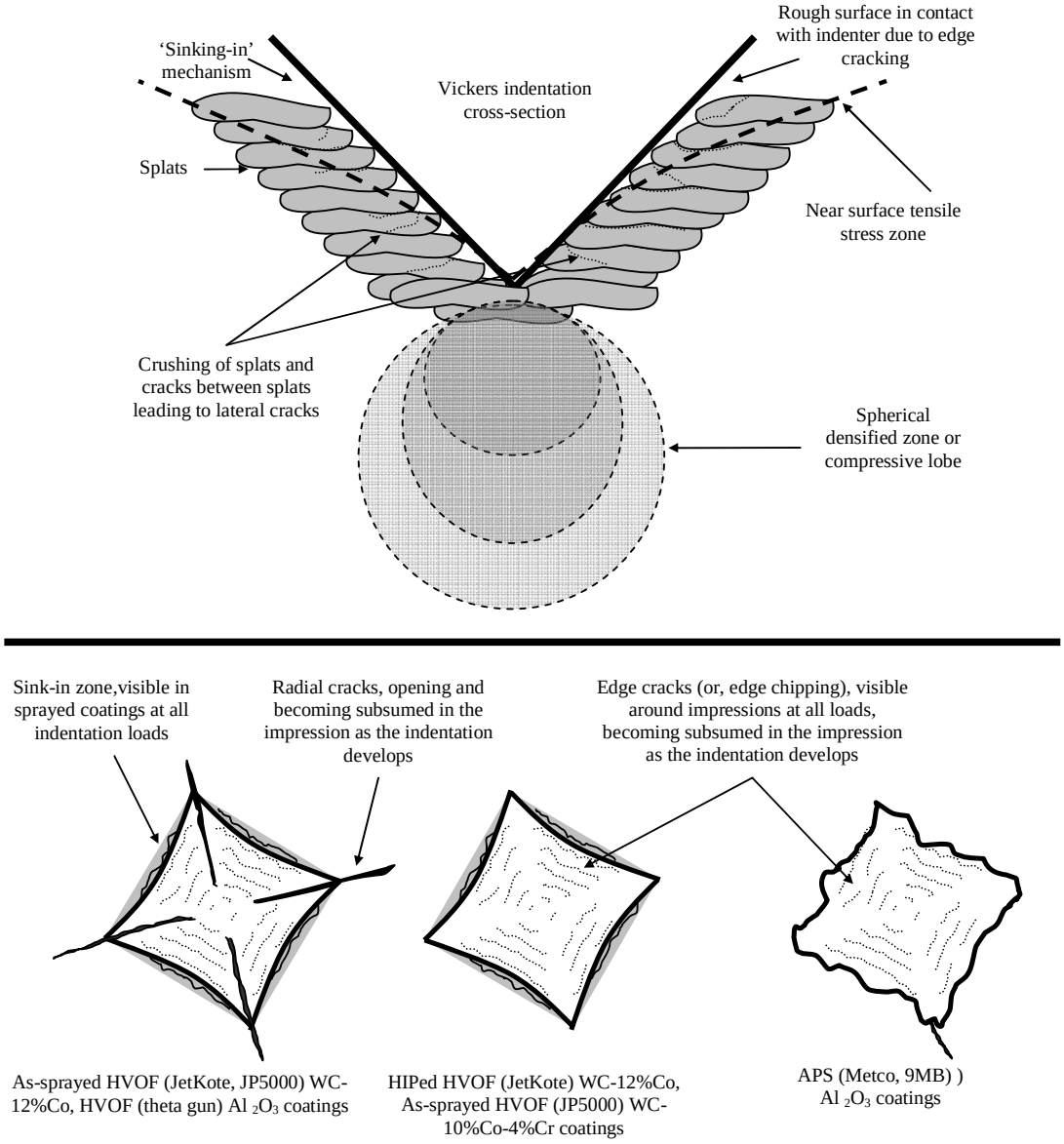

Figure 5.3 Schematic diagram showing development of an indentation impression in ceramic coatings (top: sectional view, bottom: plan view).

As categorized above (**Figure 5.1**), the Vickers indentations of coatings fracture differently and it is by no means certain that the classical approach (**Figure 2.9** and *Section 3.6.1*) of using radial crack length to deduce fracture toughness measurement will be valid when some (or all) of the cracking is distributed in relatively short edge cracks. **Figure 5.4a** shows the basis of the classical approach to indentation fracture

toughness measurement. In this approach, one of the two assumptions is made about the sub-surface shape of radial cracks. In the first of these (Nihara [8]), the length of each radial crack is taken to be visible length, *l*, and the depth, *h*, is assumed to be proportional to the impression depth. This ultimately leads to a relationship between fracture toughness, crack size, load and impression size, $K_{1c} = k_p \left[\frac{P}{a\sqrt{l_a}} \right]$. In the second approach (Lawn and Fuller [9]), the radial cracks are assumed to form part of a single crack whose length (2*c*) includes the impression diagonal and where depth (*D*) is half the length. This leads to proportionality, $K_{1c} = k_m \left[\frac{P}{c^{3/2}} \right]$.

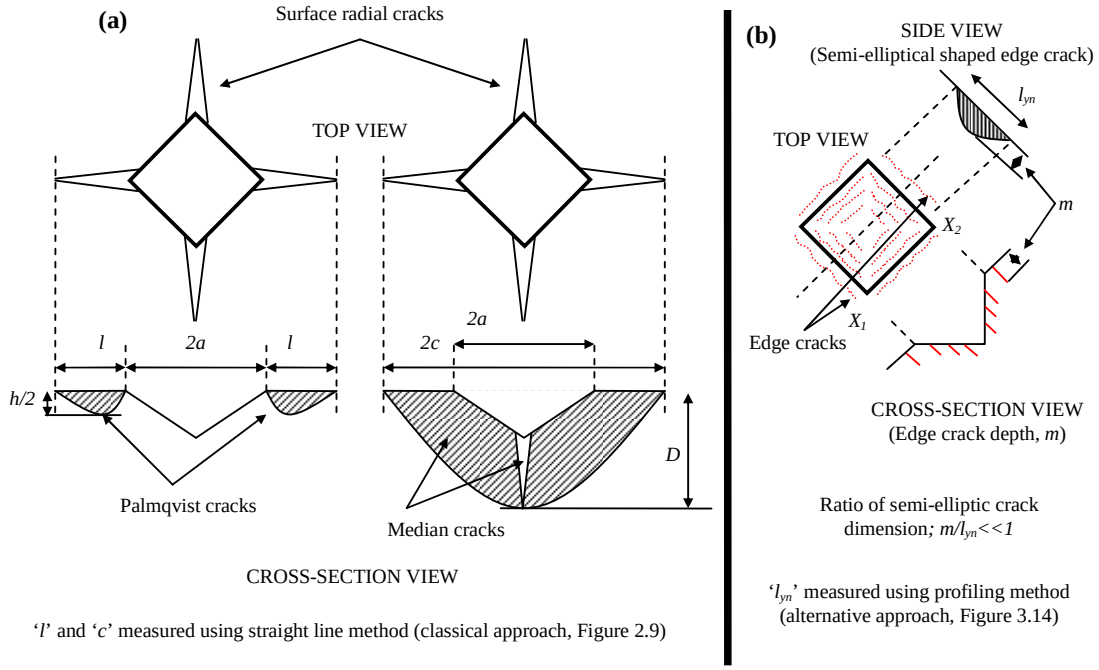

Figure 5.4 Schematic diagrams of Vickers indentation residual impression for crack prone materials: (a) Plamqvist and half-penny models by Nihara [8] and Lawn and Fuller [9], (b) edge crack model

Figure 5.4b shows an extension of the fracture mechanics model for edge cracks. Using the classical crack régimes in Vickers indentation fracture tests (*Section 2.1.1*), the average crack-to-indent ratio (l_a/a around 0.43±0.08 for as-sprayed HVOF/JetKote WC-12%Co, 0.45±0.08 for as-sprayed HVOF/JP5000 WC-12%Co; 0.88±0.21 for HVOF-theta gun Al_2O_3 fine powder), suggests Palmqvist rather than median cracks, and this is supported by the absence of sub-surface radial-median cracks in the SEM images of as-sprayed HVOF (JetKote) WC-12%Co (*Section 4.2*). It is reasonable to assume that

similar mechanics hold for edge cracks with stress being dependent upon the load and penetration depth. Using a similar assumption to the Palmqvist model (i.e. that crack depth, *m*, is proportional to impression size), the toughness can be deduced to be given by $K_{1c} = k_e \left[\frac{P}{a\sqrt{\sum l_{yn}}} \right]$. There is no reason to suppose that $k_e = k_p$ but, for combination of edge and radial cracks, the relationship between load and total surface crack length can still be considered to be an indication of fracture toughness.

Figure 5.5 illustrates the application of this analysis to the coatings studied in this work. Column A uses the classical Palmqvist approach and the average radial crack length for these coatings which exhibited any radial cracking. Using the classical constant of proportionality, $k_p = 0.0319$ (e.g. Shetty *et al.* model [10]), a value of fracture toughness can be obtained for the as-sprayed HVOF (JetKote) WC-12%Co and as-sprayed HVOF (JP5000) WC-12%Co coatings as 8.8±0.5 MPa.m$^{1/2}$ and 9.1±1.0 MPa.m$^{1/2}$, respectively. For the same coating material (WC-12%Co as-sprayed HVOF/Diamond Jet METCO), Lima *et al.* [17] have determined a value of 5.1±0.7 MPa.m$^{1/2}$ (Palmqvist based Shetty *et al.* model [10]) and 4±1 MPa.m$^{1/2}$ (Palmqvist based Nihara model [8]), although it might be noted that their indentations were made on a cross-section of the sample (as opposed to on its surface) and the fracture toughness for sprayed coatings is known to be anisotropic [15, 17, 156]. Furthermore, Lima *et al.* [17-18] have mentioned that the fracture toughness for HVOF as-sprayed WC-Co coatings determined using an indentation direction perpendicular to the coating-substrate interface is considerably higher than that for indentations parallel to the coating-substrate interface, thought to be the result of weak bonding (cohesive strength) between splats and the orientation of inter-splat boundaries relative to opening stresses. Finally, Factor and Roman [35] doubt the validity of indentation tests carried out on cross-sections of coatings, because the coating thickness is supported by the metallic substrate on one side and by mounting resin on the other, leading to an artificially constrained system in comparison with likely actual service loadings. For as-sprayed WC-10%Co-4%Cr, Mann *et al.* [154] observed radial cracks and have reported a value of 4-5 MPa.m$^{1/2}$, although they did not indicate the direction of indentation and what fracture model they used.

Assuming the Palmqvist model, the fracture toughness for the HVOF-theta gun Al_2O_3 (fine powder) coatings studied here was 5.5±0.5 MPa.m$^{1/2}$. For a similar coating material (HVOF Al_2O_3, powder size unknown), Bolelli *et al.* [155] have given a value of 2.5±0.57 MPa.m$^{1/2}$, although they did not indicate the direction of indentation and what fracture model they used. For APS (Metco 9MB) Al_2O_3 (conventional powder) coating, where a measurement of K_{1c} was not possible in this work, Bolelli *et al.* [155] have given a value of 2.33±0.36 MPa.m$^{1/2}$, although, again, powder size, indentation direction and fracture model were not specified.

Column B in **Figure 5.5** shows the application of a combined radial and edge crack model to all of the coatings studied (except the APS Al_2O_3). The upper plot (a) shows the relationship between total surface crack length and total surface edge crack length and, as can be seen, the ratio of total:edge varies between unity and about 2. More importantly, the plot of $a\sqrt{L}$ against P yields a straight line from which the fracture toughness can be determined. In order for k_{total} to be comparable with the value of k_p for Palmqvist cracks, it is necessary to divide the total crack length by 4 (in order to normalise per edge or per corner) and **Table 5.1** shows the resulting values of K_{1c} using edge and radial cracks (where these exists) and edge cracks only.

For the coatings on which the classical approach could be used (i.e. those which displayed radial cracks), the values of K_{1c} indicated by the alternative approach are generally lower and inclusion (or not) of radial cracks makes little difference to the indicative K_{1c}. The alternative approach does not change the ranking of toughness between the three coatings and gives values that are rather more compatible with the literature values. Finally, the alternative approach accentuates the toughness difference between the two versions of as-sprayed WC-Co, a result which helps to explain the differences in AE behaviour (see next section).

For the HIPed HVOF (JetKote) WC-12%Co coating, which can be expected to show improved fracture toughness over the as-sprayed coating [32], the absence of radial cracks, means that the classical approach cannot be used. However, the alternative approach gives a value of 7.4 MPa.m$^{1/2}$ compared with 4.6-5.2 MPa.m$^{1/2}$ for the equivalent as-sprayed coatings.

The difficulty in quantifying typical radial crack lengths in APS Al_2O_3 coatings has also been commented on by Luo *et al.* [51] and Sharma *et al.* [157]. However, the results shown here indicate that total surface crack length can be used to rank fracture toughness in coatings. What now needs to be established is whether AE can be used as a more convenient measure of total surface crack length.

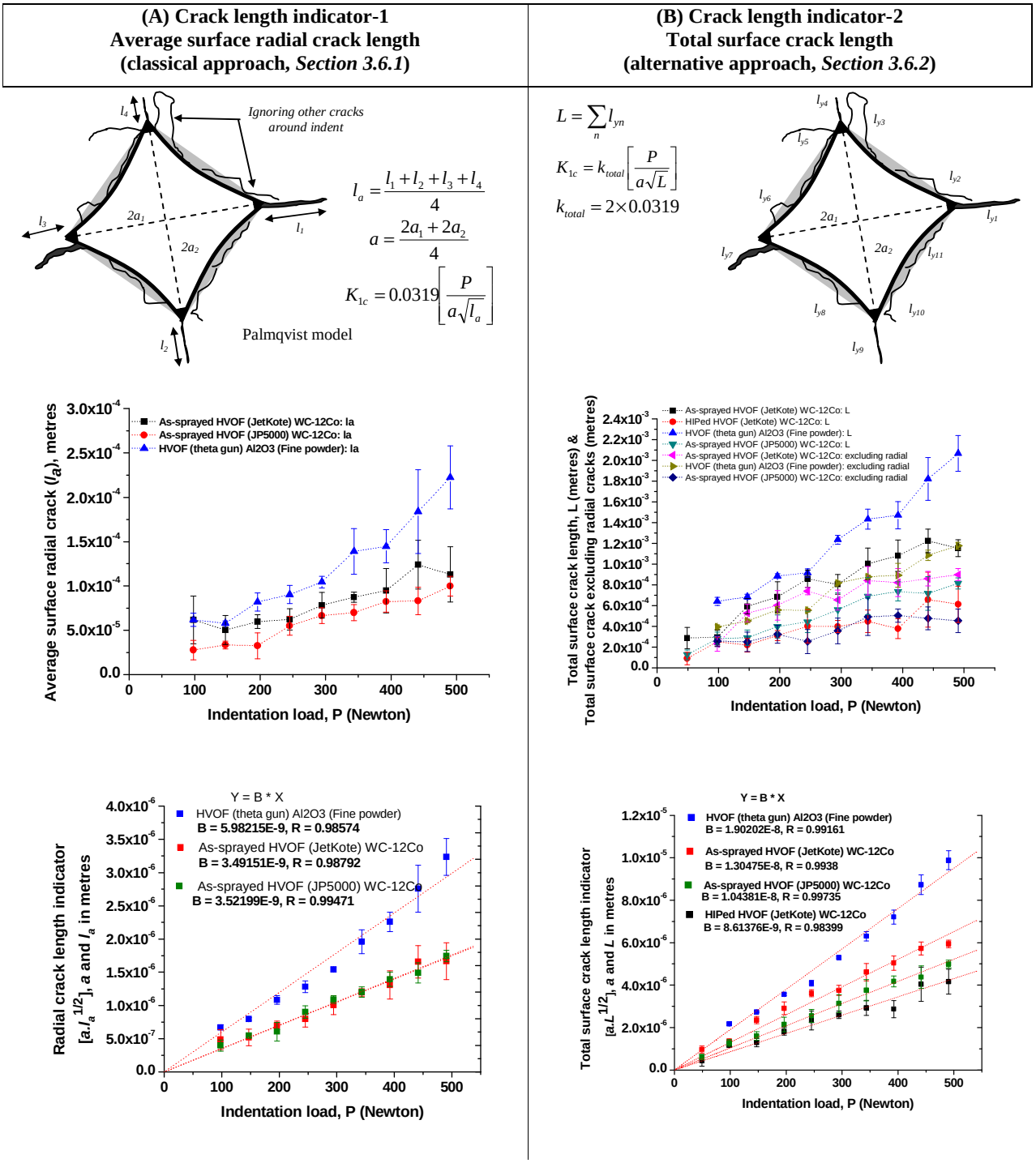

Figure 5.5 Two approaches in Vickers indentation fracture toughness assessment; Column A: crack length indicator-1 (classical approach), and column B: crack length indicator-2 (alternative approach)

Table 5.1 Summary of classical and alternative approach fracture toughness of coatings

Materials	**Classical approach (using average surface radial crack length)** K_{1c} (MPa.m$^{1/2}$)		**Alternative approach (using total surface crack length)** K_{1c} (MPa.m$^{1/2}$)	**Alternative approach (using total surface crack length excluding total surface radial cracks)** K_{1c} (MPa.m$^{1/2}$)
As-sprayed HVOF (JetKote) WC-12%Co	8.81±0.47		4.6±0.3	5.2±0.3
As-sprayed HVOF (JP5000) WC-12%Co	9.07±1.02		7.1±0.1	7.4±0.5
HIPed HVOF (JetKote) WC-12%Co	No radial cracks		7.4±0.2	7.4±0.2
APS (Metco, 9MB) Al_2O_3 (conventional powder)	Cracks not measureable		Cracks not measureable	Cracks not measureable
HVOF (theta gun) Al_2O_3 (fine powder)	5.50±0.53		3.4±0.1	4.3±0.1

5.2 AE based crack and fracture toughness measurement

As was seen in *Section 5.1*, the total surface crack length provides a ranking of fracture toughness for all of the materials in which a measure of crack length can be obtained at the micrscopical resolution chosen. As cracking becomes more distributed into smaller and smaller units, measurement of total crack length rapidly becomes impractible. Furthermore, the measurement of surface cracking patterns at the end of a test is not necessarily indicative of all of the cracking, particularly as the modes become more complex. Therefore, this section is confined to assessing the extent to which AE can be used as a more convenient measure of fracture toughness than the classical and alternative crack-length based approaches discussed above.

The fully instrumented indentation tests clearly helped in associating the AE events with the spatial location of the indenter. AE events may or may not be focussed onto particular parts of the indentation, but a systematic investigation using load-based staging and AE-based zoning criteria indicate two types of AE time evolution; where no clear zones can be identified and where clear zones can be identified. When zones are identifiable, these can be mapped onto the load-based stages, although the presence of stages does not necessarily indicate the presence of zones.

Table 5.2 summarises the percentage appearance of zones for each of the materials investigated. For the cases where cracking can be measured, it appears that zoning is associated with a large total crack length and the appearance of radial cracks. The fact that zoning also appears in the two samples where the crack length could not be

measured suggests that it is the presence of a significant amount of cracking that leads to zoning of the AE. This is consistent with cracking being a discontinuous accommodation process, unlike plastic deformation which is more continuous, and is also consistent with the literature on homogeneous materials [e.g. 77-81] where the radial cracking is seen to be discontinuous and that it leads to burst-type AE at particular critical loads.

Table 5.2 Summary of qualitative and quantitative indentation category

Materials	**Indentation residual impression category & main cracking type (ref. Figure 5.1) (Qualitative)**	**Statistics showing % of indentation with distinct AE zone A, B, C (Ref. chapter 4)**	**Prevalence of radial cracking (slope of line in m/N, ref. Figure 5.5a, column A)**	**Prevalence of edge cracking (slope of line in m/N, ref. Figure 5.5a, column B)**	**Prevalence of total (slope of line in m/N, ref. Figure 5.5a, column B)**
Hardened steel	Category 2 Not measurable	33/50 = 66%	Not measurable	Not measurable	Not measurable
WC-12%Co (as-sprayed HVOF/JP5000)	Category 4 Radial & edge	**9/50 = 18%**	**2.04×10^{-7}** (3rd largest)	**1.18×10^{-6}** (3rd largest)	**1.80×10^{-6}** (3rd largest)
WC-12%Co (as-sprayed HVOF/JetKote)	Category 4 Radial & edge	**43/50 = 86%**	**2.60×10^{-7}** (2nd largest)	**2.19×10^{-6}** (2nd largest)	**2.79×10^{-6}** (2nd largest)
WC-12%Co (HIPed HVOF/JetKote)	Category 3 Edge only	0/50 = 0%	None	**1.32×10^{-6}** (4th largest)	**1.32×10^{-6}** (4th largest)
WC-10%Co-4%Cr (as-sprayed HVOF/JP5000)	Category 3 Edge only	0/6 = 0%	None	Not measured	Not measured
Conventional Al_2O_3 (APS/Metco, 9MB)	Category 5 Spallation	**32/45 = 71%**	Not measurable	Not measurable	Not measurable
Fine powder Al_2O_3 (HVOF/theta gun)	Category 4 Radial & edge	**39/45 = 86%**	**4.09×10^{-7}** (1st largest)	**2.48×10^{-6}** (1st largest)	**4.12×10^{-6}** (1st largest)

Of the records that exhibited AE zoning, **Figure 5.6** shows that zone A always represents a small proportion of the total AE energy (also of the other measures, ring-down count and event duration), and that zone B contains the highest proportion at low loads, with zone C containing the highest at moderate to higher loads. The fact that zone C shows the biggest change with load would suggest that cracking during indentation is better discriminated using zone C, although zone B often contains the highest intensity of cracking events. The zoning of AE signals, and the associated energy (**Figure 5.6**) might be useful in understanding the evolution and nature of cracking events but the fact that it has been observed in less than half of the records examined makes it difficult to form general conclusions.

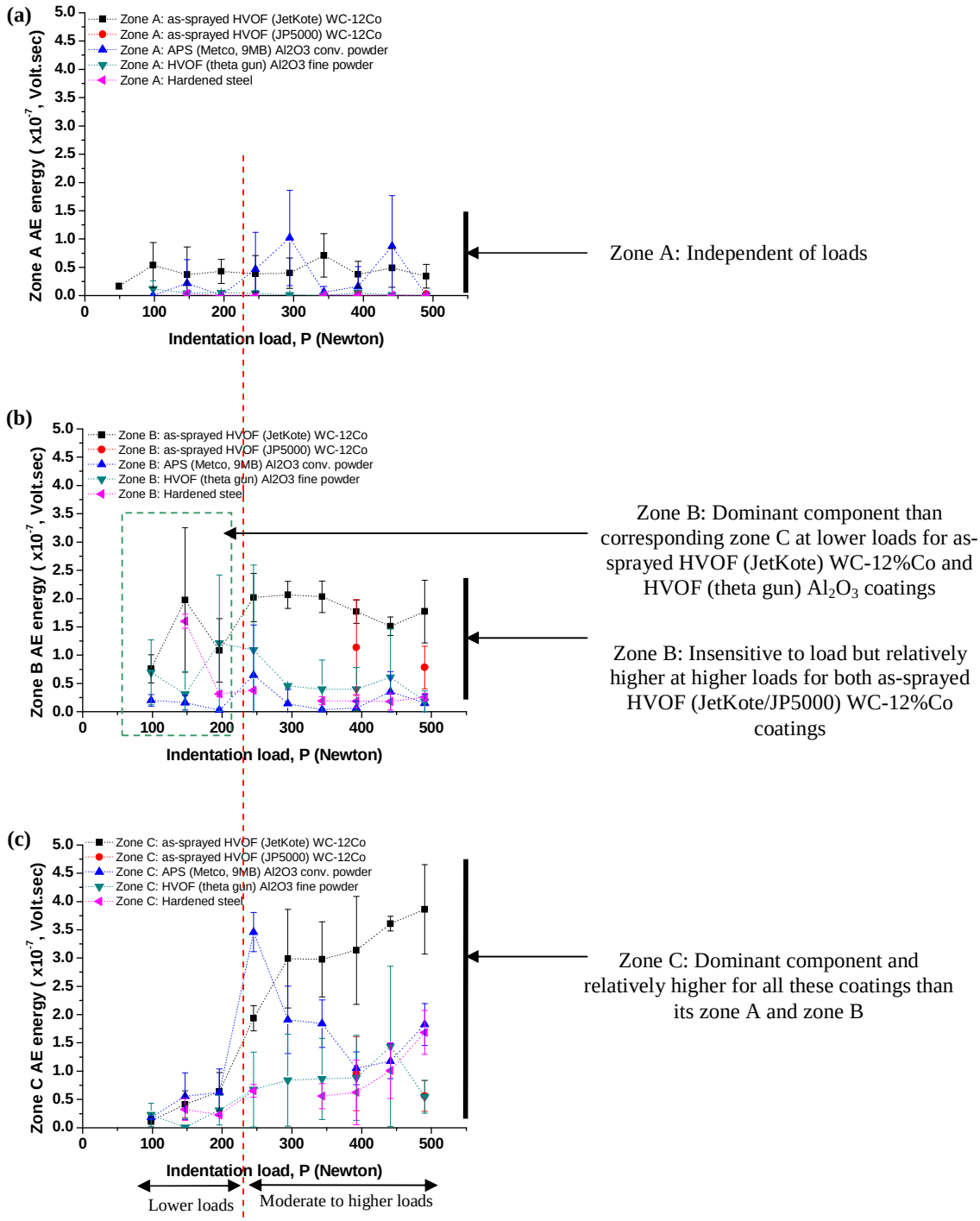

Figure 5.6 Comparison of zone AE energy: (a) zone A, (b) zone B and (c) zone C

The fracture energy, G_c, associated with a unit area of new fracture surface is given by: $G_c = \frac{K_{1c}^{\ 2}}{E_Y}$, where E_Y is Young's modulus. It is therefore reasonable to expect that cumulative AE energy throughout the indentation is a measure of total crack area

produced multiplied by the (constant) value of $\frac{K_{1c}^{\ 2}}{E_Y}$ for the material. **Figure 5.7** shows the total AE energy plotted against total surface crack length for those materials on which a measurement could be made, each labelled with the fracture toughness determined from the alternative approach (**Table 5.1**). As can be seen, the lowest toughness material shows the lowest slope, but that the ratio of slopes of the two quality zones is not in proportion to $\frac{K_{1c}^{\ 2}}{E_Y}$ nor to K_{1c}. This is almost certainly due to the fact that the overall slope of cracks in the Al_2O_3 is much simpler than in the WC-Co material and a far broader range of materials, including some homogeneous ceramics would need to be studied to in order to elucidate this fully.

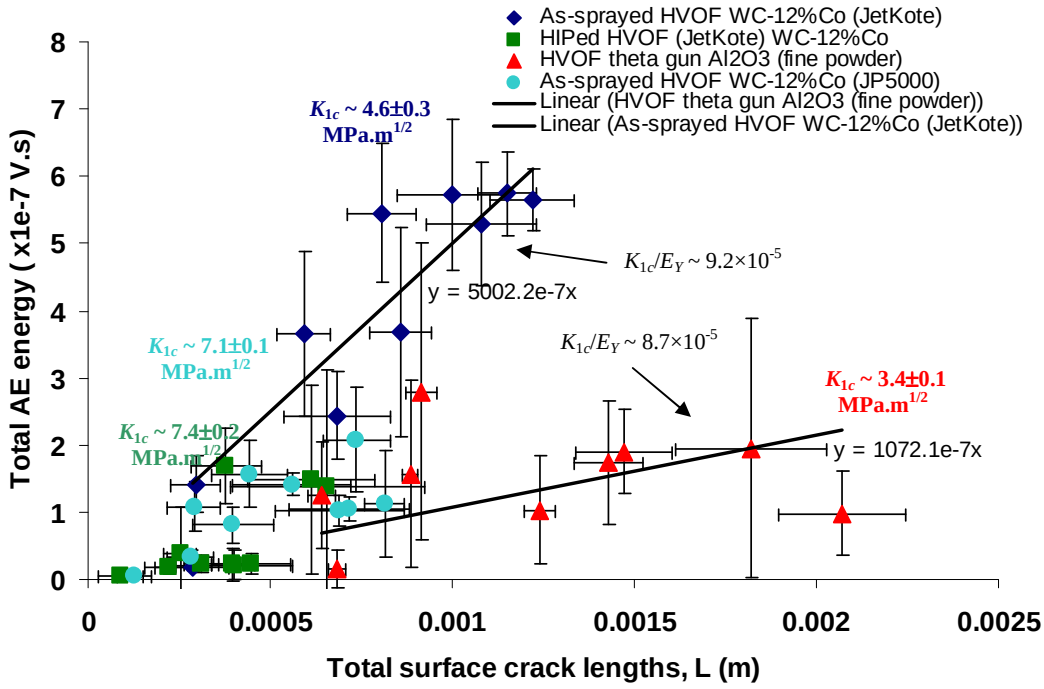

Figure 5.7 Quality zone map of coating fracture properties: total surface crack length plotted against total AE energy (E_Y for HVOF Al_2O_3 = 138 GPa [155], E_Y for HVOF WC-12%Co = 230 GPa [48])

The above analysis suggests that total AE energy may make a useful proxy measure for total crack area for material of a given fracture toughness and Young's modulus. Supposing that crack depths are approximately constant, AE could then be supposed to give a measure of total surface crack length, so that the equation given in **Figure 5.5**, column B can be modified to $K_{1c} = k_{AE}\left[\frac{P}{a\sqrt{E}}\right]$ (*Section 3.6.2*). **Figure 5.8** shows plots of $a\sqrt{E}$ against indentation load along with the associated best-fit straight lines and

Table 5.3 shows the values of the slopes and their correlation coefficients alongside the corresponding values for the AE ring-down count. The fact that these correlations are reasonably good indicates that the AE approach can be calibrated against the crack-length based assessment to allow an assessment of the toughness for the materials where an AE record is available and crack length could not be measured. **Figure 5.9** shows toughness values from **Table 5.1** (total surface crack length) plotted against the inverse of the slope of the AE ring-down count or AE energy, $1/B_R$ and $1/B_E$, along with the associated best-fit calibration (notably higher for AE energy) between K_{1c} and ring-down count and energy, respectively. For the Al_2O_3 material, a different calibration was expected and this was achieved by simple proportion. **Table 5.4** summarises the results, indicating the values of K_{1c} determined from crack length (where this was possible) and from AE ring-down count or AE energy. The values of K_{1c} determined from AE energy show the expected ranking of the fracture toughness of the materials. Those from AE ring-down count show a similar ranking.

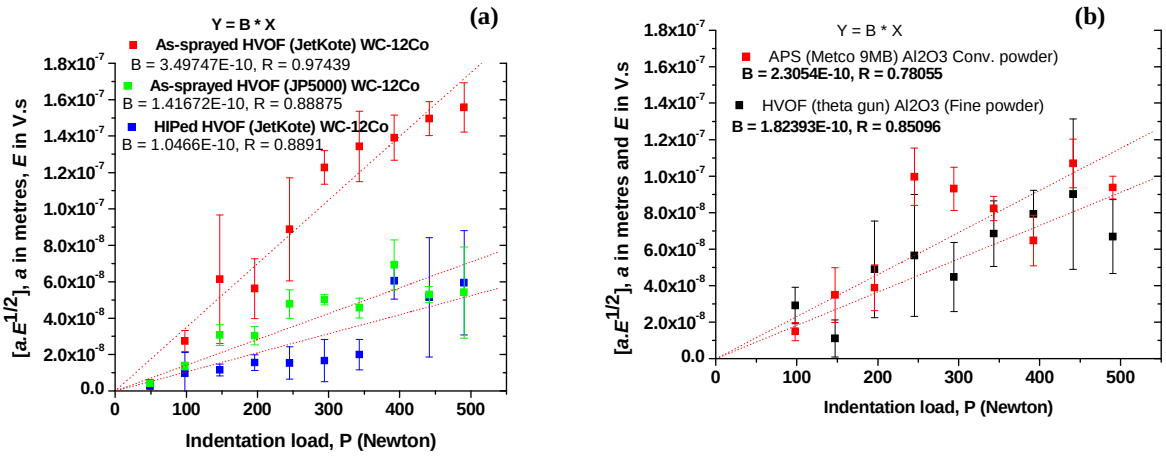

Figure 5.8 AE based (using modified generic equation) indentation fracture toughness estimation (K_{AE}) using AE energy (E): (a) WC-Co and (b) Al_2O_3 coatings [lower the slope of best fit line, higher the fracture toughness]

Table 5.3 AE based fracture toughness measurement of materials

Materials	Slope B when X = R *(ring-down)*	Correlation coefficient (r)		Slope B when X = E *(energy)*	Correlation coefficient (r)
Carbide coatings					
As-sprayed HVOF (JetKote) WC-12%Co	8.07×10^{-5}	0.9910		3.49×10^{-10}	0.9743
As-sprayed HVOF (JP5000) WC-12%Co	8.57×10^{-5}	0.9570		1.41×10^{-10}	0.8887
As-sprayed HVOF (JP5000) WC-10%Co-4%Cr (100 mm/s, P1);	6.33×10^{-5}	0.9656		1.94×10^{-10}	0.9177
As-sprayed HVOF (JP5000) WC-10%Co-4%Cr (200 mm/s, P2)	4.57×10^{-5}	0.8262		1.15×10^{-10}	0.9757
HIPed HVOF (JetKote) WC-12%Co	3.81×10^{-5}	0.8982		1.04×10^{-10}	0.8891
Ceramic coatings					
APS (Metco, 9MB) Al_2O_3 (conventional powder)	1.17×10^{-4}	0.9501		2.30×10^{-10}	0.7805
HVOF (theta gun) Al_2O_3 (fine powder)	6.94×10^{-5}	0.8435		1.82×10^{-10}	0.8509
Metal					
Hardened steel	8.65×10^{-5}	0.9739		1.77×10^{-10}	0.7965

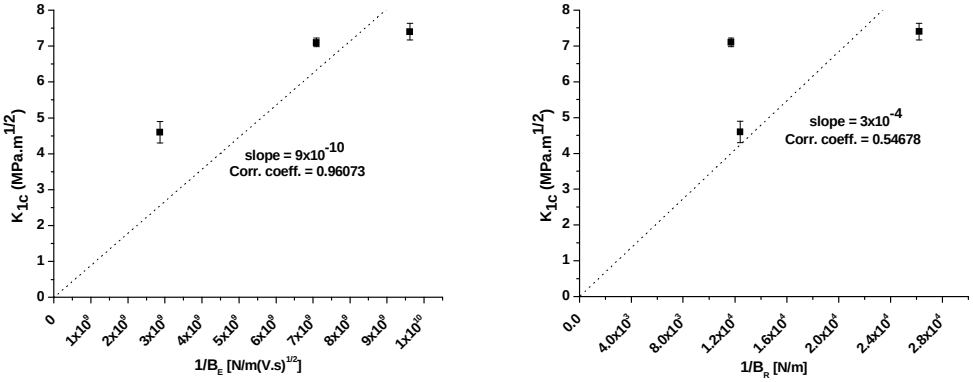

Figure 5.9 Calibration for WC-Co coatings: Fracture toughness values plotted against the inverse of the slope of the (a) AE energy, (b) AE ring-down count

Table 5.4 AE based fracture toughness measurement of thermally sprayed coatings

Material	K_{1c} (MPa.m$^{1/2}$) when X = R	K_{1c} (MPa.m$^{1/2}$) when X = E	K_{1c} (MPa.m$^{1/2}$) when X = L
As-sprayed HVOF (JetKote) WC-12%Co	3.72	2.58	4.6
As-sprayed HVOF (JP5000) WC-12%Co	3.50	6.38	7.1
As-sprayed HVOF (JP5000) WC-10%Co-4%Cr (100 mm/s, P1);	4.74	4.64	-
As-sprayed HVOF (JP5000) WC-10%Co-4%Cr (200 mm/s, P2)	6.56	7.83	-
HIPed HVOF (JetKote) WC-12%Co	7.87	8.65	7.4
APS (Metco, 9MB) Al_2O_3 (conv. powder)	2.02	2.62	-
HVOF (theta gun) Al_2O_3 (fine powder)	3.40	3.30	3.4

As pointed out in the literature review, a number of authors [e.g. 79] claim that the AE frequency spectrum can be used to distinguish between cracking and deformation

during indentation. In the current work, the ratio of power in the low frequency band (0-250 kHz) to the power in the high frequency band (250-750 kHz) did not show any pattern between loads. The HIPed HVOF-JetKote WC-12%Co and, to a lesser extent, the as-sprayed HVOF (JP5000) WC-10%Co-4%Cr coating, exhibited stronger high frequency components than other coatings (**Figure 5.10**), and it may not be coincidence that these two coatings did not contain and radial cracks, nor did they AE show any zoning. This area clearly needs further work before any conclusions can be drawn.

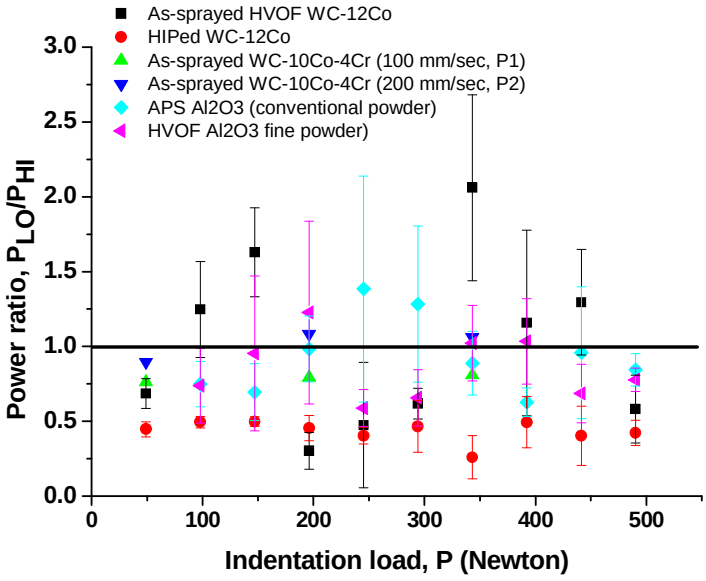

Figure 5.10 Comparison of frequency power ratio for all coating materials

5.3 AE based thermal spray process monitoring

This section discusses an AE-based approach to monitoring coating formation during a continuous thermal spraying process. As was seen in Chapter 4 *(Section 4.4)*, the slit experiments have demonstrated that spray-substrate interaction generates measurable AE, although it is by no means certain that individual particle impacts will be observable either by the time- or amplitude-resolution of the method. It is therefore of interest to develop a model (*Appendix G*) describing the approaching particle density, size and velocity distributions as an aid to analysing the data from slit and slit-free experiments.

A cross-section of the spray can be assumed to contain a constant density of particles of constant size, travelling at constant velocity towards the surface and the total particle

kinetic energy passing through a slit determined as a function of time. Based on these assumptions the energy rate, $\dot{E}$, associated with the kinetic energy of particles impinging on the substrate through the slit can be calculated from a simple kinematic model, *Appendix G*. Using the model, the energy rate is given by:

$$\dot{E}(t) = \frac{1}{2}\dot{m}_{powder} V^2 \left(\frac{A_s(t)}{A} \right) \tag{5.1}$$

where $\dot{m}_{powder}$ is the powder mass flow rate, V is the average particle speed, A is the spray spot area and $A_s(t)$ is a trigonometric function of time given in *Appendix G*.

A representative AE record is compared with the calculated kinetic energy rate in **Figure 5.11**. In the calculation; the diameter of the spray spot was taken as 10 mm, the gun transverse speed 250 mm sec^{-1}, the powder flow rate 80 g min^{-1} and the velocity of sprayed powder particles 800 m sec^{-1}. The length of time taken for the spray gun to pass a slit at the speed of 250 mm sec^{-1} is 0.052 sec. It is clear from **Figure 5.11a**, that the pulse is, in fact, wider than the calculated time, **Figure 5.11b**. This could be due to fanning of the spray, i.e. a non-uniform particle density distribution over a wider spot size and/or diffraction effects at the slits.

The AE energy was calculated as the area under the absolute of the signal above threshold using Equation 3.1. Since the continuous background noise amplitude was present throughout the process at all spraying conditions, an automatic analysis threshold level of 15% above the continuous background noise level was chosen to define significant AE activity due to coating formation. **Figure 5.12** compares the total kinetic energy of particle impact with the AE energy through slits of various sizes and spray gun transverse speeds, suggesting that, notwithstanding the fanning/diffraction effect, the model gives a reasonable approximation to the measured AE energy (i.e. that the calculated kinetic energy is proportional to the measured AE energy).

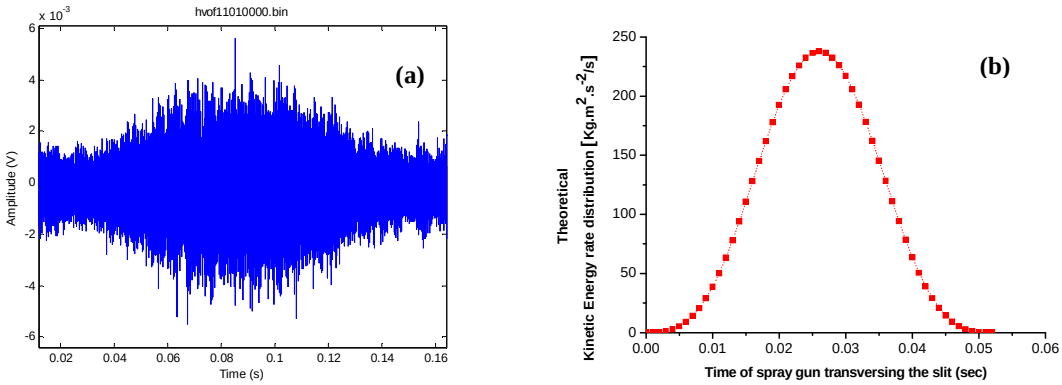

Figure 5.11 (a) AE signal at a single slit of width 3mm when HVOF (TAFA JP5000) WC-10%Co-4%Cr is sprayed at 250 mm sec^{-1} gun speed, high pressure, P1, (b) calculated kinetic energy rate $\dot{E}$ distribution due to particle impact through slit of width 3 mm × 10 mm

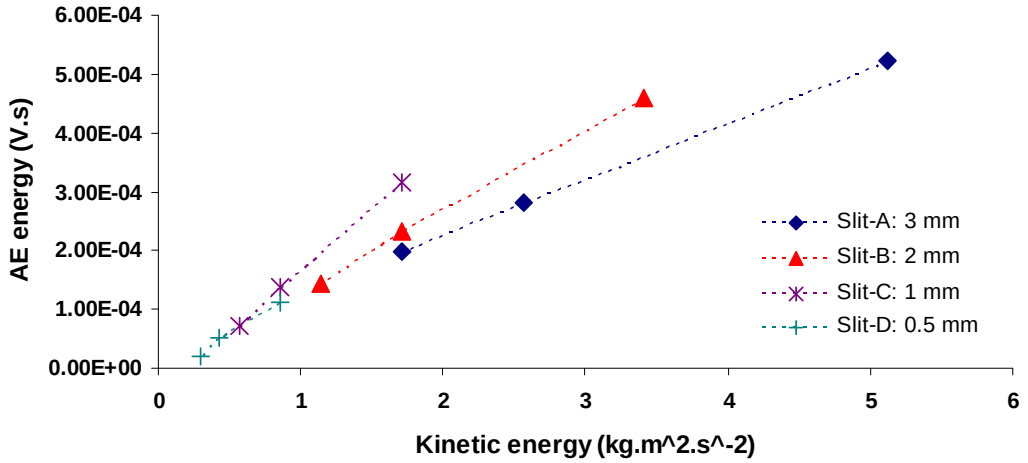

Figure 5.12 Calculated kinetic energy of particle impact plotted against measured AE energy with spray gun transverse speed for each slit sizes at high pressure, P1

The use of AE for monitoring the thermal spraying is complicated due to overlapping impact signals and noise within the coating chamber [141-144]. Nevertheless, it is obvious that the model, with appropriate modifications, will serve as a useful analytical aid for continuous *in-situ* quality monitoring, since the incident impact energy of the powder particle helps facilitate the bonding of the coating inter-splat cohesion. The complimentary nature of the information available from process monitoring and from semi-destructive testing (i.e. indentation) adds a dimension to the use of the technique.

Figure 5.13 shows a record of AE produced in continuous multilayer spraying without the use of slits. As can be seen, the AE energy within a layer goes through a maximum (circled in **Figure 5.13**) as the spray spot passes over the sensor position in the middle

of the back of the sample. As well as this, there is a general increase in AE energy for the first three layers which then remains constant as the number of layers builds up and this cannot be attributed to changes to sensor sensitivity as the back face of the substrate warms up.

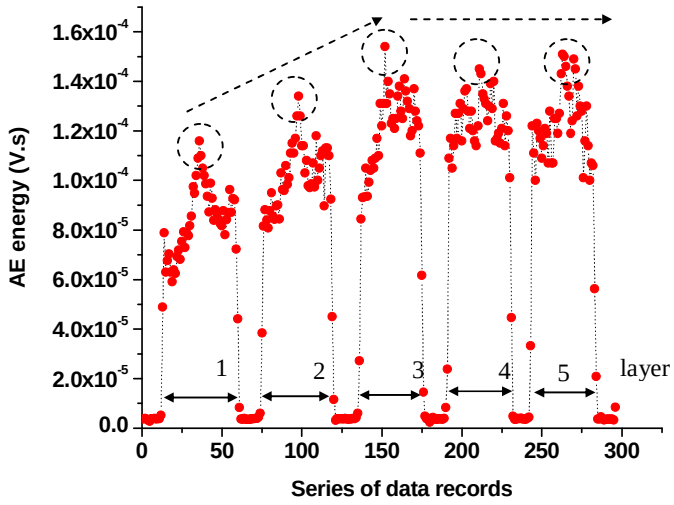

Figure 5.13 AE energy distribution during 5-layer continuous spraying with no air jet cooling (JP5000 HVOF WC-10%Co-4%Cr, lower pressure P2) on a flat 3 mm thick and 500 mm long mild-steel substrate at 200 mm sec^{-1} transverse gun speed for a series of 4 ms record lengths; 0.5 mm maximum coating thickness [2.5 s scanning time per layer]

On the basis of the foregoing, it seems that particle impingement on the substrate constitutes a significant source of AE but this would be expected to be around the same intensity for each of the passes. The physical difference between the surface with single pass and multi-pass spraying is shown in **Figure 5.14**. The relevant differences are:

- the substrate is thicker
- the substrate has a higher temperature
- the substrate is of a different material

The main source of residual stress during deposition is, σ_q, the so-called 'quenching stress' [158]:

$$\sigma_q \approx \alpha_c (T_m - T_s) E_c \qquad (5.2)$$

where α_c, T_m, T_s and E_c are the deposit coefficient of thermal expansion, lamella melting temperature, substrate temperature and deposit stiffness, respectively. This quenching stress could conceivably cause cracking in the layer being deposited which would be manifest as AE during the pass. However, this contribution would be expected

to decrease as the substrate warms up, and is therefore not the explanation for the increased AE in multi-layer deposition, seen in **Figure 5.13**.

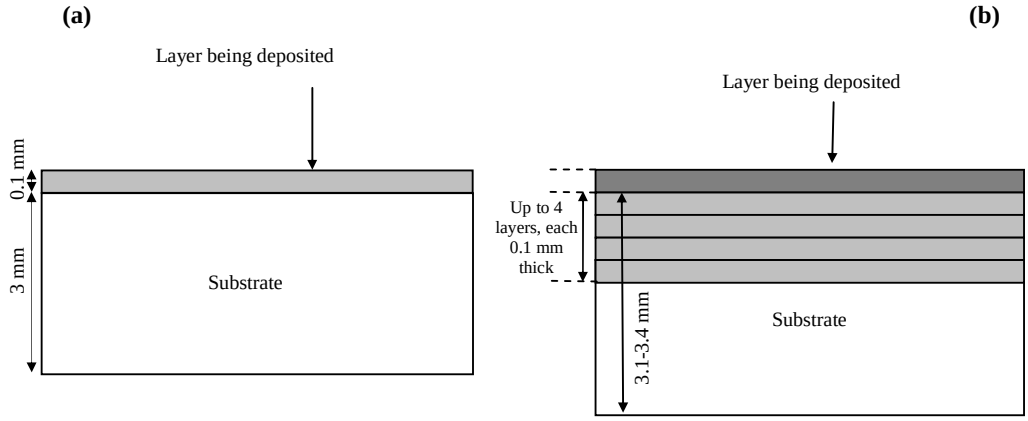

Figure 5.14 Diagram showing difference in substrate for single pass and multi-pass thermal spraying

Bansal *et al.* [159] have taken a typical value of flame heat flux (1 MW/m^2) and calculated (amongst other things) the thermal gradient in the substrate during HVOF deposition. This calculation suggests that the skin of the substrate is heated significantly over the ambient to a depth of around 50 μm. Assuming a similar penetration in the current process would mean that thermal mismatch stresses in the substrate associated with shock flame heating in the depositing layer would affect most of the immediate underlying HVOF layer, but relatively little of any deeper layers. It can therefore tentatively be suggested that the additional AE in multi-layer deposition is associated with thermal shock of the underlying deposition layers, an effect that might be expected to get greater for the first few layers and cease to grow thereafter. It is therefore possible that AE monitoring may, as well as providing information on the particle-surface encounter mechanism, might also offer some information on the quality of the coating through its response to shock heating.

Chapter 6

CONCLUSIONS AND RECOMMENDATIONS

In this work two types of tests were conducted, AE monitoring during Vickers indentation and during thermal spraying. Of these, the more significant contribution is in the understanding of indentation behaviour through analysis of AE measurements for which the large body of work cited in the literature review provided a sound technical basis. Although the work on AE monitoring during thermal spraying is of a preliminary nature, a novel approach using AE sensor to monitor thermal spray process has been demonstrated. The main conclusions are given below, followed by recommendation for future work.

6.1 Conclusions

Main conclusions from indentation fracture, crack length and fracture toughness

- Total surface crack length provides as good an indication of fracture toughness as the classical approach based on radial crack length. This provides a way forward for determining the fracture toughness of brittle materials where no radial cracks are developed.
- An alternative approach for determining fracture toughness for coating materials has been developed. Using this approach, the following values are suggested:
  3.4±0.1 MPa.m$^{1/2}$ for HVOF (theta-gun) Al_2O_3
  4.6±0.3 MPa.m$^{1/2}$ for as-sprayed HVOF (JetKote) WC-12%Co
  7.1±0.1 MPa.m$^{1/2}$ for as-sprayed HVOF (JP5000) WC-12%Co
  7.4±0.2 MPa.m$^{1/2}$ for HIPed HVOF (JetKote) WC-12%Co coatings

  These figures are in good agreement with the few available published values.

Main conclusions from fully instrumented Vickers indentation tests

- Plastic deformation in the form of 'piling-up' residual impressions in soft metals (copper and aluminium) produced little or no AE, whereas brittle fracture in the form of 'sinking-in' residual impressions in hardened steel and as-sprayed HVOF (JP5000) WC-12%Co coatings produced significant AE.

- AE may or may not be focussed onto particular stages of the indentation as defined by the force-displacement record. The brittle hardened steel showed a higher degree of zoning of AE than did the WC-12%Co coatings and this is attributed to its finer microstructure and the distribution of hard particles in a more ductile matrix.

Main conclusions from AE based crack and fracture toughness measurement

- All of the AE features can be used as a surrogate for total surface crack length and total surface crack length (using profiling method at fixed resolution) offers an improved measure of crack prevalence than traditional approaches for the coatings studied.
- For materials where cracks are not visible at the fixed resolution chosen (e.g. APS Al_2O_3 coatings and hardened steel), a full measure of crack prevalence would require fractal dimension analysis which is time consuming offering a motivation for AE-based crack monitoring.
- By using AE features (notably energy) as a surrogate for total surface crack length the system can be calibrated against the toughness values obtained from crack lengths, giving the following AE based fracture toughness values:
  3.3 MPa.$m^{1/2}$ for HVOF (theta-gun) Al_2O_3
  2.6 MPa.$m^{1/2}$ for APS (Metco, 9MB) Al_2O_3
  2.5 MPa.$m^{1/2}$ for as-sprayed HVOF (JetKote) WC-12%Co
  6.3 MPa.$m^{1/2}$ for as-sprayed HVOF (JP5000) WC-12%Co
  4.6 MPa.$m^{1/2}$ for as-sprayed HVOF (JP5000) WC-10%Co-4%Cr, 100 mm/s, P1
  7.8 MPa.$m^{1/2}$ for as-sprayed HVOF (JP5000) WC-10%Co-4%Cr, 100 mm/s, P2
  8.6 MPa.$m^{1/2}$ for HIPed HVOF (JetKote) WC-12%Co coatings
- The ratio of low to high AE frequency bands does not show any pattern with indentation load, although it is possible that AE frequency changes with the type of cracking present, as claimed by other researchers.

Main conclusions from the AE monitored HVOF thermal spray process

- For spraying through slits, the measured AE energy is correlated with the calculated kinetic energy of particles, showing that the signal associated with particle impingement can be seen in the face of considerable airborne noise.
- For continuous multi-layer spraying the general level of AE energy increases as the number of layers (and sample temperature) increases. A feature which can be

drawn that the difference is due to cracking or delamination in underlying layers, which may give an additional measure of coating quality.

6.2 Future work recommendations

Future work should be aimed at refining the investigations carried out during this project

- Whereas, the calibration approach relating surface crack size to AE energy was successful, its validation would benefit from a detailed study including surface and sub-surface examination at a variety of magnifications in a set of model materials with closely-controlled microstructures.
- A more closely-controlled indentation process, including AE monitoring may help to resolve some of the anomalies between load stages and AE zones.
- The work on thermal spray monitoring is in its infancy and more experiments on spraying through masks where the number of particles landing is limited, coupled with detailed metallography of the surface will help to establish more clearly the relationship between AE signature and splat formation.

Appendix A

Appendix A: AE systems used to study indentation

Table A.1 AE system used to study indentations on ceramics

AE data acquisition system	AE sensor	No. of sensor(s), Sensor location	Sensor frequency band / *Resonant	Gain: Pre-amp/*SCU	Ref.
Piezoelectric transducer (Brüel & Kjaer)	Piezoelectric	1, indentation surface	0-0.2 MHz/*200-300 kHz	40 dB/*0/50 dB	[71]
Piezoelectric transducer (Brüel & Kjaer)	Piezoelectric	1, indentation surface	210 kHz	40 dB/*20 dB	[74]
-	AE sensors	2, near sample but on base plate	-	-	[75]
D/E 3000 system	-	1, indentation surface	-	-	[76]
HIFREACE / Tektronix DSA 601A	Broadband ultrasonic point focus transducer of Panametrics V390, V3194	1, opposite to indentation surface	50 & 100 MHz	-	[77]
LOCAN 320 system from PAC	PZT, AE sensor	1, indentation surface	*150 kHz	40 dB	[78]
AE system from NF Corp.	Piezoelectric	1, opposite to indentation surface	0-1 MHz/*140 kHz	40 dB/*60 dB	[79]
Spartan AT	Piezoelectric	1, indentation surface	0.1-1.0 MHz/*125 kHz	40/60 dB	[80]
AE Fracture Wave Detector (FWD, Model FM-1)	Broadband transducer (DWC B1025)	-	-	40 dB	[81]
Locan 320 system from PAC	-	-	-	-	[82]

Table A.2 AE system used to study indentations on crystals

AE data acquisition system	AE sensor	No. of sensor(s), Sensor location	Sensor frequency band / *Resonant	Gain: Pre-amp/*SCU	Ref.
HIFREACE / Tektronix DSA 601A	Broadband ultrasonic point focus transducer of Panametrics V390, V3194	1, opposite to indentation surface	50 & 100 MHz	-	[77]
Locan 320 system from PAC	Piezoelectric	1, indentation surface	-	-	[83]
AECL105, UK /Digital Oscilloscope	AE sensor, M304A (Fuji Ceramics)	1, opposite to indentation surface	10 kHz-1 MHz/*300 kHz	40 dB/*60-75 dB	[84]
Mistras 2001 AEDSP-32/16, PAC	-	-	-	-	[85]
-	Piezoelectric	1, indentation surface	100 kHz-1 MHz/*160 kHz	-	[86]
Locan 320 system, PAC	Piezoelectric	1, indentation surface	3 kHz-1.2 MHz	-	[89]
Tektronics digital storage scope	Piezoelectric	1, opposite to indentation surface	10 kHz-1 MHz	*250 times amplitude	[90]
TriboAE system, Hysitron Inc.	Hysitron AE indenter sensor	1, indentation surface	0.1-1.1 MHz	-	[91-93]
AMSY-5	AE sensor	1, underneath the specimen	100-400 kHz	-	[94]
Tektronics digital storage scope	PAC S9229	1, indenter is a sensor	625 kHz	100/1000 dB	[95]

Table A.3 AE system used to study indentations on glass

AE data acquisition system	AE sensor	No. of sensor(s), Sensor location	Sensor frequency band / *Resonant	Gain: Pre-amp/*SCU	Ref.
AE Fracture Wave Detector (FWD, Model FM-1)	Broadband transducer (DWC B1025)	-	-	40 dB	[81]
AMSY-5	AE sensor	1, underneath the specimen	100-400 kHz	-	[94]
-	Broadband sensor	1, opposite to indentation surface	20 kHz-1 MHz	80 dB	[96]
-	AE sensors	2, near sample but on base plate	-	-	[97]
AET-5000	Piezoelectric	1, indentation surface	125-250/*175 kHz	*80 dB	[98]
Digitizing Oscilloscope, HP model no. 54501A	Piezoelectric translator (model: 8152A2, Kistler, Amherst, NY)	1, indenter mounted in a fixture on the end of PZT	100-900/*200 kHz	-	[99]
-	Broadband sensor	8, opposite to indentation surface	10 kHz-2 MHz	60 dB	[100]
-	Broadband sensor	8, opposite to indentation surface	-	60 dB	[101]

Table A.4 AE system used to study indentations on composites

AE data acquisition system	AE sensor	No. of sensor(s), Sensor location	Sensor frequency band / *Resonant	Gain: Pre-amp/*SCU	Ref.
SPARTAN AT	Piezoelectric	1, indentation surface	0.1-1.0 MHz/*125 kHz	40/60 dB; *30 dB	[80]
AE Fracture Wave Detector (FWD, Model FM-1)	Broadband transducer (DWC B1025)	-	-	40 dB	[81]
LOCAN 320 system from PAC	Piezoelectric	1, indentation surface	3 kHz-1.2 MHz	*0/60 dB	[89]
In-house built AE apparatus, Univ. of Surrey	-	-	-	-	[102]
-	AE Piezoelectric sensor	1, sensor mounted on indenter mandrel	-	-	[103]
SPARTAN-AT, PAC	R15, PAC	1, indentation surface	-	*40 dB	[104-105]
MD-1100S AE system	AE sensors	1, sensor mounted on indenter	-	-	[106]
PAC PCI-DSP4 AE system	Piezoelectric PAC R15 sensor	4, indentation surfaces	-	-	[107]
AET-5000	PAC type WD	1, indentation surface	100-1000 kHz	60 dB/*0/40 dB	[108]
LOCAN AT6	-	1, opposite to indentation surface	50-1000 kHz	40 dB, *20 dB	[109]
-	-	1, opposite to indentation surface	-	-	[110]

Table A.5 AE system used to study indentations on metals and metallic foams

AE data acquisition system	AE sensor	No. of sensor(s), Sensor location	Sensor frequency band / *Resonant	Gain: Pre-amp/*SCU	Ref.
System calibration by Frank Breckenridge	Piezoelectric	1, opposite to indentation surface	-	*76 dB	[112]
DAKEL-XEDO-3 AE system	LB10A AE transducer	1, indentation surface	100-600 kHz	*94, *90 & *70 dB	[113-114]

Table A.6 AE system used to study indentations on thin solid films

AE data acquisition system	AE sensor	No. of sensor(s), Sensor location	Sensor frequency band / *Resonant	Gain: Pre-amp/*SCU	Ref.
TriboAE system, Hysitron Inc.	Hysitron AE indenter sensor	1, indenter is a sensor	100-2000 kHz/*130 kHz	-	[70]
ASCO: AE system from Vallen	Piezoelectric	-	-	-	[72]
Tektronics digital storage scope	Piezoelectric	1, opposite to indentation surface	10 kHz-1 MHz	*250 times amplitude	[90]
AECL105, UK /Digital Oscilloscope	AE sensor, M304A (Fuji Ceramics)	1, opposite to indentation surface	10 kHz-1 MHz/*300 kHz	40 dB/*60-75-100 dB	[84] [115]
HP 54501A Digitizing Oscilloscope	Piezoelectric translator : Kistler 8152A2	1, sensor mounted to moveable cross-head	100-900 kHz/*200 kHz	*40 dB	[116]
Vallen AMSY4 AE system	AE sensor	-	-	-	[117]
Compu Scope, CS12100 Gage Applied Science	Piezoelectric, PAC, Type PICO	4, mounted on four end surfaces	-	60 dB	[118]
GAGE Applied, Inc.	PICO: PAC	4, opposite to indentation surface	*450 kHz	60 dB	[120]
NanoScope III, Digital Instruments Co.	Bandwidth AE sensor	1, indenter mounted in a special holder with a miniature AE sensor	0.1-2 MHz	*60 dB	[122]
AE analyzer	AE sensor	1, indenter is a sensor	-	-	123]
Piezoelectric transducer (Brüel & Kjaer, Denmark)	-	-	-	-	[125] [124]
ANSY 4, AE system from Vallen	Broad band piezoelectric, DECI / SE 150-M	1, sensor on indenter shaft	*160 kHz	40 dB	[128]

Table A.7 AE system used to study indentations on thermal spray coating

AE data acquisition system	AE sensor	No. of sensor(s), Sensor location	Sensor frequency band / *Resonant	Gain: Pre-amp/*SCU	Ref.
AC 175L AETC	Piezoelectric	1, indentation surface	-	*94 dB	[27]
AET-5000	Broad band piezoelectric	1, opposite to indentation surface	-	-	[28]
AET-5500	Piezoelectric PICO transducer, PAC	1, indentation surface	-	-	[29]
AET-5500	-	1, indentation surface	10 kHz-1 MHz / *250 kHz	*40 dB	[30]

Appendix B

Appendix B: Thermal spray process parameters

Table B.1 Thermal spray process parameters (Vickers indentation test specimens)

Thermal Spraying Gun	Industrially optimized spray conditions and powders	
JP5000 HVOF (as-sprayed) [32]	Spray material	WC-12%Co (sintered and crushed)
	Oxygen flow	940 l/min
	Powder size	15-50 µm
	Kerosene flow	0.37 l/min
	Spray distance	380 mm
JetKote HVOF (as-sprayed & HIPed)	Spray material	WC-12%Co
	Spray conditions	Coatings studied were industrially optimized by Deloro Stellite, UK. Spraying process parameters are not available due to propriety reason.
9-MB Metco Air Plasma Spraying (APS) [160]	Spray material	Conventional alumina (Al_2O_3 > 98.0%)
	Powder size	10-45 µm
	Arc current	500 A
	Arc voltage	70 V
	Primary gas	37.6 l/min (Ar)
	Secondary gas	7.1 l/min (H_2)
	Spray distance	80 mm
Theta-gun High Velocity Oxy-Fuel (HVOF) [160]	Spray material	Fine powder alumina (Al_2O_3 > 98.0%)
	Powder size	1-5 µm
	Oxygen flow rate	893 l/min
	Kerosene flow rate	0.32 l/min
	Acetylene flow rate	43 l/min
	Spray distance	150 mm

Appendix C

Appendix C: AE sensor calibration certificate

PHYSICAL ACOUSTICS CORPORATION
A MISTRAS Holdings Company

AE SENSOR CALIBRATION CERTIFICATE

Sensor Name:	MICRO-80D	**Test Date:**	7/28/03	**Max. Value (dB):**	-60.95
Sensor S/N:	91	**Tested By:**	N.M.	**Peak Freq.(kHz):**	332.03
Comment:					

Sensitivity dB ref 1V/ubar

PAC Certifies that this sensor meets all performance, environmental and physical standards established in applicable PAC specifications.
Calibration methodology based on ASTM standard E976- "Guide for Determining the Reproducibility of Acoustic Emission Sensor Response."

Appendix D

Appendix D: Thermal spray masking sheet with slits

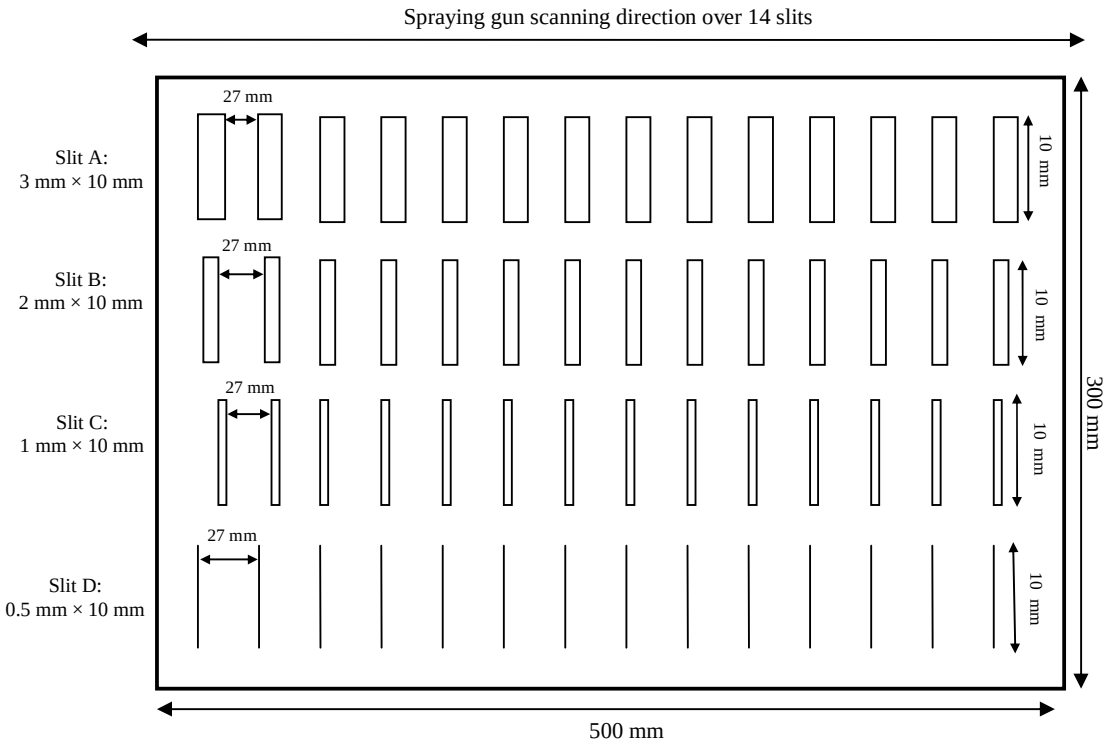

Appendix E

Appendix E: XRD patterns of thermal spray powders and coatings

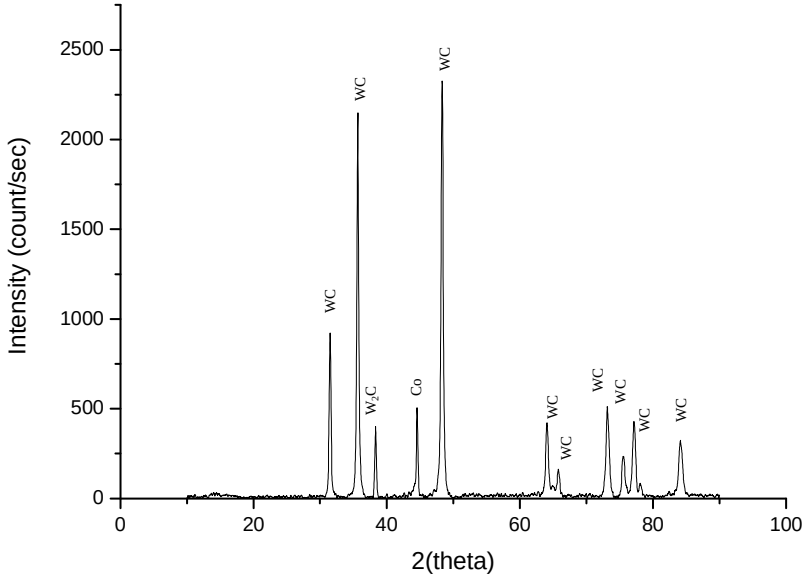

Figure E.1 XRD pattern of WC-12%Co (JP5000) powder [32]

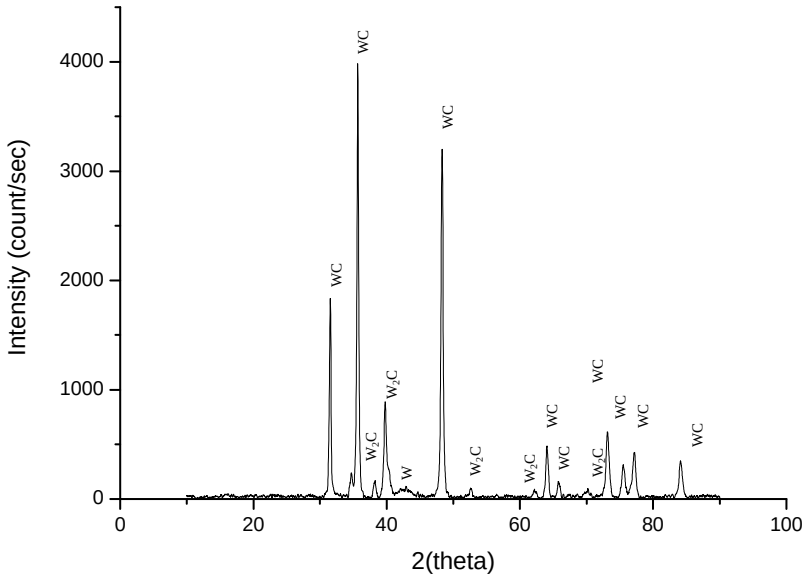

Figure E.2 XRD pattern of as-sprayed HVOF (JP5000) WC-12%Co coatings [32]

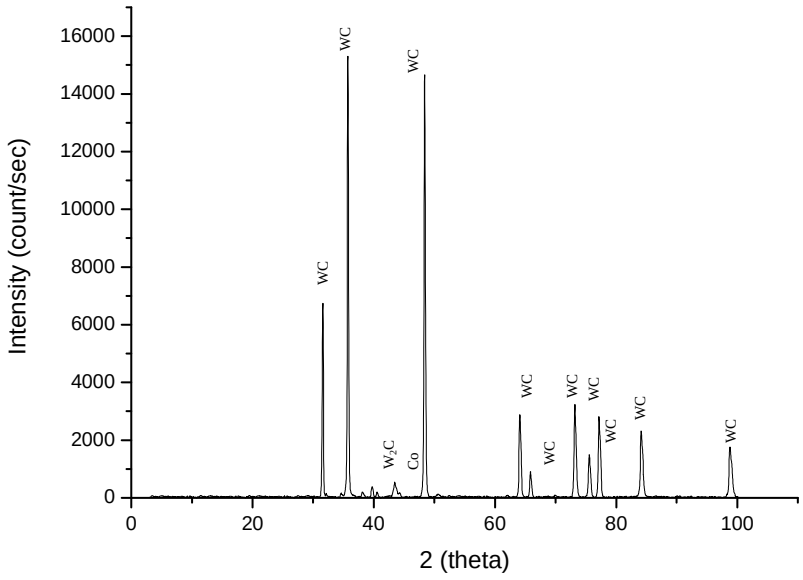

Figure E.3 XRD pattern of HVOF (JetKote) WC-12%Co powders [32]

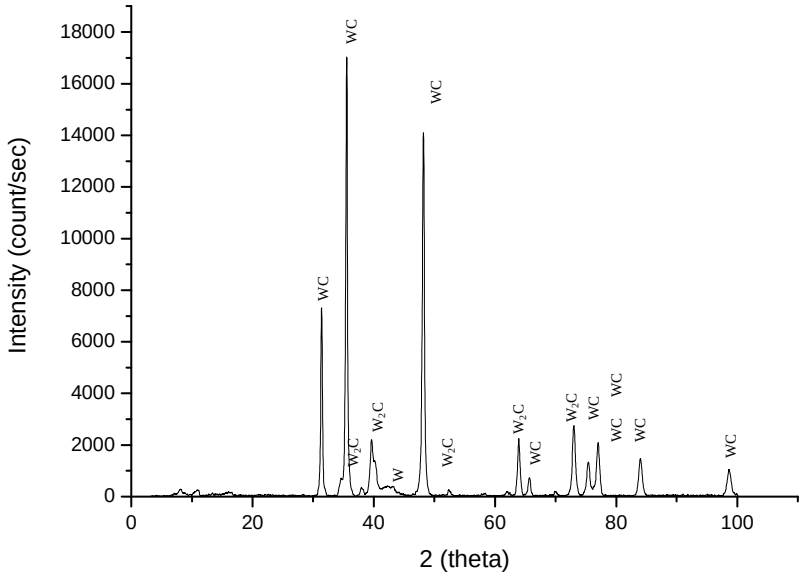

Figure E.4 XRD pattern of as-sprayed HVOF (JetKote) WC-12%Co coatings [32]

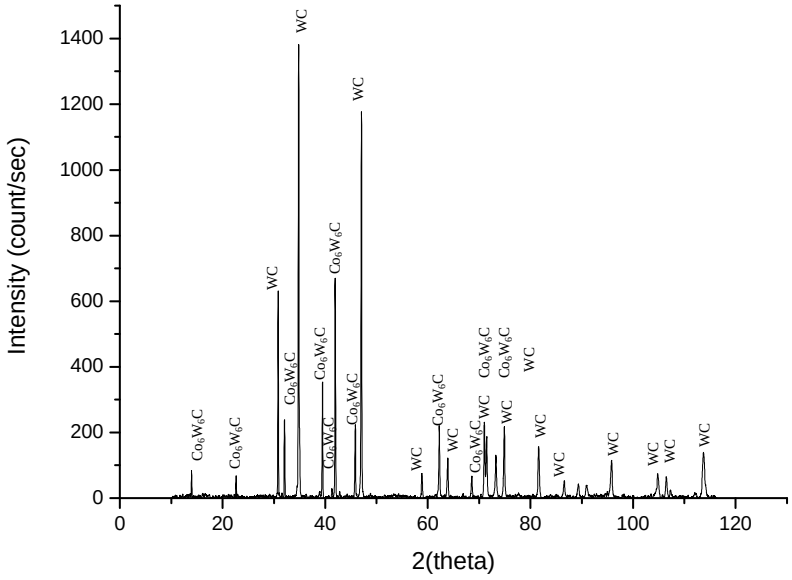

Figure E.5 XRD pattern of HIPed HVOF (JetKote) WC-12%Co coatings [32]

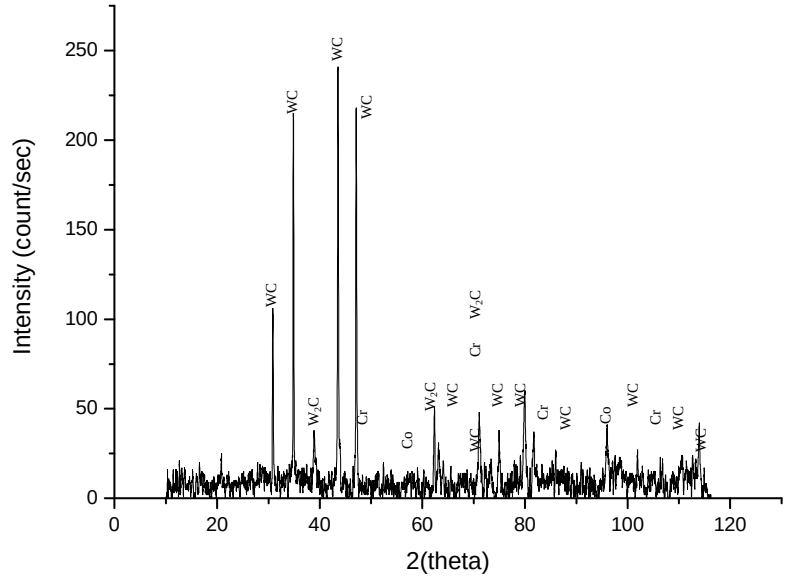

Figure E.6 XRD pattern of as-sprayed HVOF WC-10%Co-4%Cr (JP5000) coatings

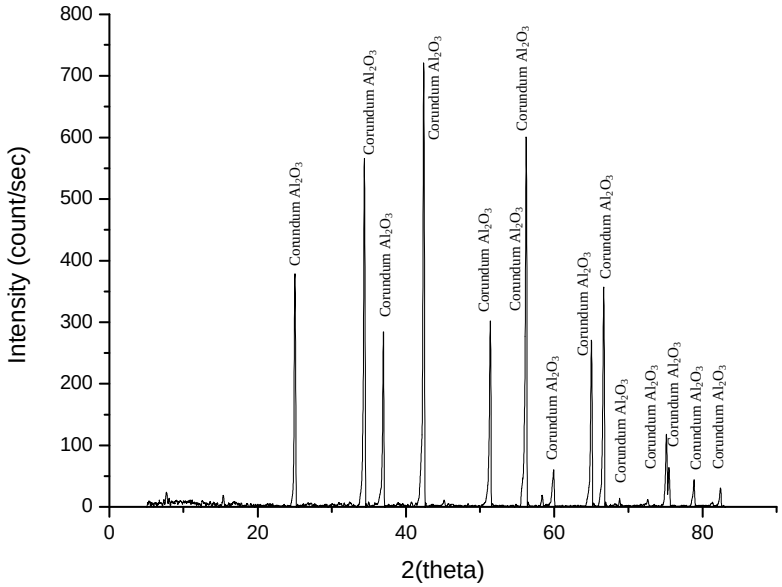

Figure E.7 XRD pattern of Al_2O_3 conventional powders

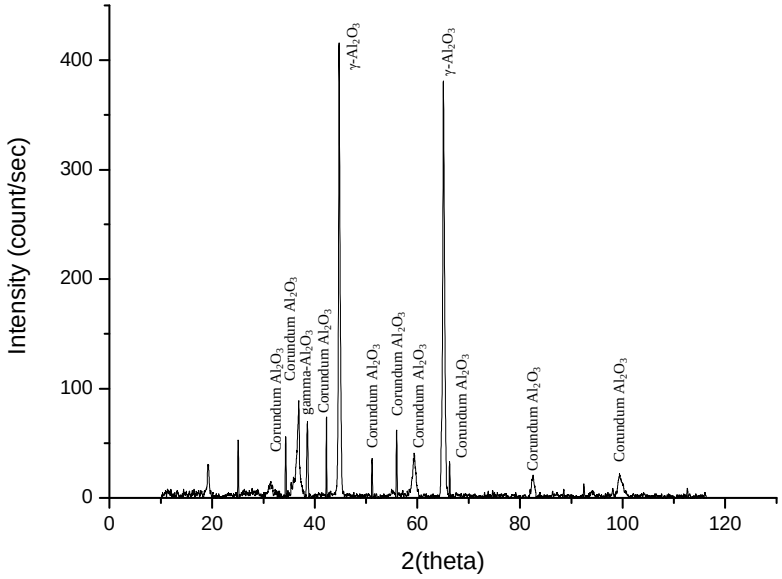

Figure E.8 XRD pattern of the APS (Metco, 9MB) Al_2O_3 (conventional powder) coatings

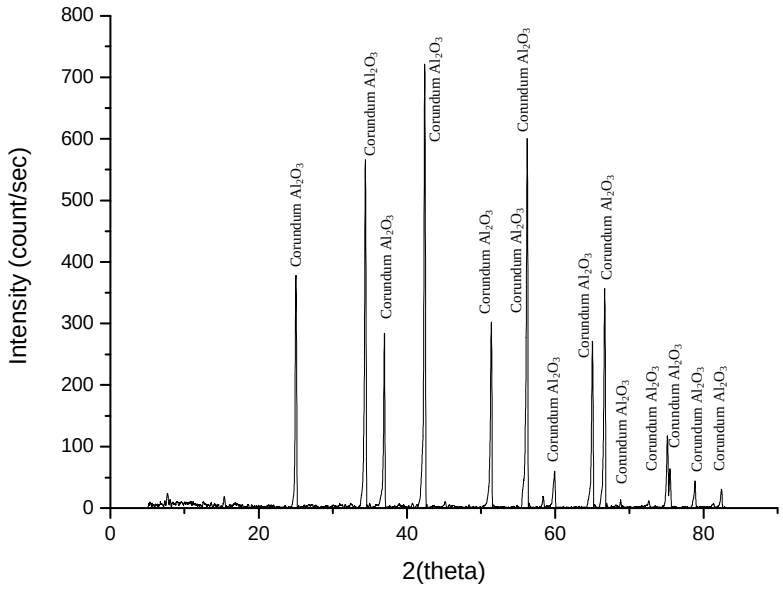

Figure E.9 XRD pattern of Al_2O_3 fine powders

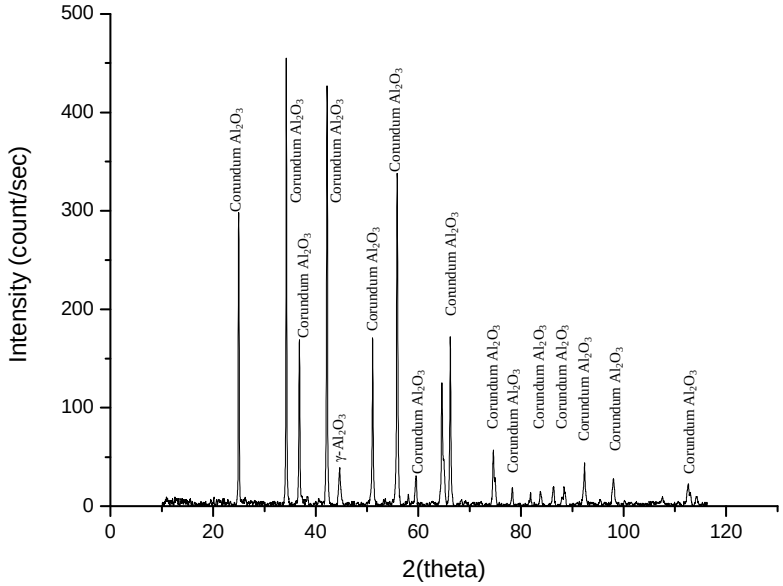

Figure E.10 XRD pattern of as-sprayed HVOF (theta-gun) Al_2O_3 (fine powder) coatings

Appendix F

Appendix F: Dynamic indentation model

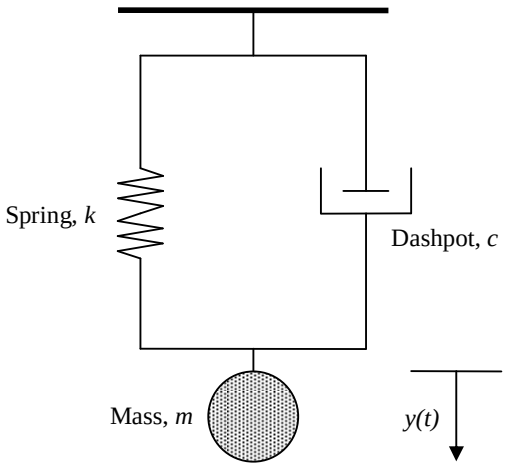

Figure F.1 A mechanical model of open loop indentation systems after landing the specimen surface (under-damped linear vibrations of a one-degree-of-freedom system

An open loop indentation system shown in **Figure F.1** has mainly three mechanical components. Those components are dashpot, mass and the spring which are arranged in series. Damping that produces a damping force proportional to the mass's velocity is referred to as viscous damping, and is graphically represented by a dashpot. Mass represents the load applied through indenter and spring represents the stiffness of material on which the indenter is landing during indentation process. To study the displacement and load profile as a function of time, the dynamic response of constant dead-weight type macrohardness indentation system has to be determined during loading phase of the indenter (i.e. after the indenter lands on the specimen).

The damping forces of these types are proportional to the velocity of the load and act opposite to the direction of motion. As the indenter lands on the specimen surface (i.e. during loading stage), the velocity of the indenter goes from the approach velocity to zero, being decelerated by the ploughing resistance of the material.

The final settling of the indenter can be regarded as a damped system, governed by the equation of motion:

$$m.y''(t) = -k.y(t) - c.y'(t) \qquad \text{(F1)}$$

where *m* is the indentation mass in kilogram, *c* is a damping constant (characteristic of the flow properties of the material in *Ns* m^{-1}), *k* is the spring stiffness (characteristic of the elastic properties of the material in *N* m^{-1}) and *y(t)* is the indenter penetration depth into the specimen. Both *c* and *k* will depend on the geometrical form of the indenter [59]. The equation of motion can be written using the analogy of a simple harmonic oscillator:

$$y''(t) + 2.\xi.\beta_n.y'(t) + \beta_n{}^2.y(t) = 0 \qquad \text{(F2)}$$

where $\beta_n = \sqrt{\frac{k}{m}}$, $\xi = \frac{c}{2\sqrt{km}}$ and the characteristic roots are:

$$r_{1,2} = \beta_n\left(-\xi \pm \sqrt{\xi^2 - 1}\right) \qquad \text{(F3)}$$

When $\xi < 1$, the roots are complex conjugates, $r_{1,2} = \beta_n\left(-\xi \pm i\sqrt{1-\xi^2}\right)$, and the system is said to be underdamped, and the motion contains a harmonic component.

The general solution of the differential equation for the underdamped case is:

$$y(t) = e^{-\xi\beta_n t}\left[C_4.Cos(\beta_d.t) + C_5.Sin(\beta_d.t)\right] \qquad \text{(F4)}$$

Using the initial conditions:

$y(t)_{t=0} = y_0$; (i.e. displacement of indenter in material at $t = 0$ is y_0) (F5)

$\frac{d}{dt}\left[y(t)\right]_{t=0} = V_0$; (i.e. initial velocity of indenter at $t = 0$ is V_0) (F6)

$$y(t) = e^{-\xi\beta_n t}\left[y_0.Cos(\beta_d.t) + \frac{V_0 + \xi.\beta_n.y_0}{\beta_d}.Sin(\beta_d.t)\right] \qquad \text{(F7)}$$

which is a sinusoidal of frequency $\beta_d = \beta_n\sqrt{1-\xi^2}$, whose amplitude shows a characteristic decay time of $\frac{1}{\xi\beta_n}$. Translating this into material terms, the indenter would be expected to settle with an oscillation frequency proportional to $P^{-1/2}$.

Appendix G

Appendix G: Kinematic model of particle impact through slit

As was seen in Chapter 4 *(Section 4.4)*, the slit experiments have demonstrated that spray-substrate interaction generates measurable AE, although it is by no means certain that individual particle impacts will be observable either by the time- or amplitude-resolution of the method. It is therefore of interest to develop a model describing the approaching particle density, size and velocity distributions as an aid to analysing the data from slit and slit-free experiments. A cross-section of the spray can be assumed to contain a constant density of particles of constant size, travelling at constant velocity towards the surface and the total particle kinetic energy passing through a slit determined as a function of time. A formulation for the effective spraying area through a slit and the distribution of kinetic energy of particles landing on the substrate are described below.

Figure G.1 illustrates a spray spot of radius, R, passing over a fixed slit at a given lateral speed, V_s. In any time interval the increase and decrease in 'effective area', of the thermal spray spot overlapping the slit determines the number of sprayed particles landing on the substrate in the time step.

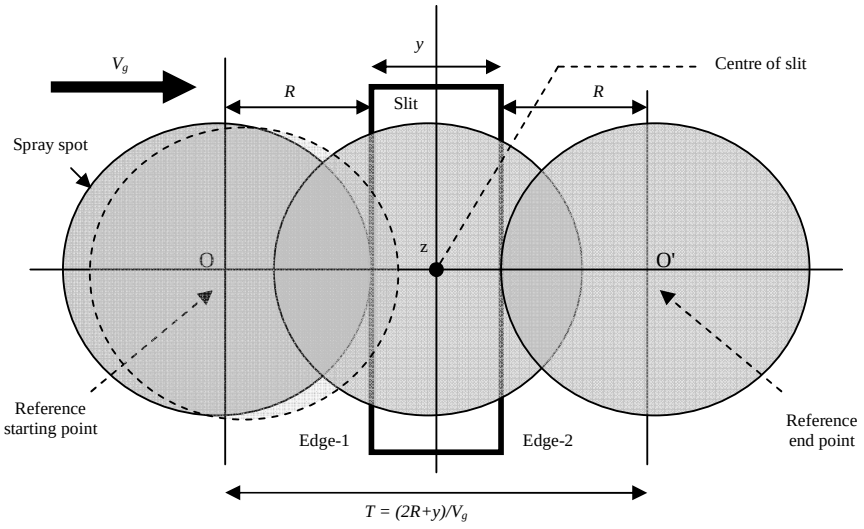

Figure G.1 Kinematics of the spray spot scanning a slit

As shown in **Figure G.1**, the effective area of spray passing through the slit increases after the spray spot leading circumference crosses the Edge-1 of the slit until the centre

of the spray spot (O) is at the centre of the slit (*z*). Thereafter, the effective area starts decreasing until the trailing circumference of the spray spot passes Edge-2 of the slit. The increment and decrement in the 'effective area' will therefore be a symmetric function, and can be formulated using the schematic diagram shown in **Figure G.2**. The angle of arc subtended at the slit Edges 1 and 2 are θ & δ, respectively, and each is a function of time, or of the position of the spray spot with respect to the fixed slit.

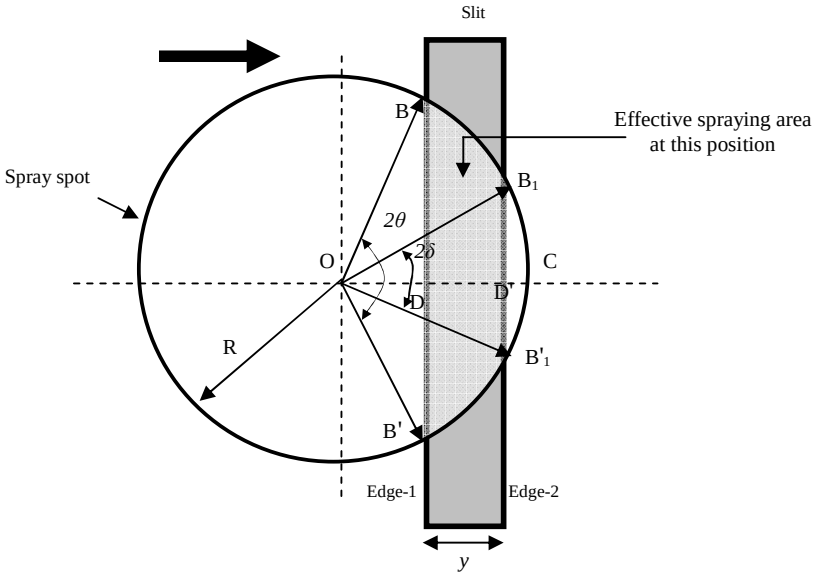

Figure G.2 Kinematics of the spray spot scanning a slit and its formulation

In the general case where the leading circumference has passed Edge-2, the effective area, $A_s(t)$, is given by the shaded area illustrated in **Figure G.2**. This area can be expressed as the difference between two circular caps where the chords are BB' and $B_1B'_1$ in **Figure G.2**. Therefore, the effective area:

$$A_s(t) = \left(\frac{1}{2}\right)\left[R^2\{2(\theta(t)-\delta(t)) - (sin2\theta(t) - sin2\delta(t))\}\right] \qquad \text{(G1)}$$

The functions $\theta(t)$ and $\delta(t)$ can be obtained by recognising that the angle (θ and δ) increase from 0 to π as the spray area centre traverses the Edge-1 and Edge-2.

Setting a time datum ($t_1 = 0$) when the spot encounters Edge-1 (at $\theta = 0$) and passes (at $\theta = \pi$) in time, T_θ, it is possible to determine the angle $\theta(t)$ from the gun transverse speed, *Vg*, the slit width and the spot radius (see **Figure G.1**):

$$\theta(t) = \pi\left[\frac{t_1}{T_\theta}\right] = \left[\frac{\pi.t_1.V_g}{2R}\right]; \qquad \text{(G2)}$$

for $0 \le t_1 \le \frac{2R}{V_g}, T_\theta = \frac{2R}{V_g}$

The angle $\delta(t)$ can be written in an exactly analogous fashion, except that the position trails that for $\theta(t)$ by an amount equal to the slit width, i.e. a time $t_y = \frac{y}{V_g}$:

$$\delta(t) = \pi\left[\frac{t_1}{T_\theta}\right] - \pi\left[\frac{t_y}{T_\theta}\right] \qquad \text{(G3)}$$

for $\frac{y}{V_g} \le t_y \le \left(\frac{y}{V_g} + \frac{2R}{V_g}\right)$

For formulating the number of sprayed powder particles passing through the slit, it is assumed that the powder particles are sprayed through the gun with a constant flux, the powder is of uniform diameter and density and the incident particle density across the spot is uniform. Thus, the number of sprayed particles passing through the slit depends on the slit width (y), gun speed (V_g), the powder mass flow rate, the flame spray spot area (A) and the powder particle kinetics [density (ρ), radius (r), and velocity (V)].

If the powder mass flow rate (g sec^{-1}) is $\dot{m}_{powder}$, and the mass of one particle $m_p = \frac{4}{3}\pi r^3 \rho$, then the number of particles approaching the slit per second is: $\dot{N} = \frac{\dot{m}_{powder}}{m_p}$. The number of particles passing through the slit per second is therefore $\dot{N}_s(t) = \frac{A_s(t)}{A}\dot{N}$, where $\dot{N}_s(t)$ is a function of time, and this can be converted to a mass flow rate impinging on the target, $\dot{m}$, of $\dot{m} = \dot{N}_s(t).m_p$, and so the energy rate, $\dot{E}$ associated with the kinetic energy of the particles is:

$$\dot{E}(t) = \frac{1}{2}\dot{m}V^2 = \frac{1}{2}m_p V^2 \frac{A_s(t)}{A}\frac{\dot{m}_{powder}}{m_p} = \frac{1}{2}\dot{m}_{powder}V^2\left(\frac{A_s(t)}{A}\right) \qquad \text{(G4)}$$

Assuming that a constant proportion of this kinetic energy is recorded at the sensor, the function $\dot{E}(t)$ ought to be of similar shape to the AE energy pulse observed as the spray passes over a slit.

REFERENCES

[1] D. Tabor, 1951, The hardness of metals, Clarendon Press, Oxford

[2] B. R. Lawn and M. V. Swain, *Microfracture beneath point indentations in brittle solids*, Journal of Materials Science, **10**, 1975, 113-122

[3] B. R. Lawn and R. Wilshaw, *Review, Indentation fracture: principles and applications*, Journal of Materials Science, **10**, 1975, 1049-1081

[4] B. R. Lawn, 1993, Fracture of Brittle Solids, 2nd Edition, Cambridge Solid State Science Series, Cambridge

[5] J. Lankford, *Indentation microfracture in Plamqvist crack regimes: implications for fracture toughness evaluation by the indentation method*, Journal of Materials Science Letters, **1**, 1982, 493-495

[6] B. R. Lawn and A. G. Evans, *A model for crack initiation in elastic/plastic indentation fields*, Journal of Materials Science, **12**, 1977, 2195-2199

[7] K. Nihara, R. Morena and D. P. Hasselman, *Evaluation of K_{1c} of brittle solids by the indentation method with low crack-to-indent ratios*, Journal of Materials Science Letters, **1**, 1982, 13-16

[8] K. Nihara, *A fracture mechanics analysis of indentation-induced Palmqvist crack in ceramics*, Journal of Materials Science Letters, **2**, 1983, 221-223

[9] B. R. Lawn, E. R. Fuller, *Equilibrium penny-like cracks in indentation fracture*, Journal of Materials Science, **10**, 1975, 2016-2024

[10] D. K. Shetty, I. G. Wright, P. N. Mincer and A. H. Clauer, *Indentation fracture of WC-Co cermets*, Journal of Materials Science, **20**, 1985, 1873-1882

[11] K. M. Liang, G. Orange and G. Fantozzi, *Evaluation by indentation of fracture toughness of ceramic materials*, Journal of Materials Science, **25**, 1990, 207-214

[12] C. K. Lin, C. C. Lin and C. C. Berndt, *Simulation of hardness on plasma-sprayed coatings*, Journal of American Ceramic Society, **78**(5), 1995, 1406-1410

[13] C. K. Lin and C. C. Berndt, *Statistical analysis of microhardness variations in thermal spray coatings*, Journal of Materials Science, **30**, 1995, 111-117

[14] S. Ghosh, S. Das, T. K. Bandyopadhyay, P. P. Bandyopadhyay and A. B. Chattopadhyay, *Indentation responses of plasma sprayed ceramic coatings*, Journal of Materials Science, **38**, 2003, 1565-1572

[15] E. L. Cantera and B. G. Mellor, *Fracture toughness and crack morphologies in eroded WC-Co-Cr thermally sprayed coatings*, Materials Letters, **37**, 1998, 201-210

[16] J. Lesage and D. Chicot, *Role of residual stresses on interface toughness of thermally sprayed coatings*, Thin Solid Films, **415**, 2002, 143-150

[17] M. M. Lima, C. Godoy, J. C. Avelar-Batista and P. J. Modenesi, *Toughness evaluation of HVOF WC-Co coatings using non-linear regression analysis*, Materials Science and Engineering A, **357**, 2003, 337-345

[18] M. M. Lima, C. Godoy, P. J. Modenesi, J. C. Avelar-Batista, A. Davison and A. Matthews, *Coating fracture toughness determined by Vickers indentation: an important parameter in cavitation erosion resistance of WC-Co thermally sprayed coatings*, Surface and Coatings Technology, **177-178**, 2004, 489-496

[19] C. M. Nygards, K. W. White and K. Ravi-Chandar, *Strength of HVOF coating-substrate interface*, Thin Solid Film, **332**, 1998, 185-188

[20] C. B. Scruby, *An introduction to acoustic emission*, Journal of Physics E: Sci. Instrum. **20**, 1987, 946-953

[21] R. L. Reuben, *The role of acoustic emission in industrial condition monitoring*, International Journal of COMADEM, **1**(4), 1998, 35-46

[22] J. A. Steel and R. L. Reuben, *Recent developments in monitoring of engines using acoustic emission*, J. Strain Analysis, **40**(1), 2005, 45-57

[23] P. Nivesrangsan, *Multi-source, multi-sensor approaches to diesel engine monitoring using acoustic emission*, PhD thesis, Heriot-Watt University, Edinburgh, UK, December 2004.

[24] M. F. Shehadeh, *Monitoring of Long Steel Pipes using Acoustic Emission*, PhD thesis, Heriot-Watt University, Edinburgh, UK, December 2004.

[25] R. M. Douglas, *Monitoring of the piston ring-pack and cylinder liner interface in diesel engines through acoustic emission measurements*, PhD thesis, Heriot-Watt University, Edinburgh, UK, July 2007.

[26] J. Miettinen, *Condition Monitoring of Grease Lubricated Rolling Bearings by Acoustic Emission Measurements*, PhD thesis, Tampere University of Technology, Tampere, Finland, 2000

[27] S. Safai, H. Herman and K. Ono, *Acoustic emission study of thermal-sprayed oxide coatings*, American Ceramic Society Bulletin, **58**, 1979, 624

[28] S. L. Ajit Prasad, M. M. Mayuram and R. Krishnamurthy, *Response of plasma-sprayed alumina-titania composites to static indentation process*, Materials Letters, **41**, 1999, 234-240

[29] K. Vijayakumar, A. K. Sharma, M. M. Mayuram and R. Krishnamurthy, *Response of plasma-sprayed alumina-titania ceramic composite to high-frequency impact loading*, Materials Letters, **54**, 2002, 403-413

[30] U. Senturk, R. S. Lima, C. R. C. Lima, C. C. Berndt, *Deformation of plasma sprayed thermal barrier coatings*, Transactions of the ASME, Journal of Engineering for Gas Turbines and Power, **122**, 2000, 387-392

[31] V. Stoica, R. Ahmed, T. Itsukaichi and S. Tobe, *Sliding wear evaluation of hot isostatically pressed (HIPed) thermal spray cermet coatings*, Wear, **257**, 2004, 1103-1124

[32] V. Stoica, *Sliding wear of post-treated thermal spray cermet coatings*, PhD thesis, Heriot-Watt University, Edinburgh, UK, 2005.

[33] C. B. Ponton and R. D. Rawlings, *Vickers indentation fracture toughness test: Part 1. Review of literature and formulation of standardised indentation toughness equations*, Materials Science and Technology, **5**, 1989, 865-872

[34] M. Factor and I. Roman, *Use of microhardness as a simple means of estimating relative wear resistance of carbide thermal spray coatings: Part 2. Wear resistance of cemented carbide coatings*, Journal of Thermal Spray Technology, **11**(4), 2002, 482-495

[35] M. Factor and I. Roman, *Microhardness as a simple means of estimating relative wear resistance of carbide thermal spray coatings: Part 1. Wear resistance of cemented carbide coatings*, Journal of Thermal Spray Technology, **11**(4), 2002, 468-481

[36] ASM Handbook Volume 8: Mechanical Testing and Evaluation (Hardness Testing), ASM International, Metals Park, Ohio, 2000.

[37] J. H. Westbrook and H. Conrad, The Science of Hardness Testing and Its Research Applications, American Society of Metals, 1973

[38] N. K. Mukhopadhyay and P. Paufler, *Micro- and nanoindentation techniques for mechanical characterisation of materials*, International Materials Reviews, **51**(4), 2006, 209-245

[39] R. Hill, The mathematical theory of plasticity, Clarendon Press, 1950

[40] W. Lee and B. Derby, *Hertzian Testing of Ceramics*, British Ceramic Proceedings, **59**, 1999, 45-60

[41] A. A. Griffith, *The Phenomena of Rupture and Flow in Solids*, Philosophical Transaction: Royal Society of London A, **221**,1920, 163-198

[42] F. C. Frank and B. R. Lawn, *On the theory of Hertzian fracture*, Proc. of Royal Soc. Of London A, **299**, 1967, 291-306

[43] T. R. Wilshaw, *The Hertzian fracture test*, Journal of Physics D: Applied Physics, **4**, 1971, 1567-1583

[44] D. J. Greving, J. R. Shandley and E. F. Rybicki, *Effects of coating thickness and residual stresses on the bond strength of ASTM C633-79 thermal spray coating test specimens*, Journal of Thermal Spray Technology, **3**(4) 1994, 371-378

[45] T. W. Clyne and S. C. Gill, *Residual stresses in thermal spray coatings and their effect on interfacial adhesion: a review of recent work*, Journal of Thermal Spray Technology, **5**(4), 1996, 401-418

[46] W. Fischer, H. Gruhn and W. Mallener, *Residual stress in plasma-sprayed ceramic coatings*, Materials Science Forum, **228-231**, 1996, 481-486

[47] F. Kroupa, *Residual stresses in thick nonhomogeneous coatings*, Journal of Thermal Spray Technology, **6**(3), 1997, 309-319

[48] R. Ahmed, H. Yu, S. Stewart, L. Edwards, J. Santisteban, *Residual strain measurement in thermal spray cermet coatings via neutron diffraction*, ASME Journal of Tribology, **129**, 2007, 411-418.

[49] R. Ahmed, H. Yu, V. Stoica, L. Edwards, J.R. Santisteban, *Neutron diffraction residual strain measurements in post-treated thermal spray cermet coatings*, Materials Science and Engineering A, **498**, 2008, 191–202

[50] D. B. Marshall, B. R. Lawn, P. Chantikul, *Residual stress effect in sharp contact cracking*, Journal of Materials Science, **14**, 1979, 2225-2235

[51] H. Luo, D. Goberman, L. Shaw and M. Gell, *Indentation fracture behaviour of plasma-sprayed nanostructured Al_2O_3-13wt. %TiO_2 coatings*, Materials Science and Engineering A, **346**, 2003, 237-245

[52] A. Roman, D. Chicot and J. Lesage, *Indentation test to determine the fracture toughness of nickel phosphorus coatings*, Surface and Coatings Technology, **155**, 2002, 161-168

[53] P. Ostojic and R. McPherson, *Indentation toughness testing of plasma sprayed coatings*, Materials Forum, **10**(4), 1987, 247-255

[54] X. Lin, Y. Zeng, S. W. Lee and C. Ding, *Characterization of alumina-3 wt. % titania coating prepared by plasma spraying of nanostructured powders*, Journal of European Ceramic Society, **24**, 2004, 627-634

[55] H. Luo, D. Goberman, L. Shaw and M. Gell, *Indentation fracture behaviour of plasma-sprayed nanostructured Al_2O_3-13wt. %TiO_2 coatings*, Materials Science and Engineering A, **346**, 2003, 237-245

[56] A. P. Buang, R. Liu, X. J. Wu, M. X. Yao, *Cracking analysis of HVOF coatings under Vickers indentation*, Journal of Coatings Technology and Research, **5**(4), 2008, DOI 10.1007/s11998-008-9106-8

[57] X. Cai, *Finite-element method for simulation of elasto-plastic indentations for various indentors*, Journal of Materials Science Letters, **11**(22), 1992, 1527-1531

[58] G. D. Quinn, P. J. Patel and I. Lloyd, *Effect of loading rate upon conventional ceramic microindentation hardness*, Journal of Research of the National Institue of Standards and Technology, **107**(3), 2002, 299-306

[59] N. M. Vriend and A. P. Kren, *Test Method-Determination of the viscoelastic properties of elastomeric materials by the dynamic indentation method*, Polymer Testing, **23**, 2004, 369-375

[60] X. Li, B. Bhushan, *A review of nanoindentation continuous stiffness measurement technique and its application*, Materials Characterization, **48**, 2002, 11-36

[61] M. R. VanLandingham, *Review of instrumented indentation*, Journal of Research of the National Institute of Standards and Technology, **108**(4), 2003, 249-265

[62] B. Bhushan, A. V. Kulkarni, *Nanoindentation and picoindentation measurements using a capacitive transducer system in atomic force microscope*, Philosophical Magazine A, **74**(5), 1996, 1117-1128

[63] B. Bhushan, X. Li, *Nanomechanical characterization of solid surfaces and thin films*, International Materials Reviews, **48**(3), 2003, 125-164

[64] S. G. Sheshadri, M. Srinivasan, L. King, *Indentation Fracture Testing of Ceramics*, Ceramic Eng. Sci. Proc., **4**(9-10), 1983, 853-863

[65] Wilson Wolpert, Micro/Vickers hardness tester, Tukon 2100

[66] Wilson Instruments, Hardness Testing with a Closed Loop Control System

[67] Struers Ltd., Hardness tester, Duramin-A300

[68] A. Gouldstone, N. Chollacoop, M. Dao, J. Li, A. M. Minor and Y. L. Shen, *Indentation across size scales and disciplines: recent developments in experimentation and modelling*, Acta Materialia, **55**, 2007, 4015-4039

[69] Private communication, Professor Sam Zhang, Nanyang Technological University, Singapore; Principal Editor: Journal of Materials Research, 2005

[70] J. M. Jungk, B. L. Boyce, T. E. Buchheit, T. A. Friedmann, D. Yang and W. W. Gerberich, *Indentation fracture toughness and acoustic energy release in tetrahedral amorphous carbon diamond-like thin films*, Acta Materialia, **54**(15), 2006, 4043-4052

[71] S. Bouras, I. Zerizer, F. Gheldane, M. T. Bouazza and B. Bouzabata, *Study of the resistance to crack propagation in alumina by acoustic emission*, Ceramics International, **34**, 2008, 1857–1865

[72] J. von Stebut, *Multi-mode scratch testing-a European standards, measurements and testing study*, Surface and Coatings Technology, **200**(1-4), 2005, 346-350

[73] J. Lankford, *Compressive microfracture and indentation damage in Al_2O_3*, Fracture Mechanics of Ceramics, **3**, 1978, 245-255

[74] S. Bouras and B. Bouzabata, *Study of Hertzian indentation on a transparent vitroceramic and on an alumina*, Materials Chemistry and Physics, **43**, 1996, 127-134

[75] H. Usami, T. Kadomae, D. Igimi and M. Mizuno, *Effect of indenter materials on indentation fracture of alumina ceramics*, Key Engineering Materials, **290**, 2005, 23-30

[76] Z. Xiaoli, W. Chongmin and Z. Hongtu, *Fracture toughness and acoustic emission in silicon carbide*, Journal of Materials Science Letters, **6**, 1987, 1459-1462

[77] F. Bergner, *High-frequency acoustic emission induced by indentation fracture in brittle materials*, Acustica, **82**, 1996, 498-503

[78] K. Kapoor, A. Ahmad, A. Laksminarayana and G. V. S. Hemanth Rao, *Fracture properties of sintered UO_2 ceramic pellets with duplex microstructure*, Journal of Nuclear Materials, **366**, 2007, 87-98

[79] J. Akbari, Y. Saito, T. Hanaoka and S. Enomoto, *Acoustic emission and deformation mode in ceramics during indentation*, JSME International Journal, Series A: Mechanics and Material Engineering, **37**(4), 1994, 488-494

[80] A. K. Ray, G. Das, N. K. Mukhopadhyay, D. K. Bhattacharya, E. S. Dwarakadasa and N. Parida, *Studies on indentation fracture toughness on ceramic and ceramic composite using acoustic emission technique*, Bulletin of Materials Science, **22**(1), 1999, 25-32

[81] S. H. Ahn, K. W. Nam and K. Ando, *The bending strength of brittle materials and the characteristics of the elastic wave signal by Vickers indentation*, Key Engineering Materials, **261-263**, 2004, 1635-1641

[82] A. L. Yurkov, E. Breval and R. C. Bradt, *Cracking during indentation in Sialon-based ceramics: kinetic microhardness and acoustic emission*, Journal of Materials Science Letters, **15**, 1996, 987-990

[83] F. Guiberteau, N. P. Padture and B. R. Lawn, *Effect of grain size on Hertzian contact damage in alumina*, J. of American Ceramic Society, **77**(7), 1994, 1825-1831

[84] M. V. Swain and M. Wittling, *Comparison of acoustic emission from pointed and spherical indentation of TiN films on silicon and sapphire*, Surface and Coatings Technology, **76-77**, 1995, 528-533

[85] B. A. Latella, T. Liu and A. J. Atanacio, *Effect of grain size on Hertzian contact damage in 9 mol% Ce-TZP ceramics*, Journal of European Ceramic Society, **22**, 2002, 1971-1979

[86] J. Lankford and D. L. Davidson, *The crack-initiation threshold in ceramic materials subject to elastic/plastic indentation*, Journal of Materials Science, **14**, 1979, 1662-1668

[87] R. P. Zhitaru and V. A. Rahvalov, *Peculiarities of prolonged plastic deformation of MgO crystals in the stress field of concentrated load*, Materials Science and Engineering B, **98**, 2003, 94-98

[88] Yu. S. Boyarskaya, R. P. Zhitaru, D. Z. Grabko and V. A. Rahalov, *Prolonged plastic deformation related to the micro-indentation of MgO single crystal*, Journal of Materials Science, **33**, 1998, 281-285

[89] E. Breval, V. Srikanth and E. C. Subbarao, *Acoustic emission and microcracking in sapphire, sintered Al_2O_3, Al/Al_2O_3 composite, and aluminum*, Journal of American Ceramic Society, **78**(9), 1995, 2541-2544

[90] T. P. Weihs, C. W. Lawrence, B. Derby, C. B. Scruby and J. Pethica, in W. D. Nix, J. C. Bravman, E. Artz and L. Ben Freund (eds.), Thin Films: Stresses and Mechanical Properties III, Materials Res. Society Symp. Proc., Pittsburgh, PA, **239**, 1992, 361-366

[91] N. I. Tymiak, A. Daugela, J. T. Wyrobek and O. L. Warren, *Highly localized acoustic emission monitoring of nanoscale indentation contacts*, Journal of Materials Research, **18**(4), 2003, 784-796

[92] N. I. Tymiak, A. Daugela, J. T. Wyrobek and O. L. Warren, *Acoustic emission monitoring of nanoindentation-induced slip and twinning in sapphire*, Mater. Res. Soc. Symp. Proc. 2003, 750, Y2.3.1-Y2.3.6

[93] N. I. Tymiak, A. Daugela, T. J. Wyrobek and O. L. Warren, *Acoustic emission monitoring of the earliest stages of contact-induced plasticity in sapphire*, Acta Materialia, **52**, 2004, 553-563

[94] P. Dyjak and R. P. Singh, *Acoustic emission analysis of nanoindentation-induced fracture events*, Mater. Res. Soc. Symp. Proc., **841**, 2005, R8.10.1-R8.10.6

[95] D. F. Bahr and W. W. Gerberich, *Relationships between acoustic emission signals and physical phenomena during indentation*, Journal of Materials Research, **13**(4), 1998, 1065-1074

[96] K. Y. Kim and W. Sachse, *Characteristics of acoustic emission signals of Hertzian and unloading cracks in glass*, Journal of Applied Physics, **55**(8), 1984, 2847-2856

[97] H. Usami, J. Sugishita, H. Kanie and K. Ohashi, *In-situ observation of Hertzian cracks in indentation damage of brittle materials*, Key Engineering Materials, **223**, 2002, 39-46

[98] S. H. Lee and H. C. Kim, *Acoustic emission during indentation fracture of soda-lime glass*, Journal of Materials Science Letters, **3**, 1984, 907-910

[99] B. V. Tanikella and R. O. Scatterwood, *Acoustic emission during indentation fracture*, Journal of American Ceramic Society, **78**(6), 1995, 698-702

[100] K. Y. Kim and W. Sachse, *Acoustic emission from penny-shaped cracks in glass. I. Radiation pattern and crack orientation*, Journal of Applied Physics, **59**(8), 1986, 2704-2710

[101] K. W. Kim and W. Sachse, *Acoustic emissions from penny-shaped cracks in glass. II. Moment tensor and source-time function*, Journal of Applied Physics, **59**(8), 1986, 2711-2715

[102] R. J. Kent, K. E. Puttick and J. G. Rider, *Indentation fracture testing of polystyrene injection mouldings*, Plastics and Rubber Processing and Applications, **1**, 1981, 55-61

[103] Y. Wang and B. W. Darvell, *Failure mode of dental restorative materials under Hertzian indentation*, Dental Materials, **23**, 2007, 1236-1244

[104] Y. C. Yang and K. S. Han, *Damage monitoring and impact detection using optical fiber vibration sensors*, Smart Materials and Structures, **11**, 2002, 337-345

[105] Y. C. Yang and K. S. Han, *Damage and failure monitoring of fiber-metals laminates using optical fiber sensors*, Key Eng. Materials, **270-273**, 2004, 690-695

[106] T. Kawaguchi, H. Nishimura, K. Ito, H. Sorimachi, T. Kuriyama and I. Narisawa, *Impact fatigue properties of glass fiber-reinforced thermoplastics*, Composite Science and Technology, **64**, 2004, 1057-1067

[107] F. Cesari, V. Dal Re, G. Minak and A. Zucchelli, *Damage and residual strength of laminated carbon-epoxy composite circular plates loaded at the centre*, Composites: Part A, **38**, 2007, 1163-1173

[108] C. Baudin, F. Cambier and L. Delaey, *Fractographic and acoustic emission of mullite-alumina-zirconia composites prepared by reaction sputtering*, Journal of Materials Science, **22**, 1987, 4398-4402

[109] P. S. Form, R. Pyrz, B. Clausen and E. Ø. Nielsen, *Indentation and acoustic emission in filtration processed platelet reinforced ceramics*, Materials Science and Engineering A, **197**, 1995, 231-236

[110] D. Rouby and H. Osmani, *Characterization of interface debonding in a ceramic-ceramic fibre composite using the indentation method and acoustic emission*, Journal of Materials Science Letters, **7**, 1998, 1154-1156

[111] D. Girodin, L. Manes, J-Y. Moraux, J-M. De Monicault, *Characterisation of the XD15N high nitrogen martensitic stainless steel for aerospace bearings*, 4th International Conference on Launcher Technology 'Space Launcher Liquid Propulsion', 3-6 December 2002, Liege, Belgium

[112] R. B. Clough and J. A. Simmons, *Reproducible acoustic emission signatures by indentation in steels*, Materials Evaluation, **39**, 1981, 1026-1031

[113] C. Kádár, F. Chmelik, J. Lendvai, N. Babcsan and Z. Rajkovits, *Acoustic emission response of metcomb foams during indentation*, Kovové Materiály, **42**, 2004, 265-274.

[114] C. Kadar, F. Chmelik, Z. Rajkovits and J. Lendvai, *Acoustic emission measurement on metal foams*, Journal of Alloys and Compounds, **378**, 2004, 145-150

[115] M. Shiwa, E. R. Weppelmann, A. Bendeli, M. V. Swain, D. Munz and T. Kishi, *Acoustic emission and precision force-displacement observations of spherical indentations into TiN films on silicon*, Surface and Coatings Technology, **68-69**, 1994, 598-602

[116] B. V. Tanikella, K. A. Gruss, R. F. Davis and R. O. Scatterwood, *Indentation and microcutting fracture damage in a silicon carbide coating on an Incoloy substrate*, Surface and Coatings Technology, **88**, 1996, 119-126

[117] M. Walter, S. Nekkanty, E. Cooke and G. Doll, *Instrumented-indentation for mechanical characterisation of boron carbide nano-composite coatings*, Mater. Res. Soc. Symp. Proc., **697**, 2002, P2.8.1-P2.8.6

[118] R. Ikeda, M. Hayashi, A. Yonezu, T. Ogawa and M. Takemoto, *Fracture observation of polycrystalline diamond film under indentation test*, Diamond and Related Materials, **13**, 2004, 2024-2030

[119] A. Yonezu, H. Cho, T. Ogawa and M. Takemeto, *Advanced indentation technique for strength evaluation of hard thin film*, Science and Technology of Advanced Materials, **7**, 2006, 97-103

[120] A. Yonezu, T. Ogawa and M. Takemoto, *Evaluations of elasto-plastic properties and fracture strength using indentation technique*, Key Engineering Materials, **353-358**, 2007, 2223-2226

[121] A. Daugela and J. T. Wyrobek, *Thin film characterization by acoustic emission monitoring of nanoindentation*, IEEE Transaction on Magnetics, **581**, 2000

[122] X.-G. Ma, K. Komvopoulos and D. B. Bogy, *Nanoindentation of polycrystalline silicon-carbide thin films studied by acoustic emission*, Applied Physics Letters, **85**(10), 2004

[123] Y. Tsukamoto, H. Kuroda, A. Sato and H. Yamaguchi, *Microindentation adhesion tester and its application to thin films*, Thin Solid Films, **213**(2), 1992, 220-225

[124] M. Belmonte, A. J. S. Fernandes, F. M. Costa, F. J. Oliveira and R. F. Silva, *Acoustic emission detection of macro-indentation cracking of diamond coated silicon*, Diamond and Related Materials, **12**, 2003, 1744-1749

[125] M. Amraval, F. J. Oliveira, M. Belmonte, A. J. S. Fernandes, F. M. Costa, R. F. Silva, *Tailored Si_3N_4 Ceramic Substrates for CVD Diamond Coating*, Surface Engineering, **19**(6), 2003, 410-416.

[126] Q. H. Fan, J. Gracio and E. Pereira, *Comparison of the adhesion of diamond coatings using indentation tests and micro-Raman spectroscopy*, Journal of Applied Physics, **86**(10), 1999, 5509-5514

[127] Q. H. Fan, J. Gracio, N. Ali and E. Pereira, *Comparison of the adhesion of diamond film deposited on different materials*, Diamond and Related Materials, **10**, 2001, 797-802

[128] J. von Stebut, F. Lapostolle, M. Bucsa and H. Vallen, *Acoustic emission monitoring of single cracking events and associated damage mechanism analysis in indentation and scratch testing*, Surface and Coatings Technology, **116-119**, 1999, 160-171

[129] A. N. Netravali, D. Stone, S. Rouff and L. T. T. Topoleski, *Continuous micro-indenter push-through technique for measuring interfacial shear strength of fiber composites*, Composite Science and Technology, **34**, 1989, -303

[130] N. Ali, Q. H. Fan, J. Gracio, E. Pereira and W. Ahmed, *A comparison study of diamond adhesion on ductile metals*, Thin Solid Films, **377-378**, 2000, 193-197

[131] M. A. Hamstad, A. O'Gallagher and J. Gary, *Effects of lateral plate dimensions on acoustic emission signals from dipole sources*, Journal of Acoustic Emission, **19**, 2001, 258-274

[132] C. K. Lee, P. D. Wilcox, B. W. Drinkwater, J. J. Scholey, M. R. Winsom, M. I. Friswell, *Acoustic emission during fatigue crack growth in aluminium plates*, ECNDT 2006-Mo.2.1.5, 1-8

[133] DD ENV 843-4 (1995), Advanced technical ceramics-Monolithic ceramics-Mechanical properties at room temperature; Part 4: Vickers, Knoop and Rockwell superficial hardness tests

[134] BS EN ISO 6507-1, 2, 3: Metallic materials-Vickers hardness test, BSI, London, 1998

[135] ASTM E 92-82 (1992), Standard test method for Vickers Hardness of Metallic Materials

[136] L. Pawlowski, 1995, *The Science and Engineering of Thermal Spray Coatings*, John Wiley & Sons Publisher, New York

[137] Surface Engineering, *Process Fundamentals and Applications, Lecture Notes of SERC School on Surface Engineering*, 16-23 July 2003, Vol. 1, Dept. of Science & Technology, Govt. of India, Hyderabad, India

[138] I. M. Hutchings, *Strain Effects in Microparticle Impact*, Journal of Physics D: Applied Physics, **10**, 1977, 179-184

[139] P. Fauchais, M. Fukumoto, A. Vardelle, M. Verdelle, *Knowledge Concerning Splat Formation: An Invited Review*, Journal of Thermal Spray Technology, **13**(3), 2004, 337-360

[140] E. Turunen, *Diagnostic tools for HVOF process optimi*zation, PhD thesis, Helsinki University of Technology, Finland, December, 2005

[141] P. Bohm, H. A. Crostack, M. Dvorak and H. D. Steffens, *Monitoring the thermal coating process by means of acoustic emission analysis*, Non-Destructive Testing, Proceedings, 12th World Conference, Amsterdam, **1**, 23-28 April, 1989, 447-452

[142] H. A. Crostack, G. Reuss, T. Gath, and M. Dvorak, *On-line quality control in thermal spraying using acoustic emission analysis*, TS93 Thermal Spraying Conference, Proceedings, DVS Berichte, No.152, Aachen, Germany; 3-5 March, 1993, 208-211

[143] E. Lugscheider, F. Ladru, H. A. Crostack, G. Reuss, T. Haubold, *On-line process monitoring during spraying of TTBCs by acoustic emission analyses*, Proceedings, United Thermal Spray Conference and Exposition UTSC '99, Dusseldorf, 17-19 March, 1999, 312-317

[144] S. Nishinoiri, M. Enoki and K. Tomita, *In situ monitoring of microfracture during plasma spray coating by laser AE technique*, Science and Tech. of Adv. Materials, **4**, 2003, 623-631

[145] BS EN ISO 14921, Thermal spraying—Procedures for the application of thermally sprayed coatings for engineering components, BSI, London, 2001.

[146] J. F. Li, C. X. Ding: '*Polishing-induced pull outs of plasma sprayed Cr3C2-NiCr coating*', Journal of Materials Science Letters, **18**, 1999, 1719 – 1721

[147] ASTM, "ASTM E976-99: Standard guild for determining the reproducibility of acoustic emission sensor response," Annual Book of ASTM Standards, Vol. 3.03, 1999, pp. 395-403.

[148] ASTM E 384-89 (1997): 'Standard test method for microhardness of materials.

[149] BS 5411-6: 1981/ISO 4516: 1980: Methods of test for Metallic and related coatings-Part 6: Vickers and Knoop microhardness tests

[150] M. Rückert, J. Wigren and K. W. Couch, *How to define the true structure of 88/12 WC/Co and how to find the correct preparation method*, A paper based on results achieved after the Plasma Spray Coatings Symposium at STRUERS, Copenhagen, May 25-27th, 1988 (Copenhagen, November 1988), 1-13

[151] J. Karthikeyan, A.K. Sinha, and A.R. Biswas, *Impregnation of thermally sprayed coatings for microstructural studies*, Journal of Thermal Spray Technology, **5**(1), 1996, 74-78

[152] J. Blaha, C. Krempaszky and E. A. Werner, *Carbide distribution effects in cold work tool steel*, 6th International Tooling Conference, 289-298

[153] K. Firth, R. D. Garwood, *Fractography and fracture toughness of 5% Cr-Mo-V ultra-high-strength steel*, Proceedings of the conference-Fracture toughness of high-strength materials: Theory and practice, Dept. of Metallurgy, University of Sheffield, 27-29 March 1968, The Iron and Steel Institute, London, ISI Publication 120, 1970, 81-89

[154] B.S. Mann, V. Arya, A.K. Maiti, M.U.B. Rao, P. Joshi, *Corrosion and erosion performance of HVOF/TiAlN PVD coatings and candidate materials for high pressure gate valve application,* Wear, **260**, 2006, 75–82

[155] G. Bolelli, L. Lusvarghi, T. Varis, E. Turunen, M. Leoni, P. Scardi, C. L. Azanza-Ricardo, M. Barletta, *Residual stresses in HVOF-sprayed ceramic coatings,* Surface & Coatings Technology, **202**, 2008, 4810–4819

[156] P .S. Babu, B. Basu, G. Sundararajan, *Processing-structure-property correlation and decarburization phenomenon in detonation sprayed WC-12Co coatings*, Acta Materialia, **56**, 2008, 5012-5026

[157] A. K. Sharma, S. Aravindhan and R. Krishnamurthy, *Microwave glazing of alumina-titania ceramic composite coatings,* Materials Letters, **50**, 2001, 295-301

[158] J. Stokes and L. Looney, *Residual stress in HVOF thermally sprayed thick deposits,* Surface and Coatings Technology, **177-178**, 2004, 18-23

[159] P. Bansal, P. H. Shipway and S. B. Leen, *Effect of particle impact on residual stress development in HVOF sprayed coatings*, Journal of Thermal Spray Technology, **15**(4), 2006, 570-575

[160] T. Morishita, S. Osawa and T. Itsukaichi, *HVOF ceramic coatings*, Thermal Spray 2004: Thermal Spray Solutions – Advances in Technology and Application, ASM International, Materials Park, OH, USA; Proceedings CD, Section: HVOF-Processes and Materials I, 1–4.